Étude quantitative TEM et STEM du mûrissement de nanoparticules de Pt et de semi-conducteur ferromagnétique Ge(Mn)

Eric Prestat

UNIVERSITÉ DE GRENOBLE

KIT

THÈSE

Pour obtenir le grade de

DOCTEUR DE L'UNIVERSITÉ DE GRENOBLE

préparée dans le cadre d'une cotutelle entre l'*Université de Grenoble* et le *Karlsruher Institut für Technologie*

Spécialité : **Nanophysique**

Arrêté ministériel : 6 janvier 2005-7 août 2006

Présentée par

Eric Prestat

Thèse dirigée par **Pascale Bayle-Guillemaud** et **Dagmar Gerthsen**

préparée au sein de l'**Institut Nanoscience et Cryogénie** et du **Karlsruhe Institute of Technology**
et de l'**Ecole Doctorale de Physique** de l'**Université de Grenoble**

Quantitative TEM and STEM Study of Pt-Nanoparticles Coarsening and Ge(Mn)-based Ferromagnetic Nanostructures

Thèse soutenue publiquement le **12 juillet 2013** à **Karlsruhe**,
devant le jury composé de :

Pr Dieter Zeppenfeld
Professeur au Karlsruhe Institute of Technology, Président

Pr Cécile Hébert
Professeur à l'Ecole Polytechnique Fédéral de Lausanne, Rapporteur

Pr Florian Banhart
Professeur à l'Université de Strasbourg, Rapporteur

Pr Jörg Schmalian
Professeur au Karlsruhe Institute of Technology, Examinateur

Pr Wim de Boer
Professeur au Karlsruhe Institute of Technology, Examinateur

Dr Pascale Bayle-Guillemaud
Directeur de recherche à l'INAC de Grenoble, Directeur de thèse

Pr Dagmar Gerthsen
Professeur au Karlsruhe Institute of Technology, Directeur de thèse

Quantitative TEM and STEM Study of Pt-Nanoparticles Coarsening and Ge(Mn)-based Ferromagnetic Nanostructures

Zur Erlangung des akademischen Grades eines
Doktors der Naturwissenschaften
von der Fakultät für Physik
des Karlsruher Instituts für Technologie (KIT)

vorgelegte
Dissertation
von

Dipl.- Phys. Eric Prestat

aus Migennes, Frankreich

Tag der mündlichen Prüfung: 12. July 2013

Referentin: Prof. Dr. D. Gerthsen
Referentin: Dr. P. Bayle-Guillemaud

angefertigt am
Laboratorium für Elektronenmikroskopie, Karlsruher Institut für Technologie (KIT)
und
Institute for Nanoscience and Cryogenics, CEA Grenoble and Joseph Fourier University

Acknowledgments

Many people have helped me during this thesis. This work is the results of collaborations with numerous people. I would like to thank all of them.

First of all, I am very grateful to my supervisors Pascale Bayle-Guillemaud and Dagmar Gerthsen for giving me the opportunity to work in their respective laboratories. The working conditions in their groups have made fruitful research possible.

I would also like to thank the referees Cécile Hébert and Florian Banhart for their reviews and comments on this work.

Radian Popescu bin ich für die Zusammenarbeit dankbar. Ich danke auch Erich Müller, Manuel Dries für die wissenschaftliche Diskussionen. Allen nicht namentlich erwähnten Mitarbeitern des Instituts danke ich ebenfalls für ihre Unterstützung mit Rat und Tat und das angenehme Arbeitsklima am LEM.

Je voudrais particulièrement remercier ceux avec qui j'ai le plus travaillé durant cette thèse : Pascale Bayle-Guillemaud pour son encadrement et son aide exhaustive ; André Barski pour ses efforts lors de la croissance d'échantillons et son aide scientifique ; Matthieu Jamet pour être le moteur des études tournant autour du système GeMn. Ce fut un plaisir de travailler avec eux aussi bien sur le plan humain que sur le plan scientifique.

Hanako Okuno a joué un rôle important dans cette thèse en m'iniciant à la préparation d'échantillon en biseau : je la remercie pour son aide et nos indénombrabes discussions.

Merci aux microscopistes grenoblois pour les discussions et les manips : Miguel Haro-Lopez, Adrien Boulineau, Eric Robin, Catherine Bougerol, P-H Jouneau, Martien Den Hertog, Yannick Martin, Donatien Robert, Christophe Arm, Jean-Luc Rouvière, Nicolas Mollard, Bastien Bonef. Merci à Laure Guetaz pour les discussions en tout genre, que ce soit sur "la microscopie de grand-père" (comme disent certains) ou d'autres sujets. I am also grateful to Jim Zuo for the fruitful collaboration.

Merci à mes collègues de L_sim: Pascal Pochet, Emmanuel Arras et particulièrement Frédéric Lançon pour les intéressantes discussions. Merci aussi à Edith Bellet-Almaric pour les manips de diffraction de rayon X. Merci à Clément Porret, Abhinav Jain, Dimitri Tainoff pour nos discussions et la croissance d'échantillons.

Merci à mes collocataires permanents ou régulièrement temporaires qui m'ont accompagné durant cette thèse : Jérémie, Ben, Piergent, Rachel, Jeff. Enfin, merci à Cédric pour ses tentatives d'aides en programmation qui n'ont pas (encore ?) vraiment portées ses fruits.

Contents

1. Introduction

Contents

Nowadays, nanotechnology becomes more and more important in the everyday life. The most obvious evidence of its impact is the huge progress in electronics mainly since 1980. Nanotechnology also contributes to the development of other fields such as production and storage of new energies (fuel cells, batteries, solar cells, ...), catalysis, medicine or biology. To achieve this development one needs to understand and control at the nanometer scale (1 nm = 10^{-9} m) the synthesis of these new nanomaterials, the phenomena involved, their aging and their related macroscopic properties. However, if nanotechnologies offer new possibilities for a lot of applications, there are plenty of phenomena which can be hardly studied mainly due to the very small scale at which they occur.

To control and manage new properties, to be able to propose new geometries leading to remarkable new properties it is necessary to understand the phenomena occurring at the nanoscale. The framework of Nanosciences is devoted to give answers to these questions and only a good understanding of nanoscaled phenomena can lead to beneficial nanotechnologies. Nanosciences and Nanothechnologies use and develop new materials to be investigated. It is obvious that electron microscopy is in most cases an interesting and powerful tool to study chemical and structural properties of these nanomaterials and provide data for the understanding of their physical properties.

This thesis deals with the study of nanostructured materials and we focused our work on Pt nanoparticles, GeMn nanocolumns or GeSi quantum dots fabricated by a bottom-up approach. All these samples were prepared by assembling atoms to the desired structures and were produced by evaporating material from pure material sources. Each of these systems have particular physical properties due to nanoscaled size and particular geometry (nanoparticles, nanocolumns, dots). The motivation of this work was therefore to investigate these nanostructured systems by electron microscopy in order to provide as much of quantitative and localized information as possible to help understand their physical properties and behavior.

Transmission electron microscopy (TEM) is a kind of microscopy that uses an electron beam to illuminate a specimen and to form a magnified image. The resolving power of transmission electron microscope could be so high today that it can image and resolve single atom. Beside its high spatial resolution, it has two important advantages:

- it gives a direct observation, *i.e.* an image of the object being studied.
- the strong interaction of electrons with matter provides a huge amount of information about the specimen.

For these reasons TEM is one of the most appropriate techniques to study nanomaterials and is widely used for materials sciences and nanosciences purposes. However, the analysis of signals generated by the interaction of the electron beam with the specimen is usually not straightforward, making transmission electron microscopy also a very interesting topic by itself. This means that a good knowledge of the signal formation is important to make a good interpretation. In this work, we have used imaging and spectroscopic techniques. Most of the microscopes used were equipped with new generation of optics like new guns or cs-correctors, and detectors. It important to point out here that most of the results presented here will not have been obtained without this new generation of TEMs. Coupling of imaging and spectroscopy measurements is very helpful for quantifying data and for this purpose we developed a new approach enabling to quantify HAADF signal using complementary EELS measurements. Moreover, the nanoscale of our sample implies that very low signal is generated by the electron beam interaction with small volumes. We had then to manage our investigations dealing with very low signal in particular for EELS analysis, so statistical analysis of the data set was necessary to get reliable information.

Much of the efforts of this thesis was devoted to use as best as possible the opportunities to work with advanced electron microscopes to study nanomaterials. Special care was then taken to extract precise and accurate information from the sample preparation, the acquisition protocol and the data analysis coupled with simulations.

TEM was then the main tool of investigation for Pt nanoparticles, GeMn nanocolumns and GeSi quantum dots and the motivations of these studies are introduced below.

1.1. Coarsening of Pt nanoparticles

Nanoparticles (NPs) are very small objects with sizes ranging between 1 to 100 nm. Due to their small size, they exhibit a large surface for a small volume (*i.e.* high surface-to-volume ratio). In most of cases this characteristics leads to unique physical and chemical properties compared to their bulk counterparts.

Understanding the formation and evolution of NPs on a surface is relevant from a fundamental and technological point of view. Metallic NPs are widely applied in heterogeneous catalysis to speed up chemical reactions at high temperatures. In electrocatalysis, Pt NPs are already used in proton-exchange membrane fuel cells operated at low temperatures where possible mechanisms for surface area loss of Pt NPs supported on carbon were studied [Shao 07]. Moreover, Pt or Au NPs are promising for future cancer therapy [Porc 10, Hain 04]. Hainfeld et al. reported the enhancement of the one-year survival from 20 % to 86 % by a single intravenous injection of 1.9 nm diameter gold NPs before x-ray therapy of tumorous mice. This improvement can be mainly explained by the preferential absorption of x-rays by high-atomic-number NPs. However, beside their high chemical reactivity and biological activity, the small size of NPs allows them to penetrate into the living cell. This can be the cause of toxicity because larger NPs are not taken up by cells [Buze 07], which have been demonstrated in case of NPs made from different materials [Karl 08, Gehr 11].

Most interesting properties of NPs depend on their size and shape [Allo 09]. Typically, an ensemble of NPs with different sizes will develop towards an ensemble with fewer NPs and larger average size. This phenomenon is called coarsening or sintering and can drastically affect their properties and therefore restrict their applications. However, despite of its importance, the kinetics of Pt-NP formation and coarsening is only understood to a limited degree due to its complexity [Wang 10]. This is the reason why only few quantitative reports were published on the coarsening mechanisms of supported Pt NPs. Many investigations performed in the past improved the understanding of nucleation and growth of supported metallic NPs. Recently, direct observations of Ostwald ripening of Pt NPs on amorphous substrates, such as amorphous SiO_2 and Al_2O_3, were reported [Simo 10, Simo 11]. Other studies were published on the coarsening kinetics of a Pt-NP ensemble or the diffusion behavior of Pt adatoms on crystalline substrates, like metals or highly oriented pyrolytic graphite [Lee 98, Bass 70, Tson 75, Kell 90, Kell 92, Kell 93a, Kell 93b, Kell 94, Lind 99]. There are also a few studies, which report the effect of substrate coverage on the Pt-NP ripening on amorphous carbon substrates [Evan 94, Blac 94, Andr 02]. However, these basic studies mainly deal with model systems to get more insight in the fundamental processes of coarsening. They can be also considered as a first step towards quantitative understanding more complex systems. In this work we extend the state of knowledge by quantitatively describing the coarsening of Pt NPs on a-C films.

1.2. GeMn-based ferromagnetic semiconductor

Spintronic is an emerging field of electronics exploiting the intrinsic spin of the electron in addition to its fundamental electronic charge. It originates from discoveries in 1970s concerning spin-dependent electron transport phenomena. A significant discovery in spintronic is the giant magnetoresistance (GMR) in metallic layer by Fert et al. [Baib 88] and Grünberg et al. [Bina 89]. This great advancement is tremendously used as magnetic field sensors in nowadays electronic devices to read data in common hard disk drive or magnetoresistive random-access memory (MRAM). The sensitivity and very small size of such magnetic field sensors make possible the unbelievable storage capacity of present hard drive disks.

The scaling down of Si-based conventional electronic devices has almost reached its physical limits, and alternative innovative solutions are required. Spintronic offer promising possibilities by adding extra degree of freedom of spin to conventional electronic devices. For example, the manipulation of spin in a semiconducting material could allow the combination magnetic storage of information with electronic readout in a single device, yielding faster and more efficient data treatment. This new scheme requires spin injection into semiconducting materials. A spin-polarized-current can not be simply obtained by contacting a ferromagnetic metallic material to a semiconducting material, since the difference in resistivity between a metal and a semiconductor create a spin accumulation at the interface and prevent any spin-polarized current injection [Schm 00]. The spin accumulation can be avoid by introducing a tunnel barrier between the metallic electrode and the semiconducting material. With this manner spin injection at room temperature was recently demonstrated in Ge by several groups [Jeon 10, Jain 11].

An other way to create spin-polarized-current is to use multifunctional material, such as ferromagnetic semiconductors (FMS). They are of great interest, as they make use of the charge and the spin of electrons in the same material. Basically, they are obtained by doping semiconductors with magnetic atoms, such as transition metals. Ferromagnetic semiconductors can create spin polarized current, which can be then injected into nonmagnetic semiconductors without resistive contact.

The best known FMS is GaMnAs, which typically contains a few percent of Mn randomly substituting the semiconductor atoms [Diet 02]. However, the highest Curie temperature (T_c) reported so far in GaMnAs is about 170 K, much lower than room temperature, preventing any practical applications in spintronics. Major efforts are made to increase the T_c until room temperature, and other systems are investigated. Group-IV (Si, Ge) FMS are of particularly interest due to their compatibility with nowadays silicon technology. Since the seminal work published in 2001 and 2002

by Park *et al.* [Park 01, Park 02] on Mn-doped germanium films, the GeMn material became intensively studied. Beside ferromagnetic order reaching the room temperature, it was found that Mn atoms segregate and form Mn-rich nanostructures [Jame 06, Boug 06, Li 07, Devi 07, Boug 09]. The occurrence of nano-scaled spinodale decompostion can be a way to fabricate FMS with high T_c and improved electrical properties [Sato 05]. In order to control the Mn segregation, Ge(Mn) thin film have been growth by low temperature molecular beam epitaxy (LTMBE). Since the magnetic properties and T_c depends drastically on the growth parameters, a detailed understanding of the formation of these nanostructure is required.

In recent years, quantum dots (QDs) have been successfully grown by self-assembling processes. For optoelectronic device applications, the quantum-dot structures have advantages such as reduced phonon scattering, longer carrier lifetime, and lower detector noise/higher emission yield due to low dimensional confinement effects. Comparing to traditional optoelectronic III-V and other materials, self-assembled Ge quantum dots grown on Si substrates as well as QDs superlattices have a potential to be monolithically integrated with advanced Si-based technology. In addition, Ge QDs in Si could be used in p-i-p or n-i-n photodetectors (PDs) for mid-infrared applications as well as in p-i-n PDs for 1.3–1.55 µm communication applications. Finally, the observation of room-temperature electroluminescence in Ge quantum dots makes them good candidates for the development of infrared light emitting diodes.

By further doping Ge QDs with magnetic impurities like Mn atoms, we aim at making them ferromagnetic. By analogy with diluted magnetic semiconductors like (Ga,Mn)As, the ferromagnetic exchange coupling between Mn atoms has to be mediated by holes introduced in the QDs by p-type co-doping. Ferromagnetic GeMn QDs could then be used in magnetic data storage [Beso 04]. Indeed, each QD can be seen as a single memory bit (O or 1) and the size and density of QDs can be adjusted by growth conditions. Moreover, because they self-assemble on Si, the integration to existing silicon technology should be easily achieved. The challenges are then room-temperature ferromagnetism for practical purpose and the electric field control of the magnetic properties in order to write the dots at very low power consumption. Recently Xiu *et al.* [Xiu 10] have shown promising results in this field. However the interpretation of their results remains highly controversial which clearly motivated this PhD work.

Chapter 2 reviews rapidly the basics of transmission electron microscopy for HRTEM and STEM imaging and EELS spectroscopy, and presents more recent techniques and quantification procedures we have used for this work. The sample preparation and data processing are emphasized to achieve accurate and precise measurements with TEM methods.

Chapter 3 deals with the investigation of the first system investigate, *i.e.* Pt nanopar-

ticles coarsening on amorphous carbon. Two different coarsening processes were identified: dynamic coalescence and Ostwald ripening. The latter have been modeled at different annealing temperatures in order to determine the surface diffusion coefficient of Pt atoms on amorphous carbon.

Chapter 4 presents investigations of Ge and Ge(Mn) quantum dots. In the first part of this chapter, a method have been developed to quantify the HAADF signal at the atomic level using correlative analysis of HAADF and EELS signal. This method have been developed to allow the determination of the surface segregation of Ge during the growth of SiGe heterostructures. In the second part of this chapter, the Mn incorporation in Ge quantum dots has been thoroughly studied using STEM-EELS techniques.

In chapter 5, the composition and the structure of GeMn nanocolumns embedded in pure Ge or GeSn matrix have been investigated using HRTEM and STEM-EELS techniques. The experimental results obtained from HRTEM and STEM-EELS investigation of the GeMn nanocolumns have been discussed with model deduced from first-principles calculations. The magnetic properties of GeMn and GeSnMn layers have been correlated with the results obtained from TEM techniques.

2. Transmission electron microscopy at the angstrom level

Contents

All this work deals mainly with the use of transmission electron microscopy (TEM) to solve material science problems. The aim of this first chapter is to give some important concepts of advanced TEM techniques used for this work for the study of materials at the angstrom scale. To that extent, crucial parameters for high resolution TEM (HRTEM), high resolution scanning TEM (HRSTEM) and electron energy loss spectroscopy (EELS) imaging are exposed.

2.1. Introduction

In microscopy, the achievable spatial resolution defined by the smallest distance between two points that can be resolved, is often limited by the diffraction limit phenomena and can be estimated with the Rayleigh criterion:

$$d = 0.61\frac{\lambda}{\mathrm{NA}} = 0.61\frac{\lambda}{\mu \sin\theta_{\max}} \tag{2.1}$$

where λ is the wavelength, NA the numerical aperture dependent on the refractive index μ and the semi-angle of collection of the magnifying lens $\theta_{\max}$. Therefore, there are two ways to increase the spatial resolution in a microscope: by increasing the numerical aperture NA or decreasing the wavelength. The relatively large wavelength of $\sim$ 400 nm used in light microscopy limits its achievable resolution. TEM was thus developed with the aim to obtain better spatial resolution than in light microscopy. In TEM, the refractive index μ is very close to 1, as the difference of electron velocity in vacuum and in the specimen is very small (mean inner potential of $\sim$ 40 eV is much smaller than the 100 keV electron beam energy). Electron microscopy can provide much smaller wavelength by increasing the energy of the electrons, as shown by the typical electron wavelength reported in Tab. 2.1. The high energy of the electron beam allows to obtain small wavelength and keeping a small numerical aperture NA. However, for the lowest beam energy in Tab. 2.1, the numerical aperture impacts significantly the capacity to resolve the matter at the atomic scale.

In 1959, Feynman introduced in its lecture “There is plenty of room at the bottom” some ideas of the future nanotechnology and suggested that the achievement of better spatial resolution in TEM could be of great help for many fields of research [Feyn 60]. At that time, the spatial resolution in TEM was about 1 nm which was 200 times larger than the diffraction limit. Since that time, huge progress have been done primarily by improved instrumentation and electron optics and the best resolution demonstrated today is better than 50 pm [Erni 09, Taka 11].

E(keV)	v/c	λ(pm)	d (nm)		
			$\theta_{\max} = 10$ mrad	$\theta_{\max} = 30$ mrad	$\theta_{\max} = 50$ mrad
1	0.062	38.75	2.36	0.78	0.473
30	0.328	6.98	0.43	0.14	0.085
60	0.446	4.87	0.30	0.10	0.059
300	0.776	1.97	0.12	0.04	0.024

Table 2.1.: Typical incident beam energy E, ratio v/c is the ratio of the velocity of electron v over the velocity of light c and wavelength λ used in electron microscopy. The corresponding resolution estimated by the Rayleigh criterion in the incoherent case.

The spatial resolution of the electron microscopes is now optimal for observations at the atomic scale and the requirement about the resolving power of microscope highlighted by Feynman is satisfied. Transmission electron microscopy has to move toward more accurate quantification and better sensitivity, to support a better understanding of the problems in materials science. A precise understanding of electron interaction with matter and the principle of image formation in a TEM is imperative.

In a transmission electron microscope, the electron beam is formed by the electron gun and below the condenser system controls this electron beam in order to obtain the desired illumination configuration: a small convergent beam for scanning transmission electron microscopy (STEM) or a broad parallel beam for conventional transmission electron microscopy (CTEM). Then, interactions take place between the electron beam and the sample to finally get an image of the sample. The imaging process in TEM can be then separated in three steps:

- formation of the electron beam,
- interaction of the electron beam with the specimen,
- transfer of the electron wave to the detector.

In this section, we focus first on the interaction of the incident electron wave with matter in the specimen leading to the exit electron wave which propagates in the microscope to form the image. The effects of optical aberrations on the propagation of the electron wave will be presented in order to highlight their consequences for imaging. Then, for each imaging mode *i.e.* HRSTEM and HRTEM, we will consider the particularities in the formation of the beam and the transfer of electron wave to the detector. Afterward, the relevant EELS parameters used for this work are introduced. Finally, the crucial stage of sample preparation is presented.

2.2. Interaction of electrons with matter

2.2.1. Electron scattering

TEM is an efficient signal-generating instrument and a wide range of signals can be generated, as illustrated in Fig. 2.1. Besides photons (X-rays, visible light), transmitted inelastic and elastic scattered electrons are generated. Elastically scattered electrons for which the incoming electrons do not lose energy are used for imaging and inelastically scattered electrons for which an energy exchange takes place within the specimen give information for chemical imaging such as EELS. To fully understand the electron collection by the various detectors used in TEM, one needs to understand the physics that governs the interaction between the electron beam and the specimen. This section does not aim to demonstrate its fundamentals, but to give some insights by explaining the physical meaning of the most important equations.

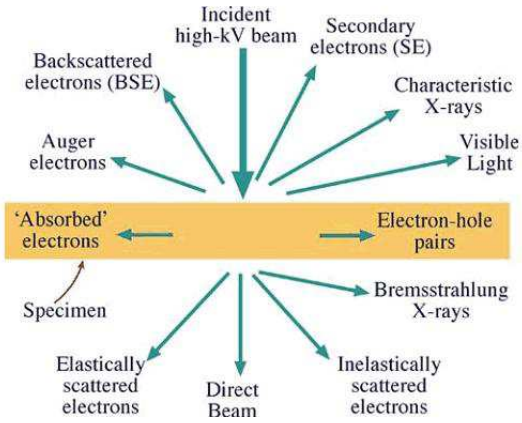

Figure 2.1.: Schematic illustration of the different signals, that can be generated after interaction of a high energy incident electron beam with the specimen in TEM. Taken from [Will 09].

The propagation of electrons in the specimen is governed by their scattering by atoms in the material. In this section, we use the particle picture of electrons to describe the electron scattering in matter. In the next section, we will use the wave nature of electrons to describe interference phenomena, resulting from the coherent interaction of the electron wave with the potential distribution in the specimen.

Elastic scattering occurs by Coulomb interaction of the incoming electrons either with the negatively charged electrons cloud, which results in small angular deviation, or with the positive nucleus resulting in larger angular deviation. The low-angle elastic scattering distribution is highly coherent and results in the formation of diffracted beams at specific angles. The high-angle elastic scattering is usually described by the Rutherford differential cross-section, which can explain the strong dependence of the

high-angle scattered electrons on the atomic number Z. We can described the elastic scattering using the atomic-scattering factor $f_e(\theta)$ which is related to the differential elastic cross section $\sigma_e(\theta)$ by [Will 09]:

$$|f_e(\theta)|^2 = \frac{d\sigma_e(\theta)}{d\Omega} \tag{2.2}$$

where Ω is the solid angle related to the scattering angle θ by $d\Omega = 2\pi \sin\theta d\theta$. $|f(\theta)|^2$ is proportional to the scattered intensity from an isolated atom. The atomic-scattering factor $f_e(\theta)$ can be written [Will 09]:

$$f_e(\theta) = \frac{\left(1 + \frac{E_0}{m_0 c^2}\right)}{8\pi^2 a_0} \left(\frac{\lambda}{\sin\frac{\theta}{2}}\right)^2 (Z - f_x) \tag{2.3}$$

where m_0 is the rest mass of the electron, c the velocity of light, a_0 the Bohr radius of the scattering atom and f_x is the scattering factor for X-rays. Eq. 2.3 shows that $f_e(\theta)$ decreases with increasing scattering angle θ, or decreasing wavelength. For any values of θ, $f_e(\theta)$ increases with Z. Moreover, it is interesting to note that Eq. 2.3 contains both the elastic nuclear scattering at high angle θ (dependence on Z) and the elastic electron-cloud scattering at low angle θ (dependence on f_x).

Inelastic scattering occurs by Coulomb interaction between a high energy incident electron and the atomic electrons that surround each nucleus. Theoretically, it is difficult to accurately describe the inelastic scattering by differential cross-section, due to the various mechanisms involved and the possibility of multiple elastic and inelastic scattering in thicker specimen [Eger 11]. A simple approximation consists in describing inelastic scattering for a given energy loss E_0 by a Lorentzian function:

$$\frac{d\sigma_i(\theta)}{d\Omega} \propto \frac{1}{\theta^2 + \theta_E^2} \tag{2.4}$$

where θ_E is the characteristic scattering angle $\theta_E = E_0/mv^2$. Fig. 2.2 compares differential cross section for elastic and inelastic scattering and shows that inelastic scattering results in much smaller angles than elastic scattering. The curves in Fig. 2.2 are obtained using the Lenz model, as explained in [Eger 11]. If the inelastic scattering is useful to generate signal for chemical analysis, it is also the cause of radiation damage, that can prevent in some situation the specimen to be investigated. Indeed, a large part of energy transfer is converted to heat (phonon) and ionization. In some specimens, it can cause bond ruptures and irreversible radiation damage.

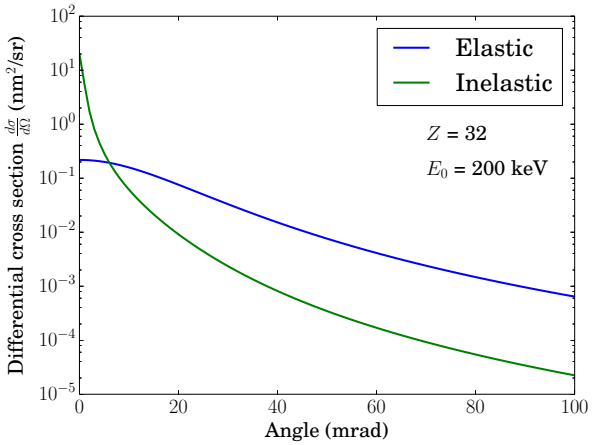

Figure 2.2.: Angular dependence of the differential cross sections for elastic and inelastic scattering calculated using Lenz model [Eger 11]. The calculation considers the scattering of 200 keV electrons by a Ge atoms.

2.2.2. Electron wave propagation in matter

For imaging, the physical quantity of interest is the electron wave after the sample, *i.e.* the exit wave which is governed by the propagation of the wave in the specimen. Only elastic scattering is considered here, as the contribution of inelastic scattering for imaging is small.

Let us start by considering a simple approximation: as TEM use high energy electron beam ($\sim$ 100 keV) and small scattering angle ($\sim$ 20 mrad), we can assume that the electron wave traveling through thin specimen does not undergo a sideways displacement of more than few angstroms. Therefore, we can assume that the electron wave suffers a phase shift corresponding to the diffusing potential distribution $V(\vec{r})$ of the specimen. In this approximation, the specimen is considered to be a phase object as it does not change the wave amplitude of the high energy electron beam. For an incident wave function $\psi_{\text{in}}(\vec{r})$ of the real space coordinate $\vec{r} = (x, y, z)$ scattered by a potential $V(\vec{r})$ of a specimen of thickness t_{tot}, the electron exit wave function $\psi_{\text{exit}}(\vec{r})$ is:

$$\psi_{\text{exit}}(\vec{r}) = \psi_{\text{in}}(\vec{r})t(\vec{r}) \tag{2.5}$$

where $t(\vec{r})$ is the transmission function of the specimen and is a function of the potential distribution $V(\vec{r})$:

$$t(\vec{r}) = \exp\left[-i\sigma \int_0^{t_{\text{tot}}} V(\vec{r'})d\vec{r'}\right] \tag{2.6}$$

with $\sigma = 2me\lambda/h^2$ the interaction parameter which define the strength of the interaction of electron waves with matter. Integrating $V(\vec{r})$ over the specimen thickness, one obtains the projected atomic potential of the specimen $V_p(\vec{r})$. The phase shift being

small ($\sigma V_p(\vec{r}) \ll 1$), the exponential can be expanded in a power series and the exit wave become [Kirk 10]:

$$\psi_{\text{exit}}(\vec{r}) = \psi_{\text{in}}(\vec{r})\mathrm{e}^{-i\sigma V_p(\vec{r})} \sim \psi_{\text{in}}(\vec{r})(1 + i\sigma V_p(\vec{r})) \tag{2.7}$$

Eq. 2.7 describes the scattering of electrons by a small projected potential $V_p(\vec{r})$. This model is called the weak phase object approximation (WPOA). The scattering function $i\sigma V_p(\vec{r})$ gives rise to the distribution of scattered amplitude in the back focal plane. For weak phase scattering, the scattered wave is always 90° out of phase with the incident beam. The phase shift is indicated by the i in the exponential function in Eq. 2.6. If an absorption term has to be included in the model, it could be introduced within the real part. Eq. 2.7 shows that the imaginary part of the wave function contains the structural information, *i.e.* the position of the atoms, of the specimen. In case of a crystal, the projected potential is periodical and creates a phase modulation of the exit wave. Generally, the WPOA is correct only for very thin specimen consisting of light elements. For example, the phase shift induced by a single heavy atoms is so large, that the WPOA is no more correct.

Moreover, the WPOA does not consider the sideways scattering, that is required for more thicker and realistic specimen. To correctly describe the electron propagation within the specimen, more sophisticated model are required. This can be done by considering more fundamental equations. One possibility is to use the time-independent Schrödinger equation with the relativistically corrected electron mass $m = \gamma m_0$ and a diffusing potential distribution $V(\vec{r})$:

$$\left[-\frac{\hbar^2}{2m}\nabla^2 - eV(\vec{r})\right]\psi_f(\vec{r}) = E\psi_f(\vec{r}) \tag{2.8}$$

where∇^2 is the Laplace operator, $\hbar = h/2\pi$ is the reduced Planck's constant, m and e are the electron mass and charge, respectively. Within the high energy approximation, the potential distribution can be considered as a small perturbation, and the wave function $\psi_f(\vec{r})$ in the specimen can be separated into a plane wave traveling in the z direction and an another wave function that vary slowly with position z.

It follows $\psi_f(\vec{r}) = \exp(2\pi i z/\lambda)\psi(\vec{r})$ and the Eq. 2.8 becomes [Dyck 80, Kirk 10]:

$$\left[\nabla_{xy}^2 + \frac{4\pi i}{\lambda}\frac{\partial}{\partial z} + \frac{2meV(\vec{r})}{\hbar}\right]\psi(\vec{r}) = 0 \tag{2.9}$$

where ∇_{xy}^2 is the sum of second derivatives with respect to x and y.

In TEM, two ways are usually considered to solve Eq. 2.9:

- the Bloch wave approach [Beth 28] describes electron scattering within a crystal as the excitation of Bloch waves. This methods works for a periodical potential, *i.e.* for a perfect crystal. Thus, each diffracted beam $\vec{k}_{\vec{g}}$ corresponding to vector $\vec{g}$ of the reciprocal space can be described as a superposition of Bloch waves.

- the multislice approach [Cowl 57] consists in a numerical iterative process to simulate the exit wave. The specimen is sliced in thin layers in order to apply the weak phase object approximation to each layer. Between each layers, the wave is propagated in vacuum over equivalent thickness layer using Fresnel propagator.

We focus here on the multislice approach as we use it for simulating HRTEM and HRSTEM images in the next chapters. Following Van Dyck [Dyck 80], two observations of the Schrödinger equation in Eq. 2.9 can be drawn for studying its physical meaning and for justifying the principle of the multislice approach:

1. If the propagation term is neglected, Eq. 2.9 can be simplified to the phase grating equation:

$$\frac{\partial\psi(\vec{r})}{\partial z} = i\frac{2me\lambda V(\vec{r})}{h^2}\psi(\vec{r}) \tag{2.10}$$

that can be solved using $\psi(\vec{r}) = \exp(i\sigma \int V(\vec{r})dz)$. This justifies the transmission function for phase object introduced in Eq. 2.6;

2. If the potential term is neglected, Eq. 2.9 can be simplified to a diffusion equation:

$$\frac{\partial\psi(\vec{r})}{\partial z} = -\nabla^2_{xy}\psi(\vec{r}) \tag{2.11}$$

The specimen is divided into thin slices which are considered as phase objects. The incident wave function is transmitted through the specimen consisting of these n slices. Fig. 2.3 illustrates the principle of this method where two slices at coordinate z and $z + \Delta z$ are drawn. For the transmission of the wave through each slice, we use the WPOA, and the transmission function $t(\vec{r})$ is calculated using the projected potential averaged between z and $z + \Delta z$. The wave is then propagated over the slice thickness to the next slice using the propagator $p(x, y, \triangle z)$.

This operation is performed by a multiplication of the wave function by the propagator in the Fourier space for all slices. The exit wave is finally determined when the wave is transmitted through the last slice. According to this principle, the multislice equation

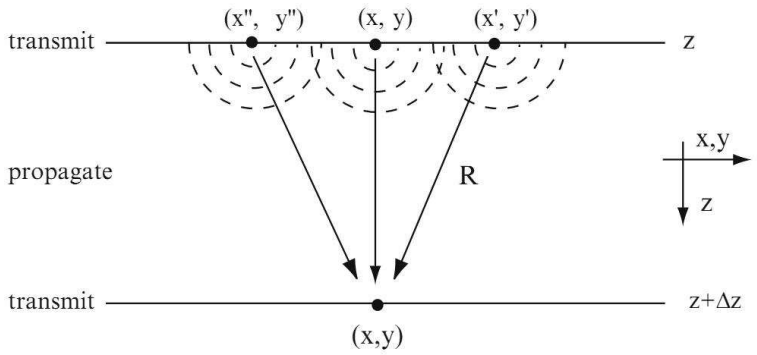

Figure 2.3.: Schematic illustration of the multislice approach. Transmission through thin slices and propagation following Huygens-Fresnel principle between the slices. Taken from [Kirk 10].

can be written as

$$\psi(x,y,z+\triangle z) = \underbrace{p(x,y,\triangle z)}_{\text{propagation}} \otimes \underbrace{[t(x,y,z)\psi(x,y,z)]}_{\text{transmission}} \tag{2.12}$$

the transmission function $t(x,y,z)$ for a thin slice corresponding to the specimen portion between z and $z+\triangle z$ is the given by Eq. 2.6. The phase grating wave $t(x,y,z)\psi(x,y,z)$ is convoluted by the propagator $p(x,y,\triangle z)$, which follows the Huygens' principle and Fresnel diffraction. The propagator function is then defined by the Kirchhoff diffraction integral:

$$\psi(x,y,z+\triangle z) = \frac{1}{2i\lambda}\int \psi(x',y',z)\frac{\exp(2\pi iR/\lambda)}{R}(1+\cos\theta)dx'dy' \tag{2.13}$$

The small angle scattering involved in TEM allows to approximate the distance R shown in Fig. 2.3 by Δz. The propagator can be then simplified to [Kirk 10]:

$$p(x,y,\triangle z) = \frac{1}{i\lambda\Delta z}\exp\left[\frac{i\pi}{\lambda\Delta z}(x^2+y^2)\right] \tag{2.14}$$

The exit wave calculated using the multislice approach takes into account the multiple scattering and the lateral spread of the electron wave through the Fresnel propagator. To minimize the computer calculation in the convolution, the highly efficient fast Fourier transform (FFT) is used. Indeed the total computation time required for direct convolution scales as N^2, whereas in case of FFT it roughly scales as $N\log(N)$.

Eq. 2.12 becomes then

$$\psi(x,y,z+\triangle z) = \mathcal{F}^{-1}\left\{P_n(k_x,k_y,\triangle z)\mathcal{F}\left[t(x,y,z)\psi(x,y,z)\right]\right\} + \mathcal{O}(\triangle z^2) \tag{2.15}$$

where the FFT is noted as $\mathcal{F}$. The high efficiency of the multislice approach allows

to simulate wave function of large models. Theoretically, no periodical conditions are required as in the case of the Bloch-wave approach. However the use of FFT computation can introduce artifacts on the side of the calculated exit wave if the atomic model does not have periodic boundaries. Indeed, the FFT calculation is a discrete Fourier transform and it implies that the sampled data is repeated indefinitely in a periodic array. This effect is known as the wrap around error as the edges of the model effectively wrap around and touch each other [Kirk 10].

2.3. Electron optics

2.3.1. Electron lens, electron wave and phase shift

In this section, the basic theory of transfer function of lenses for electron beam is briefly exposed using the wavelike character of electrons. Electron focusing lenses can either be electrostatic or magnetic , can be used as immersion lens and are more versatile for TEM columns. The most important lens in a microscope is the objective lens as it forms the first image of the object in TEM mode or demagnifies the probe on the sample in STEM mode. The characteristics of this lens mainly determine the performance of the microscope in term of attainable resolution. Nowadays, magnetic lenses in TEM are rotationally symmetric and suffer from aberrations, *i.e.* deviations from ideal lens. Lets consider a simple perfectly rotationally symmetric aberration: the spherical aberration. It is one aberration among a dozen of geometrical aberrations. Fig. 2.4 (a) and (b) shows ray diagrams of an ideal lens and a real lens with spherical aberration, respectively. In the ideal lens, all rays coming from one point P of the object plane converge to another point P' of the image plane as shown in Fig. 2.4 (a), whereas in lens suffering from spherical aberration the rays coming from point P form a disk in the image plane. Indeed, positive spherical aberration reduced the focal length of the off-axis electrons, *i.e.* rays at high angle θ are over-focused (Fig. 2.4 (b)) (θ being the angle between the electron ray and the optical axis). The image of one point P is then in the Gaussian image plane a disk of radius r_φ which dependent on the angle θ as:

$$r_{sph} = 2C_3\theta^3 \tag{2.16}$$

where C_3 is the third order spherical aberration coefficient. In Fig. 2.4(b), the plane in which the disk is smaller is called the plane of least confusion with a radius $r = C_3\theta^3/4$. The main effect of this aberration is a degradation of the capacity for electron microscope to magnify details of the sample.

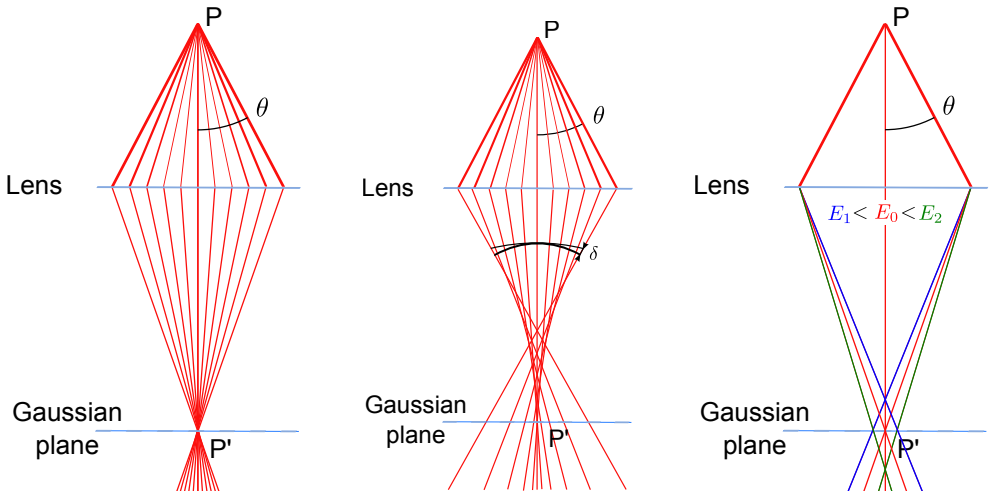

(a) Ideal lens (b) C_3 (c) C_C

Figure 2.4.: (a) Ideal lens focused all rays coming from point P of the object plane to another point P' of the image plane. Real lens with spherical aberration (b) and chromatic aberration (c), the point P is imaged as a disk in the Gaussian plane.

In addition to geometric aberrations such as spherical aberration, the chromatic aberration also cause blurring of the images: magnetic lens does not focus at the same point parallel electron rays with different energies, the point P will be magnified in the Gaussian plane to a disk of radius r_c, as illustrated in Fig. 2.4 (c):

$$r_c = C_c \frac{\Delta E}{E} \theta \tag{2.17}$$

where C_c is the chromatic aberration coefficient and ΔE is the FWHM of the energy distribution of the electron beam. Electron beam have an energy dispersion $\triangle E$ which depends on the emission process, ranging from $\triangle E = 0.3$ eV for a cold field emission gun (FEG) to $\triangle E = 2$ eV for a thermionic gun with a LaB_6 crystal. The electron guns used for this work are Schottky FEG which have a typical energy dispersion of $\triangle E = 0.7$ eV at 200 kV.

In term of wave description, the aberrations act as a deformation of the wavefront. The wavefront being orthogonal to rays the spherical aberration curves more strongly the wavefronts at larger θ that results in a deviation δ and a phase shift χ between trajectories at different θ. The geometrical aberration function $\chi(\theta)$ describes the phase difference from a ideal surface wave. In a rotationally symmetric magnetic lens $\chi(\theta)$ is required to depend only on even powers of θ as odd powers of θ provide non rotationally symmetric deviation. For a spherical-aberration limited microscope with rotationally symmetric magnetic lens, it can be written as [Reim 08]:

$$\chi(\theta) = \frac{2\pi}{\lambda}\delta = \frac{\pi}{2\lambda}(C_3\theta^4 - 2\Delta f\theta^2) \tag{2.18}$$

where Δf is the defocus defined as the deviation of the image plane from the ideal Gaussian plane. Eq. 2.18 reveals that the spherical coefficient can be counterbalanced by defocusing the lens with Δf, following the so-called Scherzer condition [Sche 49]. In the wave description, the angle θ between the rays and the optical axis is related to the wave vector $\vec{k}$ of the spatial frequency space by multiplication with the electron wavelength λ:

$$\theta = \lambda|\vec{k}| \tag{2.19}$$

This equation basically shows that high spatial resolution, *i.e.* high spatial frequency, required large angle θ. For this reason, the design of the objective lens is optimized to introduce as less as possible phase shift $\chi(\theta)$ at large angle θ. Concretely, a microscope have to be able to transfer correctly electron ray at high angle θ to perform high resolution imaging.

Following the Rayleigh criterion (Eq. 2.1), the revolving power of a geometrical-aberration limited instrument can be defined as the smallest value of θ for which the deviation δ is equal to $\lambda/4$. In term of phase χ, the maximum tolerable aberration phase shift is $\pi/2$

2.3.2. Aberration correction

In the precedent section, aberrations and their consequences on electron optics have been introduced. Theoretically, Scherzer demonstrated that electrons lens with rotational symmetric electromagnetic fields suffers from spherical and chromatic aberration [Sche 36]. In practice, the value of the spherical aberration coefficient is related to the gap width of the magnetic pole piece lens. From mechanical consideration, it can not be designed as small as desired since there is a need to be able to insert a specimen close to the objective lens. There is then a need to correct the spherical aberration in order to improve the spatial resolution. Aberration correction to improve spatial resolution can be performed either by software or hardware methods.

The software methods can be experimentally performed by reconstruction of the electron object wave either by off-line or in-line holography. The off-line holography required a bisprism insert in the TEM allowing acquisition of holograms from which the phase can be extracted. The in-line holography for phase retrieval, consists in the acquisition of series of images at different focus or different tilts of the incident beam. The amplitude and the phase of the wave can be obtained using reconstruction approach [Thus 96]. Depending on the algorithm used, artifact can be introduced and it can fail to reconstruct the high resolution wave correctly. In both cases, the reconstructed wave can be numerically corrected for aberrations. Those two post-acquisition corrections

(off-line and in-line holography) have the two main drawbacks in the high resolution case: they are difficult to perform experimentally, due to high stability requirement and low signal-to-noise ratio. Moreover, they have limited field of view since they required high sampling. For those reasons, there are rarely used.

The hardware methods uses non-rotational symmetrical lenses added in the microscope columns, such as multipole element, e. g. quadrupole, hexapole, octupoles. A multipole element consists in an even number of poles. For example, the most simple multipole is the deflector, which is made of two poles. Fig. 2.5 shows the setup of an aberration corrector in CTEM and STEM.

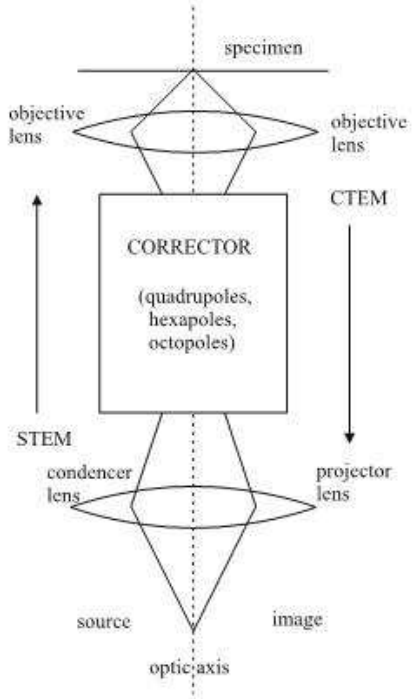

Figure 2.5.: Placement of the corrector in the column for STEM and CTEM mode. The labels on the left and right side correspond to the STEM and TEM configurations, respectively. The corrector introduce a negative C_3 to counterbalance the positive C_3 of the objective lens. Taken from [Kirk 10].

Theoretically, the principles of aberration correction are known since 1947 [Sche 47], however it was difficult to implement practically mainly due to the complicated alignment procedure of the different elements together. Indeed, aberration correctors are composed of a rather sophisticated ensemble of focusing multipole elements. The recent development of such correctors are mainly due to advances in fast computer and algorithms required for performing the alignment. The first hardware spherical aberration correction was achieved by Haider *et al.* on a 200 kV transmission electron microscope installed in Jülich [Haid 98].

In sec. 2.3.1, the defocus and spherical aberration were presented. To fully describe the aberration of electron optical system, aberrations of different order and symmetry have to be considered. The order of θ can be defined either in the wave aberration (Eq. 2.18) or in the image aberration function, which estimate the radius of the disk of least confusion (Eq. 2.16). There is a one order difference between both aberration functions, and we usually consider the order of aberration with respect to the image aberration function. The wave aberration function is illustrated for each aberration coefficient in Fig. 2.6. The aberration symmetry of the estimated phase plate can be used during corrector-alignment operation to recognize the geometrical aberration that need to be corrected.

Similarly as the the defocus $\Delta f = -(C_3\lambda)^{1/2}$ counterbalances the spherical aberration (minimization of $\chi(\theta)$ in Eq. 2.18) in C_3-limited microscope, the fifth order spherical aberration can be compensated in C_5-limited microscope by setting the third order spherical aberration coefficient C_3 to a negative value of a few micrometer $C_3 = -2.88(C_5^2\lambda)^{1/3}$, and the defocus to $\Delta f = 1.56(C_5\lambda^2)^{1/3}$, where C_5 is the fifth order spherical aberration coefficient [Chan 06]. This optimal setting is of importance, when the microscope is working at low accelerating voltage, such as 60-80 kV, because the effect of aberration is stronger on the reachable resolution. After correction of the geometrical aberration, the limiting factor is the chromatic aberration C_c. There are two manners to lower the effects of the chromatic aberration: one can either use a C_c corrector to set $C_c = 0$ or use a monochromator to reduce the energy dispersion ΔE. The C_c correction method is still in development and the first results were obtained within the TEAM project [Kabi 09]. Very recently, one of its first application with the FEI PICO microscope in Jülich were published [Urba 13]. The electron beam monochromation already demonstrated interesting results [Kisi 08] and is used for specific applications, such as surface plasmon imaging [Scha 09] or the HRTEM imaging of graphene [Meye 08].

Among the myriad of aberrations illustrated in Fig. 2.6, we consider here the most relevant aberrations for application purpose: two-fold, three-fold astigmatism, axial coma and spherical aberration. The first one is of first order and the two last one are of second order. More details about the aberration notation are given in Sawada *et al.* [Sawa 08]. Coma and astigmatism are to due to misalignment or imperfection of the optical system, and can be easily corrected using dipoles and quadrupoles, respectively. The corrector alignment for the aberrations of order ≥ 3 are stable over weeks, so they need to be change rarely, whereas the lower-order aberration have to be align very regularly. Generally, the alignment procedure is greatly enhanced by regular normalization of lenses. The hysteresis loop of the magnetic field in the lenses performed during the normalization allows a better reproducibility of the alignment procedure.

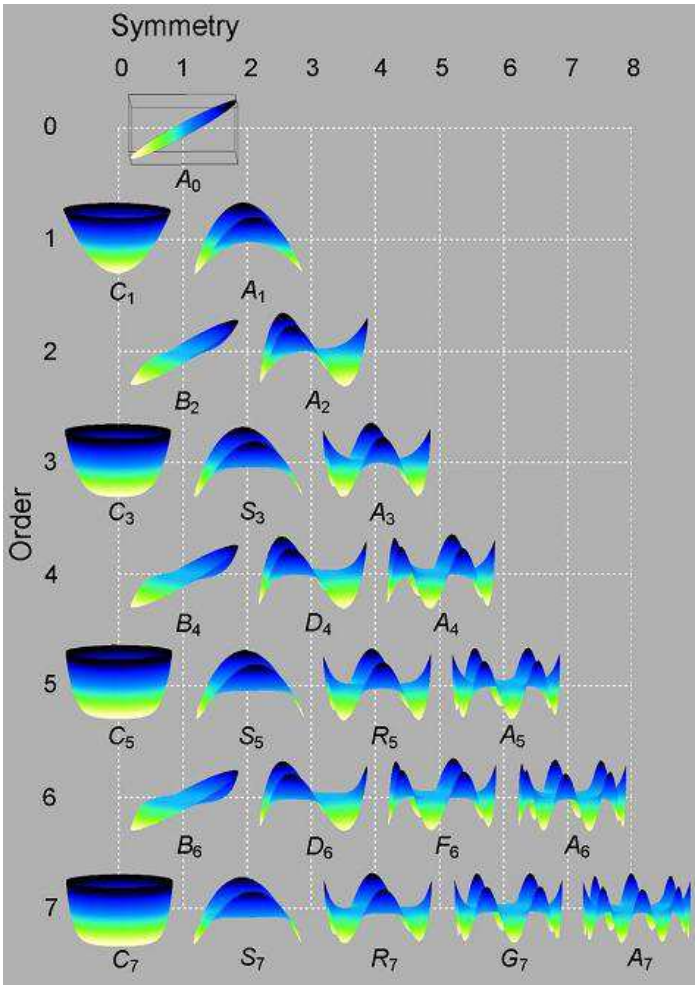

Figure 2.6.: Impact of the different geometrical aberrations on the wave surface. The wave aberration function χ is illustrated for each aberration coefficient. Note that the intrinsic geometric aberration of magnetic lens, *i.e.* the defocus $\triangle f = C_1$ and spherical aberration C_3, C_5 and C_7, are rotationally symmetric. Taken from [Erni 10].

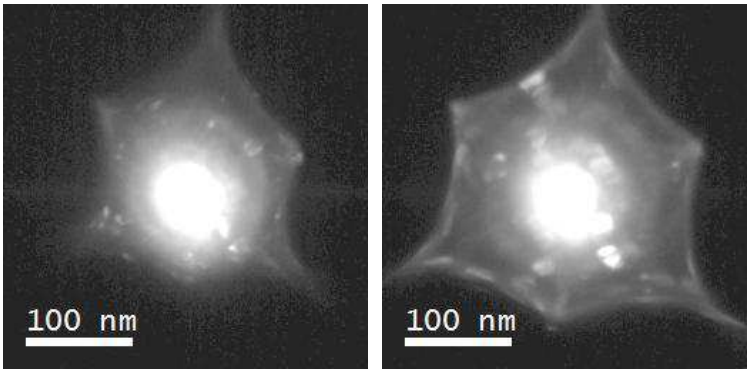

(a) Coma misaligned (b) Coma correctly aligned

Figure 2.7.: Coma alignment of the image corrector. The shadow in the image correspond the cut-off of the microscope. In (a) the transmitted beam is not centered in the corrector, whereas in (b) the centering is fine. The image intensity is shown on a non linear scale.

Indeed, the small shift of tilt required for precise alignment can be very sensitive to the actual values of the magnetic fields of the lenses. Typically, the coma and astigmatism are very sensitive and will depends on the area of the sample. In HRSTEM, coma alignment can be easily done on the ronchigram, whereas in HRTEM, it can not be accurately aligned, because the measurement method of the CEOS software is not accurate enough to correct the coma perfectly. An accurate aberration diagnosis is of importance for the analysis of high resolution imaging. Barthel *et al.* implement a method to better measure the aberrations [Bart 10] whereas Biskupek *et al.* suggest to manually correct the coma aberration on the image, knowing the effect of aberration on the imaged specimen. In their paper they present results considering single wall carbon nanotube [Bisk 12]. On flat thin films such as graphene or amorphous carbon films, the coma can be easily manually corrected by inspecting the focus variation across the image. The film appear at the same focus everywhere on the image if no coma is present. Another way to align the coma in HRTEM is to manually center the transmitted beam in the corrector. By condensing the beam and slightly defocusing (displacement of the stage along the z-axis), a shadow image appear in which the beam has to be centered, as shown in Fig. 2.5. It is a tricky task to align accurately the coma of the image corrector in this way. However, it is useful to correct the coma of the image corrector in STEM mode, for convenient imaging of the probe with minimal aberration.

Practically, aberrations are never completely corrected by the hardware corrector. In case of HRTEM, residual aberrations can be corrected using focal series reconstruction, in order to obtain aberration-free acquisition [Erni 10]. Such experiment on graphene demonstrates interesting results [Jins 11].

The commercially available aberration-corrected microscope clearly enhanced the capabilities of TEM. More precisely, aberration-corrected HRTEM imaging allows unambiguous identification of atomic columns as the delocalization effects are greatly reduced and imaging is performed close to zero defocus conditions. This is of great importance for the study of interfaces, surface, nanoparticles, etc. Before aberration-correction, images simulation was in most of cases required for the full interpretation of HRTEM images. The measurement of atomic displacement is easier and its accuracy is improved. In HRSTEM, the aberration correction allows not only to obtain smaller probe that make the resolution higher but to use larger condenser aperture and provides therefore higher currents required to increase the signal-to-noise ratio (SNR). This is particularly interesting for two-dimensional spectrum imaging as we have often used during this work where small acquisition time for each spectra is required.

For clarification, we distinguish the TEM mode with a broad beam illumination from the mode with convergence illumination by using the following abbreviation:

- conventional transmission electron microscopy (CTEM), which include HRTEM,
- scanning transmission electron microscopy (STEM), which include HRSTEM.

Each technique can elucidate a certain aspect of the specimen, and help to answer a specific problematic about the specimen. The choice of the imaging method is then related to the contrast mechanism involved in the imaging process.

2.4. High resolution transmission electron microscopy (HRTEM)

2.4.1. Coherent imaging

In CTEM, the specimen is illuminated by a broad beam, which can be described by a plane electron wave $\psi_{in}(\vec{r})$, with $\vec{r}$ the real space coordinate $\vec{r} = (x, y)$. Its wave vector $\vec{k_0}$ is parallel to the optical axis. The complex electron wave $\psi_{exit}(\vec{r})$ directly after the specimen is called the exit-plane wave and can be written with an amplitude $a(\vec{r})$ and a phase $\varphi(\vec{r})$ as:

$$\psi_{exit}(\vec{r}) = a(\vec{r})\mathrm{e}^{i\varphi(\vec{r})} \tag{2.20}$$

As explained in sec. 2.2, the exit wave contains the structural information about the specimen. We can consider the exit wave $\psi_{exit}(\vec{r})$, as a set of Bragg diffracted beams $\vec{k_g}$, and the objective lens focuses each Bragg diffracted beam $\vec{k_g}$ to a spot in the back focal plane and form electron diffraction (ED) pattern as shown in Fig. 2.8(a). Understanding HRTEM imaging consists in studying how the different Bragg diffracted beams $\vec{k_g}$ are measured by the detector.

The diffraction lies then in the back-focal plane of the objective lens and the wave function in the back-focal plane is a function of the reciprocal vector $\vec{q}$ and is given by the Fourier transform of the exit wave $\psi_{exit}(\vec{r})$, according to Fourier optics:

$$\psi_{\mathrm{bfp}}(\vec{q}) = \mathscr{F}\left[\psi_{exit}(\vec{r})\right] \tag{2.21}$$

where $\mathscr{F}$ is the Fourier transform. The intensity I_{d} of the diffraction is given by the norm of the wave function in the back-focal plane $I_{\mathrm{d}} = |\psi_{\mathrm{bfp}}(\vec{q})|$.

In case of a crystal, each Bragg diffracted beam corresponds to a particular reciprocal lattice vector $\vec{g}$. When the exit-plane wave passes through the objective lens,

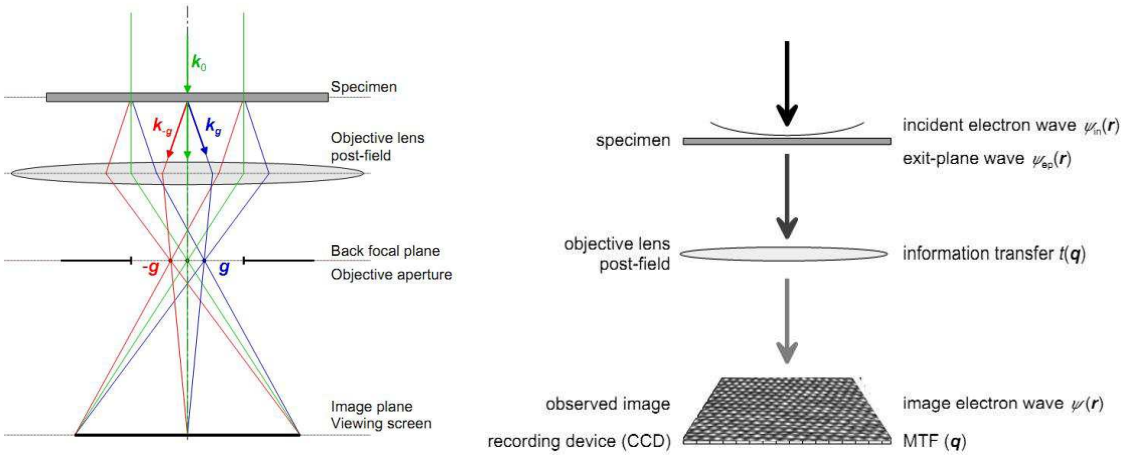

(a) HRTEM imaging (b) Information transfer

Figure 2.8.: Principle of HRTEM imaging in the TEM: (a) Illustration showing the transfer of the different Bragg diffracted beams $\vec{k_g}$ of the exit wave by the post-field of objective lens. (b) Scheme illustrating that the aberration of the objective lens are taken into account in the transfer function. Furthermore the intensity of image is affected by the modulation transfer function (MTF) of the detector. Taken from [Erni 10].

aberrations affect the wavefront (see sec. 2.3.1), as illustrated in Fig. 2.8(b). Indeed, the aberration wave function $\chi(\vec{q})$ define how each spatial frequency of the exit wave $\psi_{exit}(\vec{r})$ is shifted by the aberrations. This alteration of the wave are introduced via the transfer function $T(\vec{q})$ (TF) of the microscope:

$$T(\vec{q}) = \mathrm{e}^{i\chi(\vec{q})} \tag{2.22}$$

The image wave reaching the detector is then the convolution of the exit wave $\psi_{exit}(\vec{r})$ with the inverse Fourier transform $\mathscr{F}^{-1}$ of the TF $T(\vec{q})$:

$$\psi_{\mathrm{ima}}(\vec{r}) = \psi_{exit}(\vec{r}) \otimes \mathscr{F}^{-1}\left[T(\vec{q})\right] \tag{2.23}$$

This equation describes the coherent imaging model. The electron detectors can only measure the intensity of the image wave $I(\vec{r}) = \psi_{\mathrm{ima}}(\vec{r})\bar{\psi}_{\mathrm{ima}}(\vec{r}) = |\psi_{\mathrm{ima}}(\vec{r})|^2$. The coherent imaging model holds for ideal microscope, *i.e.* electron beam without convergence spread, energy dispersion and any instabilities.

2.4.2. Partial coherent imaging

In sec. 2.3.2, it was pointed out that the electron beam has a certain energy dispersion due to electron extraction process. Moreover, it is very difficult to perfectly collimate electron beam. For these reasons, we now introduce the partial coherent imaging model, to take into account these experimental parameters, through the damping envelope functions in the TF:

1. the temporal coherence envelope, that considers the beam instability and the energy spread of the electron source,
2. the spatial coherence envelope, that considers the finite size of the electron source and the convergence of the electron beam.

The source energy spread, high voltage and current lens instability slightly change the electron wavelength. Because of the random nature of the instability, each instability spread distribution can be approximated by a Gaussian function. Convolving each Gaussian instability distribution results in a Gaussian distribution with a standard deviation equal to the quadratic sum of each standard deviation[1]. Because the effect of the chromatic aberration is to focus electron of different energy at different planes, the total effect of temporal coherency variations is to create a Gaussian focal spread distribution of a few nm, with a standard deviation $\triangle C$ given by:

$$\triangle C = C_c \sqrt{\left(\frac{\Delta E_{\mathrm{RMS}}}{E}\right)^2 + \left(\frac{2\Delta I}{I}\right)^2 + \left(\frac{\Delta U}{U}\right)^2} \tag{2.24}$$

where, ΔE_{RMS} is the root-mean-square (RMS) energy spread of the electron beam related to the FWHM of the energy spread ΔE by $\Delta E = 2.355 \Delta E_{\mathrm{RMS}}$ [Erni 10]. This incoherent superposition of images with different defocus results in a damping of the high spatial frequencies. When the beam current is high, the Boersch effect, that describes the Coulomb repulsive interactions between individuals electrons in the beam, should be taken into account as an additional contribution to $\triangle C$.

To take into account the effect of the temporal coherence envelope, the intensity of the image wave has to be changed to:

$$I(\vec{r}) = \int I_\delta(\vec{r}) f(\delta) d\delta \tag{2.25}$$

where $f(\delta)$ is a function of the fluctuation δ around the defocus $\triangle f$, which can be described by a Gaussian distribution with a FWHM $\triangle C$. Similarly, the convergence of the electron beam and the finite source size can be modeled by the introducing a

[1] the convolution of two Gaussian function with standard deviations σ_a and σ_b is a Gaussian function with a standard deviation $\sigma_{a \otimes b} = \sqrt{\sigma_a^2 + \sigma_b^2}$

dispersion of the incident plane waves $\vec{k_0}+\vec{q}$, where $\vec{k_0}$ is the wave vector of the incident plane wave and is parallel to the optical axis. It follows for the intensity of the image wave:

$$I(\vec{r}) = \int I_{\vec{q}}(\vec{r}) s(\vec{q}) d\vec{q} \tag{2.26}$$

where $s(\vec{q})$ is the counterpart of the $f(\delta)$ function for the angular spread of the electron source. Once again it can be approximated by a Gaussian function. Combining these two effects, the intensity is finally given by:

$$I(\vec{r}) = \int \int I_{\vec{q}\delta}(\vec{r}) f(\delta) s(\vec{q}) d\vec{q} d\delta \tag{2.27}$$

Following Franck and Wade [Fran 76], this equation can be calculated within the WPOA, where the imaginary part of the TF is of importance for phase contrast imaging (no absorption results in no real part). The phase contrast transfer function (PCTF) is given by:

$$t_{\mathrm{c}}(q) = \sin(\chi(\vec{q})) \tag{2.28}$$

As the temporal damping envelope function $E_{\mathrm{t}}(\vec{q})$ describes focal variation induced by the instabilities, it is a function of the partial derivative of the aberration function $\partial\chi(\vec{q})/\partial\Delta f$ with respect to the defocus Δf. It is then given by:

$$E_{\mathrm{t}}(\vec{q}) = \exp\left[-\frac{2\pi^2}{\lambda^2}\triangle C^2 \left(\frac{\partial\chi(\vec{q})}{\partial\Delta f}\right)^2\right] = \exp\left[-\frac{\pi^2}{2\lambda^2}\triangle C^2 \vec{q}^4\right] \tag{2.29}$$

For estimating the spatial damping envelope function $E_{\mathrm{s}}(\vec{q})$, we have to consider a distribution of incident plane wave of varying wave vectors which form a cone of semi-angle θ_s. Similarly as in case of the temporal envelope function, each partial wave of the cone are affected by the aberration function and contribute incoherently to the image. $E_{\mathrm{s}}(\vec{q})$ is then a function of the gradient $\nabla\chi(\vec{q})$ with respect to $\vec{q}$:

$$E_{\mathrm{s}}(\vec{q}) = \exp\left[-\frac{\pi^2}{\lambda^2}\theta_s^2 \left(\nabla\chi(\vec{q})\right)^2\right] = \exp\left[-\frac{\pi^2}{\lambda^2}\theta_s^2(\triangle f^2 \vec{q}^2 + 2\triangle f C_3 \vec{q}^4 + C_3^2 \vec{q}^6)\right] \tag{2.30}$$

The brightness and small finite source of a FEG microscope allows to obtain illuminating beam with relatively small convergence angle of a few mrad and enough electron dose which makes the spatial envelope negligible. The temporal coherence-damping envelope is then the crucial envelope.

This approximation is correct only in case of linear imaging of phase objects. In case of strongly scattering objects or relatively thick specimens, a more general description of

the transfer function is necessary. Ishizuha developed the transmission cross-coefficient method to solve Eq. 2.27. The main difference here is that this method considers interference between Bragg peak. Indeed, intensities of Bragg peak that are strong enough cause the appearance of pseudo-high-resolution pattern and can leads to misinterpretation of high resolution pattern.

An another envelope damping which has to be considered is created by the use of non-ideal detector for the acquisition of the electron wave image $\psi_{\text{ima}}(\vec{r})$. Nowadays, acquisitions are usually performed numerically by a device consisting of a scintillator, optical fibers and a charge coupled device (CCD) camera. The scintillator converts the incoming electrons to photons, which are then transferred to the CCD camera by optical fibers. The arrangement of this detector lead to incoherent blurring of high resolution micrographs, as it has a finite pixel size of a few ten µm. Although an electron impacts an area smaller than the pixel size, the translation of the electron by the scintillator and the optical fiber spreads the incoming localized signal to a finite area of several pixels. This is described by the point spread function (PSF) of the recording device. The PSF is described in the spatial frequency space by the the modulation transfer function (MTF) by as MTF $= \mathscr{F}$ [PSF]. Fig. Fig. 2.9 shows the comparison of the MTF and PSF measured for a Gatan Ultrascan with a binning of one and of two.

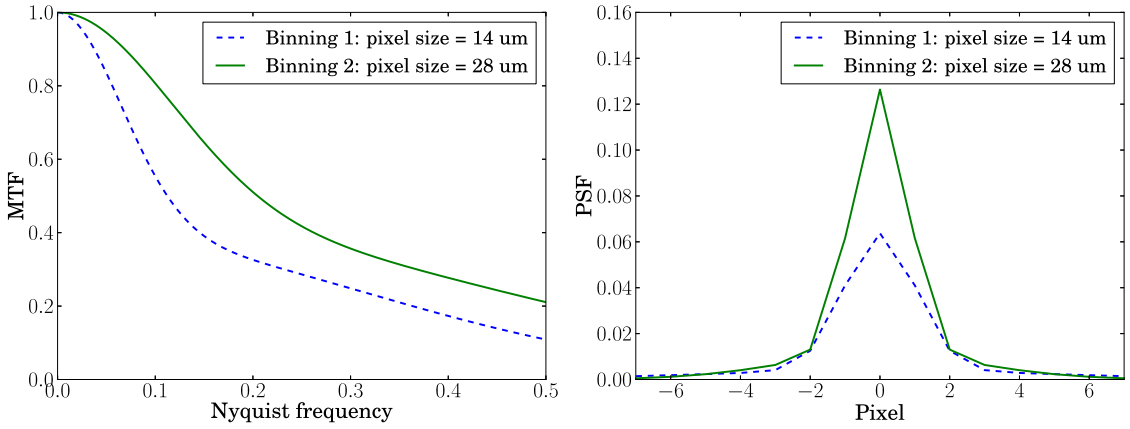

(a) MTF (b) PSF

Figure 2.9.: Typical modulation transfer function (MTF) and point spread function of a Gatan Ultrascan CCD camera with two different pixel sizes. The MTF is plotted as a function of the Nyquist frequency, which is defined as the reciprocal value of twice the pixel size.

The MTF was measured with the sharp edge method using beam stop of the microscope [Weic 95]. From this measurement, one can observe that there is a damping at high frequency and the contrast of the lattice fringes in the HRTEM image can be reduced by a large factor such as two or three. Fig. 2.9(b) demonstrated that in case of large detector pixel size, the signal from one electron will be more localized. It implies

that the transfer of particular frequencies can be optimized by choosing appropriate magnification of the microscope and binning of the CCD camera. For the Gatan Ultrascan considered here as an example, the change in pixel from 14 µm to 28 µm increase the MTF at half Nyquist frequency from 0.12 to 0.2. Finally, the CCD recording device has the advantage to be linear by calibration and can present a high dynamic it several acquisitions are cumulated. The multiple acquisition of the same image has the advantage to increase the SNR by $\sqrt{N}$ where N is the number of cumulated electrons.

2.4.3. Optimal imaging settings

In most of the case, the high spatial frequencies are mainly damped by the temporal envelope. To increase the information limit of the microscope, the defocus spread value $\triangle C$ has to be reduced. This can be performed by correction of the chromatic aberration C_c or using an electron source with lower energy spread, such as cold FEG or monochromated FEG. This extends significantly the information limit of the microscope. For a last generation microscope, the current instability of the objective lens and high tension ripple are below 0.5 ppm. For a C_c coefficient of 1.2 nm and a energy dispersion of 0.7 eV at 80 kV the defocus spread is $\triangle C = 45$ Å. Reducing the energy dispersion to 0.15 eV by the use of the monochromator decreases the defocus spread to a value of $\triangle C = 12$ Å. The consequence on the transfer function is shown in Fig. 2.10. Further optimization of the aberration coefficient C_3 and Δf, as explained in sec. 2.3.2 improve the PCTF. The benefit of optimization of energy dispersion and appropriate aberration coefficient is clearly shown by comparing Fig. 2.10(a) and (d). In Fig. 2.10(a), unoptimized condition is set, whereas in Fig. 2.10(d), the optimization of C_3 and Δf allows a increase of the homogenous transfer from 1.4 to 0.8 Å.

In Fig. 2.11, aberration-corrected HRTEM images acquired at 80 kV on a FEI Titan^3 Ultimate are compared for different energy dispersion: 0.7 eV and 0.15 eV in Fig. 2.11(a) and (b), respectively. The diffractograms of images (a) and (b) in Fig. 2.11(c) shows the differences in the transfer of spatial frequencies. On the right side of the FFT, corresponding to the lower energy dispersion of 0.15 eV, the transfer is less damped and supplementary spots at high spatial frequencies are visible. By comparing the HRTEM images in Fig. 2.11(a) and (b), one can observed, that beside the increased resolution, finer details of the carbon are present in case of the lower energy dispersion. Nowadays, with the development of aberration correctors and monochromators, the information limit and the information transfer of microscopes are greatly improved. Therefore, the choice of appropriate experiment conditions, such as aberration coefficients (C_3 and Δf), energy spread and detector settings (MTF) is of great importance for obtaining high resolution imaging combined with high SNR.

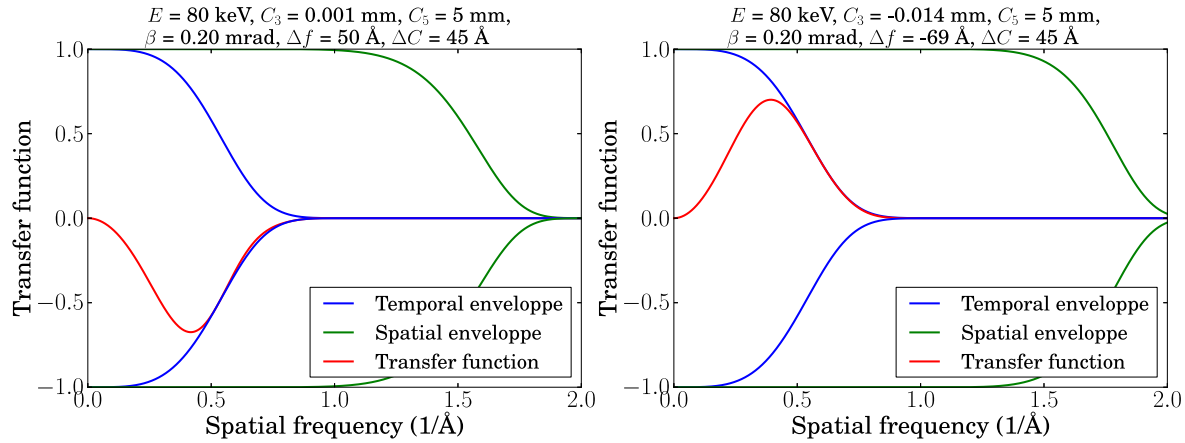

(a) $\Delta E = 0.7$ eV (b) $\Delta E = 0.7$ eV

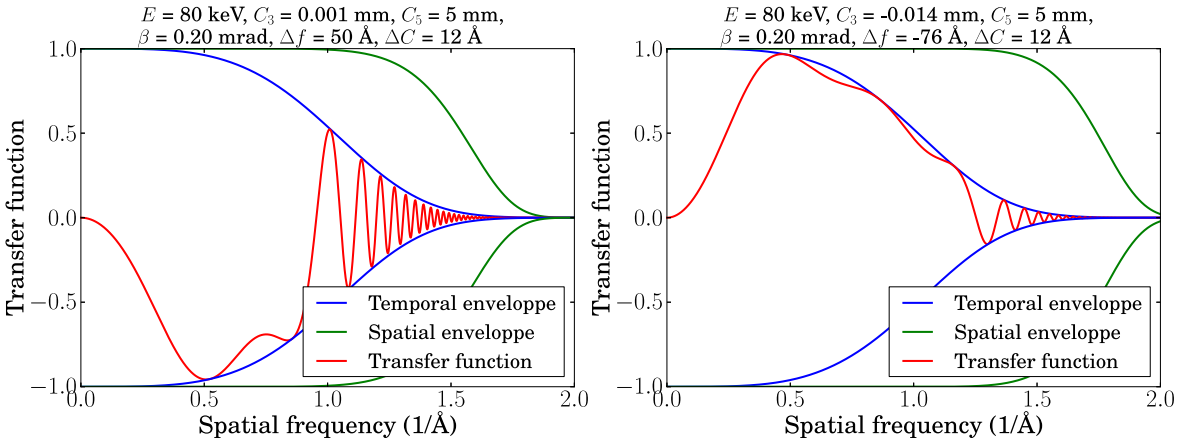

(c) $\Delta E = 0.15$ eV (d) $\Delta E = 0.15$ eV

Figure 2.10.: Comparison of PCTF at 80 kV: (a-b) $\Delta E = 0.7$ eV and (c-d) $\Delta E = 0.15$ eV. In (b) and (d), the C_3 coefficient has been optimized.

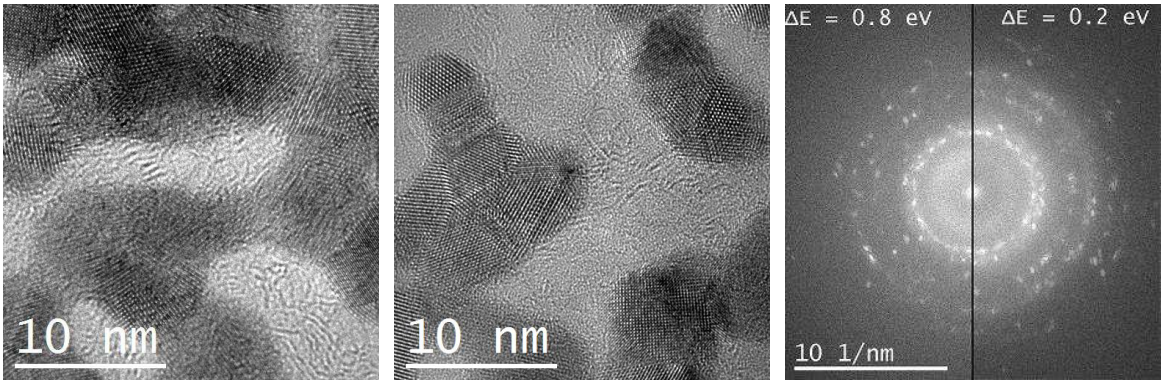

(a) Au nanoparticles, $\Delta E = 0.8$ eV (b) Au nanoparticles, $\Delta E = 0.15$ eV (c) Left: FFT of (a), right: FFT of (b)

Figure 2.11.: Comparison of HRTEM imaging (a) without and (b) with monochromator of Au nanoparticles on amorphous carbon film. In both case, the astigmatism is corrected manually, *i.e.* below 0.5 nm, whereas the coma and the C_3-aberration coefficients are below the confidence level (15 nm and 1.5 µm, respectively) of the measurement provided by the CEOS software.

2.5. High resolution scanning transmission electron microscopy (HRSTEM)

2.5.1. Image and image contrast formation

Contrary to the CTEM mode where a broad beam is used to illuminate the specimen, in STEM mode the information is collected in a serial acquisition mode. A tiny and convergent electron probe is focused at the height of the specimen and is scanned over the specimen. Then, a variety of signals can be detected as a function of probe position, forming an image. The propagation of the electron wave through the specimen follows the principle explained in sec. 2.2. In a same fashion than in HRTEM mode, a diffraction pattern is formed in the back focal plane of the objective lens' post-field. However, the ED pattern obtained in STEM consist of disk, *i.e.* a convergent beam electron diffraction (CBED) pattern, as the incident electron beam has a certain convergence angle α. The STEM setup is illustrated in Fig. 2.12.

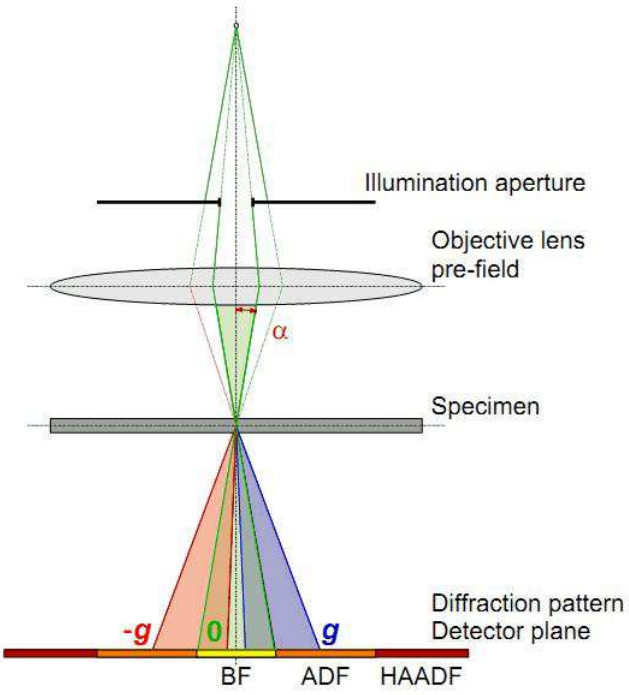

Figure 2.12.: Principle of STEM. The illumination aperture delimits the convergence angle, and the pre-field of the objective lens focuses the probe on the specimen. The scattered signal is collected by detectors as a function of the probe position, forming an image. Taken from [Erni 10].

For imaging in STEM, the signal is collected in the diffraction plane on an annular detector. The position and size of the detector determine the collection angle and the related imaging mode. The bright field (BF) consists in collecting the unscattered

and low-angle scattered (smaller than a few mrad) electrons. Most of the low-angle scattered electrons being coherent, they can interfere with unscattered electrons and form of phase contrast. Due to the reciprocal principle of illumination in TEM, the BF imaging mode can provide the same contrast and information than in HRTEM if the convergence and collection angle are equivalent to those used in CTEM. The annular dark field (ADF) detector refer to a configuration of a detector that collects electron scattered at larger angle than the convergence angle ($\alpha < \theta$), excluding electrons from the BF disk. If the inner collection angle is too low, the ADF detector collects a mixture of Bragg diffracted electrons, incoherent scattered electrons and to a less extent inelastically scattered electrons. This complicated mixture is usually difficult to analyze qualitatively. A very convenient imaging mode is the high angle annular dark field (HAADF) imaging mode, which consists in collecting incoherent signal at high angle. As explained in sec. 2.2, the signal scattered at high angle is dominated by Rutherford scattering (Eq. 2.3), and should follow a Z^2 dependence. For that reason, the HAADF imaging is usually referred as Z-contrast imaging. However, experiment and calculation demonstrate that the power is lower than expected and is around 1.6-1.8. This can be explained by the screening effect of the electron cloud on the Coulomb potential of the nucleus. Moreover the quasi-inelastic scattering of incident electrons by the phonon in the specimen, the so-called thermal diffused scattering (TDS) leads to a diffuse background intensity in the diffraction pattern and has to be taken into account for quantitative analysis.

In this work, simulation of HAADF images were performed with the multislice method using the code provided by E. J. Kirkland [Kirk 13]. This algorithm correctly describes dynamical scattering of the incident beam (as explained in sec. 2.2.2) and includes TDS which is accounted in the simulation by using a moving lattice approximation: the so-called frozen-phonon approximation. The time required for the electrons to travel through the specimen being much smaller than the oscillation of the atoms, the frozen phonon approximation consists in assuming that the position of the atom does not change when the imaging electron is inside the specimen. An experimental acquisition is made of many electrons, which have seen many different ensemble of atomic positions slightly moved away from their lattice position, *i.e.* atomic configuration. The successive imaging electrons are uncorrelated with each other, so that the detector incoherently add many atomic configuration. Therefore, the multislice approach with the frozen phonon approximation consists in incoherently averaging many multislice simulations with different configurations. The main effect of thermal vibration is to redistribute the intensity in the diffraction pattern, as it can be seen in Fig. 2.13. In Fig. 2.13(a) the high order Laue zone (HOLZ) lines are strong and there is almost no intensity between the lines, whereas in Fig. 2.13(b-d), the intensity of the HOLZ lines are significantly reduced and the Kikuchi bands appear more precisely with an

increasing number of configurations. The pattern in Fig. 2.13(c) and (d) are very similar and present the same features, the difference is in the SNR and the computation time: Fig. 2.13(d) has a better SNR than Fig. 2.13(c) but the simulations of 100 configurations requires 5 times longer computation time than only the simulations 20 configurations. Fig. 2.13(d) shows that, a good matching is obtained between experimental and simulated CBED pattern, for which the multislice approach including TDS was used.

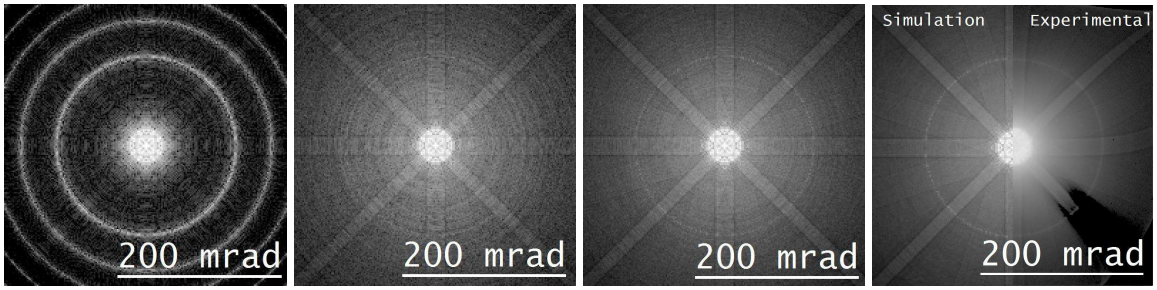

(a) Without TDS (b) 5 configurations (c) 20 configurations (d) 100 configurations and experimental

Figure 2.13.: Simulated CBED pattern of Si in [100]-zone axis for a thickness of 54 nm. Multislice simulation without (a) and with thermal vibrations for different number of configuration: 5 (b), 20 (c) and 100 (d). The main effect of the TDS is to redistribute the intensity in the diffraction plane. In (d), a experimental CBED pattern of Si in [100]-zone axis for a thickness of 54 nm (right side) is compared to a corresponding simulation (left side). Distortion of the projector system visible on the experimental pattern are due to the image corrector and the projector system. The black mark (bottom right) is an artifact coming from the shutter of the CCD camera. The simulated pattern are displayed with the same log scale.

2.5.2. Reciprocity theorem and coherence

The reciprocity theorem of scattering theory applied to TEM states that the electron intensities and ray paths remain the same if their direction is reversed. It can be formulated as follow [Poga 68]:

> The amplitude at B of a wave originating from a source at A, and scattered by P, is equal to the scattered amplitude at A due to the same source placed at B.

This theorem is due to time-inversion symmetry of the scattering process. It follows that the contrast in BF-STEM and BF-CTEM is then exactly the same if the source and the detector are interchanged, and their corresponding convergence and collection characteristics are strictly equivalent and inversed. Besides this consideration, the reciprocity theorem allows to define coherence in STEM mode on the basis of the

coherence in CTEM. From Fourier optics, the lateral coherence length perpendicular to the optical axis can be approximately estimated by [Kirk 10]:

$$\Delta x_{\text{coh}} = \frac{\lambda}{2\pi\beta_{\max}} \tag{2.31}$$

where $\beta_{\max}$ is the convergence angle of illuminating electron beam. Features much smaller than the the lateral coherence Δx_{coh} will be imaged coherently. Two points separated by distances much greater than Δx_{coh} are incoherently illuminated. In a aberration-free environment, the image resolution can be approximately estimated by $d \approx \lambda/\alpha_{\max}$, where $\alpha_{\max}$ is the maximum objective angle (*i.e.* the angle corresponding to the largest frequency transmitted). Combining the latter formula with Eq. 2.31, the condition for coherent and incoherent imaging are obtained and reported in Tab. 2.2. The ratio of the collection angle over the convergence angle β/α can be used to give a control of the coherence of the imaging process [Kirk 10]. The coherence condition being defined, the reciprocity theorem can be used to compare CTEM and STEM imaging. CTEM with $\beta_{\max} \sim 0.2$ mrad and $\alpha_{\max} \sim 30$ mrad is coherent imaging ($\beta_{\max} \ll \alpha_{\max}$), whereas HAADF-STEM imaging is typically incoherent, as $\beta_{\max} > 60$ mrad and $a_{\max} \sim 20$ mrad ($\beta_{\max} > 3\alpha_{\max}$).

Coherent imaging	Incoherent imaging
$\beta_{\max} \ll \alpha_{\max}/2\pi$	$\alpha_{\max}/2\pi \ll \beta_{\max}$
Wave interference inside Δx_{coh}	No interference
Wave functions add	Intensities add
$\lvert\psi_a + \psi_b\rvert^2 = \lvert\psi_a\rvert^2 + \lvert\psi_b\rvert^2 + \psi_a\psi_b^* + \psi_a^*\psi_b$	$\lvert\psi_a + \psi_b\rvert^2 = \lvert\psi_a\rvert^2 + \lvert\psi_b\rvert^2$

Table 2.2.: Conditions and consequences of coherent and incoherent imaging in TEM.

2.5.3. Probe size

In STEM, the characteristics of the focused electron beam directly determine the resolution achievable. As shown in Fig. 2.12, the objective lens' pre-field formed the probe and is decisive for the information transferred by the microscope. There are four main factors that can contribute to the probe shape with a convergence angle α:

- the diffraction limit $d_{\text{diff}} = 0.61\frac{\lambda}{\alpha}$ due to diffraction at the aperture, d_{diff} corresponding to the width of the central peak of the Airy function;
- the geometrical aberration, corresponding to the size of the disk of least confusion $d_{\text{geom}} = \frac{C_3}{4}\alpha^3 + \frac{C_5}{6}\alpha^5$, given in sec. 2.3.1;
- the partial temporal coherence due to energy spread of the electron beam. The size of the corresponding disk can be estimated by $d_{\text{temp}} = C_c\frac{\Delta E}{E}\alpha$;

- the partial spatial coherence and effective source size d_{spatial}, which depend on the demagnification M of the source. The brightness B of the gun is of great importance for demagnifying the source, as it relates the effective source size with the probe current I_{probe} by [Erni 10]:

$$B = \frac{I_{\text{probe}}}{\pi\alpha^2 A_{\text{source}}} = \frac{I_{\text{probe}} M}{\pi^2\alpha^2 r^2_{\text{effective}}} \tag{2.32}$$

where the source of area A_{source} is demagnified to an effective source size of area $\pi r^2_{\text{effective}} = M A_{\text{source}}$. The effective source size is then given by:

$$d_{\text{spatial}} = 2\pi\alpha\sqrt{\frac{M}{B} I_{\text{probe}}} \tag{2.33}$$

Eq. 2.33 points out the importance of high brightness to form small electron probe, as demagnification comes at the expense of beam current. Moreover, the estimation of the effective source size in Eq. 2.33 indicates that high current increases the probe size. For a microscope with a FEG source the brightness B is high enough to allow a high demagnification M, so that the effective source size d_{spatial} is not limiting the probe size. The dependence of the different contributions to the probe size d_{probe} on the convergence angle α is plotted in an log-log plot in Fig. 2.14.

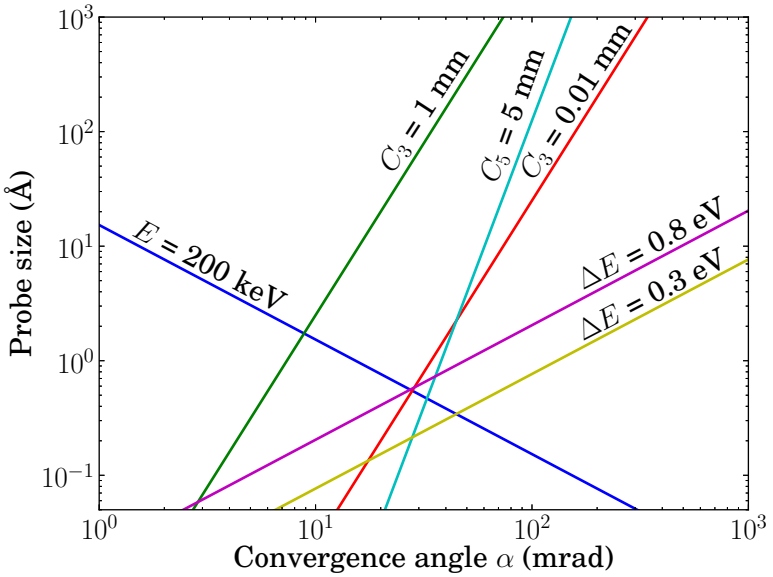

Figure 2.14.: Contribution to the probe size as a function of convergence angle α. An incident beam energy of 200 keV is considered for the diffraction limit. A C_3-aberration limited microscope is represented by the curve with C_3 =1 mm, whereas a C_5-aberration limited microscope is represented by the curves with C_3= 0.01 mm and C_5= 5 mm. The difference between C_5-aberration limited microscope with FEG and cold FEG source can be observed on the two curves with ΔE = 0.8 eV and ΔE = 0.3 eV.

As the slope of the curves depends on the power n of α^n, a change of a parameter (aberration coefficient, beam energy or energy spread) only parallel shift the curve, displayed as a line on the log-log plot. At smaller convergence angle α, the probe size is limiting by diffraction broadening at the aperture, whereas at higher α, the probe size is limited by aberrations (C_3 or C_c). This plot shows that the smaller probe size is obtained at an optimal convergence angle, which balances diffraction and other limiting aberrations. In a simple geometric optical approach the contributions to the probe size can be approximated as Gaussian spread functions and the final probe size can be estimated by a convolution of these spread functions. The limiting factors can be then added in quadrature, resulting in a probe size of $d_{\text{probe}} = \sqrt{d_{\text{diff}}^2 + d_{\text{geom}}^2 + d_{\text{spatial}}^2 + d_{\text{temp}}^2}$. This estimation of the probe size is not absolutely correct, as the different contributions does not affect the probe shape in the same way [Erni 10]. The resolution is determined by the width of the central peak, and the expressions d_{diff} and d_{geom} describe the probe size in different way: d_{diff} measures the first zero of the Airy function ignoring the probe tails, while d_{geom} measures the outermost radius of a the disk of least confusion. The achievable minimum probe size is then overestimated. Concerning the partial temporal coherence, its main effect is to increase the probe tail without decreasing significantly the width of the central peak. This results in a decrease of the image contrast, and will be explained more precisely [Erni 10].

2.5.4. Optimal imaging settings

2.5.4.1. Geometric aberration

As for HRTEM imaging, optimal imaging parameter can be chosen to optimize the experiment to be performed. The main free parameters of the electron probe formation are the convergence angle α , the aberration coefficients (Δf and C_3) and the probe current. In the following, the electron probe is described using a wave optical approach to obtain an accurate estimation of the electron probe. As explained in sec. 2.3.2, a phase shift of $\chi(\alpha) < \pi/2$ (Eq. 2.18) is small enough to be ignored, and the optimal resolution condition can be determined [Sche 49]. In case of an uncorrected microscope, the optimal defocus Δf_{opt} is chosen to compensate the spherical aberration shift within the widest $\pi/2$ band, and the optimal aperture α_{opt} is obtained by calculating $\chi(\alpha) = 0$. The optimal convergence angle α_{opt} and the probe size d_{probe} are then given by:

$$\alpha_{\text{opt}} = \sqrt[4]{4\lambda/C_3} \quad \text{and} \quad d_{\text{probe}} = 0.43\sqrt[4]{C_3\lambda^3} \tag{2.34}$$

Extending this approach to a microscope with a C_3 corrector, the defocus $\triangle f$ and the C_3 coefficient are set to balance the C_5 aberration.

The optimal C_3 coefficient, convergence angle α_{opt} and the probe size d_{probe} are given by [Inta 08]:

$$C_3 = -\sqrt[3]{3\lambda/C_5^2}, \quad \alpha_{\text{opt}} = 1.47\sqrt[6]{\lambda/C_5} \text{ and } \quad d_{\text{probe}} = 0.42\sqrt[6]{C_5\lambda^5} \tag{2.35}$$

Optimal values are calculated for different high tension in Tab. 2.3.

	Uncorrected			C_3 Corrected ($C_5 = 5$ mm)		
High Tension (kV)	80	200	300	80	200	300
C_3 (mm)	1	1	1	-0.014	-0.011	-0.011
α_{opt} (mrad)	11.4	10.0	9.4	52.2	47.9	46.0
d_{probe} (Å)	2.23	1.52	1.27	0.49	0.32	0.26

Table 2.3.: Optimal values for the convergence angle and the C_3 coefficient (in corrected microscope case) at different acceleration voltage. The probe size d_{probe} is estimated using the diffraction limit of optimal convergence angle α_{opt}.

As for HRTEM, the finite energy spread ΔE of the electron beam in combination with the chromatic aberration of the probe-forming system leads to an incoherent sum of probes with different defocus. The principal effect of the chromatic aberration is then to move intensity from the probe central peak into the probe tail, while the probe size does not change substantially [Kriv 08, Erni 09]. In other term, in case of incoherent imaging, the chromatic aberration does not affect the resolution, but the contrast decreases significantly (as the probe tail intensity is higher). Fig. 2.15 shows calculated PSF of different probe conditions. In STEM, the PSF is the intensity distribution of the focused probe and is calculated by integrating the aberration wave function over the illumination aperture $\alpha = \lambda k_{\text{max}}$ [Kirk 10]:

$$\text{PSF}(\vec{r}) = A\left|\int_0^{k\text{max}} \exp\left[-i\chi(\vec{k}) - 2\pi i\vec{k}\cdot\vec{r}\right] d^2\vec{k}\right|^2 \tag{2.36}$$

with A a normalization constant. If the astigmatism is negligible, the PSF can be simplify to the calculation of a one dimensional integral:

$$\text{PSF}(r) = A\left|\int_0^{k\text{max}} \exp\left[-i\chi(k)\right] J_0(2\pi kr)kdk\right|^2 \tag{2.37}$$

where J_0 is the zeroth order Bessel function of the first kind. The probe profiles shown in Fig. 2.15(a) has been calculated using Eq. 2.37. In Fig. 2.15(a), a C_3-aberration limited probe is compared to C_5-aberration limited probes, which are both optimized for maximum contrast, *i.e.* smallest probe tail possible.

2.5.4.2. Chromatic aberration

In Fig. 2.15(b) four calculated probes are plotted to show the effect of the chromatic aberration on a C_5-aberration limited probe with convergence angles of 20 and 35 mrad. As expected, the width of central peak is smaller with 35 mrad than with 20 mrad convergence angle. Chromatic aberration does not significantly change the width of the central peak, but the probe tail is affected, as explained before. The much larger probe tail of the 35 mrad probe demonstrated that the effect is much greater on the 35 mrad probe than on the 20 mrad probe. This is also evidenced in the inset of Fig. 2.15(b), in which the total integrated current is plotted, as a function of the distance of the probe center.

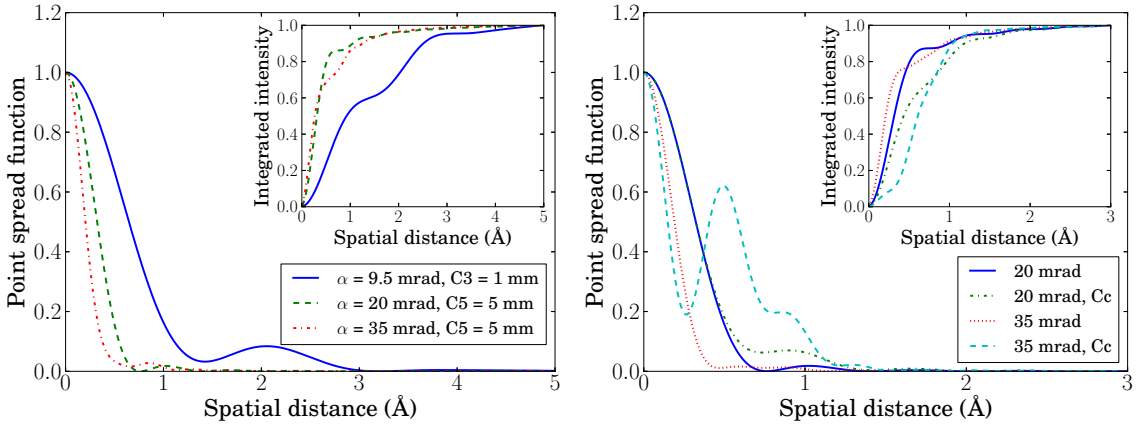

(a) Effect of geometric aberration and convergence angle

(b) Effect of chromatic aberration and convergence angle

Figure 2.15.: PSF of different calculated probes. (a) A C_3-aberration limited probe is compared to C_5-aberration limited probes with 20 mrad and 35 mrad convergence angle. (b) Effect of the chromatic aberration on C_5-aberration limited probe with convergence angles of 20 and 35 mrad. In the insets, the total integrated current is plotted as a function of the distance from the probe center. A chromatic aberration coefficient of $C_c = 1.2$, and an energy dispersion of $\Delta E = 0.7$ eV at 200 kV is considered for the calculations.

Fig. 2.15(b) points out that for C_5-aberration limited microscope with an energy spread of 0.7 eV, the convergence angle should be kept relatively small ($\sim$ 20 mrad) to avoid large probe tail. A limit imposed by the chromatic aberration can be estimated by choosing a fraction of intensity transferred from the probe-central peak to the probe tail. The intensity fraction remaining in the central peak can be approximated by [Kriv 03]:

$$f_r \sim 1 - (1 - w)^2 \quad \text{where} \quad w = 0.75 \frac{\lambda}{C_c \alpha^2} \frac{E}{\Delta E} \tag{2.38}$$

Eq. 2.38 shows that a higher convergence angle α provides a lower fraction of intensity remaining in the probe central peak f_r. The optimal value of f_r depends on the experiment to be considered. For elemental mapping, a value of f_r is required, whereas for HAADF imaging f_r can be as low as 0.5. Considering $f_r = 0.75$ ($w = 0.5$) gives:

$$\alpha_{\text{chrom}} = 1.2\sqrt{\frac{\lambda E}{C_c \Delta E}} \tag{2.39}$$

Using the diffraction limit, a resolution limit due to the chromatic aberration can be defined as:

$$d_{\text{chrom}} = 0.61\frac{\lambda}{\alpha_{\text{chrom}}} = 0.5\sqrt{\frac{\lambda C_c \Delta E}{E}} \tag{2.40}$$

Values for the convergence angle obtained from Eq. 2.39 are calculated for different high tension and energy spread of the electron beam in Tab. 2.4. This values correspond to a convergence angle for which the chromatic aberration does not create significant probe tail, Tab. 2.4 points out that cold FEG sources allow higher convergence angle because of the lower energy spread ΔE. This is particularly critical at lower voltage, where the convergence angle have to be kept as small as 22 mrad in case of energy dispersion of $\Delta E = 0.7$ eV.

	$\Delta E = 0.3$ eV			$\Delta E = 0.7$ eV		
High Tension (kV)	80	200	300	80	200	300
α_{chrom} (mrad)	36.6	44.8	48.6	22.4	27.4	29.8
d_{chrom} (Å)	0.69	0.34	0.25	1.14	0.56	0.40

Table 2.4.: Optimal values for the convergence angle considering two FWHM of the energy spread ($\Delta E = 0.3$ eV and $\Delta E = 0.7$ eV) and a chromatic aberration coefficient of $C_c = 1.2$ mm. The intensity fraction remaining in the central peak is $f_r = 0.75$.

These considerations on the optimal probe forming conditions highlight the importance of the convergence angle on the probe intensity distribution, *i.e.* the resolution and the potential delocalization effect. It highly depends on the microscope parameters and on the experiment to be performed. HRSTEM in a C_3-aberration limited microscope is usually achieved using ~ 10 mrad convergence angle. Low probe current of a few 10 pA are required to reduce the contribution of the finite source size to the final probe size (see Eq. 2.33). For C_5-aberration limited microscope, the value reported in Tab. 2.4 shows that higher convergence angle α can be used and thus much smaller probe size obtained as defined by the diffraction limit. Beside the improved resolution, the large convergence angle leads to another very beneficial effect which is the increased probe current. Indeed, for exactly the same brightness and demagnification of a microscope

source, the probe current scale with the area of the illumination aperture if we consider that the intensity of the electron wave is constant in the aperture plane. A 3 times larger convergence angle provides a probe current enhances by of a factor of 9. That is of high importance for high SNR in HRSTEM experiments, such as HAADF, EDX (Energy-dispersive X-ray) or EELS acquisitions. Aberration correctors have really opened new fields of investigation and specially for analytical analysis with high spatial resolution.

Usually HRSTEM in a C_5-aberration limited microscope is performed with a convergence angle ranging from 25 to 35 mrad, whereas slightly smaller convergence angle ($\sim$ 20 mrad) with very small tail are preferable for EELS experiment. The depth of field Δz is also of importance and is linked to the convergence angle by $\Delta z \approx \lambda/\alpha$. In some situations, it is possible to take advantage of the small depth of field Δz to perform three-dimensional imaging of individual atoms [Bent 06]. However, the reduced depth of field Δz leads to more complicated propagation of the electron in the specimen due to channeling of the electrons along the zone axis [Xin 08].

2.5.5. Quantitative analysis

The HAADF-HRSTEM imaging mode has several advantages such as easier interpretation of the contrast and high sensitivity to chemical composition as compared to HRTEM imaging. As example, dopants distribution can be studied with atomic resolution, as it has been reported for the case of Sb in Si [Voyl 02] or Tm in AlN [Okun 10].

2.5.5.1. Intensity calibration

In the last few years, progresses have been performed toward a better quantification of HAADF contrast and an experimental method has been developed to set HAADF signal on an absolute scale. The main principle of this technique is to acquire the signal response of the detector to the electron beam for a given probe current [Lebe 08a]. Fig. 2.16 displays an example of acquisition of detectors images as we have performed for this work. The images were acquired by scanning the detector with the electron probe[2], *i.e.* for each probe position the detectors response is obtained.

The values measured on and outside the detector are used to normalize the raw intensity I_{raw} of the HAADF-STEM images as [Rose 09]:

$$I = \frac{I_{\text{raw}} - I_{\text{min}}}{I_{\text{max}} - I_{\text{min}}} \tag{2.41}$$

where I_{min} and I_{max} are measured on the detector response shown in Fig. 2.16(a-b).

[2]The projector of the microscope was set in image mode.

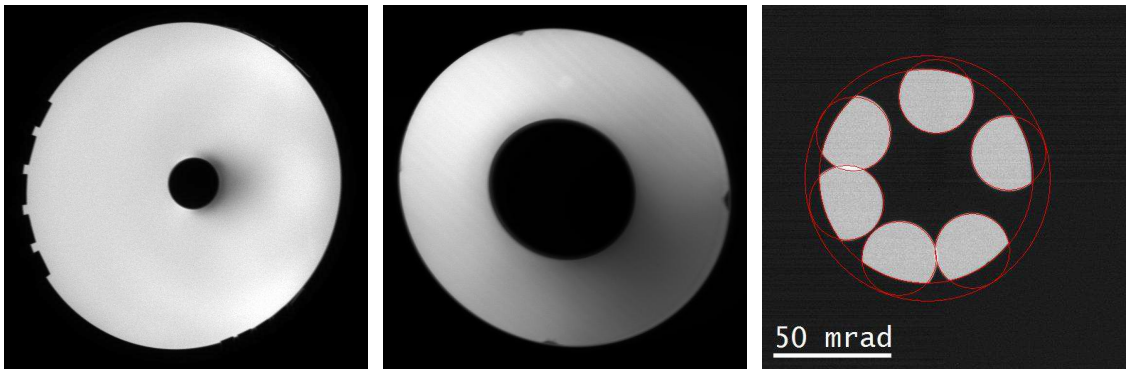

(a) Fishione ADF detector (b) Gatan ADF detector (c) ADF detector shadow

Figure 2.16.: Images of annular detector used as HAADF detector on FEI Titan microscope acquired by scanning the detector with the electron probe while the microscope is set in image mode. (a) Fishione ADF detector used in STEM mode and (b) Gatan ADF detector at the entrance of the Gatan imaging filter (GIF) used in EFSTEM mode. (c) Superposition of acquisitions of deflected beams reaching the scintillator with the shadow of the Fishione ADF detector. The two red circle marked the dead area of the ADF detector.

The images can be then calibrated in fraction of incident beam and could then be directly comparable with HAADF simulations. Using this method, the dynamic and the background of HAADF intensities acquired during set of sessions (*e.g.* different probe currents, different microscopes) can be directly and quantitatively compared with each other. The images of ADF detectors in Fig. 2.16 show that the detector response is not completely homogeneous, particularly at low collection angles. This should be taken into account for quantitative analysis of HAADF contrast based on HAADF simulations since the HAADF signal is higher at this low angles than at higher angles (see Fig. 2.2) [Rose 09, Find 13].

2.5.5.2. Inner and outer collection angle calibration

The detector image can be further used for collection angle calibration where the ratio between the inner and outer collection angle can be measured. The calibration of the inner collection detector angle was performed using the beam and the shadow of the detector acquired on the CCD camera. We deflected the beam toward the detector until a signal is measured on the ADF detector, as explained in [Lebe 08a]. This is illustrated by the image in Fig. 2.16(c) which shows the superposition of several acquisitions with the CCD camera for different position of the deflected beam touching the active area of the ADF detector. From the position of the ronchigram, one can accurately measure the inner collection angle θ_{inner}.

For calibration of the outer collection angle θ_{outer}, the cut-off of the microscope has to be taken into account. This cut-off corresponds to a limiting aperture or the pole piece of a lens and depends on the camera length in diffraction mode. This was measured by illuminating the specimen in a tick area in order to have a strong diffusion at high angle. More details about the measurement of the cut-off angle $\theta_{\text{cut-off}}$ are given in Appendix B. After a monotonous increase up to 170 mrad, θ_{outer} stops increasing at a camera length of $L = 145$ mm and stays at the same value. Therefore, the collection angle of the HAADF at small camera length are significantly affected by the cut-off of the microscope. The value for the inner and outer collection angle are plotted in Fig. 2.17 for a double-corrected FEI Titan^3 microscope used for most of the HRSTEM investigations presented in this work. These plots point out that the detector collection is much smaller at low camera length, where the inner collection angle is high. These two detectors are typically used in STEM mode for the Fishione, and in EFSTEM mode for the Gatan. The EFSTEM mode is a setting of the projector system particularly optimized for EELS experiment with high collection efficient since it allows entrance of scattering angle in the Gatan Imaging Filter (GIF) up to the microscope cut-off.

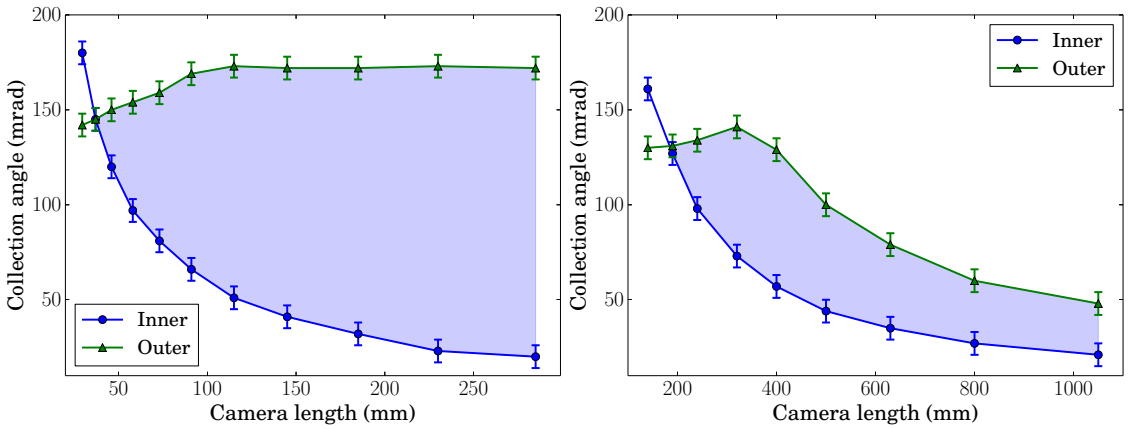

(a) Fishione ADF detector in STEM mode (b) Gatan ADF detector in EFSTEM mode

Figure 2.17.: Dependence of the collection angles of ADF detectors on the camera length. The fill area represents the scattering angles collected by the detectors. The ADF Fishione and ADF Gatan detector are respectively used as a HAADF detector in STEM mode and EFSTEM mode.

The measurements reported in Fig. 2.17 were performed on a microscope fitted with an image corrector. Other measurements performed on a probe-corrected FEI Titan microscope (without image corrector) revealed that the cut-off of the microscope is slightly higher (190 mrad). It is not trivial to explain what is limiting the scattering angle inside the microscope since the variation of the cut-off on the projector settings is not monotonic. The effect of each lens after the objective lens should be studied in more details.

2.5.5.3. Specimen thickness measurement

Another important parameter for quantitative analysis of HAADF contrast is the specimen thickness which has to be measured accurately for quantification. For thin areas, we used the position average CBED method (PACBED) consisting in acquiring a CBED pattern while the probe is scanned over a small area on the specimen [LeBe 10]. The CBED pattern produced by an angstrom-sized electron probe is composed of overlapping diffracted disks dependent on the probe position in the unit-cell. By incoherently average the CBED patterns over many probe positions the dependence on the probe position in unit-cell disappears and the obtained PACBED pattern contains highly sensitive information about the specimen thickness and orientation. PACBED patterns are displayed in Fig. 2.18.

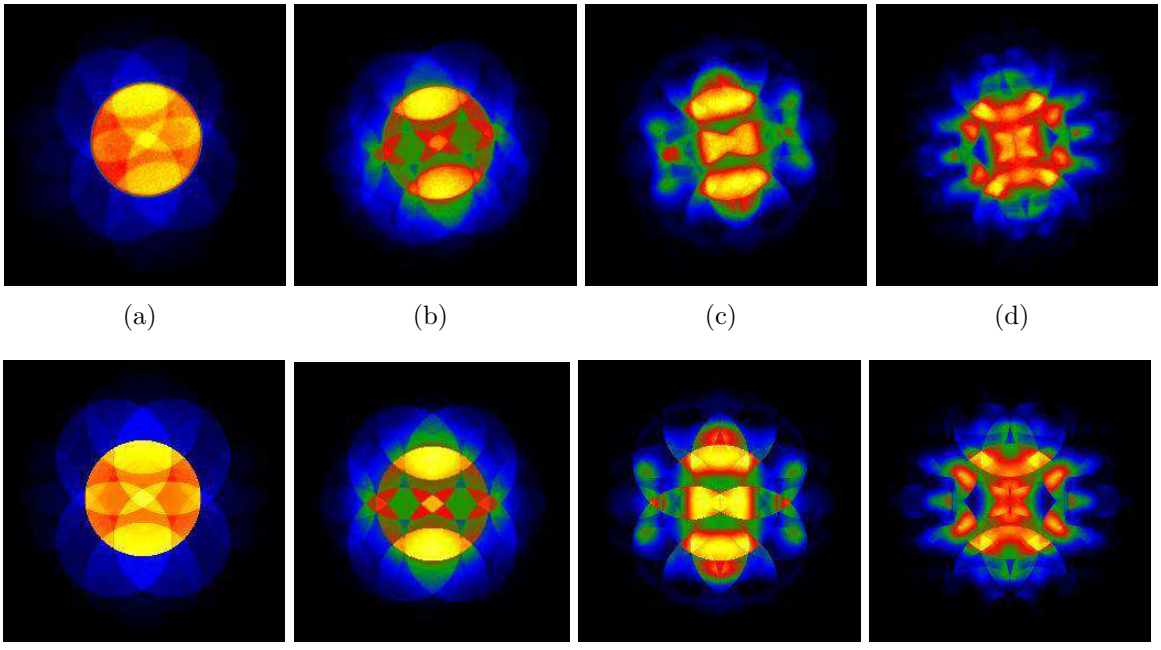

(a) (b) (c) (d)

(e) 7 nm (f) 14 nm (g) 35 nm (h) 48 nm

Figure 2.18.: (a-d) Experimental and (e-h) simulated PACBED patterns of Si in [110]-zone axis acquired in STEM mode (α = 9.2 mrad) at 200 kV for different thicknesses. By comparison of experimental with simulated pattern, the specimen thickness can be determined.

By comparing experimental PACBED pattern with corresponding simulated patterns the thickness can be determined. For easy comparison with simulation, the PACBED should not have too much overlapping of transmitted and diffracted beam. Depending on the acceleration voltage, the lattice parameter and the zone-axis the convergence angle has to be chosen correctly. Usually, it has to be not too large in order to obtain a convenient overlap of diffracted disks that will allow unambiguous comparison with simulation. Under good conditions, the specimen thickness can be determined with an

error of 1 nm. For silicon in [110]-zone axis at 200 kV acceleration voltage, Fig. 2.19 shows, that the PACBED pattern with convergence angle $\alpha = 15.3$ mrad have less contrast in the transmitted beam than the one with $\alpha = 9.2$ mrad. The comparison with simulations is then easier with the smaller convergence angle. In Fig. 2.19 (b) the construction of the overlapping Bragg diffracted disk is shown.

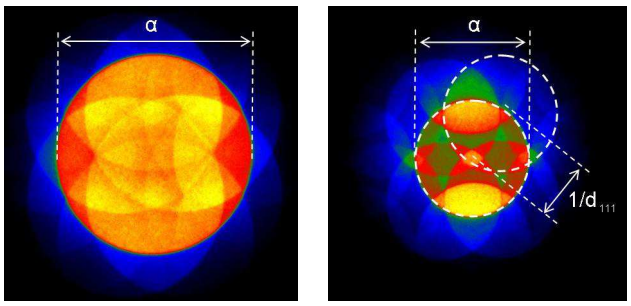

(a) $\alpha = 15.3$ mrad (b) $\alpha = 9.2$ mrad

Figure 2.19.: Comparison of experimental PACBED pattern of Si in [110]-zone axis for two different convergence angle: (a) $\alpha = 13.3$ mrad with condenser aperture 50 µm and (b) $\alpha = 9.2$ mrad with condenser aperture 30 µm.

2.5.5.4. Incoherence effect and probe size

Recently, good matching between experimental and simulated HAADF contrast has been reported by different groups [LeBe 08b, Rose 09, Kim 11]. They demonstrated that experimental HAADF images calibrated with the incident electron can be directly and easily compared with appropriate theoretical model including thermal diffuse scattering if an appropriate spatial incoherence is taken into account. The spatial incoherence was justified by "combined effects from a finite extent of the effective illumination source, instabilities, sample drift, etc.". The spatial incoherence was taken into account by convolving the simulated images with a Gaussian with a certain FWHM. Lebeau *et al.* used a FWHM of 80 pm for C_3-aberration limited microscope at 300kV, whereas Kim et al. used a FWHM of 70 pm for C_5-aberration limited microscope with a cold-FEG working at 300 kV [Kim 11, LeBe 08b]. Convolution with Gaussian functions with different FWHM clearly gives different results and rises questions about the validity of using this free parameter. More recently, good correlation between the FWHM of the Gaussian and the probe current was evidenced, indicating that the the free parameter of the FWHM of the Gaussian convolution is mainly due to spatial coherent size of the electron source [Kim 12]. This is in good agreement with the observation of Dwyer *et al.*, who have precisely measured the spatial incoherence of the electron source and demonstrated very good matching between experimental and simulated HAADF contrast without including any adjustable parameter [Dwye 12]. This

study demonstrates that absolute quantification of HAADF contrast based on HAADF simulations is possible if the microscope parameters are accurately measured.

2.6. Electron energy loss spectroscopy

2.6.1. The electron energy loss spectrum

Inelastically scattered electrons can be analyzed by EELS, as the energy lost by electrons through their interactions within the specimen gives a wide range of information such as atomic composition, chemical bonding, valence and conduction band electronic properties and surface properties. A typical EELS spectrum is shown in Fig. 2.20, where three parts of the spectra can be defined: the zero-loss (ZL), the loss-low (LL) and the core-loss (CL) regions.

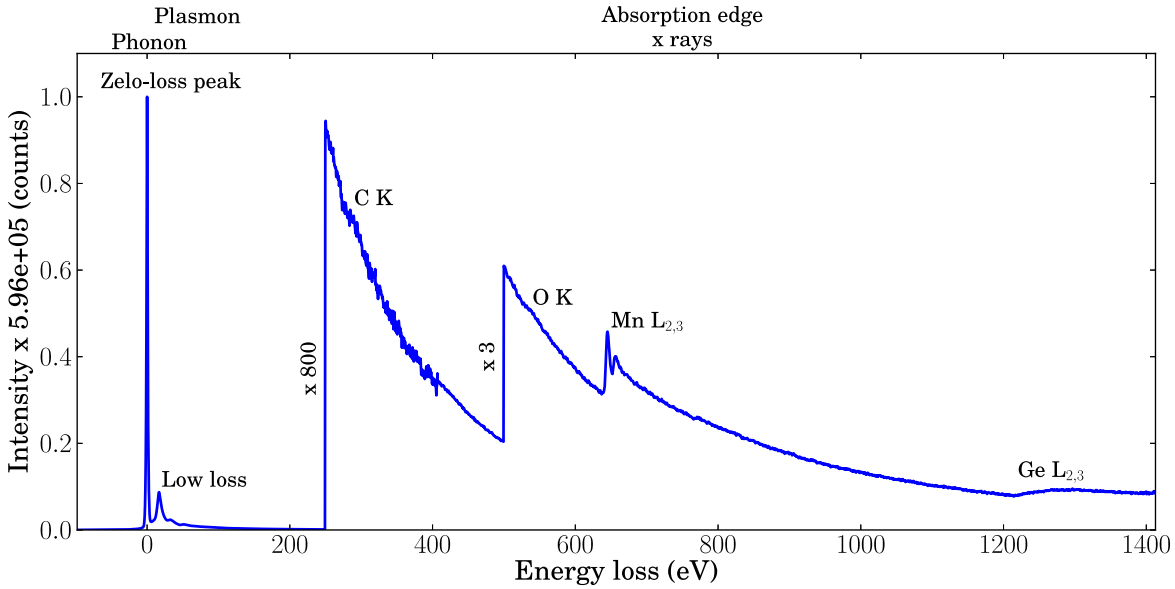

Figure 2.20.: Typical EELS spectrum of a GeMn specimen acquired in dual-EELS mode exhibiting the high dynamic range from the zero-loss peak to the core-loss edge of Ge at 1217 eV. The SNR of the carbon edge is poor as it is acquired on the same spectrum than the zero-loss peak. The core-loss spectrum acquired for longer exposure time between 350 eV and 1350 eV has a much better SNR.

The following excitation mechanism correspond to specific energy region of the energy loss:

- 1 meV - 1 eV: quasi-inelastic scattering of electrons with the phonons, mentioned in sec. 2.5, are contains in the ZL peak, as the typical energy resolution in TEM is too poor to separate them from the pure elastic peak. Indeed, the width of the ZL peak is related to the energy spread of the microscope, that range from 0.050 meV for the best monochromated system to 1.6 eV for thermionic LaB_6 source;

- 1 eV - 50 eV: most of the inelastic scattered electrons are generated after interaction with outer atomic shells and results in an energy loss of less than 50 eV in the LL region. In this energy range, collective plasmon excitations and interband transitions are predominant. They are due to electrostatic interactions of the incident electron beam with outer-shell electrons, such as conduction electron in metal, valence electrons in a semiconductor or insulator; surface plasmon oscillations for nanoparticles are also localized at the extreme valence band region (1-3 eV) and can now be analyzed thanks to new monochromated guns. Band gap for SC materials are also localized in this region of the spectrum.

- 50 eV - 3 keV: the rest of inelastic signal is generated through ionization of inner-shell (K-, L-, M-, etc. shell) electrons to vacuum. As the inner-shell electrons have binding energies of hundreds of thousands of eV, they are found in the CL region of the spectra.

Fig. 2.20 displays a typical EEL spectrum used in this work, where the C K, O K, M $L_{2,3}$ and Ge $L_{2\text{-}3}$ ionization edges are located at energy of 284 eV, 532 eV, 640 eV and 1217 eV, respectively. The characteristic ionization edges can be used first to identify the species present in the specimen and to quantify the among of each element. Energy-loss near-edge structure (0-30 eV) from edge onset gives information on the bonding with neighboring atoms. Each ionization edge is superimposed to the background which comes from high energy tail of plasmon peak or ionization edges at lower binding energy. The background is usually comparable or larger than the core-loss intensity, it is then of importance to minimize the background intensity. The most significant contribution to the background comes from the plasmon peaks. In thick specimen, electrons undergo more than one single inelastic scattering, *i.e.* plural scattering so several plasmons are generated, providing high intensity background. Therefore, the signal-to-background ratio (SBR), also called jump ratio of ionization edge is significantly reduced since the background typically increase faster than the signal of the ionization edge [Eger 11]. Moreover the plural scattering also affects the ionization edge and deconvolution is needed for quantification.

2.6.1.1. Collection efficiency

The signal generated from a particular ionization edge is directly proportional to the number of atoms and the scattering cross-section of the corresponding element. As explained in sec. 2.2, the cross-section depends strongly on the scattering angle (see Fig. 2.2) and the fraction of signal collected by the spectrometer (*i.e.* function of the collection angle β) varies as shown in Fig. 2.21.

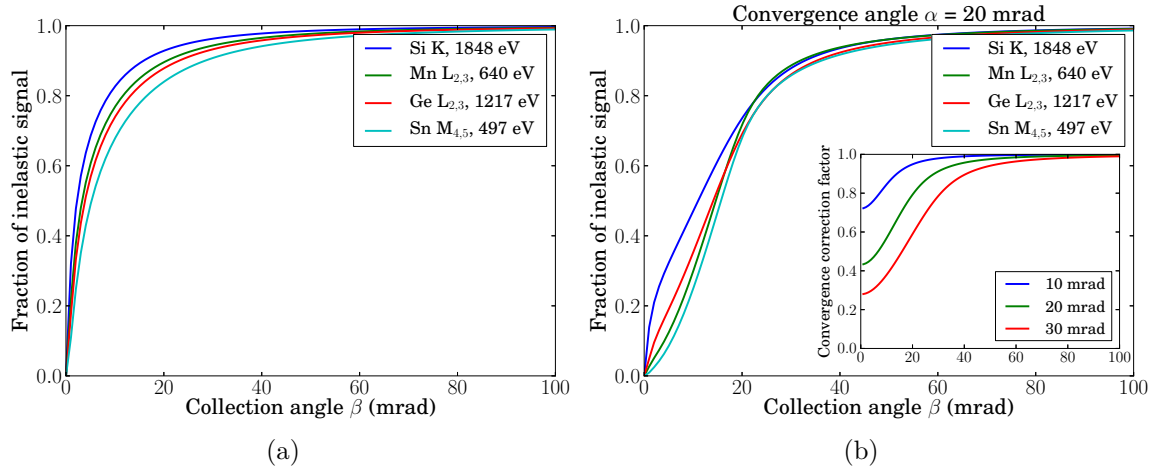

Figure 2.21.: (a) Fraction of inelastic signal collected by the spectrometer as a function of the collection angle β for different element. (b) Fraction of inelastic signal collected by the spectrometer with a correction for the convergence angle of $\alpha = 20$ mrad. Inset of (b) Convergence correction factor for different convergence angle α ranging from 10 to 30 mrad. This factor is used in quantification to take into account of the convergence angle α and highlight the decrease of ionization edge intensity for increasing convergence angle α (at same collection angle β).

The fraction of inelastic signal plotted in Fig. 2.21(a) is calculated using the Lenz cross section (see Fig. 2.2)[Eger 11]. When the EELS acquisition is performed in STEM mode with a convergence probe, a correction convergence factor is introduced to take into account the spread of ionization edge signal at higher angle. This correction factor is calculated by convolving the incident-electron intensity $dI/d\Omega$ by the inner-shell scattering $d\sigma_i/d\Omega$ [Eger 11]. The convergence correction factor is plotted as a function of the collection angle β for different convergence angle α in Fig. 2.21(b). The combination of both the fraction of inelastic scattering and the convergence correction factor is plotted in Fig. 2.21(c) and shows that the choice of the collection angle β is important for optimizing the EELS acquisition. For a convergence angle of $\alpha = 20$ mrad considered here the collection is 95 % with a 70 mrad collection angle. High collection angle ($\beta \sim 80$ mrad) provides important collection of the generated signal (higher SNR) and allows to obtained fast spectra acquisition time required for spectrum imaging acquisition (SI). However, high SNR is not the only parameter to optimize, the SBR

have also to be considered. Increasing the collection angle β significantly reduces the SBR since the background typically increases faster than the signal of the ionization edge [Eger 11]. The choice of the collection angle is therefore a trade-off between SNR and SBR.

2.6.1.2. Atomic resolution

The combination of aberration corrected STEM with high collection efficiency allows the acquisition of spectroscopic information down to the atomic scale, as shown by the atomic resolved EELS acquisition performed on a reference $SrTiO_3$ specimen in Fig. 2.22. Acquisition was performed on the FEI-Titan^3 Ultimate of CEA-Grenoble, double corrected and monochromated microscope equipped with the GIF Quantum. The 1 Å probe with a current of 140 pA used in this experiment allows to acquire EEL spectra of 20 ms with high SNR. The Sr, Ti and O map displayed in Fig. 2.22, show that the signal obtained is in good agreement with the expected position of atomic columns.

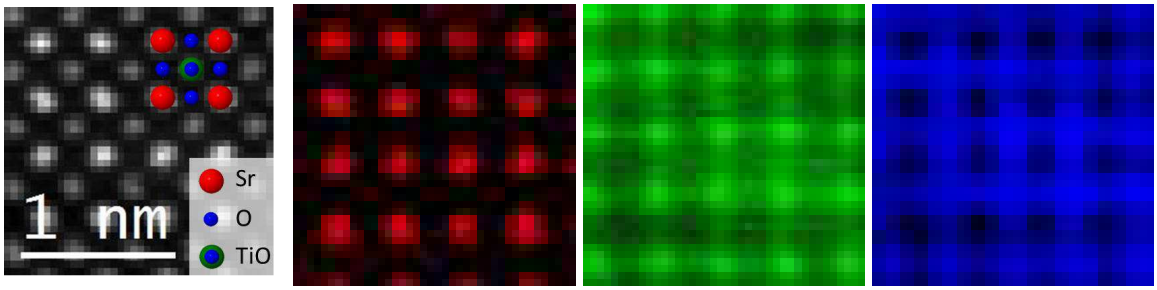

(a) HAADF (b) Sr map (c) Ti map (d) O map

Figure 2.22.: Atomic resolved EELS acquisition of $SrTiO_3$ in [001]-zone axis acquired at 200 kV, using 21 mrad convergence angle and 98 mrad collection angle. (a) HAADF images acquired simultaneously and background subtracted map of (b) Sr (c) Ti and (d) O. The current of the 1 Å probe was 140 pA allowing pixel acquisition time of 20 ms with high SNR. The total acquisition time of the EELS data set is 41 s. The specimen thickness $t = 27$ nm is estimated with the relative specimen thickness $t/\lambda = 0.33$.

However, the qualitative analysis of the signal obtained in atomic resolved EELS experiment is not straightforward and elastic-inelastic simulations are required. In the Sr map in Fig. 2.22(b), the signal of the Sr is well localized on the pure Sr atomic columns, whereas in the Ti map in Fig. 2.22(c), the Ti signal is slightly spread in the neighboring atomic columns. The O map in Fig. 2.22(d) shows, that the O signal measured on the Ti-O mixed atomic columns is slightly higher than on the O pure atomic columns. As both atomic columns contains the same number of oxygen atoms, one would expect to measure the same amount of oxygen which is not the case here. This can be explained

by a stronger channeling effect on the Ti-O columns than on the pure O columns. An example of non-trivial analysis of atomic-resolved EELS map was reported by Bottom *et al.* where they point out that in the case of atomically sharp interface the intensity profile of Ba or Sr distributions have significant tails away from the interface. Simulation suggest that this unexpected intensity arises from a background rather than the presence of the considered element [Bott 10]. They further show that the minimum detectable fraction of Ti in $SrTiO_3$ can be as low as 1 %, for optimized experimental condition (thin sample, appropriate probe current, convergence and collection angle).

Therefore, the EELS SI method can provide excellent spatial resolution combined with good detection limits. The remaining limiting factor to answer materials science problems is the limited field of view and the beam damage. This can be solved using highly stable microscope with lower incident beam energy.

2.6.2. EELS signal processing

2.6.2.1. Dark improved acquisition

In this work, the EEL spectra were acquired using the CCD camera of the GIF which provides spectrum corrected from the detector background since this CCD camera has built-in correction of gain (relative pixel sensitivity) and dark current (thermally excited electron-hole pairs). The signal after correction S_i of one pixel i of the CCD camera is given by:

$$S_i = \frac{I_i - D_i}{G_i} \tag{2.42}$$

where I_i is the measured signal, D_i the dark current reference and G_i the gain reference. A new gain reference was acquired at the beginning of each session, in order to obtain high quality gain calibration corresponding to the experiment conditions, *i.e.* a gain acquired with high statistic and a similar number of counts as for the experiment. This was necessary to prevent artifacts, such as difference of gain between quadrant of the CCD, that can become apparent after post-processing. For faster and less noisy acquisition, a 130 x on-chip binning in the non-dispersive direction was performed. Classically, Gatan acquisition routine acquires only one dark current for all the EEL spectra of the series leading to correlated noise in the EELS spectra as shows by Hou [Hou 09]. He evidences that the SNR of the EELS SI can be improved using high quality dark current reference consisting of n averaged dark current reference D_i. The dark current reference becomes then $\bar{D_i} = \sum_i D_i/n$. If the improved dark reference is not implemented in the software acquisition, the procedure can be manually performed by acquiring uncorrected spectra and post-processing the gain and the dark references.

Fig. 2.23(a) shows the normal dark correction and the improved dark reference, which consists of 400 dark references averaged. The impact of the improved correction on the EEL spectra can be observed in Fig. 2.23(b), where spectra with normal and improved dark correction are plotted for comparison.

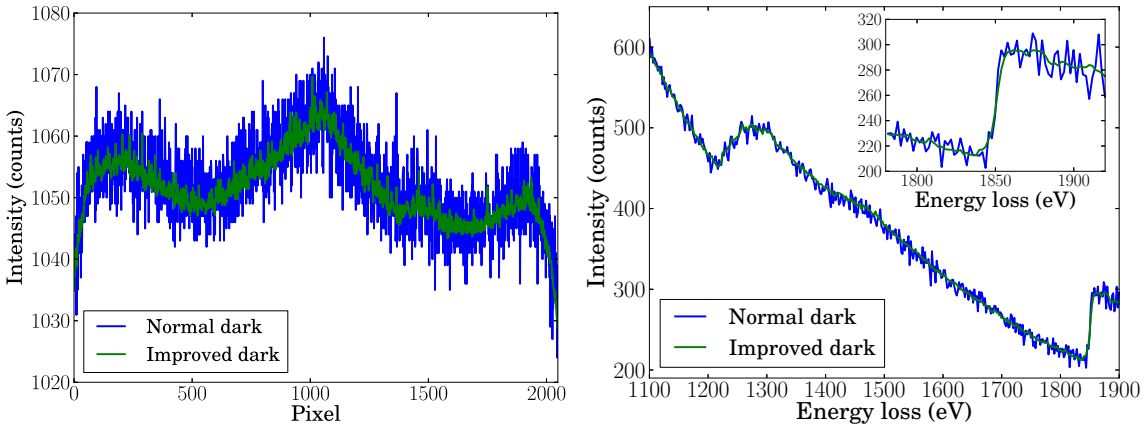

(a) Dark reference (b) GeSi ELL spectrum

Figure 2.23.: (a) Normal and improved dark-current reference and (b) the impact on typical raw EELS spectrum of a SiGe specimen with Ge $L_{2,3}$ and Si K edges. The improved dark current reference $\bar{D}_i$ was averaged over $i = 400$ dark current reference D_i acquisitions.

The improvement of the dark correction is directly transposed to the EEL spectra, as the dark correction consists in a subtraction of the dark reference signal and a normalization with the gain reference (see Eq. 2.42). This improved dark correction can be combined to the binned gain averaging method introduced by *Bosman et al.* [Bosm 08] to further improve the SNR [Hou 09].

2.6.2.2. Data post-processing

Multivariate statistical analysis method can be applied to EELS SI data set for denoising and retrieving unknown spectral features. A popular techniques is the principal component analysis (PCA), that takes advantages of the redundant spectral features in the EELS SI data set for noise removal [Treb 90, Bonn 99]. The principle of the PCA approach is to reduce the dimensionality of the large data set by finding a minimum number of variable that describe accurately the original data set [Wata 13]. The work-flow of PCA algorithm is the following:

1. diagonalization of the covariante matrix of the original SI data set;
2. ranking of the eigenvectors and corresponding eigenvalues. The magnitude of the eigenvalue indicate the amount of variance that the corresponding component contributes to the data set;
3. reconstruction of the SI data set by keeping the relevant eigenvectors.

Pre-treatment of the original data set, such as weighting, is usually performed before the PCA. The weakness of the PCA treatment lies in the choice of the number of eigenvectors to keep for reconstructing the SI data set. This usually performed by looking at the scree plot and by careful evaluation of the different components.

In this work, PCA was performed using the Hyperspy software for denoising EELS SI data set [Pena 11]. This freeware is a hyperspectral data analysis toolbox[3], which is particularly well suited for EELS data analysis. In Fig. 2.24, an example of PCA denoising treatment is presented. After the principal component decomposition, the variance of the different component are compared with the help of the scree plot in Fig. 2.24(a). The number of components to be chosen as relevant components can be estimated on the scree plot which shows that only the first two components have a variance higher than the other. A further investigation of the estimation of number of component can be done by inspecting the next components (factor and loading). For the component 2 and 3, Fig. 2.24(d) shows the corresponding factors and loadings correspond to noise, as they do not exhibit any particular feature neither in the factors nor in the loadings, and the contribution to the data set is very low, as shown by the loading maps. The 2 first components are then relevant for reconstructing the data set. In Fig. 2.24(b), one spectrum of the PCA denoised data set is compared with the corresponding spectrum of the raw EELS SI. In this example, there is very few components for two reasons: firstly, there is only 2 spectra features on this data set due to the presence of only Si and Ge ionization edge; secondly, the thickness variation is not significant, and there is thus no shape variation in the background.

2.6.3. Quantification

The ZL peak is of great interest for calibrating the energy of the system and for estimating the thickness of the specimen. The most common procedure for thickness measurement is the log-ratio method. As inelastic scattering events are independent, their occurrence follows Poisson statistics, and the probability $P_{n_{\text{inel}}}$ that a transmitted electrons is n_{inel} times inelastically scattered is given by:

$$P_{n_{\text{inel}}} = \left(\frac{1}{n_{\text{inel}}!}\right)\left(\frac{t}{\lambda_i}\right)^{n_{\text{inel}}} \exp\left(-\frac{t}{\lambda_i}\right) \tag{2.43}$$

where the total inelastic mean free path λ_i is the average distance between two scattering events, and t the specimen thickness. In the energy loss spectrum, $P_{n_{\text{inel}}}$ is the ratio of the energy integrated $I_{n_{\text{inel}}}$ of n-fold scattering divided by the total integrated intensity $P_{n_{\text{inel}}} = I_{n_{\text{inel}}}/I_t$ [Eger 11].

[3]Free software. Download at hyperspy.org

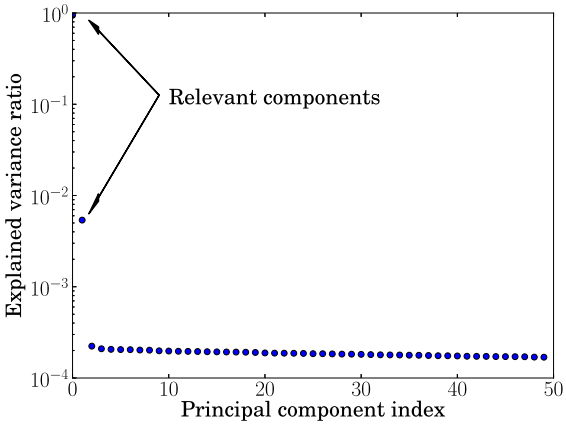

(a) Scree plot

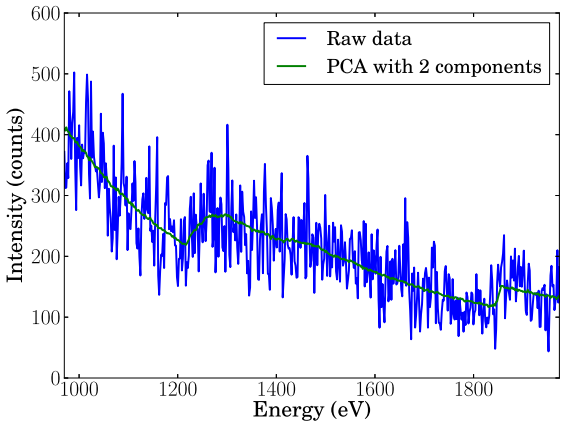

(b) Raw and PCA denoised data

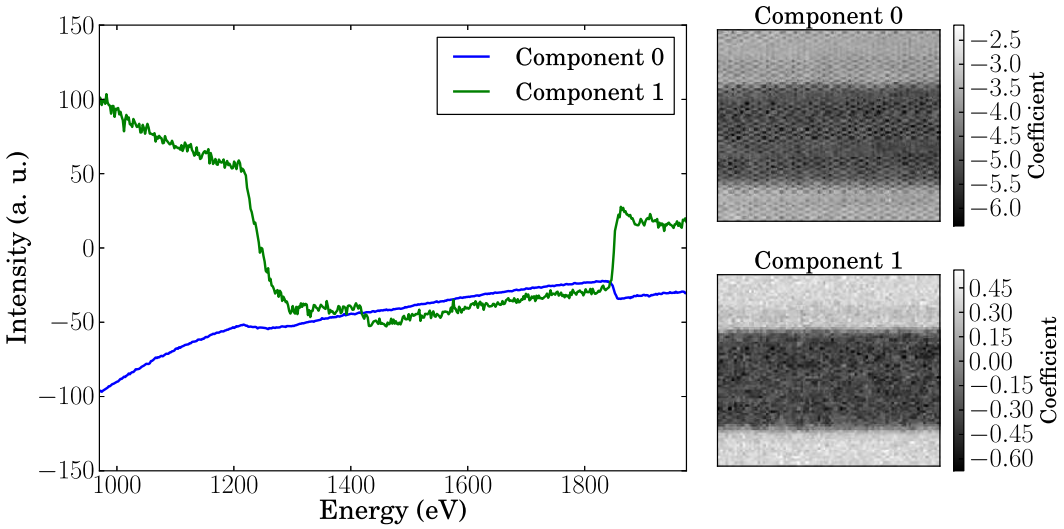

(c) Component 0 and 1

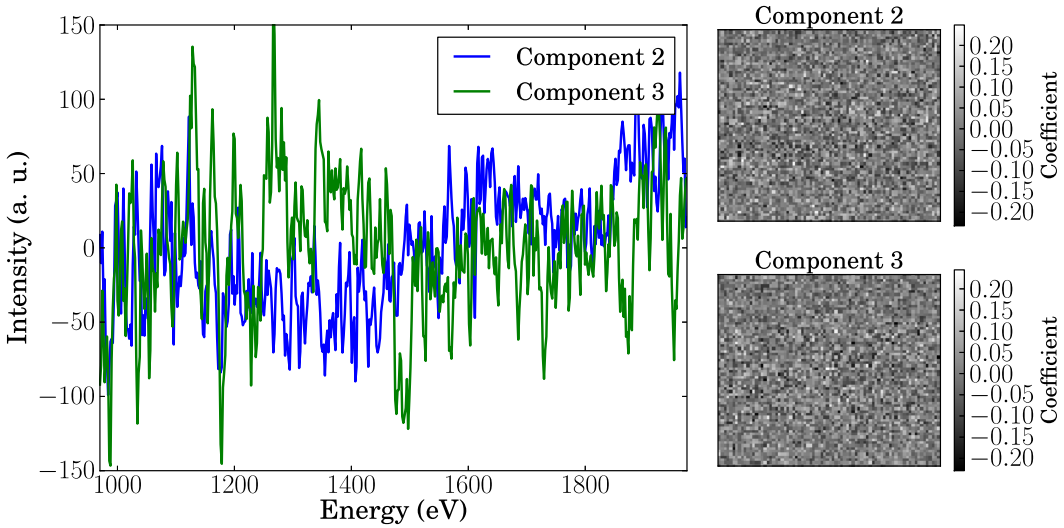

(d) Component 2 and 3

Figure 2.24.: PCA treatment of EELS SI of SiGe layers. (a) Scree plot exhibiting the relevant component. (b) EEL spectra of the same pixel without and with denoising. Factors and loadings of components 0, 1 and 2, 3 are displayed in (c) and (d), respectively. The inspection of the factors and loadings of the different component allows to discriminate between spectra features and noise.

The intensity of the unscattered electrons can be then estimated using:

$$P_0 = \exp\left(-\frac{t}{\lambda_i}\right) = \frac{I_0}{I_t} \tag{2.44}$$

The formula $t/\lambda_i = \ln(I_0/I_t)$ gives then a relative specimen thickness measurement, as the thickness t is expressed in fraction of total inelastic mean free path λ_i. The total inelastic mean free path λ_i can be estimated using a parametrized formula providing absolute thickness measurement [Mali 88]. This method, called the *log-ratio method*, usually works accurately when the collection angle is large enough $\beta > 30$ mrad and much larger than the convergence angle $\beta \gg \alpha$, as in this case the inelastic scattering obeys Poisson statistics and the main diffraction peaks enter the spectrometer. However, the log-ratio method can provide over-estimated thickness in very thin specimen area where the surface plasmon is no more negligible. Good agreement are evidenced in the comparison of thickness measurement obtained the PACBED method with the log-ratio method obtained by EELS (with high collection angle $\beta > 30$ mrad) for relative specimen thickness t/λ_i ranging from 0.2 to 0.7.

Other features of interest of the EEL spectrum are the core-loss ionization edges. Theoretically, the signal of ionization edge I_k can be quantified using standardless method, following the relation:

$$I_k = n_{\text{den}} I \sigma_k \tag{2.45}$$

where n_{den} is the areal density (atom $\cdot$ nm^{-2}) of a given element, I the total integrated number of counts in the spectrum and σ_k the cross section of ionization of an electron in the corresponding shell. In practice, 2.45 is valid for EELS acquisition in favorable experimental condition: negligible plural scattering ($t/\lambda_i < 0.5$) and appropriate collection angle (see sec. 2.6.1). In practice, the integration is performed over a finite range Δ and the total integrated number of counts I is not always measured. Nevertheless, composition ratio of element A and B can be determined using:

$$\frac{N_{\text{A}}}{N_{\text{B}}} = \frac{I_k^{\text{A}}(\beta,\Delta)}{I_k^{\text{B}}(\beta,\Delta)} \frac{\sigma_k^{\text{B}}(\beta,\Delta)}{\sigma_k^{\text{A}}(\beta,\Delta)} \tag{2.46}$$

where the integrated core-loss intensities $I_k(\beta,\Delta)$ and partial cross section $\sigma_k(\beta,\Delta)$ of each element A and B, dependent on the range of integration β of the scattering angle and of energy loss Δ.

Absolute quantification can be performed if the spectrum contains the ZL peak. The spectrum in Fig. 2.20 was acquired for energy loss ranging from 0 to 1400 eV, so that the total integrated number of counts I can be computed, and the absolute content

for each element can be estimated using 2.45. This method requires accurate cross section, which are usually calculated on the basis of atomic physics and can present systematic errors. In this work, parametrized partial Hartree-Slater cross sections or experimental k-factors have been used. The partial Hartree-Slater cross section have been calculated using the routines provided by the software Digital Micrograph. Usually, they are known within 5 % and 10 % accuracy for K and L shell, respectively [Eger 93]. For more accurate quantification of elemental ratio, experimental k-factors were determined using TEM specimen of well-known composition. From Eq. 2.46, the EELS k-factors can be determined by:

$$\frac{N_{\mathrm{A}}}{N_{\mathrm{B}}} = \frac{I_k^{\mathrm{A}}(\beta, \Delta)}{I_k^{\mathrm{B}}(\beta, \Delta)} k_{\mathrm{AB}} \tag{2.47}$$

where k_{AB} is the k-factor relative to the elements A and B. From the composition ratio $(N_{\mathrm{A}}/N_{\mathrm{B}})$ the relative concentration c_{A} of the element A is determined by:

$$c_{\mathrm{A}} = \frac{N_{\mathrm{A}}}{N_{\mathrm{A}} + N_{\mathrm{B}}} \tag{2.48}$$

2.7. Sample preparation

For TEM analysis the sample preparation is a critical key step. It depends on the material and on the investigation method that it is required [Will 09, Ayac 10]. Beside the Pt nanoparticles, the samples considered in this work consist of thin layers of about 100 nm in thickness grown on Ge or Si substrates. Pt nanoparticles sample does not required particular preparation step since the NP are deposited directly on the amorphous carbon film. The carbon film thickness and metallic grid (Au or Pt) was chosen depending on the experiment. The carbon film supported on Au grid are clearly mechanically more stable during annealing than the Cu grid. For Ge- and Si-based specimen, we have mainly performed structural and chemical investigations. For EELS experiment, it is usually convenient to have a sample thickness ranging between 0.3 and 0.5 of the mean free path for inelastic scattering. HRTEM imaging without strong dynamical effects requires thicknesses smaller than half of the extinction length. It means, that for TEM investigation of Si- or Ge-based sample at 200 kV acceleration voltage, the thickness should be smaller than 30 to 40 nm.

With the achievement of aberration-corrected TEM, the electron microscope become more and more powerful, in term of resolution, stability, sensitivity, and new challenging experiment can now be performed. However high quality sample are required to fully benefit from the microscopes performance. For example, the contrast of HAADF imaging in aberration-corrected STEM is significantly altered by the presence of amor-

phous layers at the surface [Mkho 08]. Moreover, in probe-corrected microscopes, the surface roughness or the remaining contamination present on the surface of the sample is clearly observed, as the contrast is higher. In other word, the better sensitivity we can obtained with more recent microscope is also more effective at imaging the artifacts coming from the sample preparation. To perform high sensitive quantitative investigations the samples have to be prepared with caution to get an artifacts free, very thin and very clean sample.

Cross-section preparation of semi-conductors materials for electron microscopy is usually performed by tow methods:

- parallel polishing follow by ion-milling: this is the historical and most common sample preparation method. It consists in gluing together two pieces of sample face to face. This collage is then cut in small pieces, whose faces are polished until a thickness of 20 µm or less is reached. The thinning is then finished with Ar^+ ion milling during several hours until electron transparency is reached. A more precise method consists in parallel polish the sample down to a thickness of 80 µm, use a dimpler to finer down to a few µm, and finally finish with Ar^+ ion milling during a few ten minutes.
- Focused Ion Beam (FIB): A thin lamella is extracted in the bulk sample using a micrometer-controlled tip for manipulation and a Ga^+ ion beam for milling. The FIB method has the advantage to allow site-specific and geometrically controlled preparation. However the milling with Ga^+ can induce lots of defects and/or thick amorphous and Ga implanted layer on the surface. The area of interest is usually small, because the milling rate of the Ga^+ FIB is low.

The main drawback of these methods is the ion beam for thinning the sample which can create lots of defects in the lamella and/or thick amorphous layer on the surface, depending on the material. Moreover, material redeposition is usually observed on thin lamella milled with Ar^+ broad beam.

2.7.1. Wedge polishing

To get high quality samples and for the reason explained previously, we choose a fully mechanical technique : the wedge mechanical polishing method, to prepare Ge- or Si-based samples in plan or cross-section view. Klepeis *et al.* developed this method using a tripod polisher [Klep 87]. It was further enhanced by Voyles *et al.* modifying some key parameters and using an Allied Multiprep system which is semi-automatic [Voyl 03]. A schematic view of the sample shape at the end of the preparation is shown in Fig. 2.25.

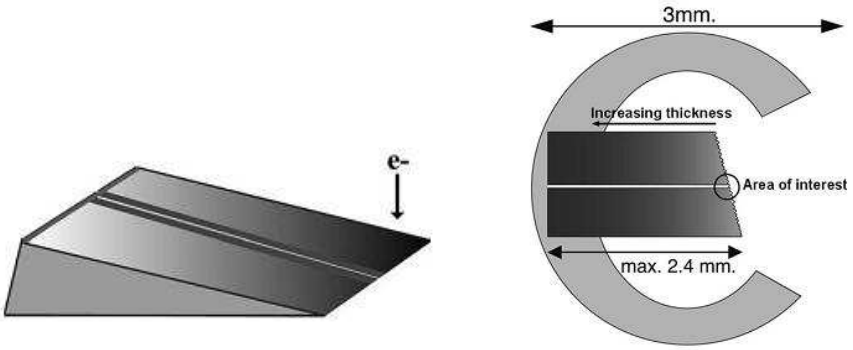

(a) (b)

Figure 2.25.: Schematic view of the prepared sample in cross-section. (a) Shape of the sample showing increasing thickness of the wedge, the glue line and the layer of interest. (b) Sample glue on a grid with two thin area of interest at the edge of the wedge. Scheme taken from [Ayac 10].

As in the case of the parallel mechanical polishing, both sides of the sample are mechanically polished for cross-section preparation. The main difference lies in the wedge angle that is set before polishing the second side. The final polishing of each side is performed with colloidal silica on polishing cloth. Finally, the wedge sample is glued on a Cu grid, as shown on the light microscopy image in Fig. 2.26 (a). For plane view preparation, the sample is glue with the layer face to the Pyrex sample holder and only the back side is polished. The area of interest is the whole edge of the wedge, that allows to have very large area of interest in one direction (perpendicular to the wedge).

Fig. 2.26 (b) displays a typical light microscopy image of a good cross-section sample ready for TEM. Indeed, one can observe that the surface is optically clean, the sample edge is not broken and the fringes show that the thickness variation close to the glue line is homogenous. No further ion milling is required, as the final polishing with the colloidal silica leaves a flat surface. More details of this methods can be found in Voyles *et al.* and Ayache *et al.* [Voyl 03, Ayac 10]. In standard wedge-prepared sample, we usually observed a faster thickness variation than the expected 2° wedge from the

border to about 10 nm within the sample. This is due to the chemical nature of the final polishing. Further away from this 10 nm, the thickness variation follows the 2° wedge. Similar observations can be seen in [Voyl 03]. This method allows to get the sample thicknesses down to 5 nm with a very clean surface and small amorphous layer thinner than 1 nm, corresponding to the native oxide layer. To get an amorphous-layer-free sample, a brief hydrofluoric (HF) acid vapor treatment of 10 s can be applied to the sample just before introduction in the microscope.

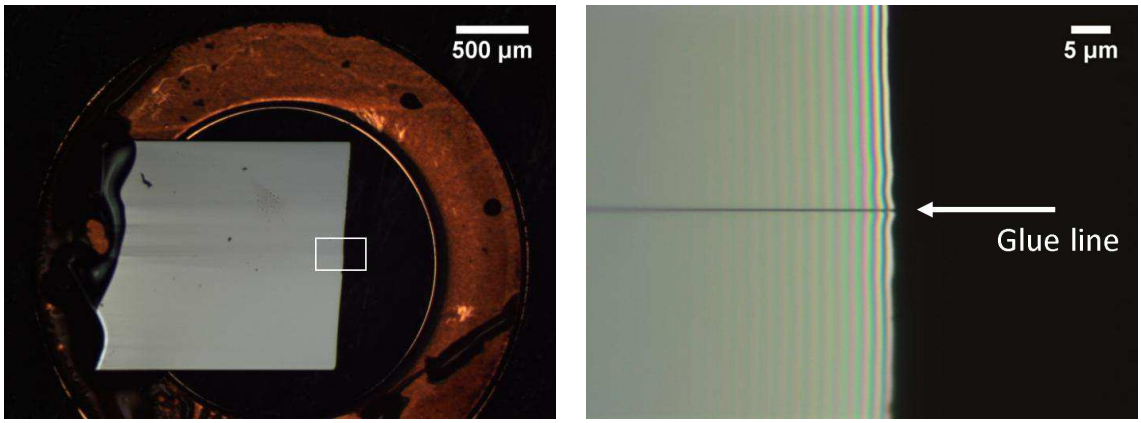

(a) (b)

Figure 2.26.: Light microscopy images of (a) Si-based 2° wedge sample glued on Cu grid and (b) zoom on the area of interest marked by a white square in (a). Two pieces of sample are glued together face to face and are separated by a glue line (dark line in (b)). The optical fringes visible in (b) are fringes of equal thickness, showing the homogenous thickness variation.

2.7.2. Artifacts in sample preparation

To compare the sample preparation method using ion milling with wedge polishing, HAADF-STEM images of Ge quantum dots in Si acquired in an aberration corrected microscope are shown in Fig. 2.27. A standard Ar^+ion milled using Gatan Precision Ion Polishing System (PIPS) and a wedge polished sample are shown in Fig. 2.27(a) and (b), respectively. On the left image Cu redeposition coming from the grid is clearly observable and a 10 nm amorphous surface layer is visible at the edge of the sample. These artifacts are very critical in the thinner area of the sample (about 10 nm thick). In comparison, the HAADF image in Fig. 2.27(b) shows an area of similar thickness of a wedge polished sample. An amorphous layer of only 1-2 nm can be seen and the contrast in the substrate is very homogenous.

BF- and HAADF-STEM image of GeMn nanocolumns in [001]-zone axis of plan-view preparation by FIB and wedge polishing are shown in Fig. 2.28(a) and (b), respectively.

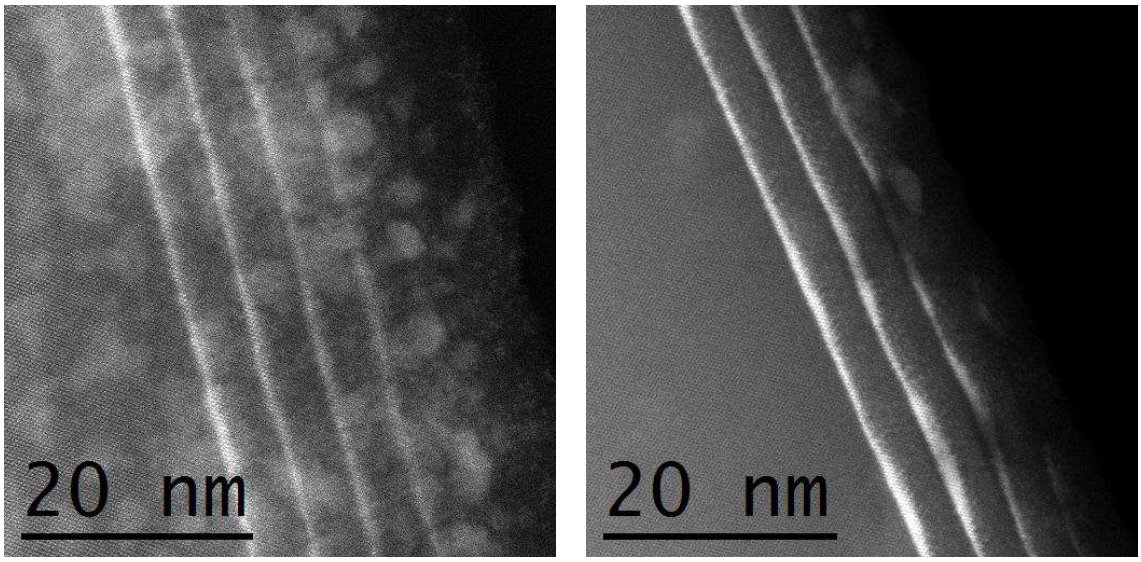

(a) Ar+ milled (b) Wedge polished

Figure 2.27.: HAADF-STEM image of Ge quantum dots in Si in [110]-zone axis (cross-section) showing the difference between Ar^+ ion-milling preparation (a) and wedge polished preparation (b). The specimen thickness is estimated to be $\sim$ 10 nm in both cases.

Although, the STEM images are from the same sample, one can observe large differences due to preparation methods. In case of FIB preparation, the contrast in the Ge matrix between the nanocolumns is not homogenous, and the GeMn nanocolumns are not well defined in comparison to the STEM images of the wedge polished sample shown in Fig. 2.28(b). Even if final milling was performed with special care by lowering the Ga^+energy at 2 kV in order to reduce the irradiation damage, the thinner area of the sample were completely amorphous (not shown here). This could suggest there is a chemical reaction between the Ga^+ ions beam and the Ge atoms of the lamella, as observed by Graham and coworkers [Grah 11].

Before introduction in the microscope, plasma cleaning of the sample for a few minutes is usually required in order to prevent the carbon contamination under the electron beam. This is particularly critical in STEM, where the electron density is very high. For wedge polished sample, the latest step of sample preparation is dissolving in acetone the wax between the sample and the Pyrex holder. This step causes a more pronounced carbon contamination during TEM investigation than in case of ion milled sample. After plasma cleaning of the sample during 15 min, we observed a copper contamination of 1-2 nm particles on the surface due to the plasma cleaning. Similar observation have been done with Au contamination during plasma cleaning [Hert 12]. By annealing the sample in vacuum at 200 °C during 2 h, carbon contamination could be entirely prevented without plasma cleaning, and this without any Cu redeposition.

Very thin and clean areas are in some situations mandatory, as we will need to lower acceleration voltage (60-80 kV) for reducing the radiation damage. The required thickness sample should then even be smaller than at higher acceleration voltage, as the total inelastic mean free path become smaller at lower incident beam energy. The calculated mean free path for inelastic scattering [Mali 88] in Si decreases from 87 nm at 200 kV to 52 nm to 80 kV. For example, atomic resolved EELS require a high electron dose and the Si does not support such a high dose at 200 kV. Lowering the acceleration voltage at 80 kV allows to perform atomic resolved EELS but the sample thickness has to be less than 25 nm. Sample preparation can be a limiting factor in TEM and is therefore a crucial step for the acquisition of high quality electron microscopy data set.

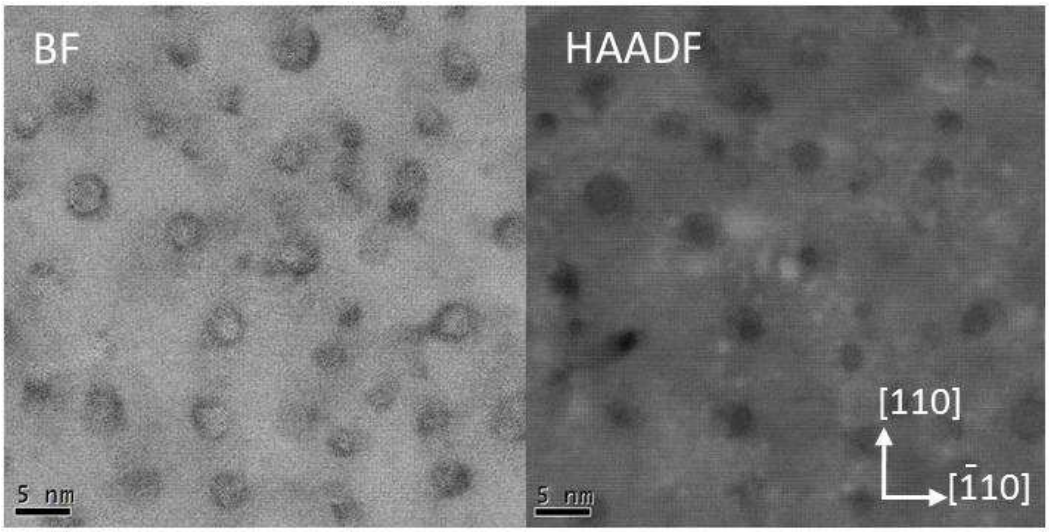

(a) FIB prepared

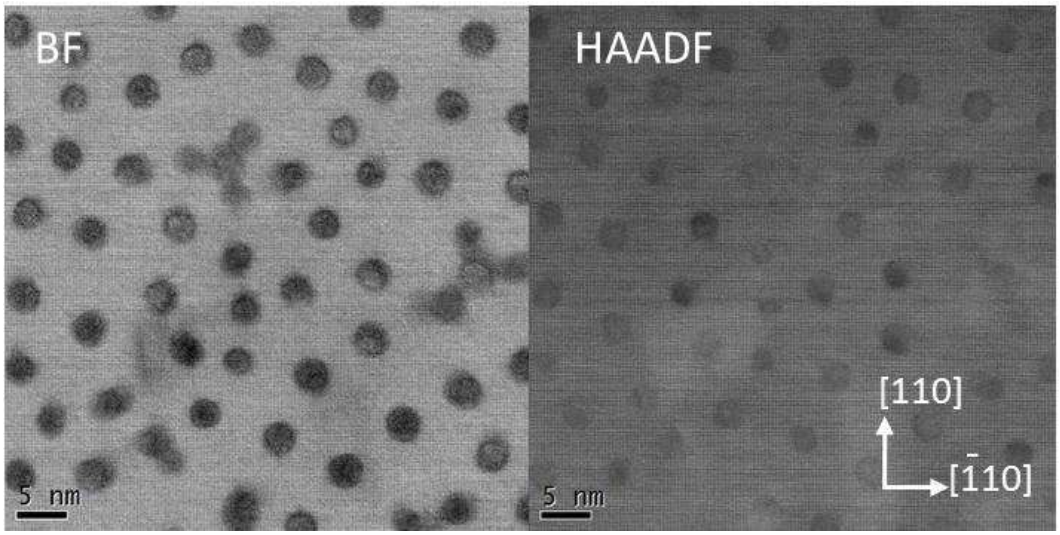

(b) Wedge polished

Figure 2.28.: BF- and HAADF-STEM image of GeMn nanocolumns in [001]-zone axis (plan view) showing the difference between FIB preparation (a) and wedge polished preparation (b). The specimen thickness is estimated to be ~ 30 nm in both cases.

3. Coarsening of Pt nanoparticles on amorphous carbon

Contents

This chapter describes the coarsening of Pt nanoparticles (NPs) on amorphous carbon (a-C) substrate after annealing at different temperatures. First the fundamentals of NP coarsening are reviewed, then the preparation and investigation methods of Pt NPs are described. In the results section, the evolution of Pt NP-size distribution is presented as a function of the annealing duration at annealing temperatures between 200 °C and 300 °C. It is found that, within the first two hours of annealing, the coarsening is dominated by Smoluchowski ripening, *i.e.* the NP coalescence due to their Brownian motion on the substrate. This is further supported by an in-situ annealing experiment in the transmission electron microscope. For annealing intervals $t > 2$ h, surface Ostwald ripening becomes the dominant coarsening process. Finally, in the discussion section, the Arrhenius-type dependence of the derived surface mass-transport diffusion coefficients is exploited to determine the activation energy for the surface diffusion of Pt adatoms on a-C substrate. The measured value is finally discussed with respect to other theoretical and experimental values reported in the literature.

3.1. Fundamentals of nanoparticle coarsening

In this work, platinum atoms obtained by electron-beam evaporation have been condensed on an a-C surface with a random distribution. After deposition a considerable redistribution of the material occurs, because the system tends to reduce its large interfacial energy. Clustering processes take place directly after deposition, because three-dimensional NPs are thermodynamically favored compared to a distribution of single adatoms. Depending on the dominant clustering process, three different stages can be defined: nucleation, early-growth stage and late-growth stage. Random nucleation of NPs on the substrate is the dominant process in the nucleation stage. This process is continuing during the early-growth stage, where the first NPs previously formed start to grow by capturing atoms from the supersaturated adatom phase. The early-growth stage represents actually the transition state between the nucleation and the late-growth stage. In the early-growth stage, the surrounding adatom concentration on the substrate exceeds the equilibrium concentration, and nanoparticles grow individually as long as the equilibrium concentration is not reached [Zink 92]. However, in this work, we will focus on the kinetics of the late-growth stage, also called the coarsening stage.

In the following the theoretical framework used to describe the coarsening of a NP ensemble taking place in the late-growth stage is outlined in detail. Within this stage, the NP coarsening is driven by the tendency to lower the total free energy of the NP ensemble by redistributing the material into fewer and larger NPs. Thereby the free energy associated with the surface energy is reduced. The NP coarsening on a surface may proceed via Smoluchowski (SR) and/or surface Ostwald ripening (OR) [Zink 92]. Both processes have different kinetic properties. Particularly, the time evolution of the average NP radius (*i.e.* the kinetics) for OR and SR can be described by a power law:

$$\bar{r}^n(t) = \bar{r}^n(0) + Ct \tag{3.1}$$

where $\bar{r}^n(0)$ is the average NP radius at $t = 0$. The exponent n and the coefficient C are parameters dependent on the growth kinetics. From Eq. 3.1, one can see that the average NP radius $\bar{r}(t)$ increases with increasing time, and that both processes slow down as the average NP radius increases. The difference between SR and OR lies in the mass-transport taking place between NPs [Rose 99]. In SR, the mass-transport occurs through the NP mobility, whereas in OR, it occurs through the exchange of adatoms between the NPs. Fig. 3.1(a) and (b) schematically shows the NP coarsening via SR and OR, respectively.

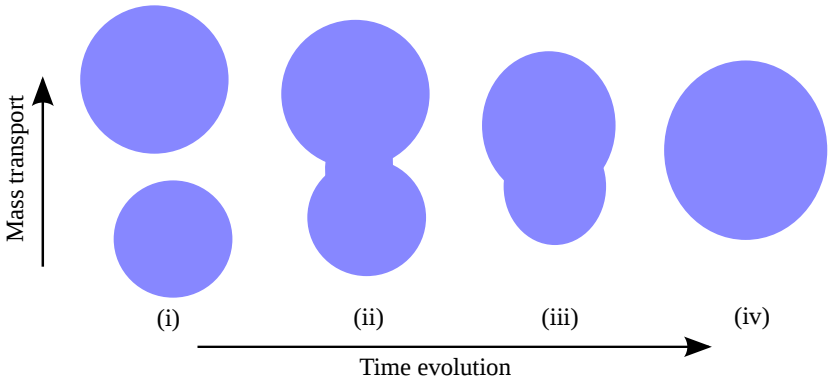

(a) Smoluchowski ripening

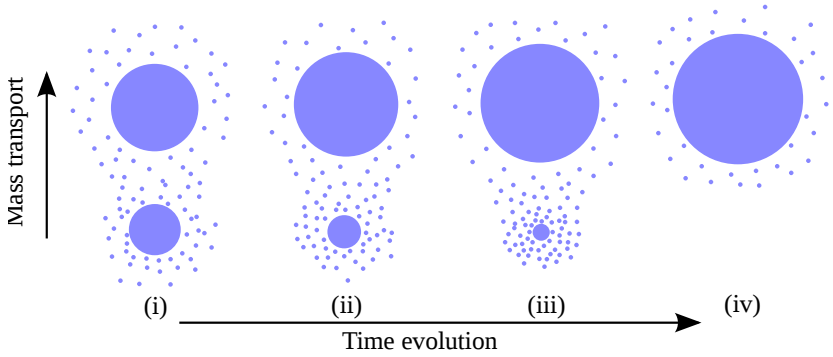

(b) Ostwald ripening

Figure 3.1.: (a) The SR of two mobile NPs, due to their Brownian motion on the substrate: (i) still separated mobile NPs, (ii) encounter each other and a neck is formed at the contact place, (iii) the neck grows and results in a single elongated NP, (iv) the NP relaxes to its equilibrium shape. (b) The OR of two fixed NPs by adatom transport between them. The adatom concentration near the small NP is larger than near the larger one, due to the Gibbs-Thomson effect. (i)-(iii) The small NP shrinks in favor of the larger one, and (iv) finally disappears.

The SR process (Fig. 3.1(a)) consists in the growth of mobile nanoparticles as a result of their Brownian motion on the substrate. This growth model is call Smoluchowski ripening, because Smoluchowski was the first who formulated a kinetic theory of coarsening via dynamic coalescence of diffusing particles in a coagulation of colloid particles in 1916 [Smol 16]. A NP ensemble can coarsen by SR, if diffusing nanoparticles encounter each other and coalesce into larger nanoparticles. Fig. 3.1(a) shows the SR process of two NPs. As can be observed here, the two mobile NPs, which are initially separated by a small distance (i), encounter each other (ii). A neck is formed at the contact place (ii), which grows with time and results in a single larger elongated NP (iii). Finally, the particle relaxes to the equilibrium shape (iv). Such a process has been already observed for metallic NPs (Au-Pd, Au, Pd, etc.) on amorphous surfaces by in-situ TEM [Jose 05].

SR strongly depends on two parameters:

1. the NP density on the substrate, *i.e.* the average distance between NPs on the substrate, as the probability of a coalescence process increases for increasing NP density, and thus decreasing average inter-particle distance;
2. the NP radius, as a strong decrease of the dynamic coalescence is expected with increasing the NP radius. The SR of two large mobile NPs will happen less frequently, as the surface-diffusion of whole NPs strongly decreases with increasing NP radius [Zink 92].

It follows that SR will be dominant for NP ensemble with high density and/or small average size. The merging process of two mobile NPs will happen less frequently for larger NPs. A high exponent n of the power law given in Eq. 3.1 is typical for SR, as compared to OR. Experimentally, exponents between 7 and 15 were found to adequately describe SR [Benn 03].

In case of surface OR (Fig. 3.1(b)), the mass transport occurs through surface diffusion of adatoms between two fixed NPs. As can be observed in Fig. 3.1(b), the adatom concentration on the substrate near the small NP is larger than near the larger one, due to the Gibbs-Thomson effect. The concentration gradient between NPs of different size leads to a diffusion of adatom from the small NP to the larger one. Thus, the small NP shrinks (i)-(iii) in Fig. 3.1(b), and finally disappears (iv) in Fig. 3.1(b) in favor of the larger one.

The adatom concentration is determined by the Gibbs-Thomson effect [Ostw 00], which relates the concentration n_r of adatoms on the substrate in the vicinity of a NP with its radius r:

$$\frac{n_\mathrm{r}}{n_\mathrm{eq}} = \exp\left(\frac{2\sigma\nu_\mathrm{m}}{r k_\mathrm{B} T}\right) \tag{3.2}$$

where σ is the surface tension, ν_m the volume of an adatom, k_B the Boltzmann's constant, T the absolute temperature and n_eq the adatom concentration corresponding to the equilibrium vapor pressure p_eq. The difference in adatom concentration in the vicinity of NPs with different sizes is the driving force for the NP growth and leads to a net flow of adatoms from the smaller to larger NPs.

Surface OR process can be described by using the Lifshitz-Slyozov-Wagner theory [Wagn 61, Lifs 61], that explains the coarsening of the size distribution of an ensemble of precipitates in a solid, adapted to the case of a NP ensemble on a substrate by Chakraverty [Chak 67]. He assumed a distribution of three-dimensional NPs with the shape of spherical caps with different radii r. This distribution can be described by its average NP radius at a given time t. Depending on the experimental conditions the kinetics of surface OR is limited either by the surface diffusion or by the "barrier

passing", *i.e.* the energetic barrier to be overcome for attachment/detachment of an atom at/from the NP surface. Accordingly, the OR kinetics is usually discussed in terms of two different limiting cases: diffusion-limited kinetics, which corresponds to the case for which adatoms diffusion is rate-determining, or reaction- or attachment-limited kinetics, where the addition or detachment of adatoms at the NP surface is the limiting process. The time evolution of the average NP radius can be described in these two cases by the power law in Eq. 3.1 [Chak 67, Wynb 75]. For surface OR with a diffusion-limited kinetics, the exponent is $n = 4$ and the coefficient $C = C_{\mathrm{d}}(D'_{\mathrm{s}}, T)$ depends on the surface mass-transport diffusion coefficient D'_s and on the absolute temperature T. In the case of reaction-limited kinetics, the exponent is $n = 3$ and the coefficient $C = C_{\mathrm{r}}(\beta, T)$ depends on the probability β to add/detach an adatom per second and on the temperature T [Chak 67, Wynb 75]. We note that Eq. 3.1 is strictly valid only for the critical NP radius $r^* = r^*(t)$, which is neither shrinks nor grows at time t [Wynb 75]. However, $r^*(t)$ is identical with $\bar{r}(t)$ as demonstrated numerically by Kirschner [Kirc 71].

SR and OR processes can be differentiated from each other by comparing the experimentally determined evolution of $\bar{r}(t)$ and the resulting exponent of the power law with the theoretical prediction provided by Eq. 3.1 [Benn 03, Daty 06, Pope 09] or by in-situ annealing experiments [Allo 07, Jose 05].

3.2. Sample preparation and investigation methods

The samples were prepared by electron-beam evaporation of Pt on a-C film substrates with a nominal thickness of 10-12 nm. The films are mounted on 400 µm mesh Au grids, which are preferred to Cu or Ni grids, because they do not produce artifacts during annealing like migration of NPs coming from the grid or graphitisation of the a-C film [Zhan 09]. A 7.4 keV electron beam was used for the Pt evaporation which yields a deposition rate of 0.02 Å $\cdot$ s^{-1} at a pressure of $3.4 \cdot 10^{-1}$torr. The amount of deposited Pt corresponds to a layer with a nominal thickness of 2 Å, which results in a narrow size distribution of small Pt NPs on the whole a-C substrate, as shown in the following.

After deposition, the samples were annealed in a tube oven in an Ar atmosphere at 200, 225, 240, 275 and 300 °C. The rate of heating and cooling the samples was of 1.5 °C $\cdot$ s^{-1}. The samples could not be annealed at temperatures above 300 °C, due to rupture of the thin carbon films at high annealing temperatures for long time intervals.

The coarsening of Pt NPs was investigated by transmission electron microscopy. The TEM experiments were carried out in a Philips CM200 FEG/ST microscope at 200 kV

acceleration voltage, in an FEI Titan^3 80-300 microscope at 300 kV and in an FEI Titan Ultimate at 200 kV. The size distribution of the Pt NPs was determined from high-magnification TEM images taken with the Philips CM200 microscope using a 2048×2048 pixels (px) CCD camera and an exposure time of 0.5 s. The TEM images employed for the structural investigation of NPs were recorded with the image-corrected FEI Titan^3 80-300 and a 2048×2048 px CCD camera with an exposure time of 0.5 s. HAADF-STEM images were acquired on a double-corrected FEI Titan Ultimate. To minimize the influence of high-energy electron-beam irradiation on the coarsening of Pt NPs, all microscope alignments were carried out on sample regions which were not considered for data collection. The sample was then moved to adjacent regions that were not exposed previously. The images were immediately taken without refocusing. Using this procedure, the total illumination time under HRTEM conditions (choice of region and recording the image) was about 2 s. In this experimental condition we measure a dose rate of $d_{\text{rate}} = 13.1$ A$\cdot$cm^{-2} and a total dose of $d_{\text{total}} = 1.6 \cdot 10^6$ electrons$\cdot$ nm^{-2} for total illumination time of $t_{\text{illum}} = 2$ s (see sec. 3.3.4.3).

3.3. Experimental results

3.3.1. Size distribution of Pt nanoparticles

The coarsening of Pt-NP ensembles was studied by investigating the time evolution of the average NP radii after annealing at 200, 225, 240, 275 and 300 °C for different time intervals t. For the evaluation of the NP radii, the projected area of the NPs on the TEM images was measured. The measured areas were evaluated by calculating the particle radius of circular projection area of the same size. TEM images shown in Fig. 3.2 and Fig. 3.3 demonstrate that the assumption of circular projections is reasonable for the description of the real NP projections for the investigated annealing temperatures and times. These radii were used to determine NP-radius distributions and the corresponding average radii at a given annealing time and annealing temperature. About 300 NPs with $r \geq 0.4$ nm on several TEM images were evaluated to obtain NP-radius distributions. Fig. 3.2 shows a representative TEM image of the NP distribution for an as-deposited sample which is characterized by a NP density $n(t = 0) = (6.4 \pm 0.5) \cdot 10^{-16}$ m^{-2} and an average NP distance of 4 nm.

An average radius of $\bar{r}(t = 0) = 0.72 \pm 0.06$ nm is calculated from the corresponding NP-radius distribution shown in the insert of Fig. 3.2. The properties of the as-deposited Pt NPs were consistently reproduced because they always yielded identical $\bar{r}(0)$ and $n(0)$ values within the error limits.

Fig. 3.3 shows TEM images of Pt NPs and the corresponding radius distributions (inserts in Fig. 3.3(a-d)) after annealing at 225 °C and 275 °C for 2 h and 30 h, respectively.

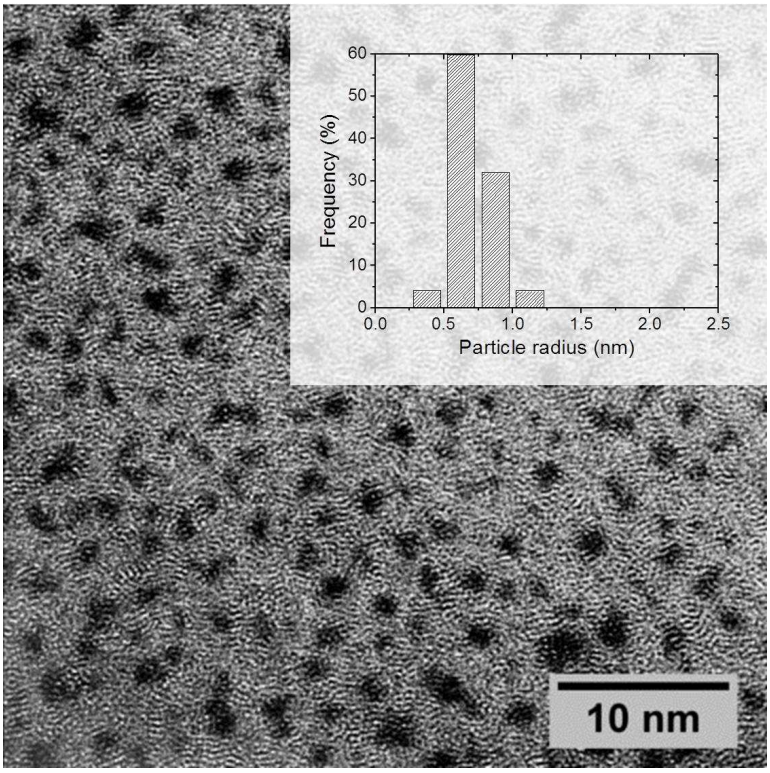

Figure 3.2.: TEM image of Pt NPs recorded directly after deposition. The inset shows the corresponding NP-radius distribution with an average radius of $\bar{r}(t = 0) = 0.72 \pm 0.06$ nm.

The images and histograms clearly demonstrate the coarsening of Pt NPs with the annealing time and temperature.

Fig. 3.4 presents the derived $\bar{r}(t)$ values as a function of annealing time for all temperatures which clearly visualize the coarsening process. Fig. 3.4(a) shows $\bar{r}(t)$ for annealing durations up to 160 h, while Fig. 3.4(b) focuses on the development of $\bar{r}(t)$ during the first 5 h of annealing. The time evolution of the average NP radii at constant T shows that, firstly, a very fast coarsening prevails within the first 2 h of annealing at all temperatures (Fig. 3.4(b)). This is particularly obvious for annealing at 275 °C and 300 °C. Then, the coarsening rate slows down with further increase of the annealing time at all investigated temperatures. This suggests the presence of two coarsening stages with different growth kinetics for annealing times $t < 2$ h and $t > 2$ h, respectively. This conclusion is supported by the results of an in-situ annealing experiment in a transmission electron microscope presented in sec. 3.3.2. Moreover, the increase of $\bar{r}(t)$ with increasing T for the same annealing time t, which is expected for thermally activated processes like surface OR and SR, is obvious from Fig. 3.4(a).

The kinetics of the ripening process during the second stage, *i.e.* for annealing times $t > 2$ h, is evaluated by a least square fit of the experimental $\bar{r}(t)$ values with the theoretically predicted behavior according to Eq. 3.1 with power law exponents $n = 3$

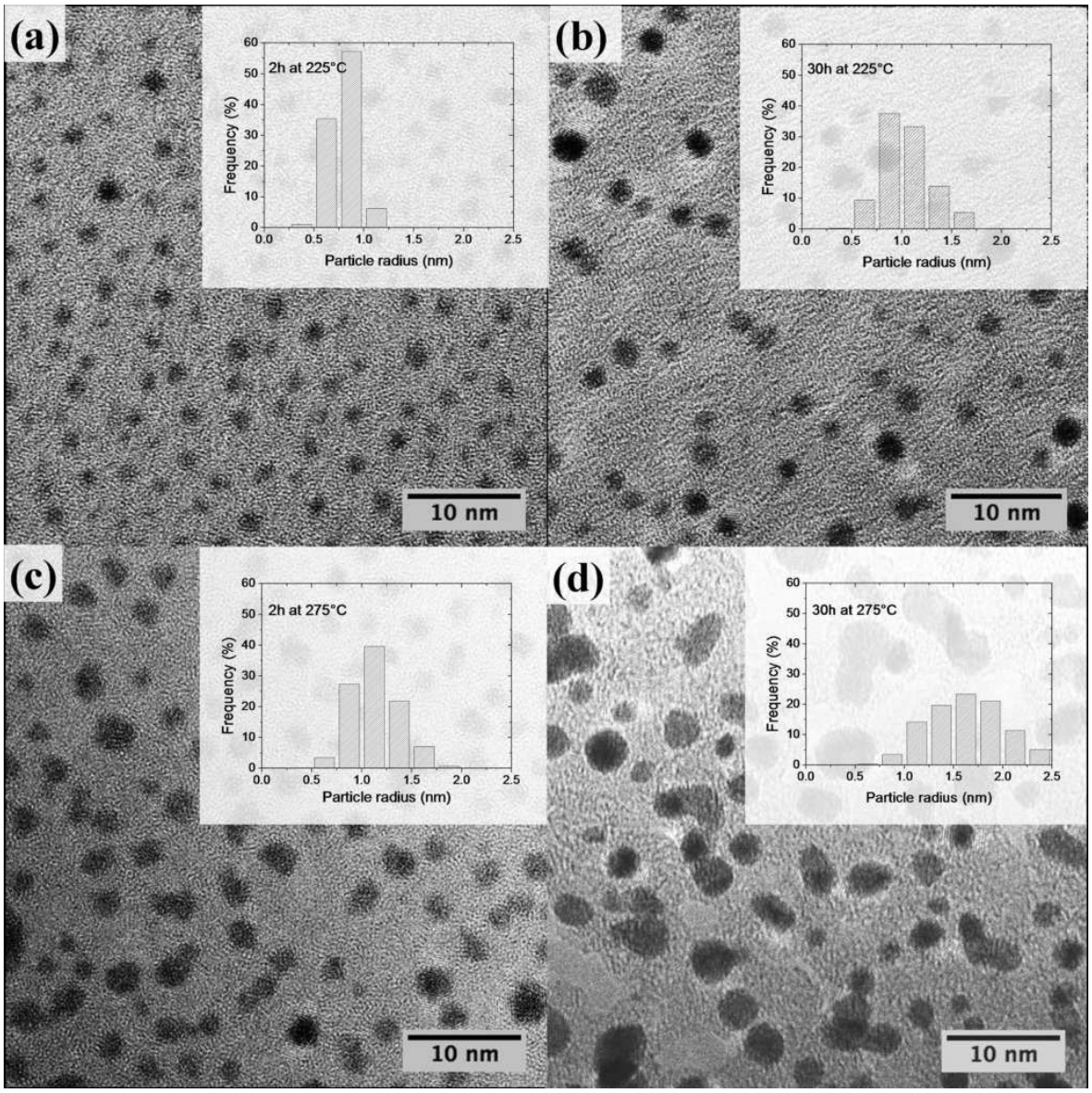

Figure 3.3.: TEM images of Pt NPs after annealing at 225 °C for (a) 2 h and (b) 30 h, and after annealing at 275 °C for (c) 2 h and (d) 30 h, respectively. Insets show the corresponding NP-radius distributions.

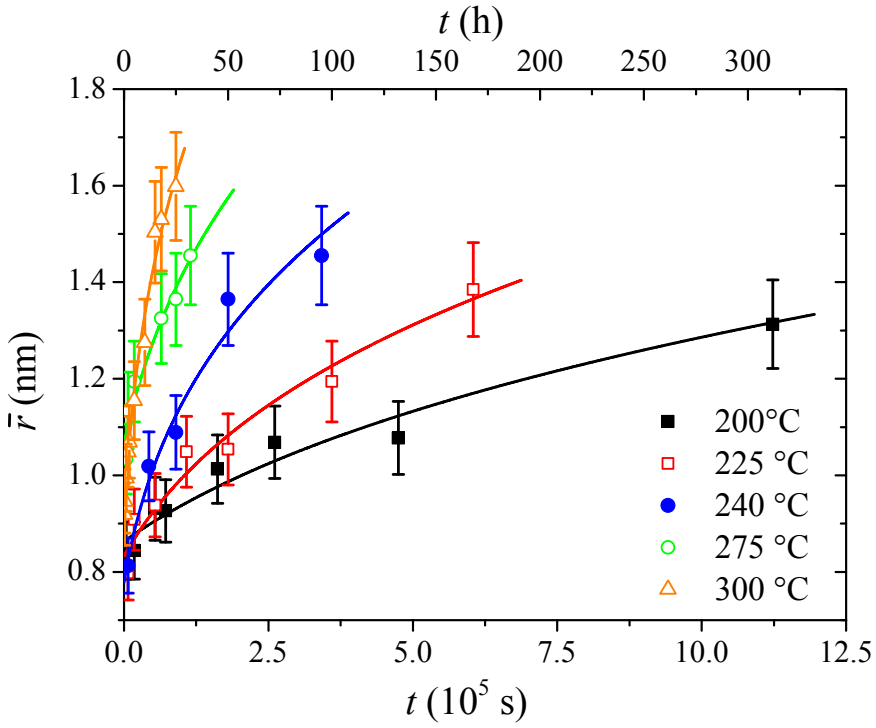

(a)

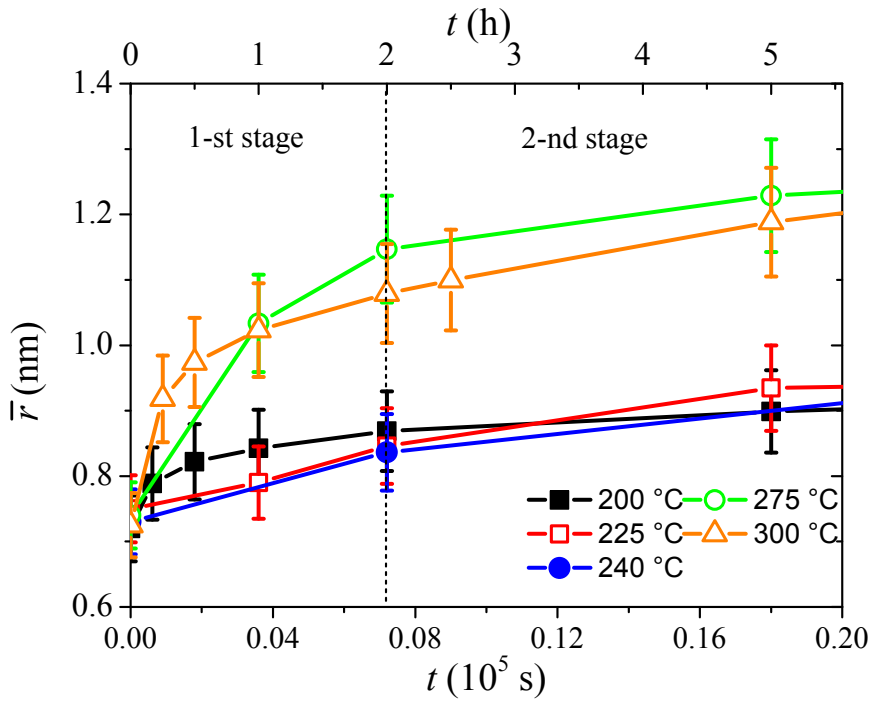

(b)

Figure 3.4.: (a) Average radius $\bar{r}(t)$ of Pt NPs as a function of the annealing time t. The solid lines represent fit curves for surface OR with a diffusion-limited kinetics in the second stage (*i.e.* $t \geq 2$ h). (b) Magnified section of (a) for annealing times up to 5 h, which emphasizes the two different coarsening stages (lines are guide to the eye). The error bar correspond to the error in the measurement of the NPs radius.

or $n = 4$. The average NP radius $\bar{r}(0)$ must be treated as a free parameter for the fit in addition to the coefficient C. The experimental value $\bar{r}(0) = 0.72 \pm 0.06$ nm cannot be used for the fit because a very active SR process takes place during the first 2 h of the ripening process as will be shown in section sec. 3.3.2. The fit quality was determined by the residual $w = \sum|\bar{r}(t_i) - \bar{r}_{\mathrm{th}}(t_i)|/\sum \bar{r}(t_i)$, which measures the average relative deviation between the experimental values $\bar{r}(t_i)$ and $\bar{r}_{\mathrm{th}}(t_i)$ of the fit curve, where the index i runs over all data points $t_i > 2$ h at a given temperature. The best fit curves in Fig. 3.4 are obtained for an exponent $n = 4$ in Eq. 3.1, which describes coarsening by surface OR with a diffusion-limited kinetics [Chak 67, Wynb 75]. The high fit quality given by $1.8\% \leq w \leq 3.3\%$ for all temperatures demonstrates that surface OR with a diffusion-limited kinetics can well account for the evolution of $\bar{r}(t)$ during the second coarsening stage. It is noted that these w values are more than 40 % smaller than the w values calculated for OR with a reaction-limited kinetics which supposes an exponent $n = 3$ in Eq. 3.1. We conclude that the kinetics of surface OR for Pt NPs on an a-C substrate corresponds well to the diffusion-limited case during the second coarsening stage ($t \geq 2$ h) in the temperature range between 200 °C and 300 °C .

3.3.2. In-situ study of Pt-nanoparticle coarsening

An in-situ annealing experiment in the Philips CM200 transmission electron microscope was carried out to investigate the coarsening mechanisms for a time interval of up 3 h which comprises both kinetics regimes. For that purpose, an as-deposited sample was in-situ annealed at a nominal temperature of 470 °C. The real sample temperature was presumably lower because the thermocouple used for temperature measurement is located in some distance from the investigated sample region. TEM images were successively taken from the same sample region every 30 min, starting just after the sample reaches 470 °C, taken in this case as $t = 0$ min, up to $t = 188$ min. To avoid any possible influence of the illumination with high-energy electrons on the coarsening process, the electron beam was removed from the region of interest between two successive image acquisitions. The NP-radius distribution determined from TEM images, which were recorded just after the sample reached 470 °C, results in an average radius $\bar{r}(t = 0) = 0.73 \pm 0.07$ nm similar to the value of the as-deposited sample. This allows us to exclude significant coarsening during the time interval that is necessary to heat the sample up to 470 °C. Fig. 3.5 shows several images of the TEM time series. The arrows in Fig. 3.5 mark small NPs, which decay and finally vanish in favor of larger ones due to the surface OR. Encircled regions in Fig. 3.5 mark mobile NPs, which encounter each other and coalesce into larger particles due to SR. For example, the coalescence of three NPs marked in the lower part of Fig. 3.5(a) is terminated after about 106 min

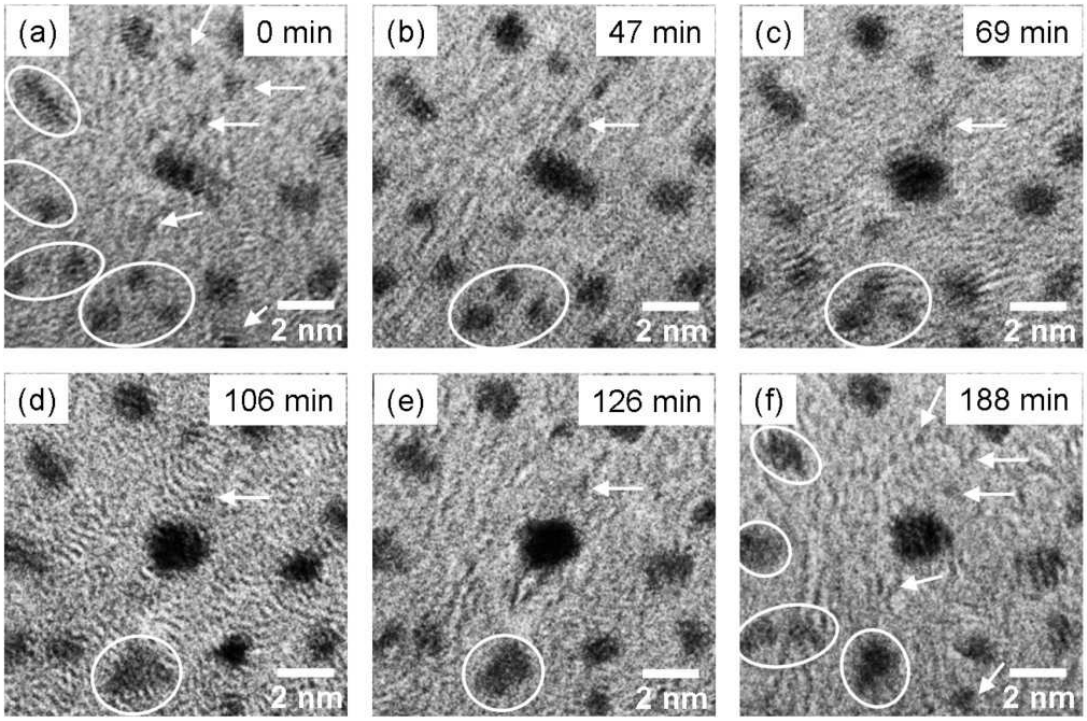

Figure 3.5.: Series of TEM images of the same sample region recorded during an in-situ annealing experiment at 470 °C, which started just after the sample reached 470 °C at (a) $t = 0$ min and ended at (f) $t = 188$ min. The arrows mark small Pt NPs, which decay and vanish in favor of larger ones due to the surface OR. Encircled regions point out mobile NPs, which coalesce by SR.

(Fig. 3.5(d)). This in-situ TEM study shows that a dominant coalescence of mobile Pt NPs takes place for $t < 2$ h in addition to OR. SR becomes negligible for $t \geq 2$ h, as suggested by the decreasing number of dynamic coalescence events (in fact no event could be observed after $t = 126$ min). Responsible for that are the reduction of the surface diffusion coefficients of Pt NPs with increasing NP sizes, and the increase of average inter-NP distances with decreasing NP density on the substrate. This allows us to neglect SR during the second ripening stage ($t \geq 2$ h), where the surface OR becomes the dominant ripening process.

3.3.3. Structure and shape of Pt nanoparticles

3.3.3.1. Structure of Pt nanoparticles

The crystal structure of Pt NPs can be investigated using electron diffraction (ED). For that, ED patterns of Pt NPs on a-C substrate were recorded on the CM200 microscope using image plates, which were later scanned with a Ditabis scanner. Compared to the CCD camera image plates have the advantage of a high dynamic range of image intensities, which allow to measure simultaneously weak diffracted beams and the very intense transmitted beam. The need to use the beam stop of the microscope to prevent

damaging of the camera is in this case not required. For the small Pt NPs considered in this work, it is necessary to perform acquisition with a high dynamic range, as the diffracted beams of our samples are weak. Because the samples are composed of randomly oriented NPs, their diffraction patterns will consist of concentric rings, which gives rise to the so-called Debye-Scherrer ED patterns. One can radially average these ED patterns, which are rotationally invariant, and calculate the corresponding radial scans. The radial averaging consists in averaging each spatial frequency $q = \mid \vec{q} \mid = 2\sin(\theta)/\lambda \simeq 2\theta/\lambda$[1]. The deformation induced during the scanning process is corrected by fitting the Debye-Sherrer rings by ellipses and then transforming them into circle. Let us consider the ED pattern of Pt NPs on a-C substrate after deposition (Fig. 3.6(a)) and its corresponding radial scan (blue color curve in Fig. 3.6(c)). From this curve, one can subtract the radial scan representing the contribution of a-C substrate (black color curve in Fig. 3.6(c)) calculated from the ED pattern measured independently on the a-C film before deposition of Pt NPs (Fig. 3.6(b)). This method permits to determine the contribution of Pt NPs to the ED pattern, as shown in Fig. 3.6(c) by using the blue curve. At a first view, the ED pattern of small Pt NPs on a-C substrate displayed in Fig. 3.6(a) seems to be the ED pattern of an amorphous material, very similar to the ED pattern of the a-C film shown in Fig. 3.6(b). However, after radial averaging the ED patterns in Fig. 3.6(a-b) followed by the subtraction of the background corresponding to the a-C substrate, diffuse intensity remains at the position of Pt Bragg reflections, as shown by the blue curve in Fig. 3.6(c).

Fig. 3.6(c) points out how the subtraction was performed, as well as the superposition of the radial scan of Pt NPs with that of the a-C film. This method allows to investigate the evolution of the crystallinity of Pt NPs as a function of the annealing time, and to get more insight in the structural evolution of Pt NPs with annealing treatment. Fig. 3.7 shows three ED patterns of Pt NPs on a-C film taken from a series of samples after annealing at 300 °C, while Fig. 3.7(d) displays the radially averaged ED patterns after background subtraction for the whole serie. A close resemblance is found between the experimental radial scans measured for Pt NPs annealed few hours at all investigated temperature and simulated diffraction patterns of NPs with face-centered cubic (fcc) cuboctahedral (CO) or truncated-octahedral (TO) structure reported in [Zanc 01]. Moreover, other diffraction patterns, which correspond to Pt NPs with icosahedral or decahedral structure have different Bragg reflection positions and/or different intensity ratios between the reflections, compared with experimental ED patterns [Zanc 01]. In Fig. 3.7(d), one can observe that the Bragg reflections become sharper with increasing annealing time. This is attributed to the increase of the average NP or crystallite size (Pt NP are monocrystalline), as well as to a decrease of the strain or disorder in large Pt NPs, as compared to that of smaller ones. An increased annealing time

[1] $\theta \leq 1$ mrad in TEM

and thus a larger average NP radius results in a improved structural relaxation of the strain accumulated during NP growth, pointing out a structural evolution of NPs towards well-ordered fcc structure of bulk Pt. Series of ED patterns acquired at other temperatures show a similar evolution.

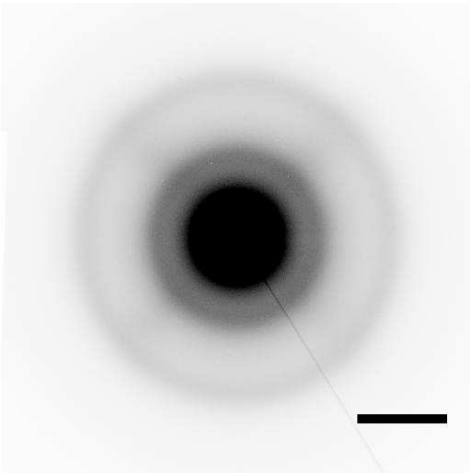

(a) ED pattern of Pt NPs after depositon

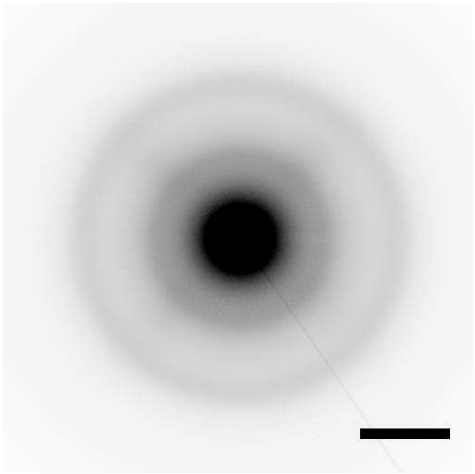

(b) ED pattern of a-C substrate

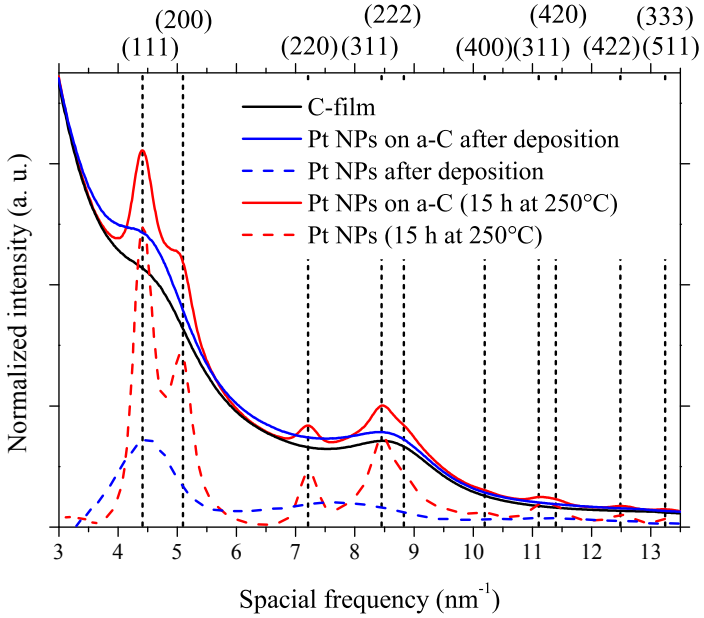

(c) ED pattern after radial averaging and background subtration

Figure 3.6.: (a) ED pattern of Pt NPs with an average radius $\bar{r}(t) = 0.72 \pm 0.06$ nm on a-C substrate taken directly after deposition. (b) ED pattern of the a-C substrate. (c) Corresponding radial averaging of ED patterns shown in (a) and (b) and the contribution of Pt NPs (dash blue curve) obtained after subtraction of the background induced by the a-C substrate. Raw (red curve) and background subtracted (dash red curve) radial averaging of ED patterns for Pt NPs on a-C substrate annealed 15 h at 250 °C. The vertical dashed lines indicate the calculated position of Bragg reflections with their corresponding Miller indices (hkl) on the top for fcc bulk Pt with a lattice parameter of $a_{\mathrm{Pt}} = 0.3925$ nm. The scale bar is 5 nm^{-1} in (a) and (b).

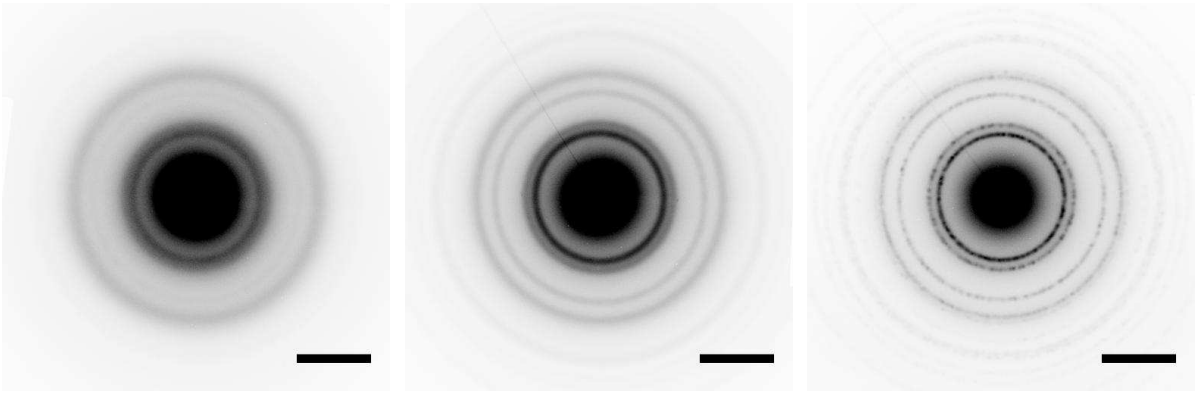

(a) 30 min annealing (b) 5 h annealing (c) 15 h annealing

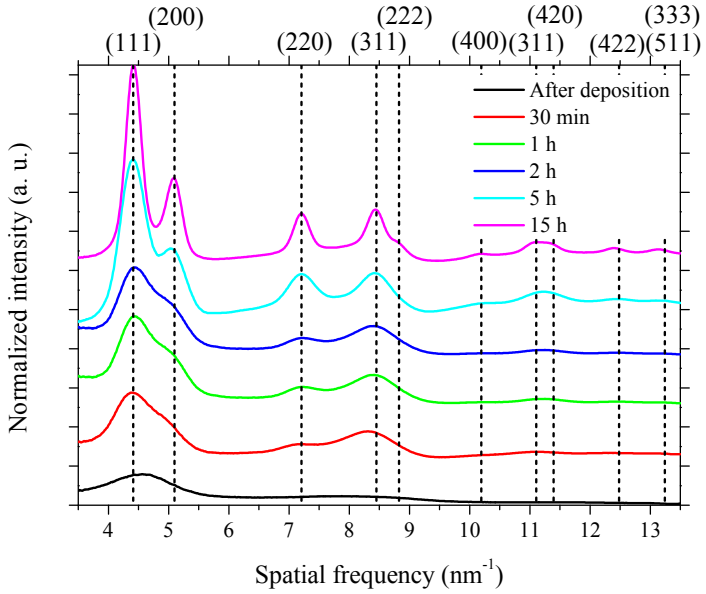

(d) Evolution of the Pt NP cristalline structure during annealing

Figure 3.7.: ED patterns of Pt NPs on a-C substrate after annealing at 300 °C for (a) 30 min (b) 5 h and (c) 15 h. The Debye-Scherrer rings become more and more sharper with increasing the annealing time. The scale bar is 5 nm^{-1} for the three ED patterns. (d) Radial average ED curves after background subtraction showing the evolution of the Pt NP structure towards the well-ordered fcc structure of bulk Pt.

3.3.3.2. Shape of Pt nanoparticles

The evaluation of the coarsening data with respect to the determination of mass transport-diffusion coefficients in sec. 3.4 requires information on the NP shape. For this purpose, we performed a tilt experiment in the Philips CM200 microscope, where the sample was tilted by 30° and the projected NP area measured at normal illumination (0°) was compared with the corresponding area measured in the tilted position. Spherical NPs would not change their projected areas after tilting the sample. Otherwise the NPs must have facets, even if the facets do not appear in the projected outline of NPs on TEM images. An increase of the projected area is explained by NPs with vertical facets, whereas a decrease of the projected area is explained by flat NPs.

The projected areas at normal and tilted position of 16 NPs located on a sample annealed for 5 h at 240 °C are given in Fig. 3.8. The projected NP area increases on the average by 12.9% on the tilted position (estimated on the basis of 29 NPs, some of them are shown in Fig. 3.8), which excludes spherical particles. To increase the projected areas in the tilted position by 12.9 %, vertical particle facets with a height $h = 0.82 \cdot r$ are required, where r is the projected NP radius at normal illumination. This measurement is consistent with CO or TO shapes.

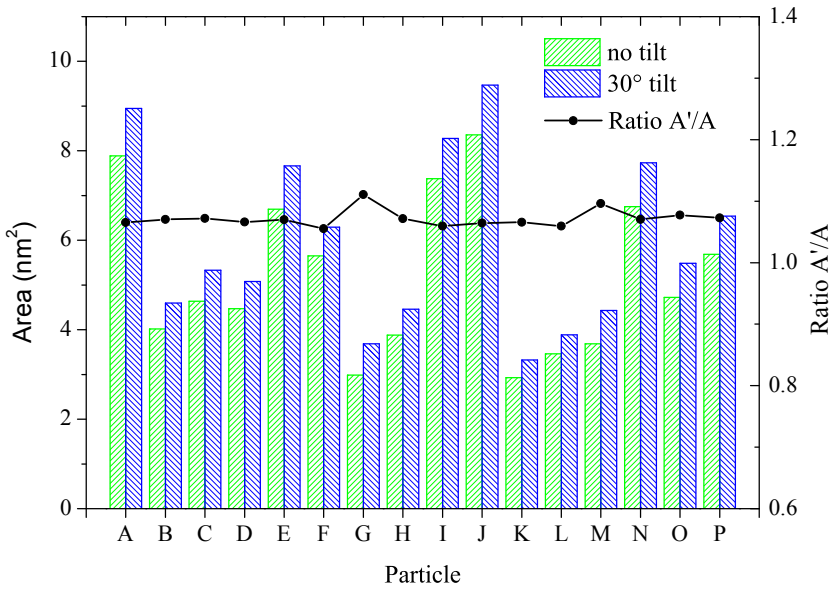

Figure 3.8.: Experimental projected area of Pt NPs and the corresponding ratio between area: at normal illumination (0°) and after tilting by 30°.

Ab-initio calculations on the basis of ultrasoft pseudopotential and projected augmented wave methods indicate that Pt NPs with a monocrystalline fcc structure and a truncated-octahedral or cuboctahedral shape are the most stable structures for Pt NPs with more than 38 atoms [Kuma 08, Nie 07, Jose 01, Wang 00]. It was also shown that a transition to a closed-packed icosaedral structure is unlikely even after heating

the Pt NPs up to 600 K [Kuma 08]. These results suggest that most Pt NPs in our study have an fcc TO or CO structure, which is in good agreement with our shape and structural investigations presented in the following.

However, to be able to differentiate between CO and TO shape, HRTEM images of Pt NPs were recorded in the aberration-corrected FEI Titan^3 80-300 microscope. The investigated sample was annealed for 25 h at 240 °C. HRTEM images in Fig. 3.9(a-b) show Pt NPs with fcc structure in the [110]- and [001]-zone axis, respectively, recorded with 10 nm overfocus. The distinction between TO and CO shapes is based on the qualitative comparison of the experimental HRTEM images and corresponding simulated images using the multislice algorithm of the JEMS Software [Stad 87]. Three-dimensional structure models of Pt NPs with TO and CO shapes for image simulations were first built by using a dedicated program described in Ref. [Bern 98]. The ideal models are then slightly modified from the perfect TO or CO shape (Fig. 3.9(e,h)) to improve the agreement between experimental and simulated HRTEM images. For simulations, the atomic potential of Pt atoms was calculated by inverse Fourier transformation from Weickenmeier-Kohl form factors [Weic 91]. The partial temporal coherence of the incident electron wave was described by a defocus spread of $\Delta C = 4$ nm for the FEI Titan^3 80-300. The spherical aberration was set to 1 µm in simulations, which corresponds to the experimental value obtained with the aberration corrector. The image detection by the CCD camera was taken into account by convoluting the simulated image with the modulation transfer function of the CCD camera which was measured by the edge method [Weic 95]. The comparison of the experimental image Fig. 3.9(a) and the simulated images Fig. 3.9(c,f) indicates that image simulations in the [110]-zone axis are not sufficient to distinguish between fcc Pt NPs with CO or TO shape. However, a criterion for discrimination between these two shapes is provided by [001]-zone-axis images in the right column of Fig. 3.9 where the {200} planes are differently oriented with respect to the projected NP shape for TO and CO NPs. The {200} planes are aligned parallel to the projected edges for CO NPs (Fig. 3.9(g)). In contrast, the {200} planes are oriented along the NP diagonals (Fig. 3.9(d)) for TO NPs which is in agreement with the experimental image (Fig. 3.9(b)). This also applies for the "truncation" of the corners which is visible for TO (Fig. 3.9(d)) but not for CO (Fig. 3.9(g)) NPs. This suggests that Pt NPs with a monocrystalline fcc structure and TO shape must be considered as relevant in our case. However, as can be observed on the TEM images shown in Fig. 3.2 and Fig. 3.3, many Pt NPs seem to have rather an irregular than a TO shape. This can be attributed to the large number of Pt NPs which are randomly oriented on the a-C substrate. Due to the amorphous substrate structure a preferential alignment of the NPs can indeed not be expected. Moreover, the NP ensemble is not in equilibrium and OR induces a permanent change of the number of Pt atoms in NPs. As a result, only few NPs will exhibit a perfect TO shape.

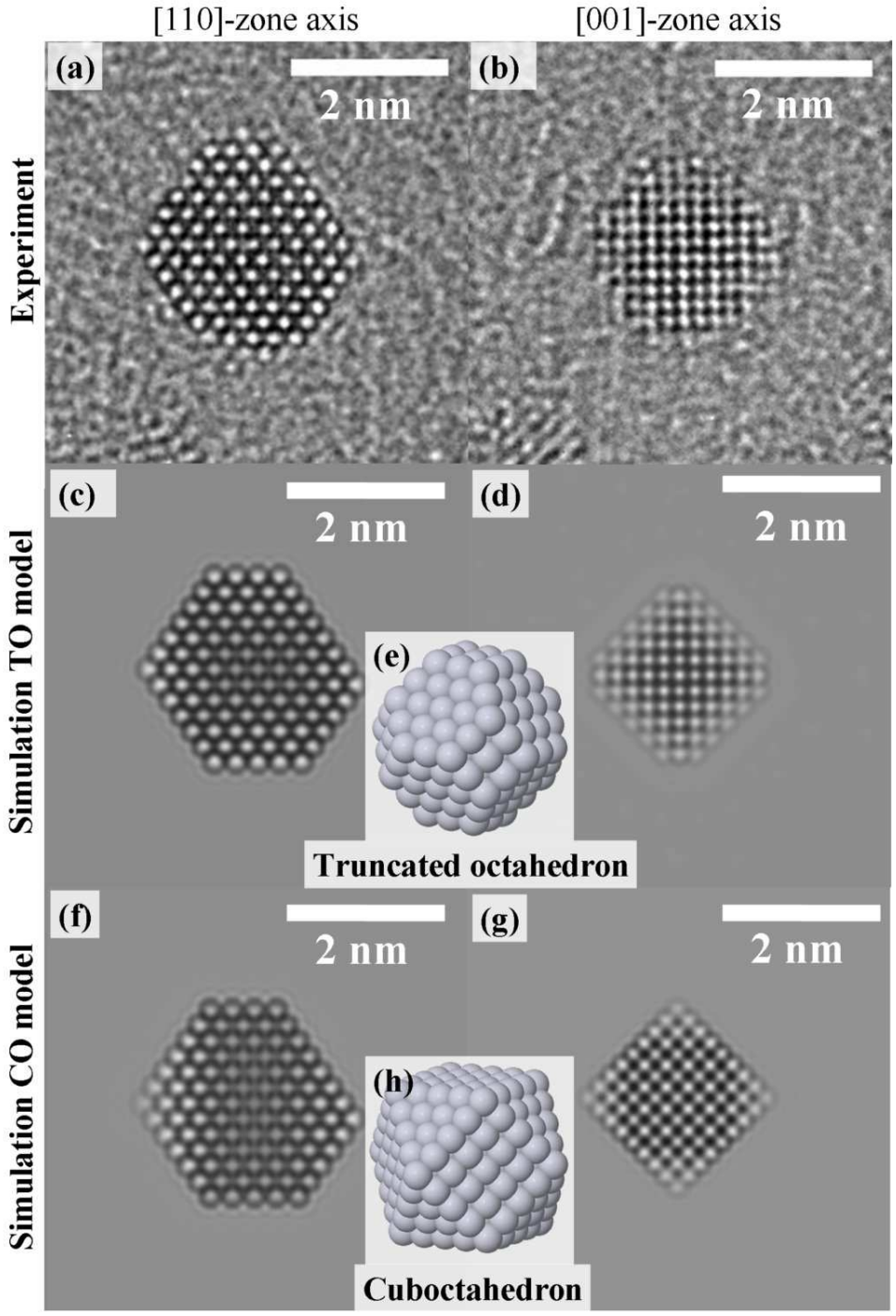

Figure 3.9.: Experimental HRTEM images of Pt NPs with fcc monocrystalline structure in the (a) [110]- and (b) [001]-zone axis. (c,d) Simulated HRTEM image of NPs with truncated octahedral shape in [110]- and [100]-zone axis, (e) structural model of NP with truncated octahedral shape. (f, g) Simulated HRTEM images of Pt NPs with cuboctrahedral shape in [110]- and [100]-zone axis, (h) structural model of NP with cuboctahedral shape.

3.3.4. Effect of electron-beam illumination

3.3.4.1. High-resolution transmission electron microscopy

The illumination with high-energy electrons in a transmission electron microscope may have a complex influence on the coarsening of NPs. It is already known from previous studies that high-energy electrons may contribute to the attachment/detachment of adatoms at/from the NP surface and may promote NP coalescence via SR by enhancing their Brownian motion on the substrate [Flue 88, Banh 08]. Both processes could modify the distribution of Pt NPs and alter it in an uncontrolled way. These aspects motivate a separate study on the effect of irradiation with high-energy electrons on ripening processes of NPs. Fig. 3.10 shows TEM images of the same region of a sample that was annealed at 200 °C for 20 h prior transferring it in the transmission electron microscope. The TEM images in Fig. 3.10 were taken immediately after exposing this region to the electron beam (Fig. 3.10(a)) and after 20 min (Fig. 3.10(b)) of continuous illumination in the microscope with a dose rate of $d_{\text{rate}} = 13.1\ \text{A}\cdot\text{cm}^{-2}$ (see sec. 3.3.4.3).

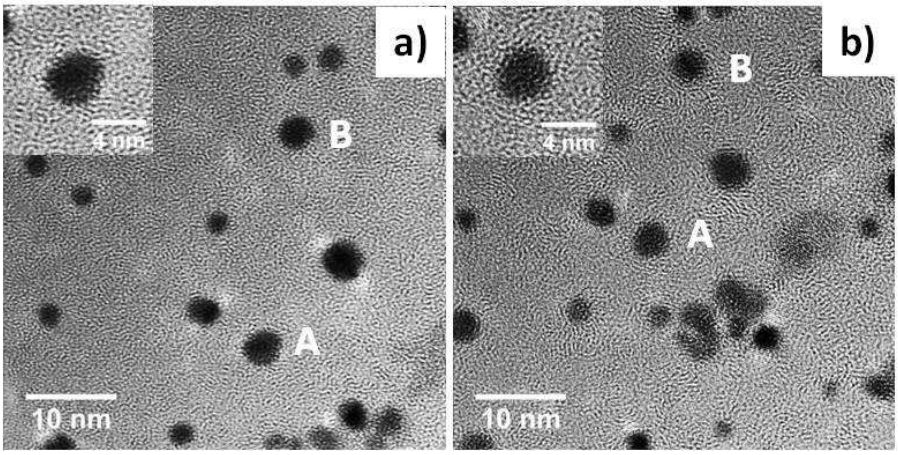

Figure 3.10.: HRTEM images of the same sample region recorded at (a) $t' = 0$ s and (b) after $t' = 20$ min of continuous illumination in the Philips CM 200 microscope with 200 keV electrons. The inserts in (a) and (b) represent the magnified Pt NP labeled by A, which does not show any change of its area after 20 min illumination.

During this time interval one TEM image was recorded every 30 s. The largest change of inter-NP distances is observed for the NPs marked by A and B (see Fig. 3.10(a-b)) which indicates a velocity $3 \cdot 10^{-3}\text{nm}\cdot\text{s}^{-1}$. With an average inter-NP distance of 6 nm, more than 30 min of illumination time would be necessary to induce NP coalescence by SR. The attachment/detachment process of Pt adatoms at/from the NP surface can be quantified by measuring the change of NP size as a function of the illumination time. During the first 20 min, no measurable change of the NP size was detected (see inserts in Fig. 3.10), which demonstrates that attachment/detachment of single Pt adatoms

do not lead to a significant size change under typical measurement conditions in our study with illumination times of about 2 s.

3.3.4.2. High-resolution scanning transmission electron microscopy

HAADF imaging in HRSTEM mode provides high contrast images of Pt NPs lying on a-C film. It allows easier quantification of the NP size, as the NPs can be better distinguished from the substrate. Moreover, HAADF images is also interesting for the investigation of NP shape.

Contrary to HRTEM, a strong influence of the electron beam illumination was observed in HRSTEM, where a single scan across the sample induces a noticeable impact on the Pt NP-size distribution. A time serie of HRSTEM images of the same area on a fresh deposited sample is used to study the evolution of Pt NP distribution during 5 min continuous illumination in HRSTEM at 200 kV with a beam current of 47 pA. Fig. 3.11 shows the HRSTEM images of a part of this time serie, which starts with (a) the 1^{st} scan at $t' = 0$ and ends with (f) the 10^{th} scan at $t' = 300$ s. The electron dose in HRSTEM and HRTEM will be considered in the next section.

The average NP radius measured on the HRSTEM image just after exposing the region to the electron beam of $\bar{r}(t = 0) = 0.68 \pm 0.1$ nm is in fair agreement with $\bar{r}(t = 0) = 0.72 \pm 0.1$ nm obtained by HRTEM. After 5 min continuous illumination in HRSTEM, the average radius of Pt NPs located on the same area of the sample increased to $\bar{r}(t' = 5 \text{ min}) = 0.88 \pm 0.1$ nm. This time serie highlights the evolution of Pt NPs after different successive scans. Between the first and the second HAADF-STEM images, *i.e.* $\triangle t' = 30$ s, the energy transferred from the incident electron beam to the sample was high enough to promote the Brownian motion of some Pt NPs and start their fusion via SR (see NPs marked by ellipses in Fig. 3.11). Moreover, the increase of the average radius of Pt NPs between the first and the last HAADF-STEM image (Fig. 3.11(a-f)) demonstrates that 5 min continuous illumination (or 10 successive scan) in HRSTEM is sufficient to induce a significant coarsening of Pt NPs. These observations point out that HRSTEM is not a reliable technique for the quantitative analysis of small NP-size distributions. Nevertheless the time series of HRTEM images in Fig. 3.11 can be further used to qualitatively describe the coarsening processes taking place shortly after deposition.

The HAADF-STEM image in Fig. 3.11(a) shows the presence of many small Pt species, like Pt atoms, dimers, trimers, etc. indicated by arrows in between the Pt NPs on the substrate. This observation suggests that due the short deposition time of Pt on a-C,

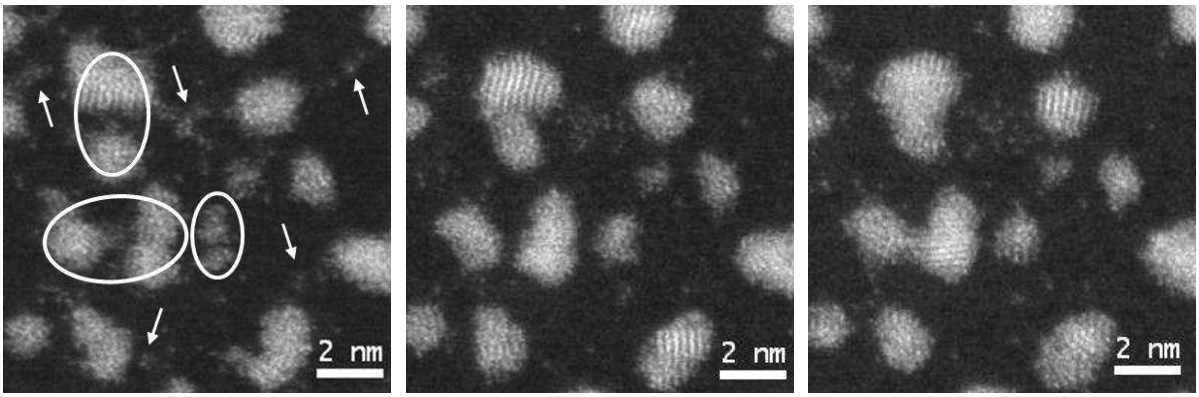

(a) 1st scan, $t' = 0$ (b) 2nd scan, $t' = 30$ s (c) 3td scan, $t' = 60$ s

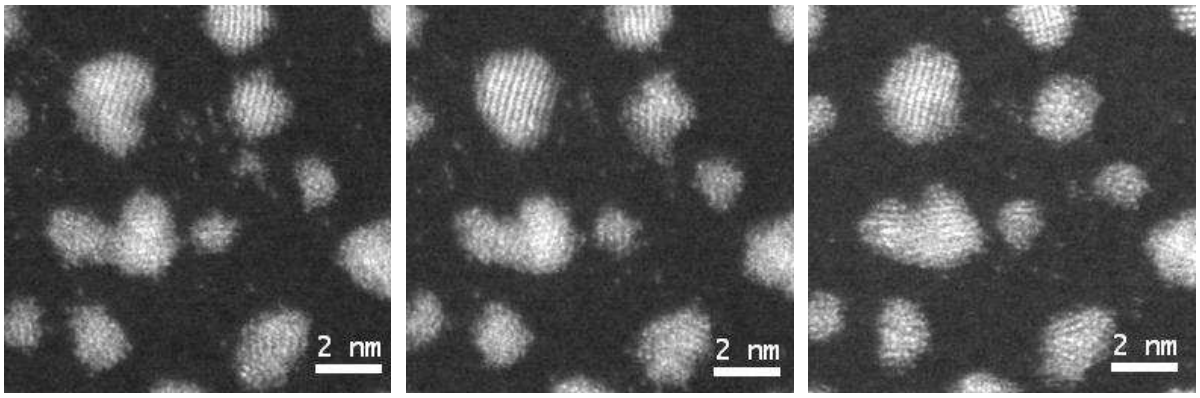

(d) 4th scan, $t' = 120$ s (e) 5th scan, $t' = 150$ s (f) 10th scan, $t' = 300$ s

Figure 3.11.: Magnified 200kV HAADF-STEM images of a part of the time serie recorded from the same region on the sample during continuous electron beam illumination. The sequence of images starts with (a) the 1st scan taken at $t' = 0$ and ended with (f) the 10th scan recorded at $t' = 300$ s. Encircled regions point out mobile NPs, which coalesce by SR, and arrows indicate very small Pt species, like atoms, Pt dimers, trimers, etc. lying on the a-C substrate between the Pt NPs.

the early-growth stage (transition between nucleation and coarsening process) is not completely finished just after deposition. It also demonstrates, that the high density and the small size of Pt NPs favors Smoluchowski coarsening, as previously mentioned in the in-situ TEM experiments. HAADF-STEM images in Fig. 3.11(a-f) allow also a clear identification of different stages of a SR process (see Fig. 3.1(a)), starting with two separated mobile NPs (Fig. 3.11(a)), which meet together and a neck is formed at the contact region (Fig. 3.11(b)); the neck grows and results in an elongated particle (Fig. 3.11(c-d)), which finally relaxes towards the equilibrium shape (Fig. 3.11(e-f)).

The effect of the illumination with the incident electron beam in (HR)STEM can be clearly evidenced by examination of the low magnification HAADF-STEM image in Fig. 3.12, where different contrasts of Pt species located in areas inside and outside the dashed squares can be observed. In the area within the dashed squares, which were used to record time series of (HR)STEM images, Pt NPs have higher contrast as

compared with NPs located outside. The low contrast outside the dashed squares can be attributed to the large number of Pt atoms, dimers, trimers, etc. located between the Pt NPs on the substrate, as shown previously in Fig. 3.11(a). This contrast difference evidences that after HRSTEM image acquisitions, very small Pt species disappear in favour of larger Pt NP, which grow. This is further demonstrated by the larger average NP size found within the dashed squares of $\bar{r}(t' = 5 \text{ min}) = 0.88$ nm as compared with $\bar{r}(t' = 0 \text{ min}) = 0.68$ nm value calculated for the outside region.

Moreover, under illumination at low magnification and short acquisition time in (HR)STEM mode such as the acquisition condition of the HAADF image in Fig. 3.12 (pixel size of 0.1 nm, pixel time of 1 µs and beam current of 47 pA), the HAADF contrast did not change significantly as opposed to that of HRSTEM images recorded at higher magnification (5-10 times higher), where a single cross scan already induces an atomic scale reorganization of the material. This indicates that the electron dose significantly affects NP coarsening and will be considered more precisely in the next section.

The observation of small Pt species was not possible using HRTEM images (Fig. 3.2) and only the qualitative analysis of HAADF-STEM images highlight it. However, the use of substrates with a thickness ≤ 5 nm allows the observation of single Pt, Mo or Co atoms ([Allo 12])[Gamm 12]).

Finally, we note that the contamination in the STEM mode is usually more pronounced than in the HRTEM mode, due to the higher beam current density in STEM (see next section). To prevent contamination, there are two common possibilities: plasma cleaning the sample or backing in vacuum. Both solutions are not suitable for our experimental requirements, as they could affect the NP-size distribution. Degassing the sample in vacuum (1 mTorr) during one day prior to experiment, results in a reduced but still present contamination.

3.3.4.3. Electron total dose and dose rate

To analyze the difference between the effects of the irradiation with an electron beam on the Pt-NP coarsening in HRTEM and HRSTEM mode, it is necessary to determine the electron dose rate (or current density) and the total electron dose in both modes. Firstly, we emphasize that the acceleration voltage was 200 kV in HRTEM and HRSTEM mode. The electron dose rate d_{rate} is defined as the incident beam current I_{beam} divided by the illuminated area S_{illum}. Its usual unit is the ampere per square centimeter ($\text{A} \cdot \text{cm}^{-2}$). In the literature, the total electron dose is the electron dose rate multiplied by the illumination time t_{illum} and is expressed in electrons per square nanometer ($\text{electrons} \cdot \text{nm}^{-2}$).

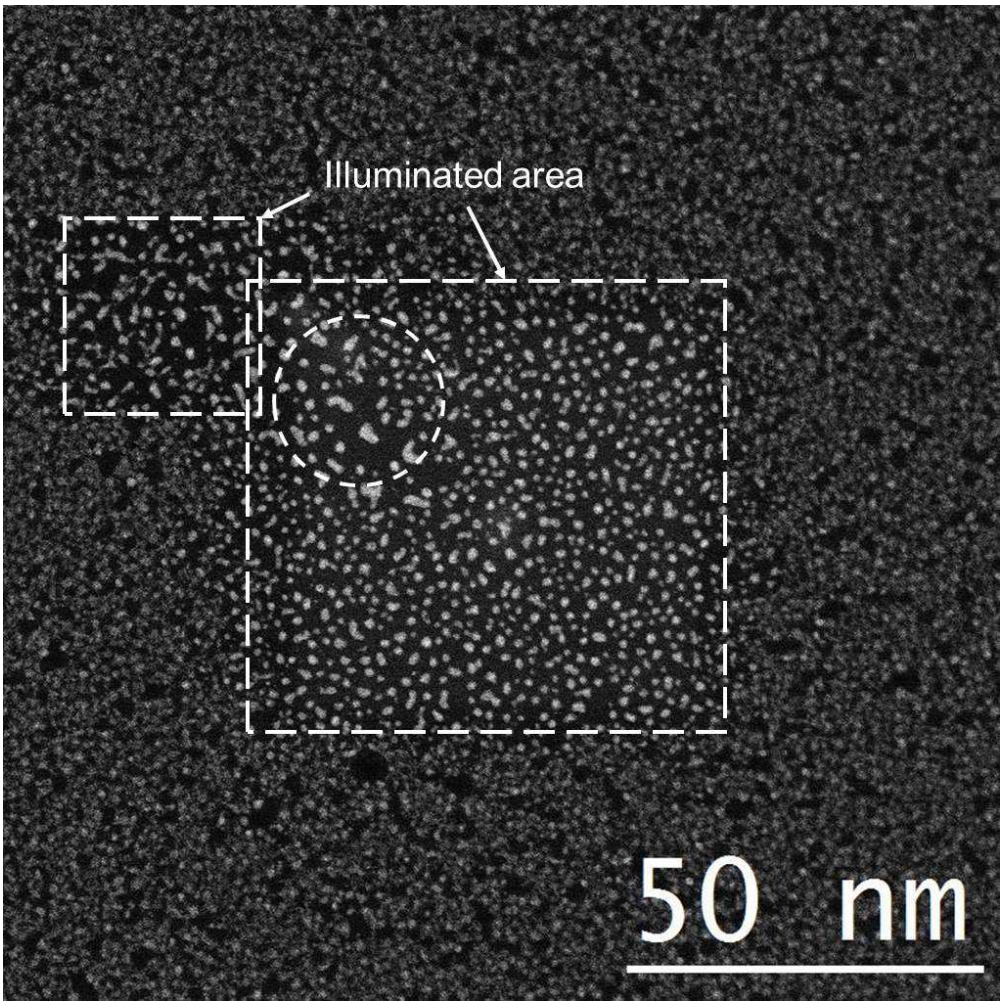

Figure 3.12.: Low-magnification 200kV HAADF-STEM images showing the difference between area illuminated in HRSTEM mode at high magnification and non-illuminated area. The dashed squares and circles indicate area which were used for imaging and for alignment, respectively.

The electron dose rate and the electron dose are related by:

$$d_{\text{total}} = d_{\text{rate}} \cdot t_{\text{illum}} = \frac{I_{\text{beam}}}{S_{\text{illum}} \cdot e} \cdot t_{\text{illum}} \tag{3.3}$$

where e is the charge of electrons. In HRTEM mode, the electron beam is broad and the whole area is illuminated during the acquisition, so that t_{illum} is the total acquisition time. In HRSTEM mode, the probe scans the specimen, so that each area of the specimen undergoes the electron beam irradiation only during a interval time t_{illum}, which is related to the pixel acquisition time t_{pixel}, the pixel area A_{pixel} and the probe area A_{probe} by $t_{\text{illum}} = t_{\text{pixel}} \cdot A_{\text{probe}}/A_{\text{pixel}}$. This definition of t_{illum} is valid for $A_{\text{pixel}} \leq A_{\text{probe}}$, *i.e.* above a certain magnification.

For the CM200 microscope, the beam current was estimated using the calibration formula given by the manufacturer $I_{\text{beam}} = 4.875 \cdot 10^{-9}/t_{\text{exp}}$, where t_{exp} is the exposure

time indicated by the microscope, and obtained by measuring the electrons hitting the big fluorescence screen. The calibration formula was checked by measuring the beam current using a Faraday cup mounted on a Gatan specimen holder. A difference of 1 nA was found between the calculated value and the measured one, which demonstrates that the calculated value is enough accurate to be used to determine the beam current.

With typical experimental conditions for measuring of the NP-size distribution in HRTEM mode, the indicated exposure time was $t_{\text{exp}} = 0.20$ s, which corresponds to an estimated beam current of $I_{\text{beam}} = 24.3$ nA, and the illuminated area was measured to be $S_{\text{illum}} = 1.83 \cdot 10^{-13}$ m^2 $= 0.183$ µm^2. This experimental condition corresponds then to a dose rate of $d_{\text{rate}} = 13.1$ A·cm^{-2} and a total dose of $d_{\text{total}} = 4.11 \cdot 10^5$ electrons·nm^{-2} for acquisition time of $t_{\text{illum}} = 0.5$ s.

In the HRSTEM, a incident beam current of $I_{\text{beam}} \sim 47$ pA was measured with the fluorescent screen. A dose rate of $d_{\text{rate}} = 5.98 \cdot 10^5$ A $\cdot$ cm^{-2} is calculated for a probe size diameter of 1 Å. The HAADF images were recorded with a pixel acquisition time of $t_{\text{pixel}} = 1.6$ µs and a pixel size of 12 pm ($A_{\text{pixel}} = 1.44 \cdot 10^{-22}$ m^2), leading to a value of $t_{\text{illum}} = 87.3$ µs. It follows a electron total dose of $d_{\text{total}} = 3.26 \cdot 10^7$ electrons $\cdot$ nm^{-2} for the STEM mode. We note that the pixel acquisition time of $t_{\text{pixel}} = 1.6$ µs are short in comparison to the standard $t_{\text{pixel}} = 20$ µs used in HRSTEM, since we choose to shorten the pixel acquisition time during the experiment in order to reduce the total electron dose.

The values of dose rate d_{rate} and total dose d_{total} calculated in both modes are in the same range with values reported in the literature [Buba 10, Jian 12, Eger 13]. Based on these calculations, one can conclude that the dose rate and the total dose are 10^4 and 10^2 times higher in HRSTEM than in HRTEM, respectively. The difference of electron dose rate and total dose between the both modes can be explained by the following consideration: as the HAADF signal is significantly lower than the bright field signal used in HRTEM, the total electron dose has to be higher to acquire an HAADF image with a signal-over-noise ratio high enough.

However, the factor of $\sim 10^2$ between the total dose of both modes is not so large as the factor of 10^4 for the dose rate between both mode. This is mainly due to the factor of $\sim 10^3$ in the illumination time between both mode that is much larger in HRTEM ($t_{\text{illum}} = 0.5$ s) than in HRSTEM ($t_{\text{illum}} = 87.3$ µs). Moreover, as mentioned in the preceding section (sec. 3.3.4.2), decreasing the magnification in STEM mode (*i.e.* larger pixel size) reduces significantly the effect of electron beam irradiation. Indeed, for the same probe size A_{probe} an increase of the pixel size A_{pixel} from 0.01 nm to 0.1 nm leads to a decrease of t_{illum} with a factor of 100. Then, the total electron dose in HRSTEM mode can approach that in HRTEM mode.

From these calculations, one can not conclude if the relevant parameter for the observation of NP distribution is the electron dose rate d_{rate} or the total electron dose d_{total}, as both are higher in HRSTEM. Nevertheless they are of interest for understanding the cause of the strong effect on the NPs distribution.

Egerton recently reported calculations of the beam-induced motion of the adatom in TEM [Eger 13], where the lateral displacement rate of adatoms is directly proportional to the current density, *i.e.* dose rate. This explains the large effect of the electron beam illumination observed in HRSTEM, as the dose rate is high ($d_{\mathrm{rate}} = 5.98 \cdot 10^5$ A$\cdot$cm^{-2}). For an activation energy for surface diffusion of an adatom of 0.8 eV, Egerton calculates a displacement rate of adatom of $\sim 10^4$ s^{-1} in HRSTEM conditions ($d_{\mathrm{rate}} = 10^5$ A $\cdot$ cm^{-2}) at 200 kV. Thus, an electron beam-induced motion of adatom occurs in less than 0.1 ms. As the calculated illumination time in HRSTEM is of $t_{\mathrm{illum}} = 87.3$ µs, the electron-beam induced motion of adatoms is not negligible. It follows, that preventing the effect of the electron beam in the HRSTEM mode requires the reduction of either the illumination time t_{illum} or the dose rate d_{rate}. Further experiments at fixed total dose and different dose rate could give more precise insights in the effect of electron-beam irradiation on small Pt NPs in HRSTEM, thus possibly determining optimal experimental conditions without disturbing the observed specimen.

3.4. Discussion

The experimental results of our study show that two stages can be distinguished during the coarsening of small Pt NPs at temperatures between 200 °C and 300 °C. Fast coarsening of NPs occurs by SR taking place besides the surface OR during the first stage for $t < 2$ h (see Fig. 3.4(b)), which could be directly observed by in-situ annealing in a transmission electron microscope (Fig. 3.5). In the second stage for $t \geq 2$ h, surface OR with a diffusion-limited kinetics becomes the dominant coarsening mechanism. This is concluded from the time dependence of the increase of the average NP radius, which can be best described by an exponent $n = 4$ in Eq. 3.1.

The experimental observation of dominant SR during the first 2 hours is consistent with theoretical considerations. The effect of SR can be estimated by calculating the ratio $\tau_{\mathrm{OR}}/\tau_{\mathrm{SR}}$, where τ_{OR} and τ_{OR} are the times necessary to double the average NP size by surface OR and SR, respectively [Imre 99, Imre 00]. If $\tau_{\mathrm{OR}}/\tau_{\mathrm{SR}}$ is much smaller than unity, SR can be neglected. As shown in Refs. [Imre 99, Imre 00] this condition is equivalent to

$$\frac{\tau_{\mathrm{OR}}}{\tau_{\mathrm{SR}}} = 1350 \frac{\ln(l_{\mathrm{sc}})\alpha(\theta)k_\beta T\zeta}{\bar{r}^2(t)\sigma} \tag{3.4}$$

where $\zeta = \pi \bar{r^2} n$ is the normalized surface coverage of the a-C film with NPs. l_{sc} is the screening distance (expressed in units of r) and represents the distance from a NP with radius r at which the Pt-adatom population on the substrate recovers its equilibrium value. It is assumed to be a constant given by $l_{sc} = 2.5$ according to Ref. [Chak 67]. k_B is the Boltzmann constant, T is the absolute annealing temperature in K and $\sigma = 3.0\ \mathrm{J{\cdot}m^{-2}}$ is the Pt surface energy [McLe 66]. The parameter $\alpha(\theta) = (2 - 3\cos\theta + cos^3\theta)/4$ depends on the contact angle θ between NP and substrate [Chak 67, Wynb 75], which cannot be deduced from TEM images. However $\alpha(\theta)$ is used to express the NP volume, which is given by $V = \frac{4\pi}{3} r^3 \alpha(\theta)$ according to Refs. [Chak 67, Wynb 75]. The volume V and the circumscribed radius r of Pt NPs with TO shape, which are relevant in our case, can be geometrically calculated and results in a corresponding value of $\alpha(\theta) = 0.683$. A ratio value of $\tau_{OR}/\tau_{SR} < 0.413$ can be calculated from Eq. 3.4 for Pt NPs characterized by $n(0) = 6.4 \cdot 10^{16}\ \mathrm{m^{-2}}$ and $\bar{r}(0) = 0.72$ nm at 300 °C. The ratio decreases to $\tau_{OR}/\tau_{SR} < 0.056$ after annealing the sample for $t = 2$ h at 300 °C, because of a reduction of the NP density to $n(t = 2\ \mathrm{h}) = 8.6 \cdot 10^{15}\ \mathrm{m^{-2}}$ and an increase of the radius $\bar{r}(t = 2\ \mathrm{h}) = 1.08$ nm . These theoretical calculations support the observed SR at the start of the coarsening process ($t < 2$ h). The reduction of τ_{OR}/τ_{SR} by one order of magnitude after 2 h of annealing at 300 °C indicates that coarsening via surface OR is more relevant for $t \geq 2$ h.

More detailed information about the rate of OR at different temperatures can be obtained by comparing their surface mass-transport diffusion coefficients D'_s. The D'_s values can be calculated as a function of temperature from the corresponding C_d values derived from the fit curves in Fig. 3.4 on the basis of the Eq. 3.1 [Imre 99, Imre 00]

$$D'_s = \frac{45 \ln(l_{sc}) \alpha(\theta) k_\beta T}{4 \nu_{Pt}^2 \sigma n_0} \cdot C_d \tag{3.5}$$

where $\nu_{Pt} = a_{Pt}^3/4 = 1.5117 \cdot 10^{-29}\ \mathrm{m^3}$ is the atomic volume of Pt atoms calculated for fcc bulk Pt with a lattice parameter of $a_{Pt} = 0.3925$ nm. The density of surface sites n_0 for Pt NPs with fcc structure is given by $n_0 = 2/a_{Pt}^2 = 1.298 \cdot 10^{19}\ \mathrm{m^{-2}}$. Inserting these values in Eq. 3.5, surface mass-transport diffusion coefficients with values between $(1.26 \pm 0.03) \cdot 10^{-23}$ and $(48.4 \pm 0.86) \cdot 10^{-23}\ \mathrm{m \cdot s^{-2}}$ are determined for annealing temperatures between 200 °C and 300 °C (see Tab. 3.1).The activation energy E_d for surface diffusion of Pt adatoms on an a-C substrate can be derived by assuming an Arrhenius-type dependence of D'_s according to Eq. 3.6. The linear fit of $\ln(D'_s)$ as a function of $1/T$ shown in Fig. 7 yields D'_0 from the intercept of the fit curve with the D'_s axis and E_d from the slope of the fit curve.

Temperature T (°C)	$C_\mathrm{d} \cdot 10^{-42}$ ($\mathrm{m}^4 \cdot \mathrm{s}^{-1}$)	$D'_\mathrm{s} \cdot 10^{-23}$ ($\mathrm{m}^2 \cdot \mathrm{s}^{-1}$)
200	2.44 ± 0.06	1.26 ± 0.03
225	5.55 ± 0.17	3.02 ± 0.09
240	15.35 ± 0.51	8.60 ± 0.28
275	30.21 ± 0.63	18.09 ± 0.37
300	77.31 ± 1.37	48.40 ± 0.86

Table 3.1.: Values of the fit parameter C_d and corresponding surface mass-transport coefficient D'_s calculated for surface OR of Pt NPs with a diffusion-limited kinetics.

The dependence of D'_s on the absolute temperature (Fig. 3.13) is then given by

$$D'_\mathrm{s} = 1.12 \cdot 10^{-14} \exp\left(-\frac{(0.84 \pm 0.08)\mathrm{eV}}{k_\mathrm{B} T}\right) \mathrm{m}^2 \cdot \mathrm{s}^{-1} \tag{3.6}$$

Values for surface diffusion of Pt atoms on graphene were calculated to be as small as $0.14 - 0.19$ eV·atom^{-1} [Tang 11, Kong 06] in contrast to experimental values of $2.2 - 2.5$ eV·atom^{-1} [Gan 08]. Such high activation energies were explained by the strong covalent bonding between metal and carbon atoms with calculated site-dependent bonding energies between 1.4 and 8 eV [Okaz 10, Tang 11]. Assuming defect sites in graphene to be a reasonable model for a-C, the activation energy of 0.84 eV for Pt-surface diffusion on a-C is plausible. Published E_d values for Pt diffusion on Pt surfaces are also high between 0.53 and 0.84 eV·atom^{-1} depending on the surface direction [Bass 78]. In the case of a W substrate, $E_\mathrm{d} = 0.7$ eV·atom^{-1} was reported in Ref. [Kell 90]. We also note that the coarsening behavior of Pt- and Au-NP ensembles on a-C is similar. This can be inferred from $E_\mathrm{d} = 0.84 \pm 0.08$ eV·atom^{-1} for Pt on a-C, which agrees within the error limits with $E_\mathrm{d} = 0.88$ eV·atom^{-1} for Au atoms on a-C [Utla 80].

The limitation of the OR process by surface diffusion as opposed to reaction limitation is rationalized in the following way. Surface diffusion is expected to dominate, if the activation energy for the detachment of a Pt atom E_det from a supported Pt NP is lower than the activation energy for surface diffusion E_d. The detachment activation energy is approximately given by $E_\mathrm{det} \approx E_\mathrm{Pt\text{-}Pt} - E_\mathrm{Pt\text{-}C}$ with the cohesive energy per Pt atom from a Pt NP $E_\mathrm{Pt\text{-}Pt}$ and the bonding energy between carbon support and a Pt atom $E_\mathrm{Pt\text{-}C}$ [Loof 93]. The cohesive energy $E_\mathrm{Pt\text{-}Pt} = 5.6$ eV·atom^{-1} for bulk Pt [Kuma 08] decreases for small NPs according to the Gibbs Thomson effect to values of 3.7 eV·atom^{-1} and below for Pt NPs with radii ≤ 0.5 nm [Kuma 08, Nie 07]. E_det is further reduced by the large bonding energies between Pt atoms and carbon support which makes reduction of E_det below $E_\mathrm{d} = 0.84$ eV·atom^{-1} plausible.

Finally, we point out that numerous studies, e.g., [Loof 93, Lars 12] were performed on the coarsening of Pt NPs on SiO_2 or Al_2O_3 which are common supports in catalysis.

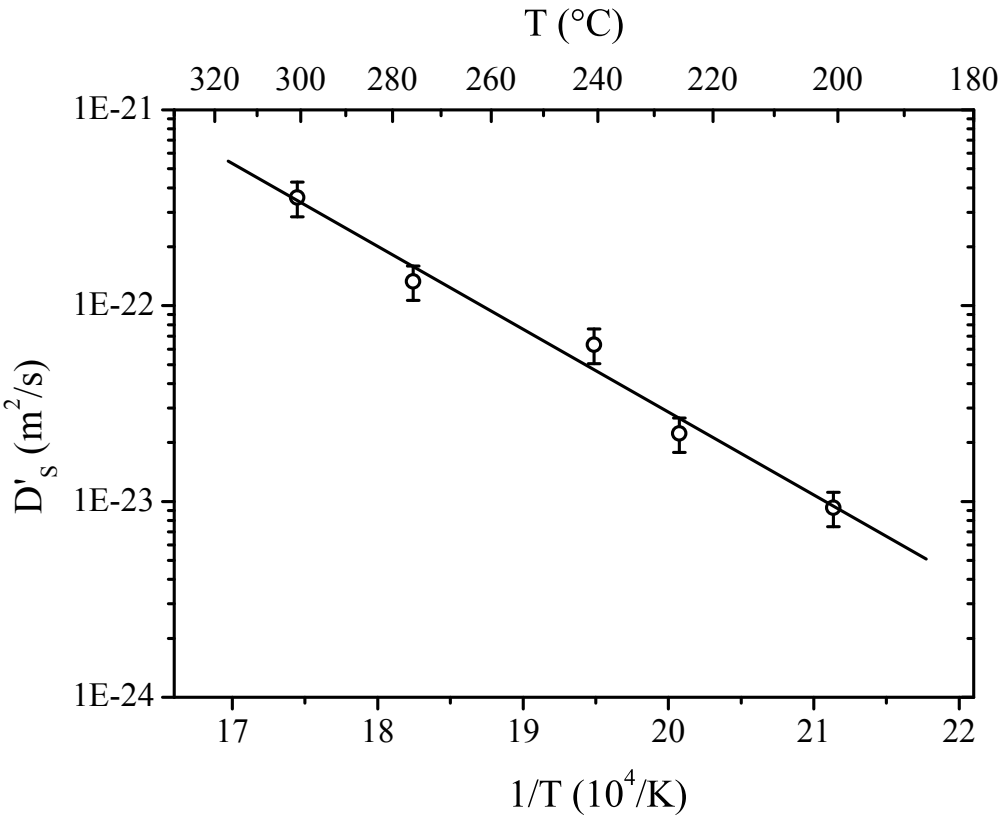

Figure 3.13.: Arrhenius plot of the surface mass-transport coefficients D'_s as a function of the reciprocal temperature.

In these studies, a strong influence of the gas environment on Pt-NP coarsening was observed. Negligible coarsening was found for Pt NPs in a pure Ar atmosphere after annealing at 700 °C for 60 min while significant coarsening takes place in oxygen-containing atmospheres [Loof 93]. The striking stability of Pt NPs in Ar is explained by the high Pt-cluster stability and weak Pt-substrate interaction on oxidic supports. Coarsening in oxygen-containing atmospheres is attributed to the oxidation of Pt NPs at temperatures above 500 °C which lowers the cohesive NP energy. Moreover, an increase the bonding energies between the oxidic support and PtO_x species is invoked. Since oxidation of Pt NPs at temperatures $\leq$ 300 °C can be excluded in our study (see Ref. [Loof 93]), the coarsening is clearly associated with the comparatively high bonding energies of Pt atoms on the carbon support.

3.5. Conclusion

Pt NPs with a narrow size distribution were deposited on a-C substrates by electron-beam evaporation. The coarsening of the NP ensemble was studied by TEM after annealing at temperatures between 200 °C and 300 °C for up to 160 h. The possible influence of 200 keV electrons on the coarsening was systematically studied by illuminating the same sample region for 20 min in HRTEM with a dose rate of $d_{\mathrm{rate}} = 13.1\ \mathrm{A \cdot cm^{-2}}$. Neither enhanced SR nor a significant change of the NP sizes was observed under the chosen illumination conditions. However, HRSTEM imaging can change significantly the smallest NPs since a single cross scan can already induce an atomic-scale reorganization of the material.

High-resolution TEM was applied to analyze the NP shape. Experimental and simulated images along the [100]- and [110]-zone axes were compared to distinguish between cuboctahedral and truncated octahedral fcc NP structures. [100]-zone axis HRTEM images are suitable to discriminate between these two NP types which yield a truncated octahedral shape as being relevant in our study. Measured NP-size distributions yield average radii which increase with annealing time and temperature. Coarsening proceeds fast during the first 2 hours of annealing and slows down for longer annealing times. An in-situ TEM annealing experiment demonstrates that coarsening is dominated by a very active coalescence of small mobile NPs via SR during the first coarsening stage ($t < 2$ h). SR can be neglected during the second ripening stage for annealing times of more than 2 h. The coarsening kinetics during the second stage is best described by surface OR with a diffusion-limited kinetics. A quantitative description of the surface OR process is performed by evaluating surface mass-transport diffusion coefficients, which range between $(1.25 \pm 0.03) \cdot 10^{-23}\ \mathrm{m \cdot s^{-2}}$ and $(48.40 \pm 0.86) \cdot 10^{-23}\ \mathrm{m \cdot s^{-2}}$ for the investigated temperature interval between 200 °C and 300 °C. The Arrhenius-type dependence of the surface mass transport diffusion coefficient is exploited to derive the activation energy for surface diffusion of Pt atoms on an amorphous carbon substrate. The limitation of the OR process by surface diffusion as opposed to reaction limitation can be understood by the reduction of the detachment activation energy of Pt atoms in small NPs and the high bonding energies between Pt atoms and the carbon support.

4. Ge and Ge(Mn) quantum dots

Contents

4.1. Introduction

Mn doped Ge quantum dots (QDs) are particularly interesting since their small size and the quantum confinement effects affect the electronic structure and the spin interaction and thus ferromagnetic properties [Knob 00]. For example, room-temperature

ferromagnetism and electric-field-controlled ferromagnetism was demonstrated in self-assembled $Mn_{0.05}Ge_{0.95}$ QD [Xiu 10]. The electric-field manipulation of ferromagnetism is of great interest for the development of new device concept with reduced power consumption [Niko 08]. Since the formation of GeMn nanostructures is not well understood, the problematic of this chapter aims to understand and to control the fabrication of ferromagnetic semiconductors by incorporating Mn in Ge quantum dots (QDs).

To that extend, we focus first on the measurement of the Ge content in the wetting layer (WL) since the control of the growth of Ge islands and QDs layers required a detailed knowledge of the formation of the WL. To that extend, a precise and accurate quantification of the inter-diffusion or surface segregation process during the growth is necessary. Then incorporation of Mn by co-deposition with Ge during molecular beam epitaxy (MBE) growth is studied. Growth parameter, such as Mn concentration, growth temperature and thickness are explored.

This chapter is organized as follows: it begins with a short review of the principle of Stranski-Krastanov (SK) growth of Ge on Si(001), necessary to the understanding of the results presented here. Then a methodological development for the quantification of HAADF contrast in STEM mode is presented. This quantification method allows us to precisely measure the Ge content at the atomic scale. This method is applied to measure the Ge surface segregation in the case of Ge WLs in Si grown by MBE. Finally, the incorporation of Mn in Ge quantum dots structures is presented and discussed with respect to recent work reported.

4.2. Fundamentals of the growth of Ge quantum dots

Hetero-epitaxial growth of Ge on Si(001) has been studied, since it has great application in electronic and optoelectronic and it is a prototypical system for studying growth mode from a fundamental point of view. The MBE growth of hetero-structures is inherently a non-equilibrium process, the formation of self-assembled nanostructures is both complex and sensitive to growth and overgrowth conditions. The formation of Ge islands is a spontaneous process that occurs after the Ge deposition that exceeds a critical thickness of Ge. It follows one of the three primary modes by which thin films grow epitaxially, the so-called Stranski-Krastanov (SK) growth mode or “layer-plus-island growth”. The principle of the SK growth mode is schematically illustrated in Fig. 4.1. Generally, the driving force of the spontaneous formation of island is the relief of the elastic strain accumulated in the epitaxial film due to the lattice-mismatch of a few percent. The layer growth starts in a 2D fashion (Fig. 4.1(a)) and undergoes a transition towards 3D growth, as the accumulation of elastic strain in the epitaxial layer changes the balance between the surface energy and the elastic strain energy

(Fig. 4.1(b)). Si can be further epitaxially grown on top the Ge islands layer and (d) others layers can be grown, as shown by Fig. 4.1(c-d).

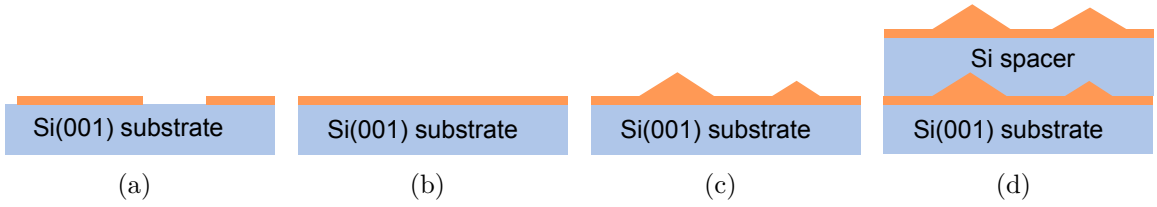

Figure 4.1.: Schematic illustration of the Stranski-Krastanov growth mode: (a-b) a wetting layer of Ge is deposited on the Si substrate; (c) beyond a critical thickness, the strain in the WL is too high and three-dimensional island are formed. (d) Si can be further epitaxially grown on top the Ge island layer to convert the island into SiGe QDs and the growth can continue with others SiGe QDs.

In the following we will focused on the two regimes of the growth of Ge on Si [Mull 96]:

1. Ge WL embedded in Si: Ge growth is stopped before the formation of QD *i.e.* thickness < 4 monolayers (MLs)
2. Ge QDs embedded in Si: thickness > 4 MLs and formation of Ge QD

4.2.1. Formation of the Ge wetting layer

In order to reduce the number of dangling bonds of the Si atoms lying on the initial surface of the Si substrate, a surface reconstruction takes place. The Si(001) surface exhibit a (2×1) reconstruction, consisting of dimers arranged in rows. Fig. 4.2 shows that in case of the unreconstructed surface, each Si surface atom has two dangling bonds, whereas in case of the (2×1) reconstructed surface, each Si surface atom has one dangling bond. For a dimer axis oriented along the [110] direction, the dimer row is oriented along the $[\bar{1}10]$ direction, *i.e.* perpendicular to the dimer axis [Voig 01].

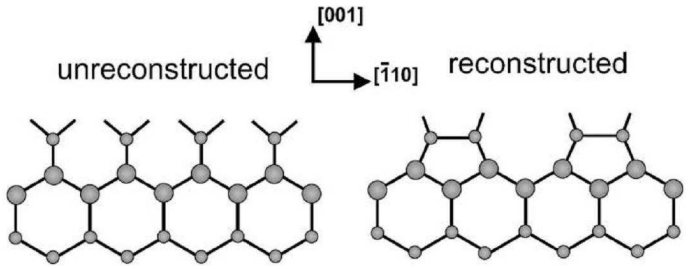

Figure 4.2.: Comparison of unreconstructed and reconstructed surface of Si(001). Taken from [Voig 01].

During the deposition of Ge atoms on the Si(001), the surface rapidly changes to$(2\times N)$ reconstruction, which consists of a periodic array of missing dimers of the (2×1) reconstruction, *i.e.* every N^{th} dimer is missing. The driving force of this transformation is due to the strain energy which increases with increasing coverage. More complicated surface reconstruction, such $(M \times N)$ can occur during the formation of the Ge WL [Miga 04]. The numbers M and N are determined by a balance of the strain energy and the energy necessary to remove a dimer raw. It thus changes as a function of the coverage and the experimental growth conditions. The first regime of the growth of the Ge WL consists in the formation of a 2D pseudomorphically strained layer, *i.e.* the in-plane lattice parameter of the Ge WL is the same as the Si substrate one. The Ge quantity deposited on Si is controlled by Reflection high-energy electron diffraction (RHEED) measurements which can follow the transition from 2D to 3D regime and then allow to stop the deposition when needed.

For heterostructures, Si-Ge intermixing in the Ge WL during Si overgrowth can take place creating a chemically mixed Si-Ge layer. This can be due to the fact that even if the Si-Ge inter-diffusion can be negligible at temperatures lower than 500 °C, dimer raw vacancies can create possible path to Si diffusion from the capping in the Ge WL [Miga 04]. On top of that, surface segregation of Ge in Si have to be considered. It is caused by the lower dangling bond energy, *i.e.* lower surface energy of Ge as compared to Si. The driving force of surface segregation is then the energy difference between the surface (adsorbed) and subsurface (incorporated) states E_{b}. Fig. 4.3 illustrates the principle of surface segregation by the so-called two-state model, the two states considered here being the surface and subsurface state.

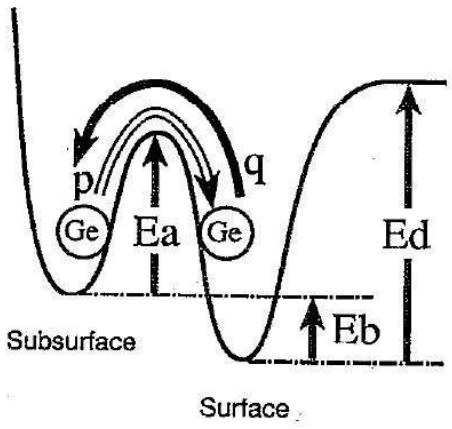

Figure 4.3.: Energy diagram of the two-state model to explain atom exchange process between surface and subsurface states. E_{a} is the kinetic barrier E_{d} is the desorption energy. The segregation energy is defined by $E_{\text{b}} = E_{\text{d}} - E_{\text{a}}$. p and q are the jump rates of the Ge atoms toward the surface and backward. Taken from [Fuka 91].

The surface segregation leads to intermixing and asymmetric concentration in coherently grown SiGe structures and if affects the equilibrium of SiGe structures, since it change the surface energy of the layer [Ters 94]. Our observations detailed in the following confirm this intermixing and quantitative analysis of the chemical profiles will be presented to get better understanding of this segregation effect.

4.2.2. Formation of Ge quantum dots

Due to the large lattice mismatch of 4,2 % between Ge and bulk Si, an elastic strain energy builds up in the Ge WL. The formation of 3D islands provide a way to release this elastic strain energy stored in the Ge WL when the Ge content is too high. The 2D to 3D transition was modeled by Tersoff and LeGoues by the competition of surface energy necessary to form facets E_{surf} and the elastic strain energy $\triangle E_{\text{relax}}$ [Ters 94]. This model is illustrated by plotting the variation of $E_{\text{relax}} \sim x^3$ and $E_{\text{surf}} \sim x^2$ in Fig. 4.4, where x is the island size. The energy difference between the 3D and the 2D morphology is then given by $\triangle E = E_{\text{surf}} - E_{\text{relax}}$. For an island size $x < x_{\text{crit}}$ the 3D morphology is not favorable ($\triangle E > 0$), whereas for an island size $x > x_{\text{crit}}$ the 3D becomes favorable as $\triangle E < 0$. x_{crit} corresponds to the island size x where the gained elastic relaxation energy is equal to the surface energy.

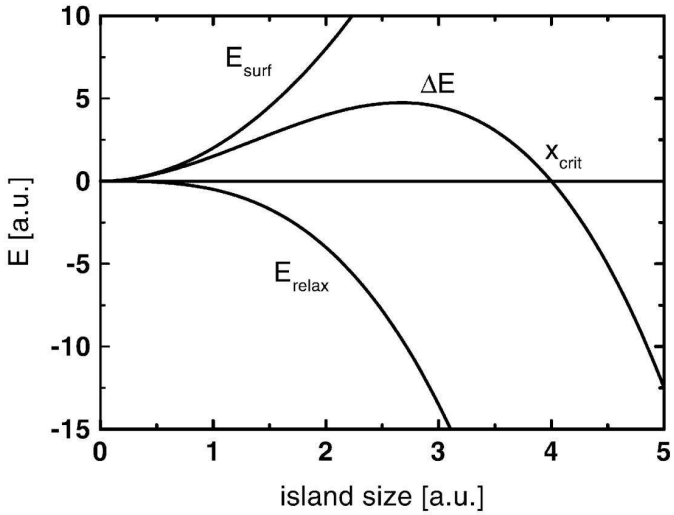

Figure 4.4.: Island total energy *versus* island size, *i.e.* deposited volume. For island size larger than the critical size x_{crit}, the island formation is energetically favorable (3D growth). Taken from [Voig 01].

This simple model gives some insights in the driven force of the 2D to 3D transition in the SK growth mode. Kinetics effects or particular shape of island change significantly the balance between the energy E_{relax} and E_{surf}, and thus the value of x_{crit}. Usually, the Ge WL starts to relax at a coverage of ∼3 ML and Ge island are formed.

The shape of Ge island on Si(001) can be complicated since several different types of 3D QD have been observed. The 3D morphology of the most common Ge island on Si(001) are shown in Fig. 4.5. The shape of the Ge island changes with increasing its size. The smallest ones are {105} faceted huts with rectangular or square base (pyramid). Then larger islands form dome with additional {113} and {102} facets, and base size ranging from 50 to 100 nm. The higher aspect ratio of the dome allows a relaxation by 50 % of the strain, that is significantly larger then the relaxation by 20 % in case of the huts. Finally, plastically deformed super-dome islands can be observed with misfit dislocations at the island-substrate interface.

Another way to reduced the energy associated to the strain in the island is the inter-diffusion between the Ge island and the Si substrate. Independent and accurate determination of both chemical composition and strain is far from trivial in such island, due to the small scale of such nanostructures and its particular geometry.

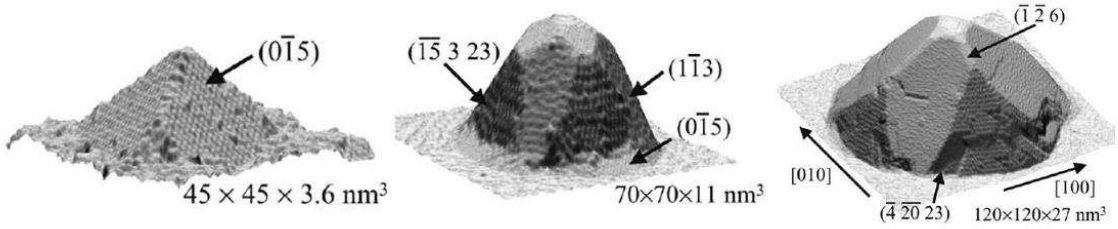

Figure 4.5.: Typical evolution of Ge QDs on Si(001) as observed by scanning tunneling microscopy (STM) topograph of Ge quantum dots on Si(001). The shape of the Ge quantum dots changes with increasing its size. At small size {105} faceted pyramids with square base (a) are formed and with increasing the size additional {113} and {102} facets are created in the dome (b). Plastically deformed super-dome are finally formed with misfit dislocation(c). Note that the figures are stretched along the growth direction to highlight the facets. Taken from [Duja 06].

For the conversion of Ge islands into optical QD, the islands have to be embedded in a semiconducting matrix consisting of a capping of Si, as shown in Fig. 4.1(d). This also offers the possibility to grow heterostructures by repetition of the Si/Ge(QD)/Si period.

For the magnetic measurements on the Ge(Mn) QD using superconducting quantum interference device (SQUID), a minimum volume of magnetic material is required to get a good SNR. The magnetic material in each QD being small in the case of $Ge_{0.94}Mn_{0.06}$ quantum dots studied in this work, heterostructures have been grown to increase the total quantity of magnetically active species.

Note that the capping of Ge islands by Si can significantly change their composition and their shape. The study reported by Rastelli *el al* clearly evidenced the flattening

of the Ge island by capping at temperatures higher than 300 °C [Rast 02]. This shape evolution is characterized by an increase of the base size and a simultaneous height reduction. A similar observation was reported in the case of SiGe islands [Sutt 98]. In both cases, these observations were explained by Si-Ge intermixing caused by the Ge surface segregation during Si capping. Reducing the growth temperature of the Si capping kinetically hinders the Si-Ge intermixing, thus the shape evolution and the Ge content in the QDs [Rast 02].

All these studies from literature show that a good knowledge of the Ge-Si intermixing is important to understand the growth mechanism and also gives a good interpretation of the optical or magnetic properties of such systems.

4.2.3. Ge Surface segregation in Si

Depending on the growth conditions, surface segregation of Ge can take place during the growth of Si capping on SiGe nanostructures, *i.e.* QWs or QDs: some Ge atoms remain at the growth front during the growth process. Consequently, the Ge content in the Si capping or spacer is not zero even if no Ge was deposited at this stage of the growth. This occurs because the surface and bulk sites are energetically different for Ge and Si atoms, as explained in sec. 4.2, *i.e.* the surface energy of Si(001) is reduced when terminated by a Ge adlayer. Nevertheless, the introduction of a third element during the growth can lower the surface energy of both Si and Ge [Cope 89]. Such a element (for example As of Sb) acts as a surfactant and can drastically change the growth process by controlling surface segregation [Hoeg 94, Cope 89]. It can also be suppressed by hydrogen surface passivation [Grut 93]. Hydrogen is believed to change the surface energy by terminating the surface dangling bonds as well as the rate of the Si-Ge atoms exchange. This is illustrated by the SiGe QWs we have used for the calibration of the EELS $k_{\mathrm{GeL}_{2,3}}$ factor, as shown in Fig. 4.13. No surface segregation was observed by EELS measurement and HAADF imaging. This can be explained by a modification of the Si–Ge exchange probability during the growth, which depends on the Si precursor and its associated H surface coverage during the reduced pressure-chemical vapor deposition (RP-CVD) growth [Kim 97, Vinc 09]. This observation already indicates that the surface segregation is drastically affected by the growth conditions.

The growth mechanisms of SiGe nanostructures has been extensively studied in the last decades [Zalm 89, Fuka 91, Godb 92]. Many techniques have been used to investigate the composition of SiGe nanostructures in order to determine the chemical distribution. This surface segregation of Ge in Si is usually studied by surface-sensitive in-situ techniques such as Auger electron spectroscopy (AES)[Butz 92, Li 95] or X-ray

photo-electron spectroscopy (XPS) [Fuji 91]. These techniques are sensitive to the surface and probe the top few monolayers. Ge concentration profiles were also measured on photo-luminescence technique [Breh 08]. The quantification of the Ge concentration were obtained by the analysis of the peak positions photo-luminescence spectra combined with band structure calculations. Ex-situ techniques such as medium-energy ion scattering (MEIS) [Cope 89] and SIMS [Zalm 89, Fuka 91] were also used. TEM techniques in cross-section were also employed to study the surface segregation of Ge atoms, but no quantitative analysis of the segregation profile was reported [Walt 99, Bene 03, Bari 06].

4.3. Experimental methods

All the samples studied in this work were grown using a Riber MBE 32 chamber with a base pressure of a few 10^{-11} Torr. Standard Knudsen cells were used for Ge and Mn evaporation. Prior to the growth of Ge layers, a 40 nm thick Si buffer layer was systematically grown on Si(001) and annealed at 800 °C during 15 minutes (). The growth rate of Ge layers was 6 ML $\cdot$ min^{-1} = 1.8 nm $\cdot$ min^{-1}. Lattice relaxation was permanently controlled by RHEED observations. For Ge wetting layers growth on Si, Ge deposition has to be stopped before the thickness of Ge layer the exceeds critical thickness of elastic relaxation. The growth rate of Ge and GeMn layers was 1.3 nm $\cdot$ min^{-1}.

Almost all the TEM experiments shown in this chapter have been performed using the HRSTEM-HAADF imaging and HRSTEM-EELS spectroscopic modes at 200 kV. Experiments were carried out on:

- a double-corrected FEI Titan^3 Ultimate operating at 200 kV. Electron Energy Loss Spectroscopy (EELS) was performed in HRSTEM mode using the probe-corrected mode (DCOR corrector from CEOS) and a Gatan Image Filter (GIF) Quantum ER equipped with Ultra fast acquisition, dual EELS acquisition and 2 kV drift tube. EELS acquisition were performed with the convergence angle α = 20 mrad and the collection angle β = 98 mrad. The Digiscan II scanning unit and Digital Micrograph software from Gatan were used to record simultaneously the EELS and HAADF signals. Dark reference of the CCD camera was improved by averaging hundreds of dark reference recorded directly after the EELS acquisition.
- a probe-corrected FEI low-base Titan 80-300 microscope equipped with a GIF Tridiem with an energy dispersion of 1 eV. The FEI scanning unit and TIA software were used to record HAADF and EELS signals. EELS acquisition were performed with the convergence angle α = 18 mrad and the collection angle β = 44 mrad.

On each microscope, the typical probe current was between 60 and 80 pA. Energy dispersion was set so that EELS edges of Mn $L_{2,3}$ at 640 eV, Ge $L_{2,3}$ at 1217 eV and Si K at 1839 eV could be acquired during experiments on the same spectrum or in dual EELS mode in order to perform quantitative treatment of the data afterward. Post-processing denoising of the data set, *i.e.* line scan or spectrum image, was performed using the PCA algorithms implemented in the Hyperspy software. The relevant component was estimated by careful inspection of factors and loadings, as explained in sec. 2.6.2. For the EELS quantification, the integration windows were set to 60 eV.

The plane views and cross-sections of Ge or Ge(Mn) QDs samples were prepared for observations by chemical mechanical wedge polishing in order to get very thin and clean areas.

Magnetic properties at various temperatures were measured using a superconducting quantum interference device (SQUID).

4.4. Methodological development of HAADF quantification

4.4.1. Experimental observations of Ge quantum dots

Fig. 4.6 shows a typical HAADF-HRSTEM image of two layers of Ge embedded in Si. Both layers consist of equivalent 4 MLs content of Ge grown on Si(001) at a temperature of 380°C. The HAADF signal scales as Z^{γ}, where Z is the atomic number and γ ranges from 1,7 to 2, depending on the experimental conditions [Penn 88, Kriv 10]. Since the Ge and the Si atomic number are $Z_{\mathrm{Ge}} = 32$ and $Z_{\mathrm{Si}} = 14$, the atomic columns containing Ge atoms appear brighter than Si pure atomic columns. The layers with high content of Ge are then the two bright layers with a thickness of approximately 1 nm. The high contrast for this system on the HAADF image shows that the interface between the Si substrate and the first Ge rich layer is almost atomically flat, whereas it is not the case for the second interface with the Si spacer which exhibits roughness. This observation shows that we have already overcome the pure WL regime and that the transition toward the 3D growth has take place from 4 MLs of Ge grown on Si. This transition is inherent to the SK growth mode, as explained previously in sec. 4.2, and the small thickness variation could be already seen as small Ge rich QDs.

4.4.1.1. Detection of segregated Ge atoms in Si by HAADF imaging

Above these Ge QDs, in the Si spacer, some atomic columns appear brighter than others. In comparison, the contrast of atomic columns in the Si substrate is very homogeneous and does not exhibit such bright atomic columns. It means that the brighter atomic columns in the Si spacers could be attributed to the presence of Ge atoms since the specimen contains only Si and Ge. Fig. 4.6(b) shows a zoom on the upper layer of the HAADF image to highlight these bright dots. Orange arrows indicate some atomic columns among the myriad of atomic columns, that are brighter than those of the pure Si substrate.

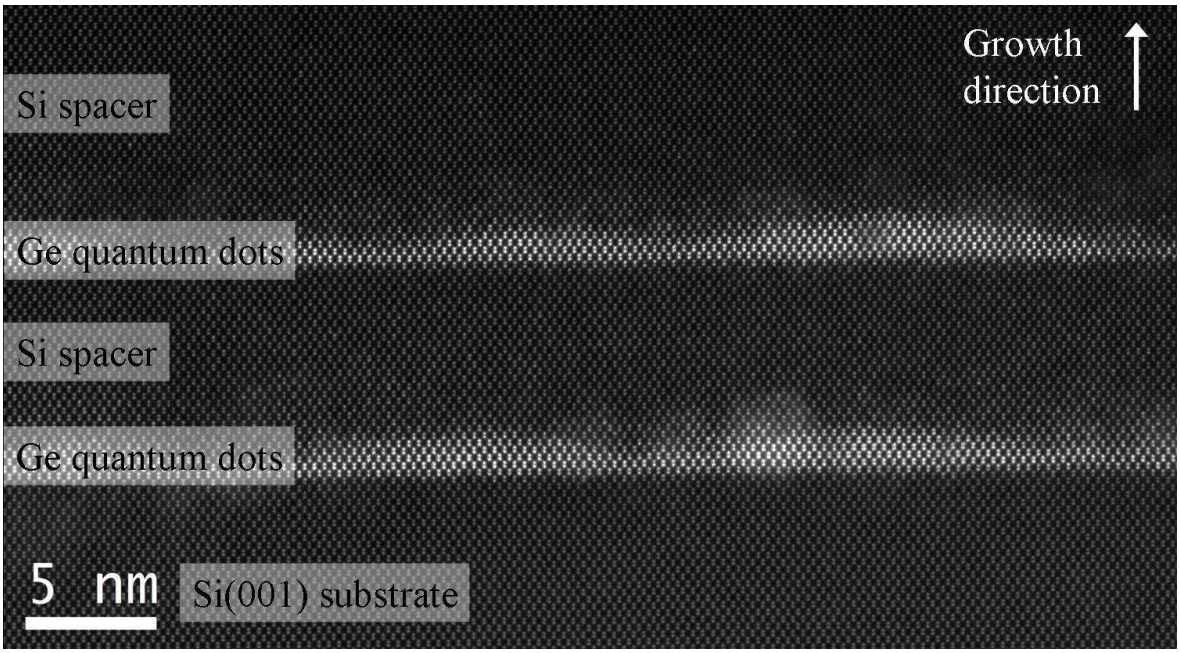

(a)

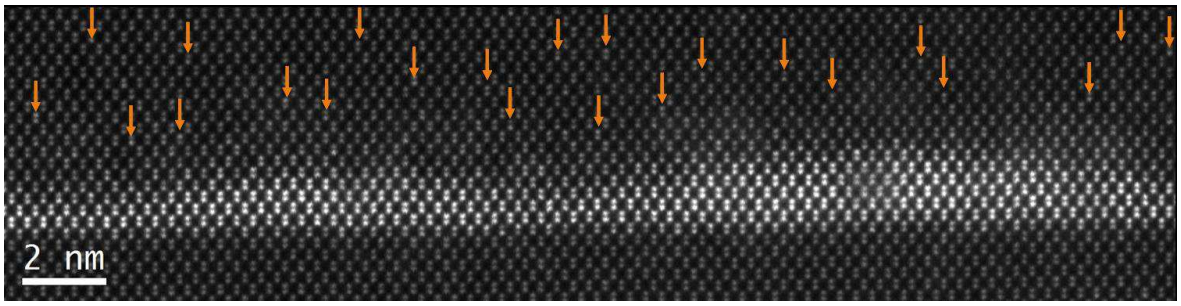

(b)

Figure 4.6.: (a) Typical high resolution HAADF images of two layers of Ge QDs embedded in Si. For these two layers, 4 ML of Ge have grown on Si. (b) Zoom on the upper layer of the HAADF image in (a). The arrows indicate some atomic columns in the Si spacer with brighter intensity than in the Si substrate. The specimen thickness is 13 nm.

The detection of Ge atoms in Si spacer is hard to perform as it is shown on the Fig. 4.7 showing HAADF images of the same Ge QDs acquired for three different specimen thicknesses. Thin areas with thickness of 6 nm, 14 nm and 21 nm are shown in Fig. 4.7(a,b,c) respectively taken on equivalent region of the sample. One can notice that the contrast of the brightest atomic columns with respect to the Si substrate is much higher for the thinner area (6 nm) and strongly reduced for too thick area (21 nm). These observations show clearly that the detection of small amount of Ge in Si implies to work with very thin and clean samples to get a good visibility. For too thick samples visibility is very low: Ge atoms are almost not detected but are nevertheless present in the Si spacer.

In order to investigate in more details the contrast variation between the Si substrate and the Si spacer, HAADF intensity profiles across a Ge QDs layer are plotted in Fig. 4.7(d) for each thicknesses. As the HAADF images have been normalized relative to the incident probe intensity using the detector image procedure (Fig. 2.16(a)), they can be then compared quantitatively. The unit scale of the HAADF signal is thus the fraction of incident beam (f.i.b.). In the HAADF intensity profiles shown in Fig. 2.16(c), two features are remarkable:

- the intensity distribution on the atomic columns;
- value of the background of the HAADF image, *i.e.* the value between the atomic columns.

By examining the background for the three thicknesses plotted here, one can observed that the background value increases with thickness and is higher on the Ge QDs compare to Si. For the two thinner areas (6 and 14 nm) the background value of the Ge QDs is lower than the maximum value of the Si atomic columns, whereas it is the opposite in the case of the 21 nm thick area. These observations indicate that the background variation depends strongly on the sample but also on the quality of the thin lamella.

Colored bands drawn in Fig. 4.7(d) represent the distribution of intensity of the Si atomic columns in the substrate and spacer. The experimental HAADF intensities have a certain distribution due to noise and the intensity distribution in the Si substrate is taken as a reference for our experimental setup. The mean full width of the reference distribution is 0.005 f.i.b. for the thinner area and 0.007 f.i.b. for the thicker area of 21 nm. For the thinner area, the intensity of some atomic columns in the Si spacer are 0.005 f.i.b. higher than the mean atomic column intensity in the Si substrate corresponding to an increase of 25 %. For the thicker area, the maximum intensity in the Si spacer is 0.003 f.i.b. higher than the mean reference distribution value of 0.059 f.i.b. providing an increase of 5 %. These values indicate that the contrast of the brightest atomic columns in the Si spacer reduced drastically with increasing thickness.

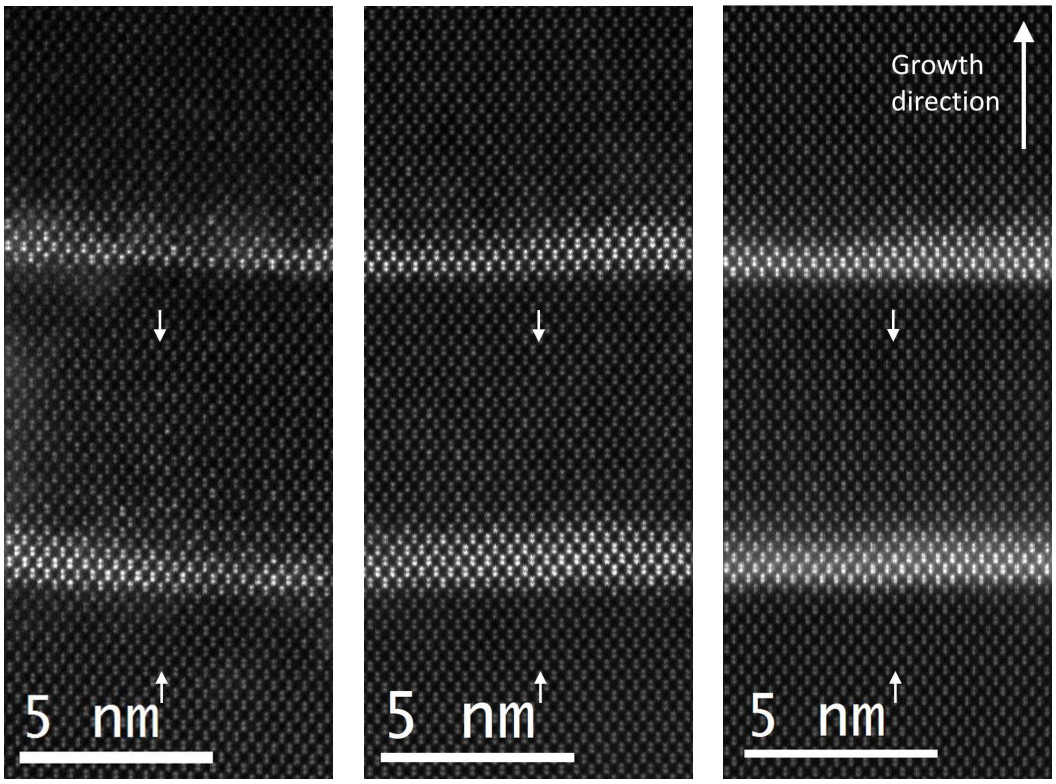

(a) 6 nm (b) 14 nm (c) 21 nm

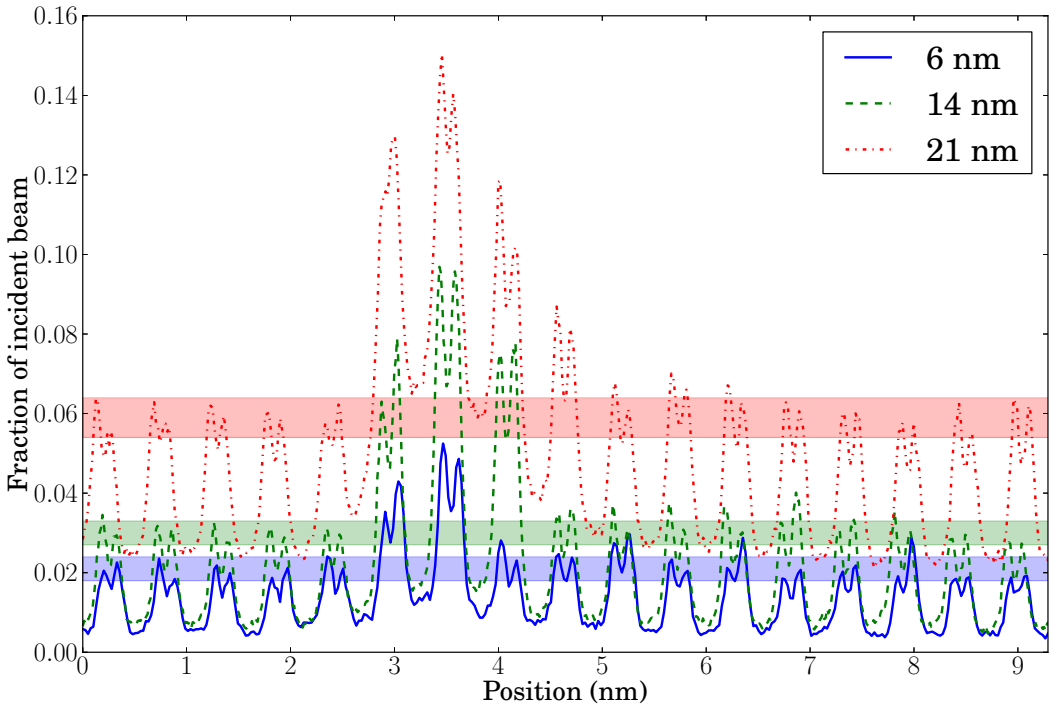

(d)

Figure 4.7.: HAADF-STEM images of 4 ML Ge QDs with different thickness: (a) 6 nm, (b) 14 nm and (c) 21 nm. (d) HAADF Intensity profile across the HAADF images of Ge QDs (a-c). The profiles are measured in the area between the two arrows by averaging over narrow width of 1 Å.

4.4.1.2. Atomic resolution EELS

In order to confirm that the brightest atomic columns in the Si spacer are due to the presence of Ge dopants, atomic resolution EELS experiments have been performed on the Titan^3 Ultimate microscope. Note that to reach the atomic detection, the microscope voltage has to be set to 80 kV in order to avoid any beam damage during acquisition of SI with small pixel size of 0.5 Å for high resolution. The use of such very stable and powerful microscope is required for such advanced experiments. Fig. 4.8(a) shows the HAADF image of a Ge QDs layers with the Si substrate on the left and the green square indicates the area of the EELS acquisition. The convergence and collection angles were 21 and 70 mrad, respectively. For the acquired 164 × 62 px SI, the pixel time was 50 ms giving a total acquisition time of about 9 min. During the acquisition, the HAADF image is acquired simultaneously with the EELS signals on Ge $L_{2,3}$ and Si edges. HAADF image and chemical maps of Ge and Si after PCA treatment are shown in Fig. 4.8(b, c, d) respectively.

In Fig. 4.8(a-b) some atomic columns in the Si spacer appear brighter than in the Si substrate. At the same localization on the Ge map, Ge signal was also detected demonstrating the link between brightest atomic columns on the HAADF image and the presence of Ge atoms. EELS intensity profiles shown in Fig. 4.8(f) evidence more clearly this observation: in the Si substrate the Ge signal is close to zero whereas in the Si spacer, Ge signal is measured at a position of around 6 nm.

These atomically resolved EELS acquisitions give a direct measurement of the Ge profiles above the Ge QDs. Nevertheless, the quantification is nowadays still difficult and requires a lot of computation (much more than HAADF image simulation) for accurately quantify the chemical content at the atomic scale. Up to now, only one work has been reported on quantitative chemical mapping at the atomic scale [Xin 11]. Moreover, the field of view is extremely small (3 x 8 nm) and does not suit very well if one has to deal with a complete study of inter-diffusion in Material Science.

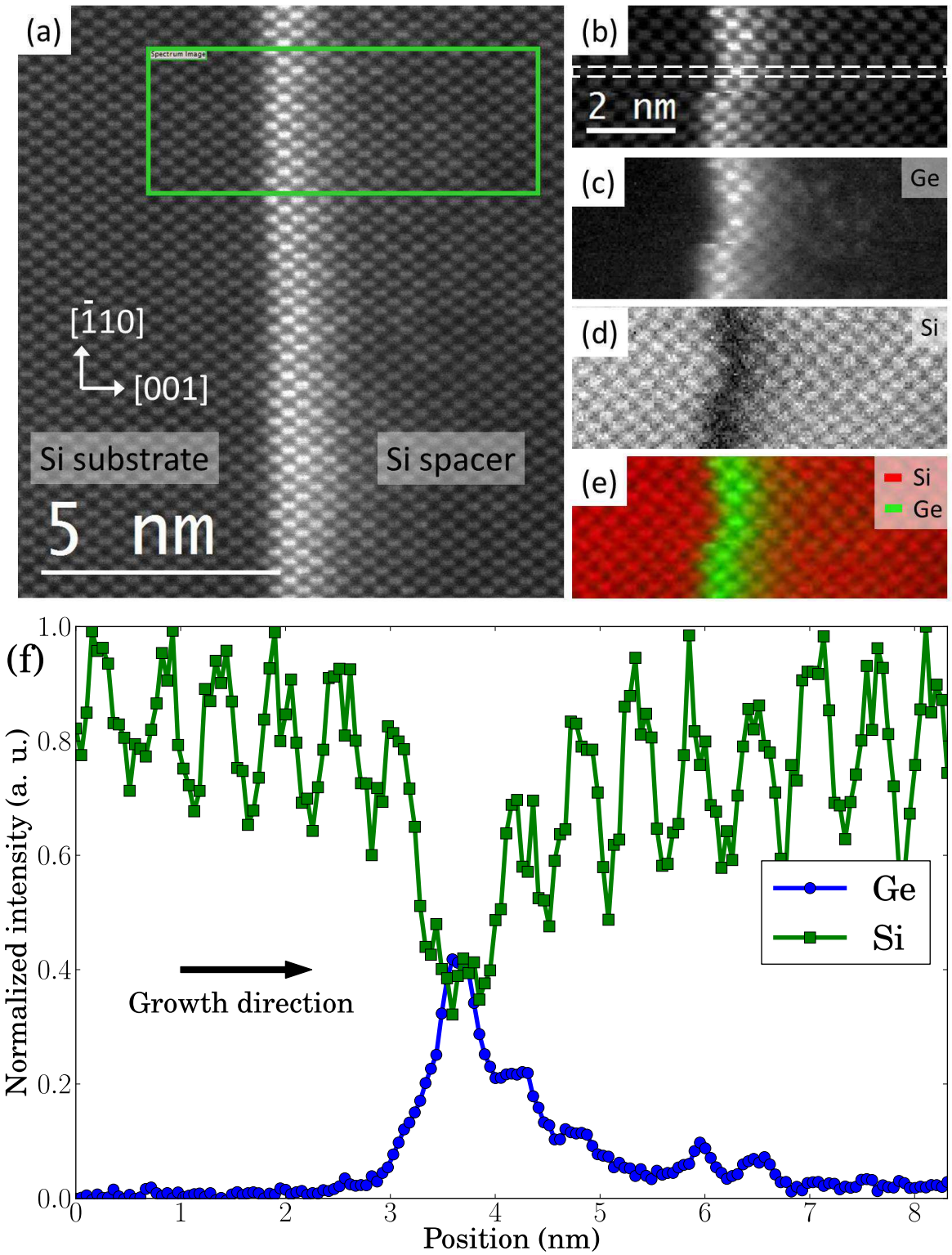

Figure 4.8.: Atomic resolution EELS of 4 ML Ge embedded in Si performed at 80 kV (no drift correction).. (a) HAADF-STEM image before acquisition; the green square marks the actual area from which the EELS signal was acquired. (b) HAADF image of the mapped area acquired simultaneously with the EELS signal: (c) Ge $L_{2,3}$ map at 1217 eV, (d) Si K map at 1839 eV. (e) Ge (green) versus Si (red) composite map. (f) Ge and Si composition profile taken in the position marked with a white dashed square. PCA denoising was performed with three components.

4.4.1.3. HAADF image simulations of substitutional Ge atoms in Si

To obtain some insights on the dependence of HAADF signal as a function of the thickness at the atomic level, we performed series of HAADF images simulations which results are summarized in Fig. 4.9. HAADF images were calculated using the multi-slice approach (see sec. 2.2.2) implemented in the TEMSIM software[1] [Kirk 10]. The simulations were performed with Si supercells containing one or two Ge atoms in substitutional position built for thickness ranging from 2 nm to 25 nm. The substitutional Ge atoms were positioned in the center of the supercell. The simulation of thermal diffuse scattering (TDS) were performed within the frozen phonon approximation with 20 configurations. A 200-keV aberration-corrected probe has been employed ($\alpha = 20$ mrad, $C_3 = 5$ µm and $\triangle f = -5$ nm) and an experimental probe size of 1 Å was assumed in the calculation. The inner and outer collection angle of the annular detector were set to 70 mrad and 160 mrad, respectively.

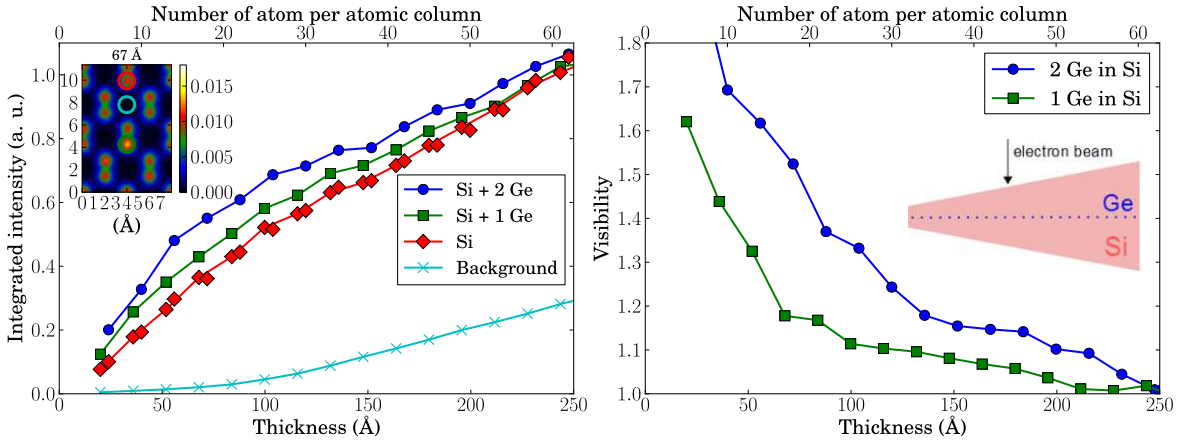

Figure 4.9.: (a) Calculated HAADF signal as a function of the thickness on a Si atomic column containing 2 Ge atoms (blue dots), Si atomic column with 1 Ge atom (green square), pure Si atomic column (red diamond) and the background, *i.e.* between Si atomic columns (cyan cross). Inset: simulated HAADF image showing the disk used for integrating the HAADF signal at the different position. (b) Visibility of 1 or 2 Ge atoms in Si atomic column as a function of the thickness.

Fig. 4.9(a) shows the variation of HAADF intensity as a function of the thickness for four position in the supercell:

- Si atomic column containing 2 Ge atoms (blue dots),
- Si atomic column with 1 Ge atom (green square),
- pure Si atomic column (red diamond),
- the background, *i.e.* between Si atomic columns (cyan cross).

[1]Free software, download at `http://people.ccmr.cornell.edu/~kirkland/cdownloads.html`.

The HAADF signals were integrated over a disk as shown in the inset of Fig. 4.9(a). From Fig. 4.9(a) one can observe that the HAADF signal integrated over atomic columns increases with increasing thickness and with increasing Ge content. As observed experimentally and mentioned previously, the background signal also increases with thickness. These curves also show that indeed the presence of one atom of Ge in Si is detectable under some conditions. To go further and analyze more quantitatively the contrast, we introduce here the notion of visibility which is defined as [Okun 10]:

$$V = \frac{I_D}{I_H} \tag{4.1}$$

where I_D is the intensity of a doped atomic column and I_H is the intensity of a non-doped atomic columns. The visibilities of atomic columns containing one and two Ge atoms are plotted in Fig. 4.9(b) as a function the thickness. The visibility of one or two Ge dopants in Si is high at low thicknesses and converges to one at higher thickness. The visibility of one Ge atom is quite high for very thin areas (< 10 nm) but decreases rapidly when thickness is higher than 10 nm. Between 10 to 20 nm thicknesses, the visibility is of only few percents and above the detection of one Ge atom is no longer possible. It is important to note the effect of the depth position of the dopant in the thin lamella: dopant positioned at the border of the lamella provide a smaller visibility [Radt 13].

These HAADF image simulations support the previous experimental observations presented in Fig. 4.7. They also confirm that with a proper sample preparation of thin lamella, the detection of single Ge atom in Si is possible using HAADF imaging.

4.4.2. Quantification of HAADF imaging by template matching method

The results presented in the previous section point out that HAADF imaging allows the detection of Ge atoms in the Si spacer. In this section, we present a method to analyze HAADF contrast by combining spatial averaging and image fitting techniques based on the template matching method. This approach was originally developed by Ourmazd and his collaborators and applied to HRTEM images containing chemically sensitive reflections, such as in the zinc-blende system [Ourm 89]. More recently, Zuo and his collaborators developed a similar method for the quantification of HAADF images [Kim 13]. In this work we use the Digital Micrograph plug-in implemented by Zuo to map the diffusion of Ge atoms in the Si spacer on large areas. This approach consists in fitting reference patterns to the original image.

4.4.2.1. The template matching method

The first step consists in obtaining a reference pattern, which will be used to quantify the HAADF signal of each atomic columns. Fig. 4.10 illustrates this procedure by using a Si-dumbbell pattern averaged on a series of Si dumbbells (Fig. 4.10(a)) of an experimental image.

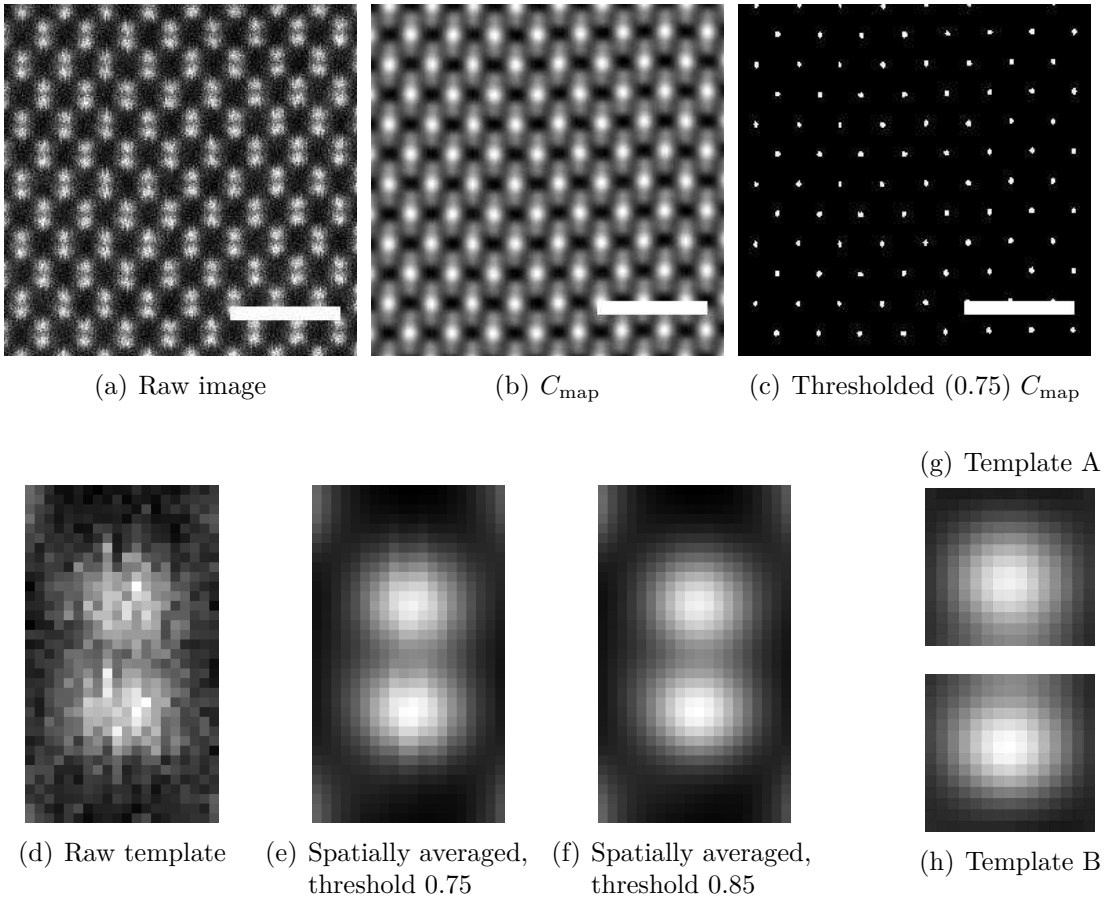

(a) Raw image (b) C_{map} (c) Thresholded (0.75) C_{map}

(g) Template A

(d) Raw template (e) Spatially averaged, threshold 0.75 (f) Spatially averaged, threshold 0.85 (h) Template B

Figure 4.10.: Spatial averaging and determination of reference pattern. (a) Raw HAADF image. (b) Coefficient map C_{map}, resulting from the template matching. (c) Threshold of 0.75 applied to the coefficient map C_{map}. (d) Raw template, (d-e) spatially averaged template after different iteration with a threshold increasing from 0.75 and to 0.85. (g) Template A and template B used in the quantification.

The reference pattern is spatially averaged for reducing the signal-to-noise ratio (SNR). We used the template matching method technique to find the positions of the raw HAADF image that match well with the reference pattern in order to localize the dumbbells. The template matching algorithm scans the template over the source image (reference area of the raw HAADF image) and calculates at each pixel position (i, j) the matching. This matching uses cross-correlation which is known to provide good results. The matching is given through the normalized coefficient provided by the

cross-correlation at each pixel of the source image. A normalized coefficient map C_{map} (Fig. 4.10(b)) contains values between [-1,1] [Kim 13]. Value close to one corresponds to very good matching between the reference pattern and the sub-image $I(i,j)$ of the source image. The normalized cross-correlation image is then thresholded (Fig. 4.10(c)) to get accurate localization of the dumbbells. Finally the reference pattern is averaged using all well-localized dumbbells of the reference area on the raw HAADF image. This provides a new reference pattern with a much higher SNR (Fig. 4.10(e-f)). One can notice that the high SNR reference pattern is very sensitive to the remaining aberrations and misorientation of the specimen. For example here, the reference pattern in Fig. 4.10(f) points out a very small asymmetry: the lower atomic column of the dumbbells is 10 % brighter than the upper atomic column. This can be explained by a very small misorientation of the specimen with respect to the incident beam.

The second step consists in determining the best fit between the reference pattern and the sub-images $I(i,j)$. Once again, this is performed by template matching of the reference pattern with the whole raw HAADF image. The coefficient map C_{map} contains peaks corresponding to the best match between the template and the sub-image and the raw HAADF image. Thus, the position (i,j) are obtained by fitting the maximum of the coefficient map C_{map}.

In the third and last step the reference pattern is fitted to the HAADF image at each location (i,j) obtained previously. The equation of the fit is here given by:

$$I(i,j) = a \cdot T + b \tag{4.2}$$

where $I(i,j)$ is a sub-image of the raw HAADF image, T is the reference pattern, a is an amplitude coefficient and b is an offset coefficient. The choice of the reference pattern and the reference area is of course of importance for extracting quantitatively the information.

4.4.2.2. Template matching on HAADF images of Ge quantum dots

In our case, we worked with two templates: one for each atomic columns of the Si dumbbells (template A and B in Fig. 4.10(g-h)). This allows to get more precision in the analysis compare to that proposed by Zuo for InAs/GaSb system [Kim 13], in order to differentiate in our case the two atomic columns of each dumbbell. Kim *et al.* quantified the intermixing of InAs and GaSb layer by fitting a linear combination of two templates (one for InAs and the other for GaSb) at the position of each dumbbell. In our case, we used the template matching approach in a different manner: the amplitude coefficient a in Eq. 4.2 is used as a direct measurement of the visibility as defined by 4.1 and the offset coefficient b is related to the background of the HAADF image.

The Si substrate of the raw HAADF image was chosen as the reference area and the reference patterns are Si pure atomic columns one each side of the dumbbell.

Fig. 4.11 shows a typical example of application of this method on a normalized HAADF image of our Ge QDs in Si. Thickness measurements were performed by PACBED in this area. One experimental PACBED pattern taken in the center of this area (Fig. 4.11(a)) is compared to a simulated one (Fig. 4.11(b)) and allows to determine a thickness of 9 nm. Series of PACBED analyzes across this area determine that the thickness increase from 6 nm at the edge of the specimen (outside of the HAADF image on the top) to 11 nm in the Si substrate (bottom of the image). Fig. 4.11(d) presents in false color, the result of the template matching applied on the whole area of Fig. 4.11(c). The amplitude is directly linked to the content of Ge in Si atomic column. Due to thickness variation the HAADF intensities decrease slowly toward the border of the specimen. leading to long range variation of the amplitude [Voyl 02, Rose 11] and can be subtracted to straighten contrasts. Fig. 4.11(e) presents the result of this background subtraction. The amplitude map (Fig. 4.11(e)) shown in false color is rich of information and allows to classify different families of atomic columns:

- amplitude around 1 is the reference amplitude on the Si pure substrate
- amplitudes > 3.0 correspond to atomic columns in the Ge QDs and between 2.0 and 3.0 to the diffuse chemical profile above these Ge QDs.
- amplitudes comprise between 1.0 and 2.0 correspond to columns in the Si spacer containing some Ge dopant atoms due to the segregation process during the growth.

This example demonstrates that the template matching method provides a very good way to analyze the contrast variation of atomic columns on high resolution HAADF images. This method is very efficient if performed with pertinent choice of the reference patterns combined with good quality of the sample preparation for a good area to be analyzed.

Further steps are required to provide better quantification of the HAADF image. Usually, HAADF intensities are quantified by comparison with HAADF image simulation [Gril 08, Rose 09] but this procedure is not so easy to perform due to two main reasons: the computation time is long (up to weeks) and the quantitative results of the simulations are always convolved by a function with a standard deviation σ depending on experimental parameters. Before the work of Dwyer *et al.* [Dwye 12], the value of σ was used as adjustable parameters. Another way could be to compare the amplitude of the template matching procedure with calculated visibility obtained by HAADF image simulations since this amplitude is directly linked to visibility, as explained previously. One can also analyze the amplitude distribution on the amplitude map in order to

(a) Experimental PACBED

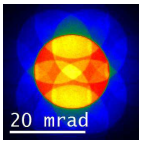

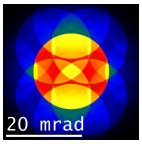

(b) Simulated PACBED 9 nm

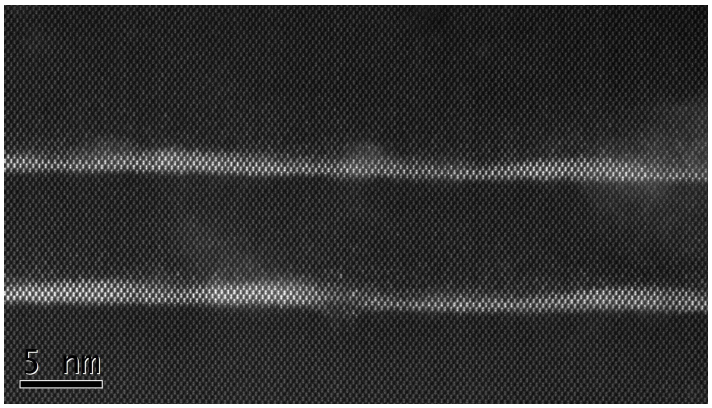

(c) Raw HAADF image

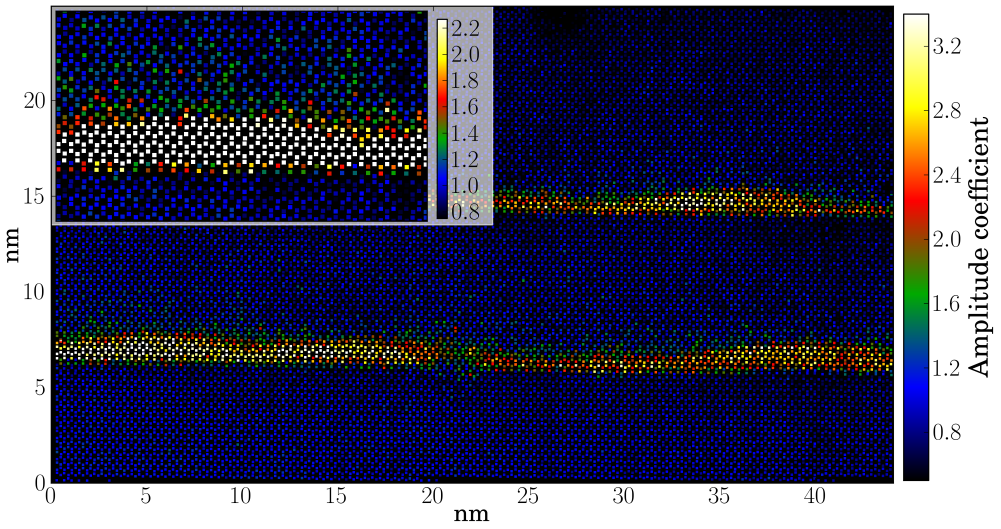

(d) Raw amplitude map

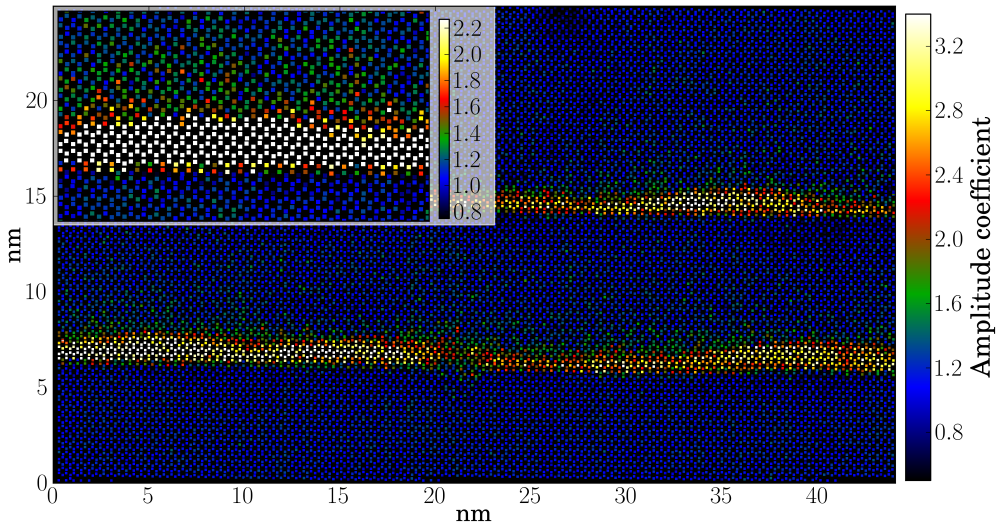

(e) Amplitude map after background correction

Figure 4.11.: (a) Experimental PACBED pattern measured between the two layers of Ge QDs. (b) Simulated PACBED pattern for a crystal thickness of 9 nm corresponding to (a). (c) HAADF image of Ge QDs. (d,e) Amplitude map obtained using the template matching method, before and after background subtraction. The inset in (d-e) shows the zoomed area indicated by a dashed square in (d-e). The contrast have been saturated to highlight the difference between the Si substrate and the Si spacer.

classify the different families of columns described above. Fig. 4.12 shows three histograms of amplitude distribution taken on three different areas on the amplitude map (Fig. 4.11(e)): in the Si substrate (in blue), in the Si spacer (in green) and in the Ge QDs (in red). Since the template was chosen in the Si substrate, the amplitude distribution in the Si substrate is well centered around 1, as expected. Its standard deviation of 0.08 gives a estimation of the sensitivity of our measurements using the template matching method. The amplitude distribution of the Si spacer is similar to that of the Si substrate, but it has a tail at higher amplitude with maximum amplitude values reaching 2.0. The difference observed between the amplitude distribution in the Si substrate and the Si spacer indicate that it is possible to discriminate low Ge concentration in Si by using HAADF imaging. The amplitude distribution of the Ge QDs (in red) lies at much higher amplitude than the Si substrate.

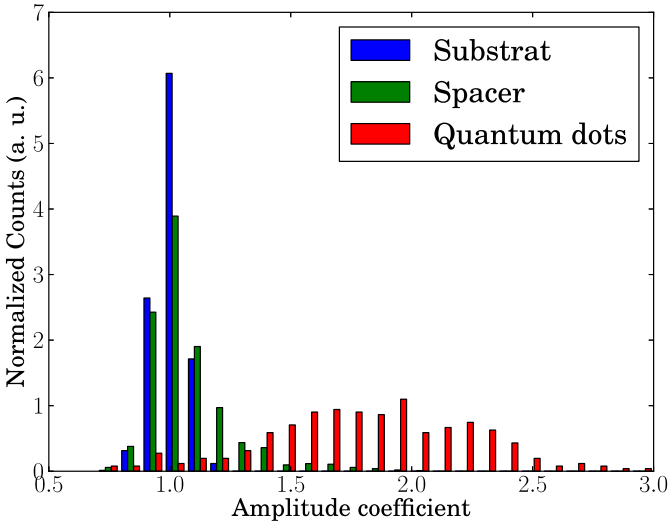

Figure 4.12.: Histograms of amplitude distribution measured in different area: (blue) Si substrate, (green) Si spacer and (red) Ge quantum dots

4.4.3. EELS mapping

EELS mapping is a complementary technique to HAADF imaging for studying chemical distribution of Si and Ge content. Thanks to the spectrum imaging (SI) method, large areas can be scanned with the aberration-corrected STEM probe and HAADF signal combined with localized EELS spectra around Ge $L_{2,3}$ and Si K edges can be acquired simultaneously. In order to scan large fields of view (few 10 nm^2) in an acceptable time, we set the pixel size to a larger value as compared to the previously atomic resolution EELS mapping (Fig. 4.8): the pixel size is set to 3 Å as compare to 0.3 Å previously. This is a good compromise to acquire data over several minutes and even depending on the size of the area, over 10 to 20 minutes .

4.4.3.1. Calibration of EELS sensitivity factor

To go further, the EELS signal needs to be quantified in order to get a better knowledge of the Ge relative distribution in Si with high accuracy. We used calibrated k factor for this quantification. Multilayers heterostructures of Si_xGe_{1-x} quantum wells grown by reduced pressure-chemical vapor deposition (RP-CVD) [Hart 02] were used as reference. The EELS spectra were measured using the same experimental conditions as for the Ge QDs: the most important being the integration range (60 eV), the convergence angle (α = 20 mrad) and the collection angle (β = 98 mrad). The nominal Ge concentration of the four Si_xGe_{1-x} quantum wells were preliminary measured by secondary ion mass spectrometry (SIMS) and Ge concentration of 45 %, 38 %, 31 % and 20 % were obtained for the QWs shown in Fig. 4.13 from the left to the right [Bech 09, ?].

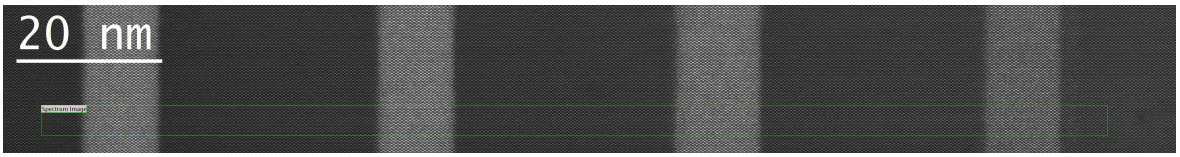

(a) HAADF image

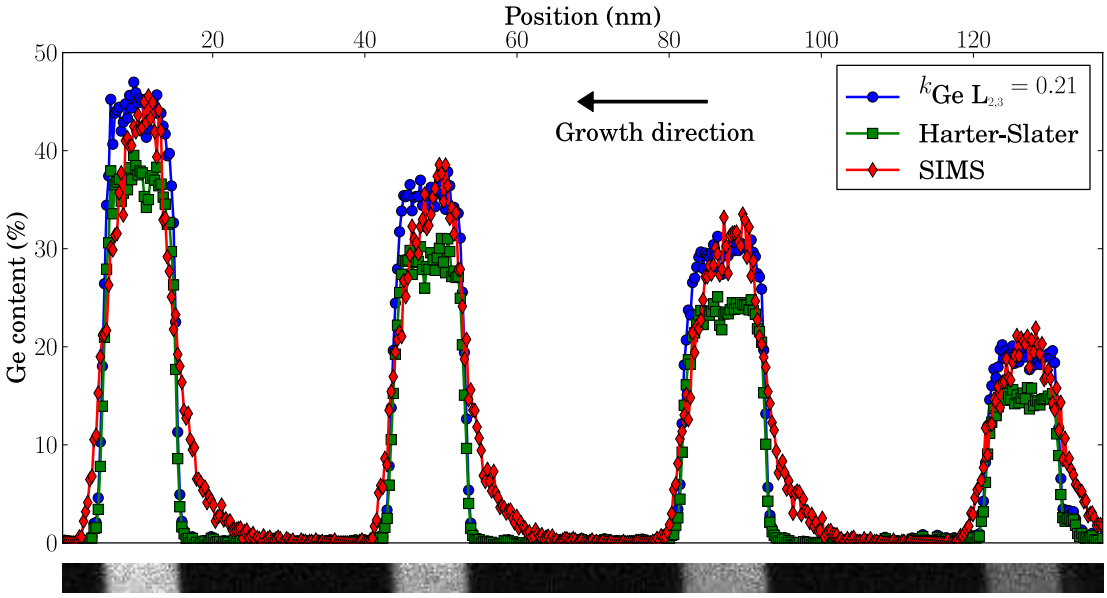

(b) Ge concentration profile and map

Figure 4.13.: (a) HAADF images of the four SiGe quantum wells indicating the location of the acquired EELS SI (green square) (b) Ge concentration profile and map of four SiGe quantum wells used for the calibration of the $k_{\text{Ge L}_{2,3}}$ factor. The concentration profile obtained by SIMS is plotted in red diamond. The Ge concentration measured by EELS using Hartree-Slater partial cross-section and $k_{\text{Ge L}_{2,3}}$ factor are plotted in green square and blue dots, respectively. The nominal Ge concentration is 45 %, 38 %, 31 % and 20 % from the left to the right.

The good agreement of quantitative strain measurements using nano-beam electron diffraction and dark-field holography analysis on the same sample, with the Ge concentrations obtained by SIMS confirmed the accuracy of the concentration [Coop 09]. The EELS Ge concentration profile measured on this identical sample (Fig. 4.13(a)) shows that a deviation of 10 % is observed between the real concentration value (SIMS data) and the computed one using classical Hartree-Slater partial cross-section implemented in the Digital Micrograph software for EELS spectra analysis. Therefore, in order to fit EELS signal with SIMS content, we found out that the sensitivity factor of Ge $L_{2,3}$ relative to Si K edge is $k_{\mathrm{Ge\ L_{2,3}}} = 0.21$ for our experimental conditions (Fig. 4.13 (a)). More details about the EELS quantification using k factors are given in the Appendix A. Note that the Ge profile obtained by EELS is very sharp at the interfaces compare to the SIMS ones. This is mainly due to experimental artifacts during acquisition for the latter. This example shows clearly that the EELS acquisition is much more spatially resolved than SIMS. Indeed, the aberration corrected electron probe (<0.08 nm for the experimental conditions used) for EELS measurements ensures a very good spatial resolution and the EELS signal delocalization is considered to be small at these energy edges > 1000 eV.

4.4.3.2. EELS analysis on Ge quantum dots

Fig. 4.14 shows a typical results of EELS spectrum image (SI) analysis on our Si/Ge QDs system. This EELS SI data set is made of 107 × 73 px with acquisition time per pixel of 50 ms, providing a field a view of 33 × 22 nm. The total acquisition time was less than 11 min and depends both on the pixel acquisition time but also on the readout time of the CCD signal. Spectra are acquired using binning of 130 px in the non-dispersive direction to speed up the acquisition and increase the SNR. A fast acquisition mode of digit scan software from Gatan were also used. The HAADF image (Fig. 4.14(a)) is recorded simultaneously using the "sub-pixel" scanning option. The electron probe is scanned in a mosaic fashion, *i.e.* one pixel on the EELS SI Fig. 4.14(b) corresponds to a square of 16 × 16 px on the HAADF image Fig. 4.14(a). The benefit of the "sub-pixel" feature is to keep the high resolution pattern in the HAADF imaging, while acquiring EELS SI with larger pixel size. The 3 Å pixel size of the EELS SI is an interesting trade off between pixel size and field of view and corresponds in the Si [110]-zone axis to two atomic columns or one dumbbell. A first comparison between Fig. 4.14(a) and (b) shows a very good matching between the high resolution HAADF image and the Ge map regarding the localization and shape of the Ge QDs.

Three background subtracted spectra of unique pixel are plotted in Fig. 4.14(d) to show typical Ge $L_{2,3}$ and Si K edges after PCA treatment obtained in the Si substrate (blue dots), the Ge QDs (green squares) and the Si spacer (red diamonds). A very good

sensitivity of detection of small amount of Ge in the Si spacer is obtained (red curve) and this is mainly due to optimized signal acquisition and PCA treatment presented in the first chapter (see sec. 2.6.2). Fig. 4.14(c) presents the Ge content distribution obtained from SI analysis using the calibrated $k_{\mathrm{Ge\ L_{2,3}}}$ factor.

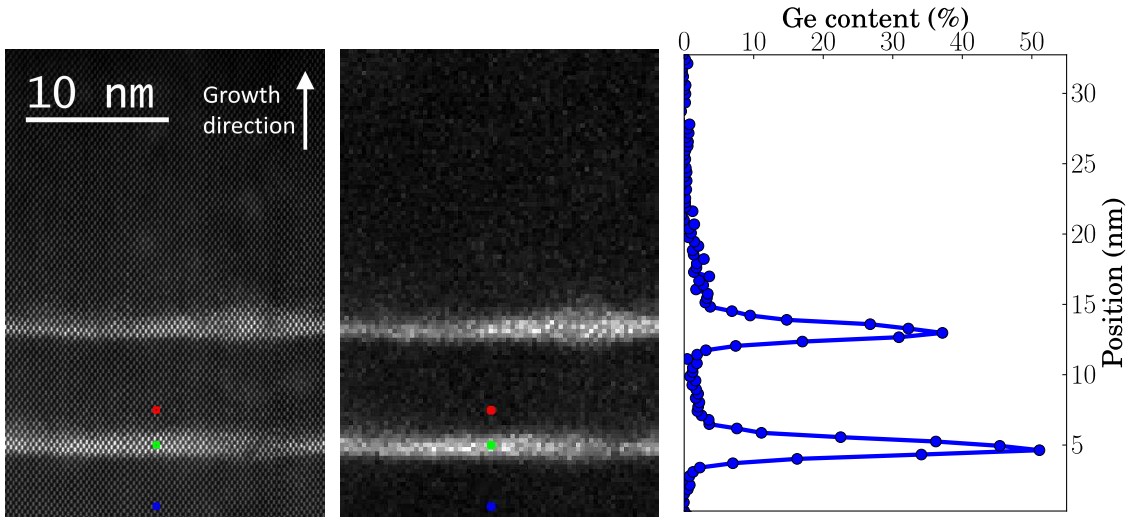

(a) HAADF image (b) Ge map (c) Ge profile

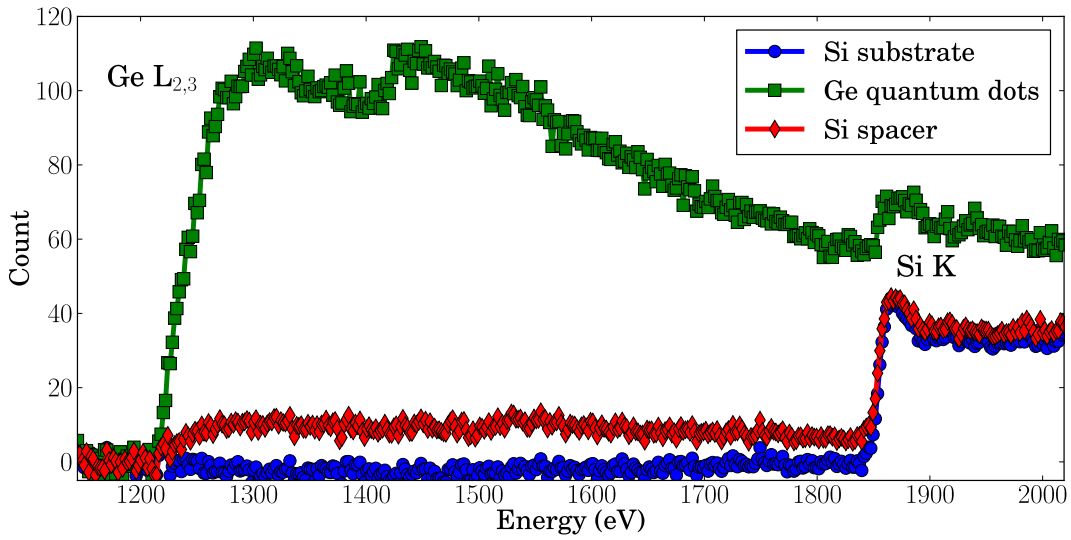

(d)

Figure 4.14.: (a) HAADF image acquired simultaneously with the EELS SI. (b) Ge map obtained by EELS. (c) Ge concentration profile across the Ge quantum dots averaged over 20 pixels. (d) Background subtracted EELS spectra extracted of unique pixel at different position of the EELS SI as indicated the square of the corresponding color in (a) and (b). For EELS acquisition the probe current was 85 pA and PCA denoising was performed with three components.

A high content of Ge is found localized on the Ge QDs but note that the content does not reach 100% meaning that these QDs have in fact a Si_xGe_{1-x} composition. Moreover, the Ge profile across the Ge QDs exhibits an asymmetry with a sharp interface below

but more diffuse above the QDs. The tail extends on few nm and corresponds to a very low content of Ge (1 to 2 %) at the end. This confirms the presence of Ge atoms in small quantity in the Si spacer and is in good agreement with a segregation process. Unique ELLS spectrum acquired in the Si spacer (red diamonds EELS spectrum in Fig. 4.14(d)) detects small Ge content. This demonstrates that with low acquisition times such as the 50 ms combined with the 85 pA probe current, elemental concentrations of a few percents can be measured, even at relatively high energy loss (Ge $L_{2,3}$ at 1217 eV).

4.4.4. Correlation of HAADF and EELS signals

The previous sections showed that the Ge distribution concentration in Si can be detected by HAADF imaging and EELS acquisition. The HAADF signal is not straightforward to convert to an accurate measurement of the Ge concentration but can provide high sensibility and high spatial resolution. Template matching is a good way to quantify the amplitude distribution of the signal. EELS acquisition is a good way to quantify Ge content with a accuracy down to 1 %[2] and a precision of 4 % in our experimental conditions. Nevertheless the acquisition of high spatially resolved EELS Ge map is extremely difficult since the acquisition of EELS SI requires a much longer time than HAADF (a least 1000 times longer). A good alternative to get both atomic resolution, high chemical sensitivity and quantification is to combine the two signals and obtain high resolution and accurate Ge map concentration on large field of view of several tens of nanometers.

In practice, this correlative analysis requires a data set consisting of a EELS SI with a pixel size of ~ 3 Å and a HAADF image acquired simultaneously with a pixel size much smaller than that of the EELS spectrum image in order to obtain atomic resolution on the HAADF imaging. A typical example of such an acquisition was shown previously in Fig. 4.14. The simultaneous acquisition of HAADF and EELS signals in such a data set ensures a good correlation of both signals as they are recorded from exactly the same position and at the same time.

Fig. 4.15(a) shows the distribution maps for three different intervals of the amplitude coefficient of template matching analysis:

- The amplitude interval $[0.8, 1.2]$ corresponds to pure Si atomic columns, as mentioned previously by inspecting the amplitude distribution in sec. 4.4.2. The corresponding distribution map covers almost the whole map excluding the Ge QDs and some position in the Si spacer.
- The amplitude interval $[1.2, 1.4]$ highlights the position of amplitudes in the Si spacer and at the border of the Ge QDs. On this map, there is almost no contribution from the Si substrate.

[2]The good accuracy is explained by the quantification with k-factor and the limited systematic error in the EELS background subtraction of the high energy loss edges (Ge $L_{2,3}$ at 1217 eV and the Si K at 1839 eV).

- The last amplitude distribution map shown in Fig. 4.15(a) for the interval [1.4, 2.4] clearly corresponds to the Ge QDs.

Fig. 4.15(b) shows the three plots of mean EELS spectra obtained by averaging all the spectra of pixels belonging to the same amplitude interval.

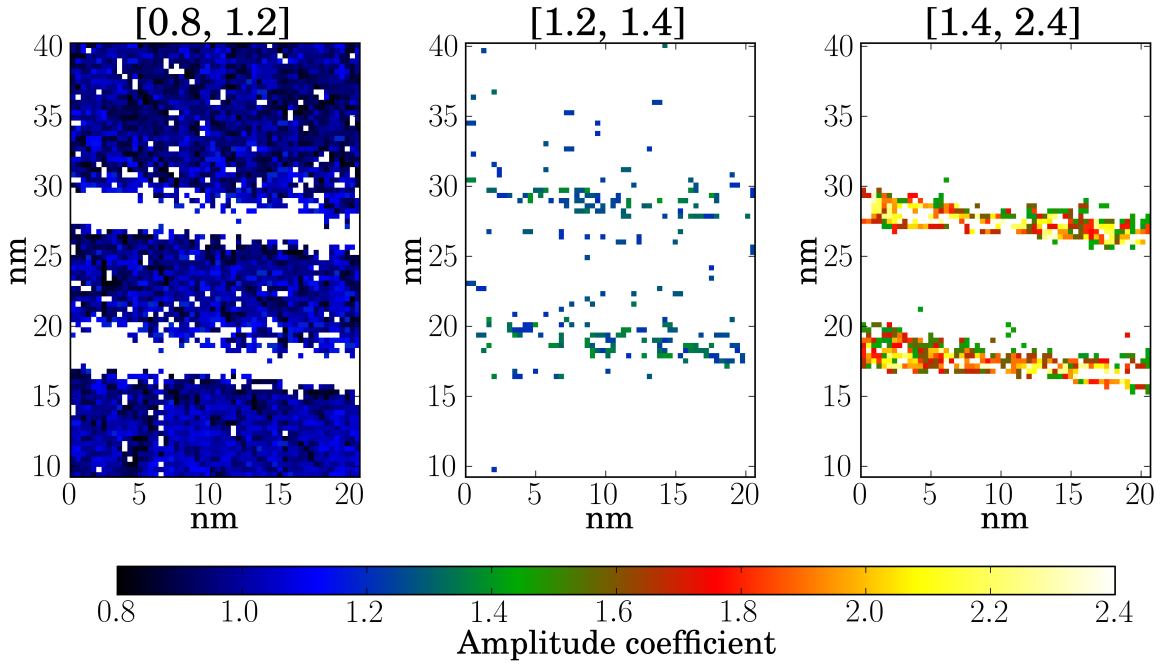

(a) Amplitude distribution map

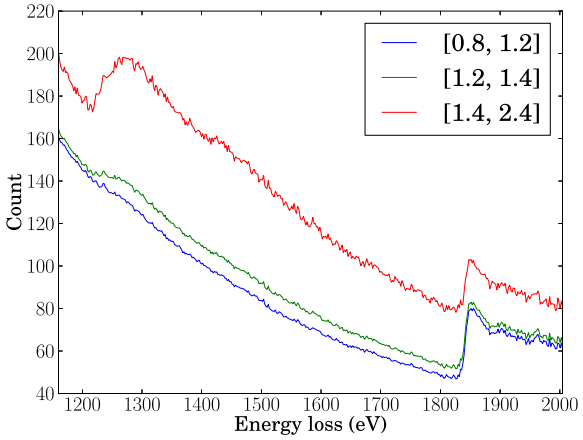

(b) EELS signal

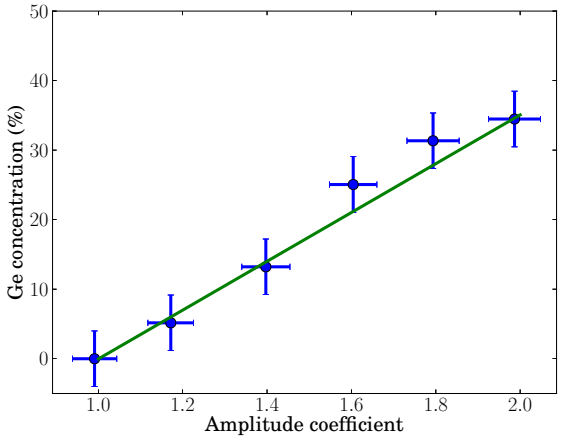

(c) HAADF-EELS Correlation plot

Figure 4.15.: (a) Amplitude distribution maps for three different intervals: [0.8, 1.2], [1.2, 1.4] and [1.4, 2.0]. The amplitude map was measured on the HAADF image shown in Fig. 4.14(a) which was acquired simultaneously than the EELS SI. (b) Averaged EELS spectra for the three distribution considered in (a). (c) Dependence of the Ge concentration obtained by EELS as a function of the amplitude coefficient. The green line represents a linear fit of the experimental data in blue dots. The error bar represent the standard deviation of the distributions.

This points out that the intensity of the Ge edge at 1217 eV increases when increasing the mean amplitude, *i.e.* by increasing the values delimiting the interval. This observation already indicates a correlation between the HAADF signal and the EELS signal as we can expect due to the chemical sensitivity of both signals.

Following this approach, we plot the dependence of the averaged Ge concentration as a function of the amplitude coefficient in Fig. 4.15(c). Each point of the curve corresponds to an amplitude interval of 0.2 on which an EELS spectrum is averaged over all the pixels belonging to this interval and afterward, the spectrum is quantified in Ge content. The experimental data (blue dots) can be well modeled with a linear fit, given by the equation $y = a_0 + b_0 \cdot x$, where x is the amplitude coefficient and y is the Ge concentration. The fitting parameters a_0 and b_0 were set as free parameter and the fit quality was determined by the residual $w = \sum|y_i - y_{\mathrm{th}_i}|/\sum y_i$, which measures the average relative deviation between the experimental values y_i and the theoretical value y_{th_i} of the fit curve, where the index i runs over all data points. A least square fit provides $a_0 = -32.9$ and $b_0 = 34.1$ with a residual of $w = 6.7\%$, confirming the good fit quality.

This curve gives the correlation law between amplitude STEM signal and Ge content and allows now to convert amplitude maps to Ge contents maps: *i.e.* to quantify HAADF-STEM contrast.

For an amplitude coefficient of 1 corresponding to Si pure atomic columns, the fitted straight line provides a value of less than 1 %, which is within the error bar of the EELS quantification ($\sim$ 1 %). High amplitude coefficient provides higher Ge concentration: as an example, an amplitude coefficient of 2 gives a Ge concentration of 35 %.

The conversion of the whole amplitude map to a Ge concentration map is performed and compared to the Ge concentration map obtained from the EELS data set acquired simultaneously in Fig. 4.16. The intensities of the two maps in Fig. 4.16(a) are displayed on the same color scale. These two maps exhibit a striking resemblance. Moreover, from the profiles shown in Fig. 4.16(b), which were measured across the Ge QDs on both maps, one can observe that the quantification obtained from the HAADF signal is in good agreement with the Ge signal obtained from EELS. This demonstrates that this method successfully quantifies the Ge concentration based on the analysis of HAADF signal when knowing the correlation law between the amplitude and the Ge content.

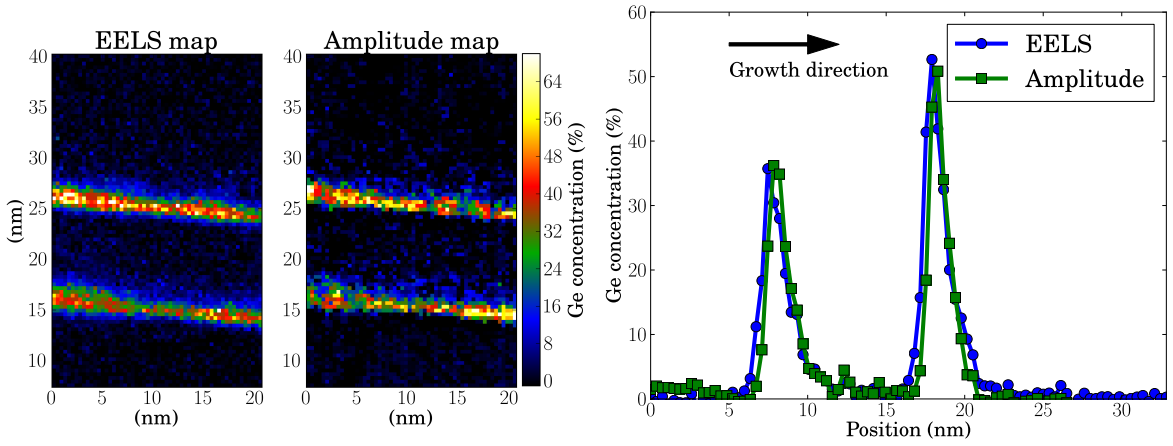

Figure 4.16.: Comparison of the amplitude quantified in Ge concentration (%) with the Ge concentration obtained by EELS shown as map in (a) and as profile in (c).

4.4.5. The protocol in a nutshell and its limitations

The previous section has shown that it is possible to quantify STEM/HAADF contrasts on atomically resolved images. One of the interest of this method is to show that the conversion procedure proposed above can be apply to other HAADF images and then provide very efficient quantitative chemical analysis on a large data set.

The synoptic representation of this work is illustrated by Fig. 4.17. The required experimental data set are a EELS SI and HAADF-HRSTEM images recorded simultaneously and a set of HAADF images acquired from areas of similar thickness. The left part of this figure corresponds to the data analysis presented in previous sections:

- analyze the HAADF image with the template matching method and background variation removal (usually required) to get the visibility map,
- quantification of Ge EELS signals to get Ge EELS concentration maps,
- correlation between amplitude map with the Ge eels concentration map,
- the fit of the correlation curve provides the parameters to convert the amplitude signal into Ge concentration map.

At this step, any other HAADF images acquired in areas of equivalent thicknesses can be analyzed first with the template matching method and then quantified in terms of Ge concentration map on the right side of Fig. 4.17.

Moreover, since the background variation in the amplitude map is related to the specimen thickness, thickness map can be deduced from the background image. Complementary techniques, such as PACBED can be used to measure the thickness at one position of the map and allows calibration of the thickness map as the amplitude map

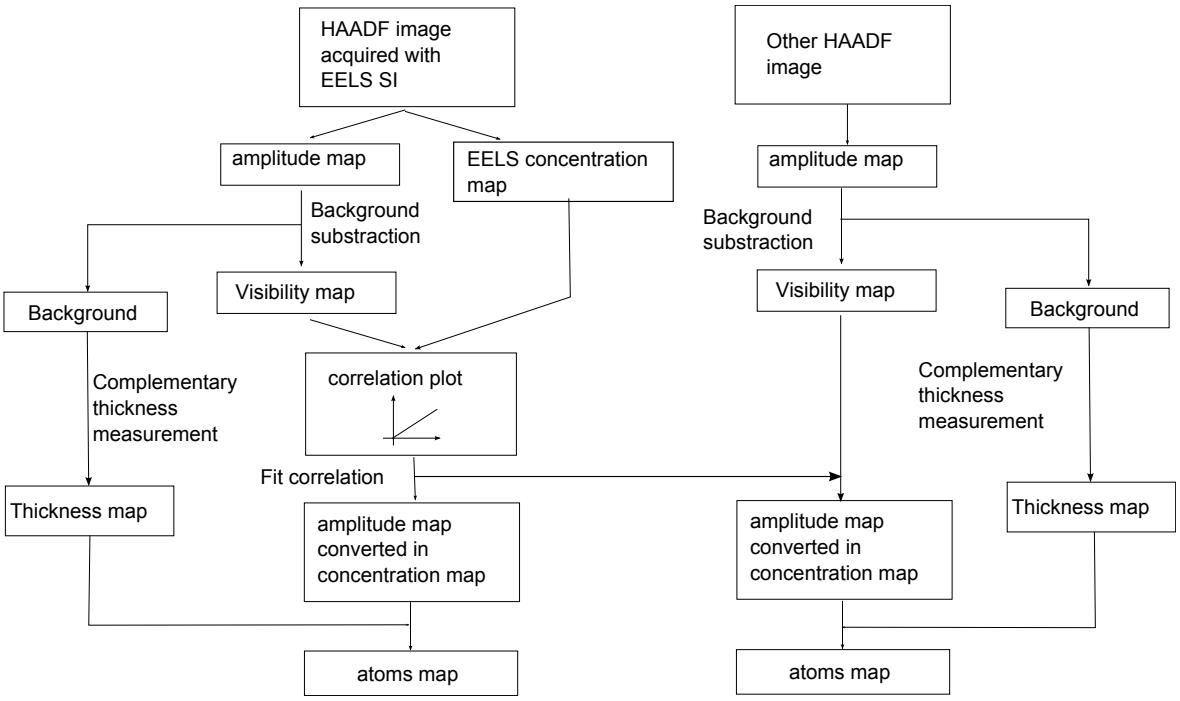

Figure 4.17.: Protocol of the correlative analysis of HAADF and EELS signals.

background increases exactly as the thickness. This provides an easy way to extract a quantitative specimen thickness map from HAADF image.

The limitations of this approach are mainly determined by those inherent to the HAADF imaging. To measure small concentration, the specimen preparation is a crucial step: the specimen surface has to be very clean and flat to get homogeneous specimen thicknesses, *i.e.* the HAADF signal variation have to be small. Ion beam prepared specimen suffers from surface roughness leading to large distribution of HAADF signal in the Si reference areas. This clearly prevents the analysis of small HAADF variation in the region of interest. Radtke and co-authors [Radt 13] used gentle ion milling at low voltage (< 500 eV) on Linda Gentle mill system to analyze similar Ge surface segregation in SiGe QW grown by MBE using HAADF-HRSTEM.

Fig. 4.18 shows different background models that can be used for background subtraction of an amplitude map. First, we consider two analytic functions, a plane (Fig. 4.18(a)) and a cubic polynomial (Fig. 4.18(b)). Second, we consider a rolling-ball algorithm (Fig. 4.18(c)) implemented in the software ImageJ[3], which determines a local background for every pixel by averaging over a very large ball around the pixel [Ster 83]. Profiles of the raw amplitude image and the different background models across the two Ge QDs layers are plotted in Fig. 4.18(d). The decrease of the amplitude above the two layers of Ge QDs appear clearly on the right of the profile (corresponding to the top of the images shown in Fig. 4.18(a-c)). This variation is attributed to a speci-

[3]Website: http://rsb.info.nih.gov/ij/index.html

men thickness variation that occurs at the edge of the thin lamella, and was confirmed by the relative thickness map obtained by EELS. This is common in wedge-polishing preparation of specimen: the last step consisting of chemical-mechanical polishing, the sharp edge of the specimen is usually rounded. Since the background variation are not always linear, the fitted plane shown in Fig. 4.18(a) can fail to correctly model the background. The cubic polynomial function and the rolling-ball algorithm estimation describe fairly well the stronger variation at the top of the image (Fig. 4.18(b-c)). This comparison shown in this plot points out the importance of a correct background modeling to measure small amplitude variation of a 5 % or less.

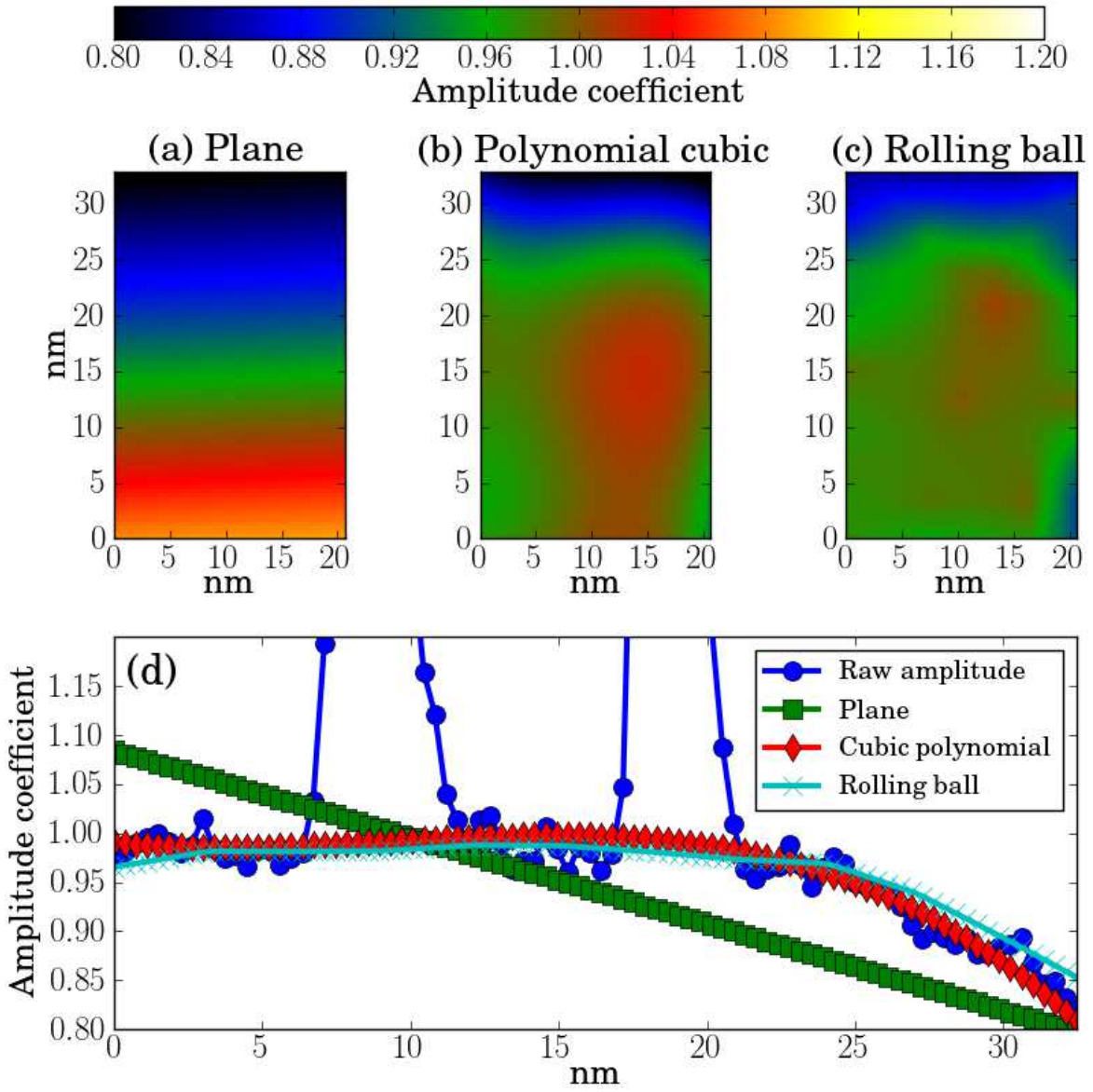

Figure 4.18.: Comparison of different background model for the amplitude map shown in Fig. 4.16(a). Analytic function (a) plane, (b) cubic polynomial and non-analytic (c) Rolling-ball background model. (d) Plot of the profiles of raw amplitude (blue dots), and model background: plane (green square), cubic polynomial (red diamant) and Rolling ball (cyan cross).

4.4.6. Sensibility and accuracy

Following the protocol summarized in Fig. 4.17, we quantified the HAADF-HRSTEM images shown in Fig. 4.11(c). First the HAADF image has been quantified in amplitude and the thickness variation has been removed by subtracting the background (*i.e.* the thickness map) shown in Fig. 4.19(a). A cubic polynomial has been used to model the background. Fig. 4.19(a) shows that the thickness ranges from 7.5 nm at the top of the image (close to the edge of the specimen) to 11 nm at the left bottom. The values were confirmed by PACBED measurements at the top and the bottom of the image.

Using the fitted values of the correlation between EELS and HAADF signal, the amplitude map has been converted to a Ge concentration and the result is shown in Fig. 4.19(b).

The HAADF images being now quantified in Ge concentration, we can study the concentration distribution and the profile concentration with a high statistic and on a larger field of view compared to EELS SI atomic mapping. The variation of the depth position of the Ge atoms in the lamella will lead to a distribution of HAADF intensity, which can be approximated by a Gaussian function [Voyl 03, Radt 13]. It follows that the Ge concentration on the HAADF image has to be measured statistically. This can be performed by averaging profiles or by fitting histogram of concentration (or amplitude) distribution with Gaussian functions [Voyl 02, Radt 13]. To discuss the sensitivity and the accuracy of the method, we investigated more precisely the distribution of the amplitudes and of the Ge concentration in the Si substrate (reference area) compared to the Si spacer (area between the two Ge QDs layers). Their histogram of amplitude (and corresponding Ge concentration) distributions are shown in Fig. 4.20(a-b) respectively.

The experimental amplitude distributions were fitted by a linear combination of Gaussian functions given by:

$$G(x) = \sum_i \lambda_i \frac{1}{2\pi\sigma} \exp(-\frac{(x-\mu_i)^2}{2\sigma^2}) \tag{4.3}$$

where x is the amplitude coefficient, σ is the standard deviation, μ_i are the mean value of the Gaussian functions and λ_i are the free parameters. The index i runs over the number of Gaussian functions.

- The standard deviation is regarded as a parameter of our experimental conditions and was determined by the standard deviation of the Gaussian function fitted in the Si substrate (reference area): $\sigma = 0.08$.
- The distance $\triangle\mu$ between the Gaussian functions ($\triangle\mu = \mu_{i+1} - \mu_i$) was fixed to the expected increase of amplitude coefficient due to presence of an additional

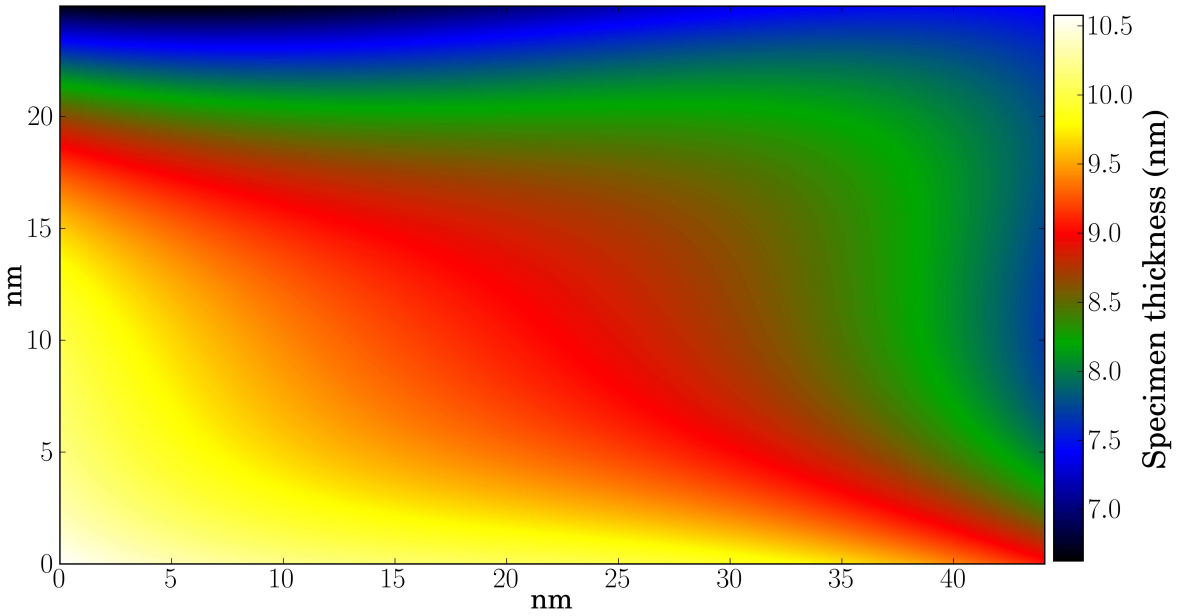

(a) Thickness map

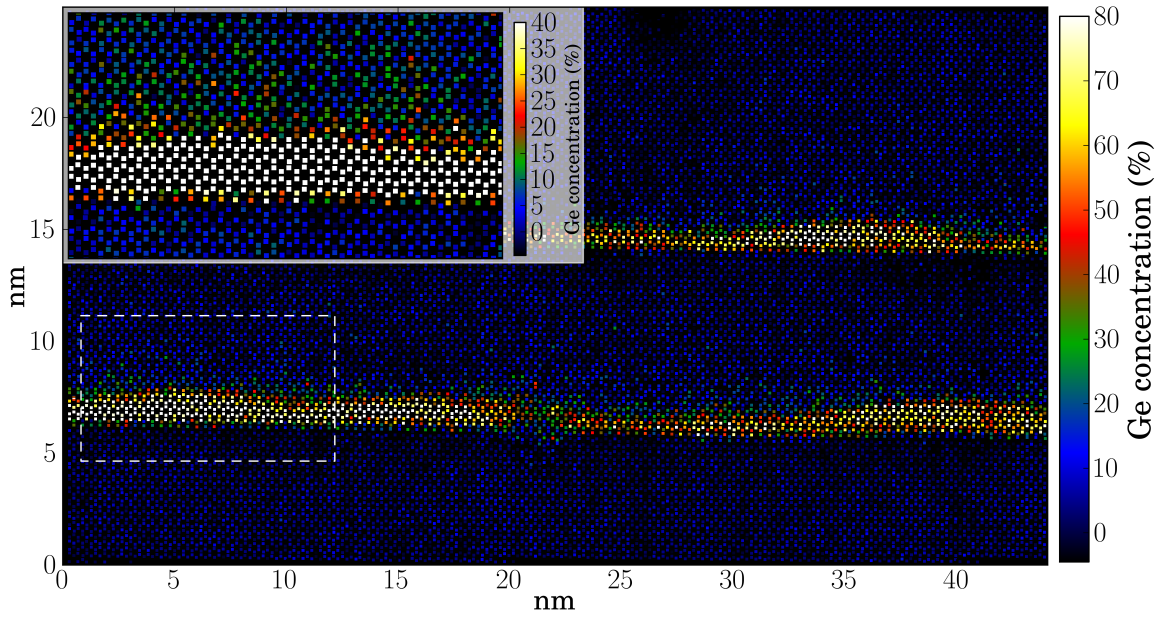

(b) Ge concentration map

Figure 4.19.: (a) Thickness variation of the HAADF image shown Fig. 4.11(c). (b) Amplitude map converted in Ge concentration (%). The inset in (b) shows the zoomed area indicated by a dashed square in (b). The contrast have been saturated to highlight the difference between the Si substrate and the Si spacer.

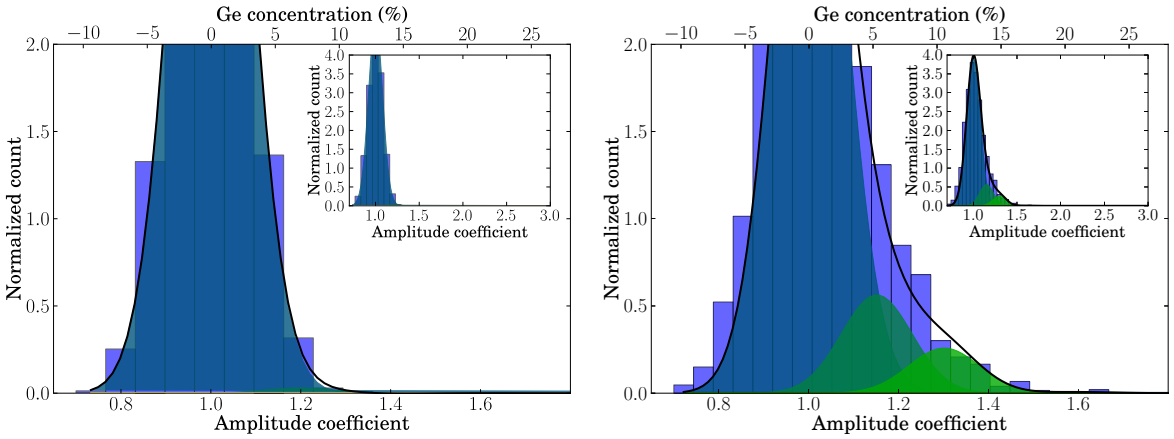

(a) Si substrate (b) Si spacer

Figure 4.20.: Zoomed amplitude distribution (lower axis) and corresponding Ge concentration (upper axis) in the Si substrate and in the Si spacer in (a) and (b), respectively. The integrated count of the distribution have been normalized to one. The linear combinations of Gaussian functions are plotted with a black solid line on the histogram. The general view of the histogram are plotted in the insets. The histograms integrate about ~ 3000 atomic columns for both distributions.

Ge atoms in an atomic column.

We determine this value $\triangle\mu$ using the correlation between the amplitude coefficient and the Ge concentration. The determination of the thickness has to be accurate in order to determine an absolute number of atoms. In projection along the $[\bar{1}10]$-zone axis of the Si diamond structure, there are two atoms per unit column in one unit cell, *i.e.* one atom along a distance of $a_{\mathrm{Si}}\sqrt{2}$, with a_{Si} the Si lattice parameter ($a_{\mathrm{Si}} = 0.543$ nm). Then, the number of Ge atoms n_{Ge} per atomic column in the $[\bar{1}10]$-zone axis is related to the thickness t and the Ge concentration c_{Ge} by:

$$n_{\mathrm{Ge,\ 110}} = \frac{2 \cdot t \cdot c_{\mathrm{Ge}}}{a_{\mathrm{Si}}\sqrt{2}} \tag{4.4}$$

For a measured thickness of 9 ± 1 nm by PACBED, the expected Ge concentration is $c_{\mathrm{Ge}} = 4.27 \pm 0.38$ % for one Ge atom in the column corresponding to $\mu_0 = 1.15$. The presence of one Ge atom provides an average increase of the amplitude coefficient of 0.15 and then determines our step between two consecutive Gaussian functions.

The results of the fitting by the function $G(x)$ of amplitude distributions for the Si substrate and the Si spacer are summarized in Tab. 4.1. The linear combination of the Gaussian functions used for the fit is plotted with a black solid line in Fig. 4.20(a-b).

This fit provides then a way to obtain the distributions of amplitude coefficients corresponding to discrete number of Ge atoms (i = 0, 1, 2, 3...) in the atomic columns. In that way, the bump around amplitude coefficient of 1.2 and the tail of the curve

	Index i	Coefficient λ_i	μ_i	Ge concentration (%)
Si substrate	0	1.0	1.00	-0.02
Si spacer	0	0.765	1.00	-0.02
	1	0.130	1.15	4.27
	2	0.052	1.30	8.51
	3	0	1.45	12.78

Table 4.1.: Fitted values of the linear combination of the Gaussian functions in the Si substrate (one Gaussian function) and in the Si spacer (linear combination of four Gaussian functions)

for the Si spacer, due to the presence of Ge atoms can be fitted. The coefficients λ_i in the linear combination of Gaussian functions give the estimation of the ratio between the different populations of atomic columns with 0, 1, 2 and 3 Ge atoms. In the analyzed area of this example, the coefficient $\lambda_0 = 0.765$ indicates that the majority of the atomic columns does not contains Ge atoms. The coefficients $\lambda_1 = 0.130$ and $\lambda_2 = 0.052$ indicate that the tail of the amplitude distribution is due to the presence of one or two Ge atoms per atomic columns in the Si spacer, respectively and no column have 3 Ge atoms as $\lambda_3 = 0$. This analysis on histogram of amplitudes gives a complementary information to the Ge concentration value, by describing the distributions of atomic columns having a given number of Ge atoms.

We can apply this analysis to describe the Ge concentration profiles which has been extracted from the quantification of the HAADF image shown in Fig. 4.19(b) and plotted in Fig. 4.21. The profiles have been averaged over different width: one atomic column (blue dots), a band of 2.5 nm in width (green square) and 5 nm (red diamond).

Large variation on the Ge concentration profile can be seen if the integration width is low (0.12 nm) in comparison to the profiles with larger width. As mentioned previously, the HAADF signal of a given kind of atomic column can be assumed to follow a Gaussian distribution. Averaging over a width of several atomic columns significantly reduces the statistic variation, as demonstrated by the improved statistics of the 2.5 and 5 nm width averaged profiles (green square and red diamond, respectively). The mean value of the Gaussian distribution being the reliable Ge concentration, the profile averaged over a width of several nanometers provides an accurate measurement of the Ge concentration at each point of the profile. In the Si substrate, the statistical variation is of 1 % for the 5 nm width profile of Ge concentration. This points out the sensitivity of the quantification of HAADF signal using correlative analysis of HAADF and EELS signal. The asymmetrical shape of concentration profile already indicates the presence of surface segregation of Ge atoms during the growth, as it will be discussed in the next section. On the right-hand axis of the plot in Fig. 4.21(a), the mean number of

Ge atoms per atomic columns have been calculated for a specimen thickness of 10 nm. Since the mean number of Ge atoms per atomic column ranges from 0 to 12 atoms, it highlights the sensitivity of this method to probe low chemical compositions with high spatial resolution.

Histograms of the amplitude distributions are plotted in Fig. 4.21(b-d) for three areas localized in the Si spacer above the Ge QDs: (b) close to the Ge QDs layer, (c) in the middle and (d) at 5 nm above the Ge QDs. The three amplitude distributions were fitted as previously (Fig. 4.20) using Gaussian fitting. This analysis shows clearly the evolution of the population of the different kind of nanocolumns with regards to the distance from the interface. At these distances of the interface, the Ge composition is low and is mainly described by Si pure columns and few SiGe columns having only one or two Ge atoms. The weight of the second Gaussian function is always higher than the third one showing that the probability to have a column with only one Ge atom is higher. Their weight decreases respectively when moving away for the Ge QDs where the Ge concentration is very low. This technique enables then to describe the Ge concentration profile by quantifying the distribution of Ge atoms into the Si columns and gives then a more precise description of the segregation process.

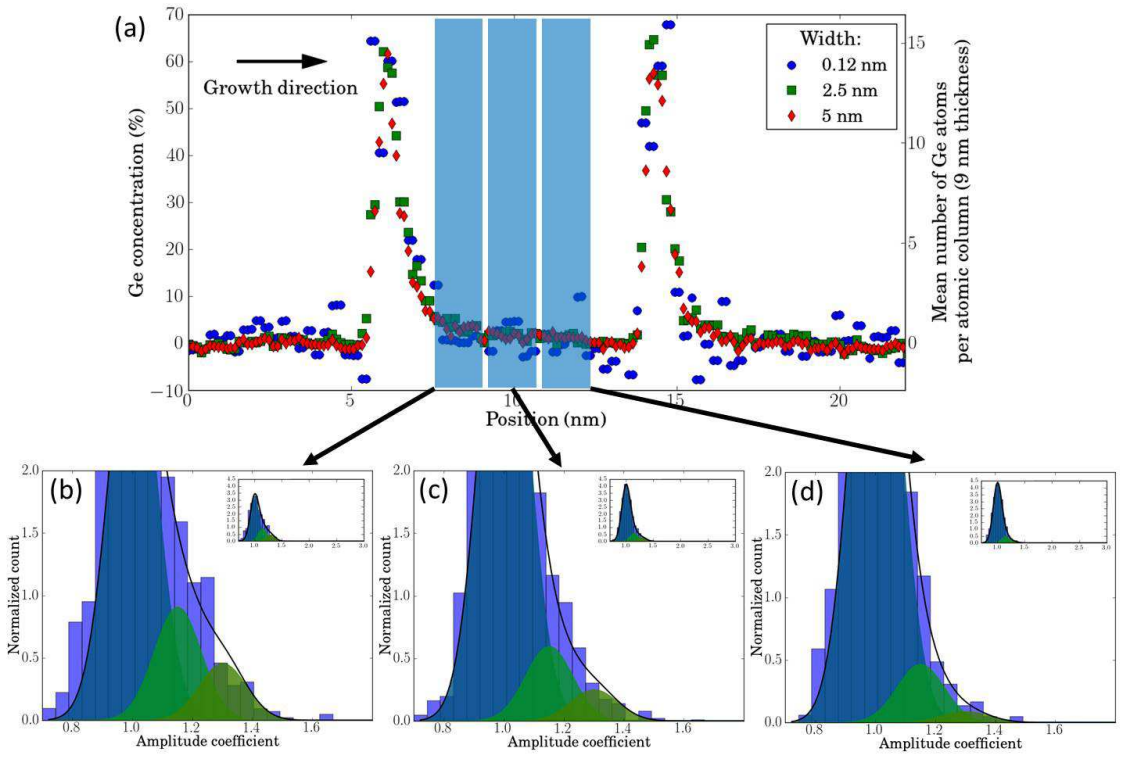

Figure 4.21.: (a) Ge concentration profiles obtained from the quantification of the HAADF image. The profiles have been averaged over a width of one atomic column (blue dots), 2.5 nm (green square) and 5 nm (red diamond). Zoomed amplitude distribution measured in three different area of the Si spacer as indicated in (a): (b) close to the Ge QDs layer, (c) in the middle and (d) further away. The integrated count of the distribution have been normalized to one. The linear combinations of Gaussian functions are plotted with a black solid line on the histogram. The general view of the histogram are plotted in the insets.

4.5. Direct measurement of Ge surface segregation in Si

Our comparison of the Ge concentration profiles obtained by EELS with that of SIMS, highlights the importance of using a technique providing high spatial resolution, *i.e.* at the atomic level coupled with a high sensitivity (see Fig. 4.13). This is clearly highlighted by the significant difference in the profile symmetry and shape (sec. 4.4.3.1) obtained between the EELS and SIMS Ge concentration profile.

This section aims now at describing the chemical profiles obtained by the quantitative chemical analysis presented above. The presence of Ge atoms has been clearly detected in the Si spacer and chemical profiles have been quantified. The features of these Ge chemical profiles are explained as being due to segregation processes and we are now discussing about the model associated with this phenomenon.

We used a phenomenological approach to describe the surface segregation of Ge in Si. Following the model provided by Muraki *et al.* [Mura 92], we assume that a certain fraction R of the Ge atoms subsurface layer N segregates on the top of the next layer $N+1$ on the surface. The fraction R is called segregation efficiency. The rest portion $(1-R)$ remains incorporated in the layer N. During the Si overgrowth on Ge, the Ge content x_{Ge} in the N^{th} layer can be then given by:

$$x_{Ge} = x_0 R^N \tag{4.5}$$

where x_0 is the nominal Ge content at the interface between the Ge layer and the Si overlayer and n is the number of the monolayer. Fig. 4.22 (a) shows the Ge concentration profiles obtained by EELS measurements across two Ge layers of nominal thickness of 4 MLs grown on Si(001) at 380 °C. The concentration profiles were measured on EELS SI by averaging over 15 lines, corresponding to a width of 4.5 nm. For clarity, the Ge concentration profiles are separated by an offset of 20 % in the y axis .

A zoom in the area delimited by dashed line in Fig. 4.22(a) is plotted in Fig. 4.22(b). The interface Si/Ge is more abrupt than the Ge/Si. This can be due to the Ge surface segregation mentioned previously (see Fig. 4.21) but also due to the beginning of relaxation that take place at 4 ML. As can be observed in Fig. 4.19(b), the Ge/Si interface is rough: the thickness of the Ge QDs layer change from 3 ML in the thinner area to 6 ML in the thicker area (1 ML corresponds to one dumbbell). To exclude the effect of the begin of relaxation of the Ge/Si interface, the surface segregation have been fitted from 5 ML after the Si/Ge interface. The fitted area is indicated by a filled blue square in Fig. 4.19(b). The fitted models and their corresponding experimental data are plotted in Fig. 4.23 with lines and dots, respectively.

From the fit performed on 16 Ge concentration profiles (8 profiles are shown here), we obtained a value for the segregation efficiency of $R = 0.72 \pm 0.01$. The fit quality determined by the residual w (see sec. 4.4.4) indicates a fair fit quality since $6.6\% \leq w \leq 16\%$.

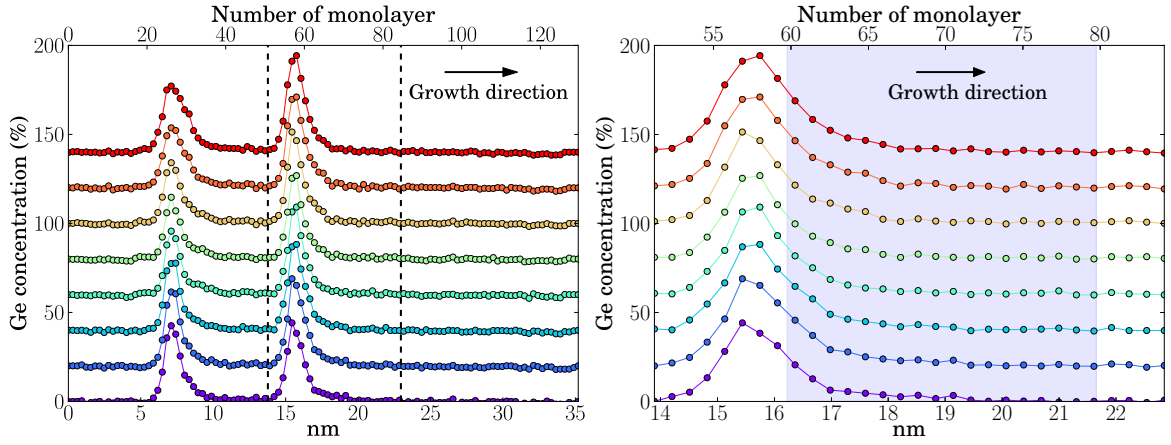

(a) Ge concentration profile (b) Zoom on a Ge QDs layer

Figure 4.22.: (a) Ge concentration profiles across two layer of 4 ML Ge grown on Si(001) substrate obtained by EELS measurements. (b) Zoomed area taken in the region delimited by the dashed lines in (a). The blue filled square indicates the experimental data used for the fit. For clarity, the Ge concentration profile are separated by an offset of 20 %.

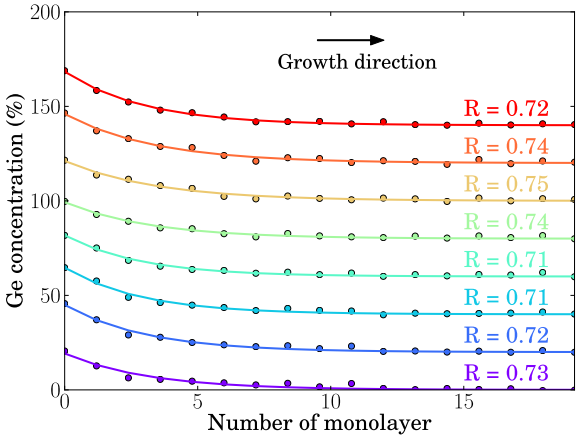

Figure 4.23.: Experimental data (dots) and fitted model (lines) of surface segregation profile of Ge in Si. For clarity, the Ge concentration profile are separated by an offset of 20 %.

4.6. Ge(Mn) quantum dots

In this section, we will first study the growth of large Ge QDs as compare to those of the previous section, which in fact correspond to larger nominal amount of Ge deposited on Si. It was described at the beginning of this chapter that there is a transition from a 2D layer by layer mode to a 3D island mode in order to reduce strain. We will next discuss the incorporation of Mn in this Ge QDs. We mentioned before that segregation phenomena in non-equilibrium growth methods, such as the MBE technique, are related to the surface energy of the forefront growth layer. Following this idea, we will intend to change the growth equilibrium in order to achieve the incorporation of Mn in strained Ge, such as Ge QDs.

4.6.1. State of the art of Ge(Mn) quantum dots

In the last few years, several groups reported on the formation of GeMn QDs and their associated magnetic properties. Incorporation of Mn in Ge QDs was firstly tried with ion implantation. Ion implantation creates a lot of defects in the crystal structure and the crystalline recovery was usually performed by post-annealing. This post-treatment generally results in the formation of undesirable metallic precipitates, such as Ge_3Mn_5 or Ge_8Mn_{11} precipitates [Chen 07, Ko 08, Yoon 10]. This technique is thus not appropriate for the fabrication of GeMn QDs for spintronics applications. The formation of GeMn QDs grown by MBE has been achieved recently [Xiu 10, De P 12, Kass 12b]. Concerning the magnetic properties, the most striking result is first the observation of room-temperature ferromagnetism in Ge(Mn) QDs and the electric-field-controlled ferromagnetism of these QDs [Xiu 10]. However, the magnetic properties was not reproduced by other groups who reported on formation of GeMn QDs grown by MBE. De Padova *et al.* [De P 12] observed the formation of $Mn_5Ge_1Si_2$ precipitates which exhibit ferromagnetic behavior with a Curie temperature of ∼225 K . Kassim *et al* [Kass 12b] reported Mn solid solutions in Ge/Si (001) QD hetero-structures. Their TEM investigations show that Mn-rich compounds are formed close to the Ge QD with back-diffusion in the Si substrate. They did not observe robust room temperature ferromagnetism, although their TEM observations are similar to those of Xiu *et al* [Xiu 10].

Fig. 4.24 reviews the TEM investigations reported in [Xiu 10, De P 12, Kass 12b]. In Xiu *et al.* and Kassim *et al.,* the presence of Mn in the Ge QD was confirmed by EDX analysis or EELS mapping and Mn back diffusion was observed (Fig. 4.24(a) and (b)). Kassim *et al* performed a more detailed TEM study of the Ge QD underlying Mn-rich areas and observed Moiré patterns which were interpreted as the formation of silicide phases (Fig. 4.24(b)). The formation of $Mn_5Ge_1Si_2$ precipitates was demonstrated by

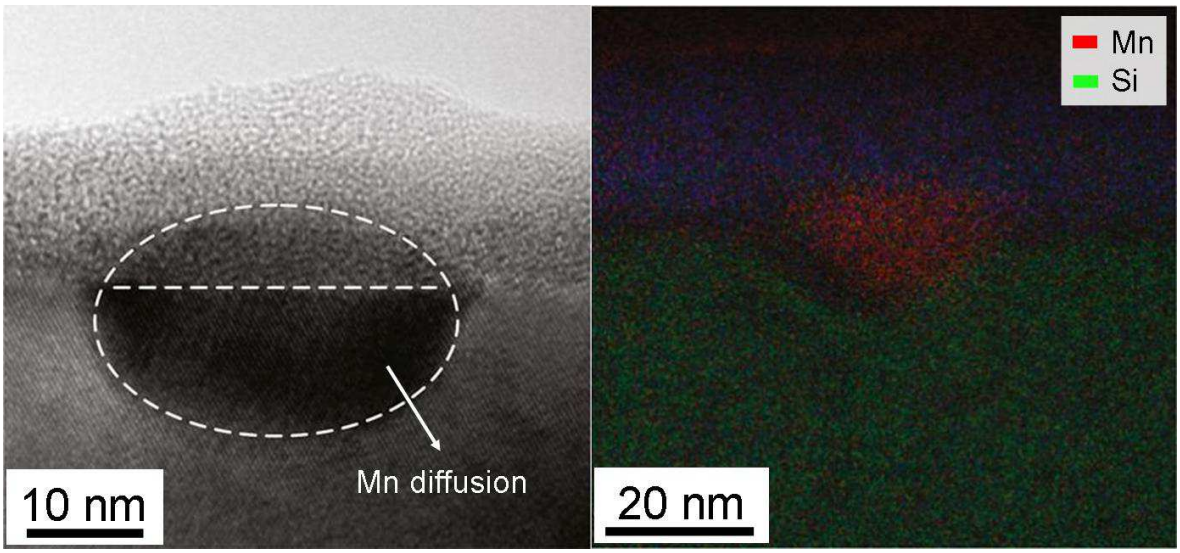

(a) Xiu et al. 2010

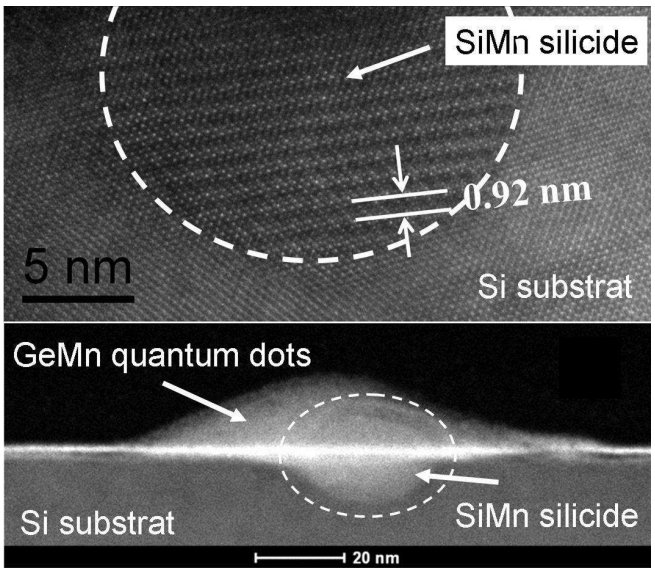

(b) Kassim et al. 2012

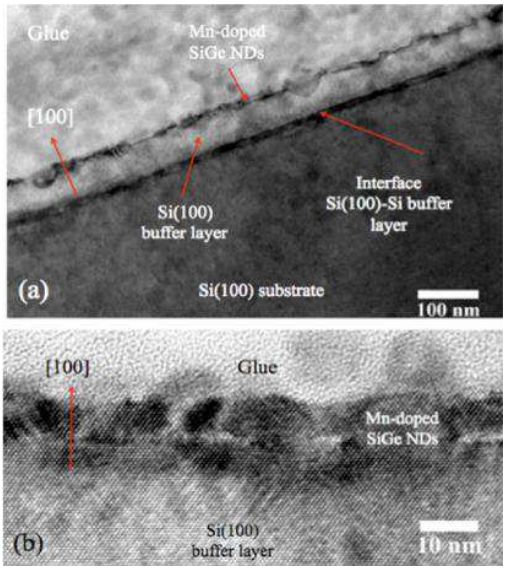

(c) De Padova et al. 2012

Figure 4.24.: TEM observations of GeMn QD on Si(001) substrate. (a) Left: HRTEM image of a GeMn QD. (a) Right: EDX mapping of a GeMn QD, where Mn and Si are red and green, respectively. The element associated to the blue color is not explicitly specified in the *Nat. Mat.* publication, but it seems to correspond to Al_2O_3. (b) Top: HRTEM images showing Moiré pattern corresponding to silicide precipitates in the Ge QD underlying Mn-rich area. (b) Bottom: HRSTEM image showing the position of the silicide precipitate with respect to the Ge QD. (c) Top: TEM image of the overview of the specimen. (c) Bottom: HRTEM image showing the Mn_doped SiGe QD. Adapted from [Xiu 10, De P 12, Kass 12b] for (a), (b) and (c), respectively.

EXAFS measurements and the precipitates were observed in HRTEM investigations, as shown in Fig. 4.24(c).

These papers indicate that the fabrication of GeMn QDs in Si is not well controlled and understood at the moment. All these studies noticed the same feature: Mn atoms always trend to diffuse making the incorporation difficult and giving rise to the question about the dilution of Mn in strained structures, such as the Ge QDs considered here. Achieving the incorporation of Mn in Ge QDs involves significant control MBE growth and a understanding of the growth mechanisms.

4.6.2. Experimental results

4.6.2.1. Growth of Ge quantum dots

Fig. 4.25 presents the growth transition from 2D to 3D inherent to the Stranski-Krastanov growth of Si(001)/Ge/Si. These HAADF-HRSTEM images corresponding at three samples with nominal Ge thickness of 3 ML, 4 ML and 6 ML Ge on Si(001) are shown on Fig. 4.25(a,b,c) respectively.

- For 3 MLs nominal thickness Ge has a pseudomorphic growth on the Si substrate, *i.e.* the in-plane lattice parameter is the same than that of the Si substrate. This means that due to the lattice mismatch between Si and Ge, Ge in-plane lattice is in compression (smaller lattice parameter than the bulk cell). It results then that the out-of-plane lattice parameter is in expansion. The Ge layer remains fairly flat and homogeneous in this regime, as well as free of defect, such as dislocations to relax the structure.

- At 4 MLs of nominal thickness of Ge, the WL starts to relax by creating thickness modulations, *i.e.* roughness as described before: this is the first step toward the formation of islands.

- The increase of Ge quantity up to 6 MLs of nominal thickness, implies the formation of larger QDs as shown in Fig. 4.25(c). These QDs have a relatively large volume with a basal surface with a diameter reaching several tens of nm and a height of about 10 nm. They are only very few such large QDs if the Ge nominal thickness is low. In the standard growth conditions used here (temperature growth of 380 °C and a Ge flux of 0.1 ML/s), the Ge QDs are domes with {112} and {112} facets. The base plane size ranges from 50 to 70 nm and some of the QDs are plastically relaxed, *i.e.* some dislocations have been observed.

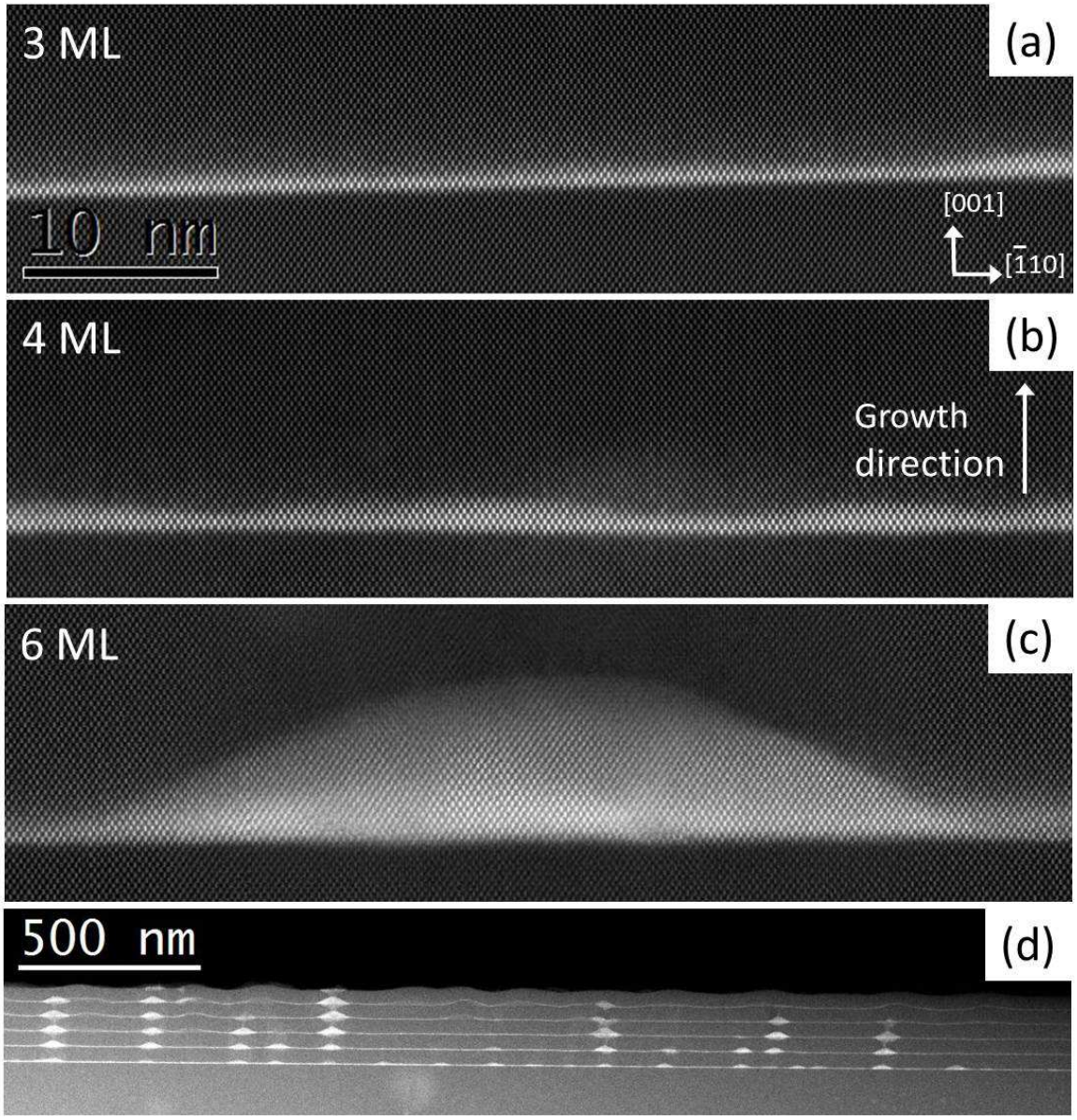

Figure 4.25.: Transition from 2D to 3D growth mode. HAADF-HRSTEM images of (a) 3 ML, (b) 4 ML and (c) 6 ML Ge grown at a temperature of 380 °C. (d) General view of the 6 ML Ge shown in (c).

4.6.2.2. Growth of Ge(Mn) quantum dots

The incorporation of Mn in these Ge QDs or WLs has been analyzed by STEM-EELS mapping. Let us starts with the study of Ge(Mn) QDs consisting of an equivalent nominal thickness of 6 ML grown at 380 °C on a Si(001) substrate. These conditions are similar to those reported in [Xiu 10, De P 12, Kass 12b]. A typical Ge(Mn) QD is shown in HAADF-HRSTEM (Fig. 4.26(a)). Fig. 4.26(b) (c) and (d) show the EELS maps obtained from SI technique acquired using Mn $L_{2,3}$ (640 eV), Ge $L_{2,3}$ (1217 eV) and Si K (1839 eV) edges, respectively. The Ge and Mn maps evidence the strong segregation of the Mn and instead of having Mn incorporated in the Ge QD, large Mn rich precipitates are observed. Fig. 4.26(e) shows that there are some region of the precipitates that does not overlap with the Ge QD. In these area, no Ge was measured demonstrating that these precipitates are Ge free. Since the thickness of this area estimated by EELS is 55 nm, we are observing an overlap of the Si matrix with the QDs (Fig. 4.26(d)). Nevertheless, the fact that the decrease of Si signal in the area of the precipitates is small indicates that the precipitates contain Si. Moreover, it is not possible on this view to conclude on the exact location of the Mn-rich area with respect to the QDs along the [110] direction (electron beam direction).

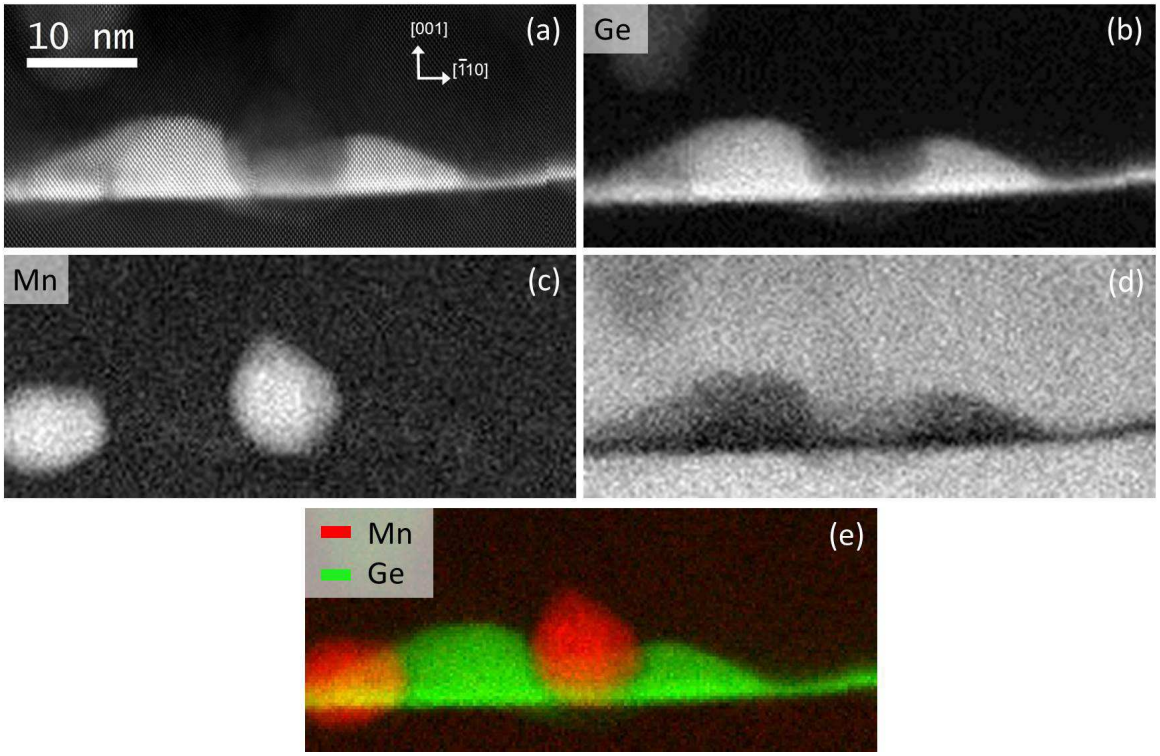

Figure 4.26.: Cross-section EELS analysis a Ge(Mn) QD. (a) HAADF-HRSTEM images in the [110]-zone axis acquired simultaneously than the EELS SI. (b) Ge map, (c) Mn map and (d) Si map obtained from the EELS SI. Ge (green) versus Mn (red) composite map. PCA denoising was performed with five components.

To provide better insight on the spatial location of these Mn-rich areas, one layer of Ge(Mn) QDs (6 ML) has been grown on a Si substrate with the same growth conditions, and the STEM-EELS observation were performed in plane view geometry, *i.e.* along the [001]-zone axis. An amorphous Si capping has been deposited on top of the layer in order to protect the Ge(Mn) QDs during the TEM sample preparation. Fig. 4.27 (a-b) show large field of view BF- and HAADF-STEM images.

Since the Ge QDs have a higher mean atomic number and the specimen thickness is locally thicker than the Si substrate in between (area between the QDs), the Ge(Mn) QDs appear as bright squares in the HAADF-STEM image. In the BF-STEM images, the Ge QDs exhibit Moiré patterns due to diffraction effects caused by strain relaxation. Fig. 4.27(c-f) show the results obtained from EELS analysis. Two Ge(Mn) QDs can be recognized on the HAADF image (Fig. 4.27(c)) presenting the area of the SI analysis. The Ge and Mn maps shown in Fig. 4.27(d) and (e) respectively, evidence the strong segregation of Mn atoms to form Mn-rich precipitates as shown in the cross section view (Fig. 4.26).

The plane view provides an additional information by allowing the localization of these Mn rich precipitates and the observation of the shape of these nanostructures. From Fig. 4.27(d) it is clear that the shape of the Ge QD is no longer an homogeneous dome as it is for pure Ge QD on Si, but exhibits now a hole in the middle or at the border, keeping a square base plane. This hole in filled with a Mn rich precipitate as evidence by the superimposition of the two Ge and Mn maps (Fig. 4.27(f)). The Ge map points out that the Mn-rich precipitates does not contain Ge, whereas the Si map indicates a slight increase of the Si signal at the location of the Mn-rich precipitates. This evidences that the Mn-rich areas are SiMn compounds.

Due to the 3D geometry of these nanostructures, it is very difficult to accurately determine the stoichiometry of this Mn-rich areas. The EELS quantification using Hartree-Slater partial cross-section could provide the absolute number of atoms N (in atom/nm^2) at each position following Eq. 2.45. Assuming a particular geometry it could be possible to determine the stoichiometry but we showed previously that the Hartree-Slater cross-section of Ge and/or Si gives an error up to 25 % in the quantification of the Ge concentration. The k factor approach provides a concentration between two elements. Since the measured signal comes from a overlap of the Si substrate, the Ge WL and/or the Mn-rich regions, it is hazardous to determine the stoichiometry of this Mn-rich areas with the concentration of Ge, Mn and Si.

The STEM-EELS observations unambiguously identify the Mn-rich areas that can be seen in the BF-STEM image in Fig. 4.27(a). White arrows indicate some of these Mn-rich areas on the BF image. On this large field of view we can notice that the Mn-rich precipitates are mainly located on Ge QDs but some of them can be found at some places where there is no Ge QDs, as shown in the middle of the BF-STEM image in Fig. 4.27(a).

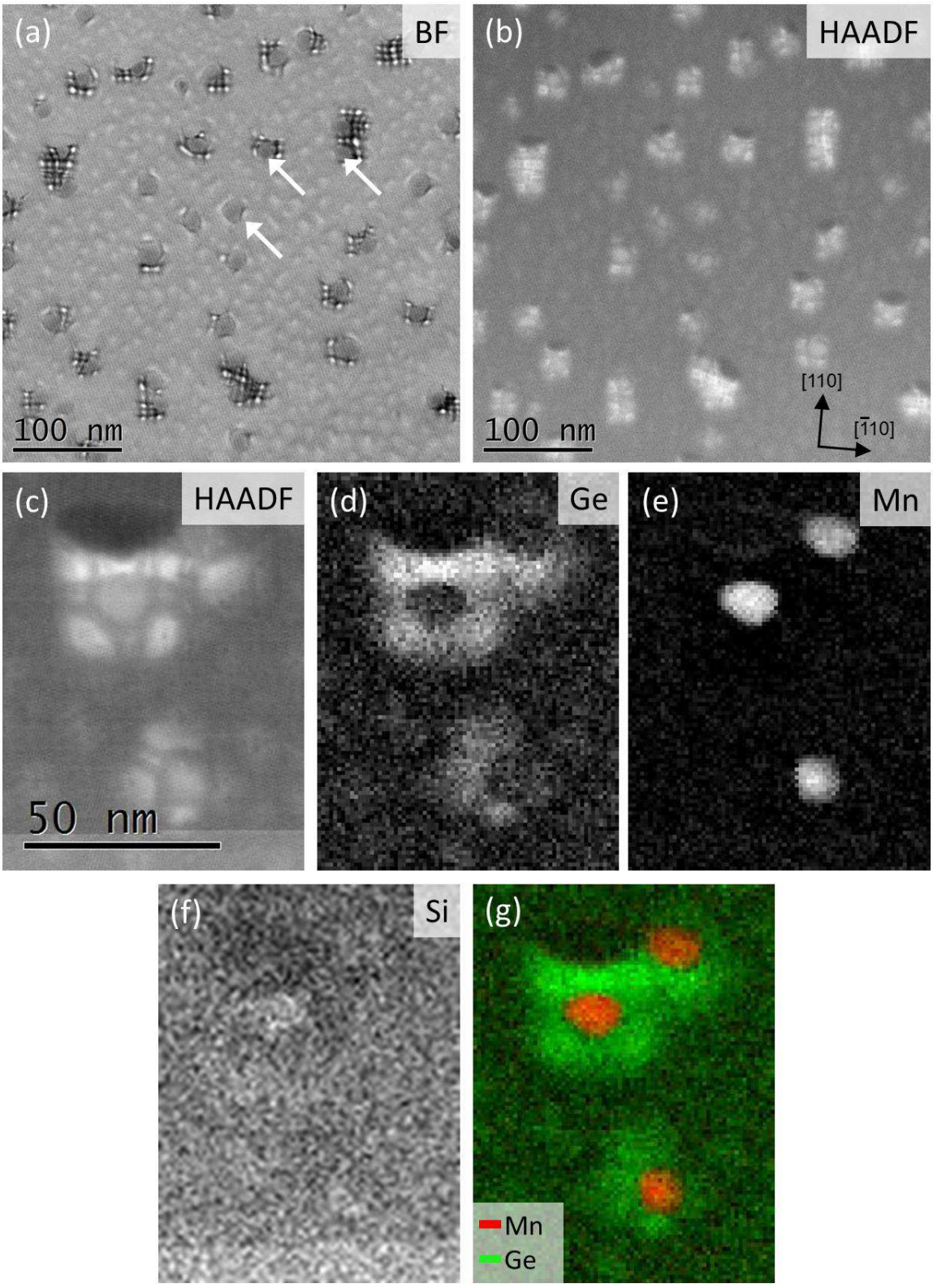

Figure 4.27.: (a) BF- and (b) HAADF-STEM images in the [001]-zone axis of one Ge(Mn QDs layer grown on Si substrate. (c-f) Plane-view EELS analysis of two Ge(Mn) QDs. (c) HAADF-STEM image acquired simultaneously than the EELS SI. (d) Ge map (e) Mn map and (f) Si map obtained from the EELS SI. (g) Ge (green) versus Mn (red) composite map. PCA denoising was performed with three components.

4.6.2.3. Growth of Ge(Mn) wetting layers

In the previous section, we demonstrated that a strong lateral segregation of Mn occurs during the MBE growth of Ge(Mn) QDs at standard growth temperature.

Fig. 4.28 shows a STEM-EELS observation of a specimen consisting of an heterostructures made of four Mn-doped Ge WLs with a thickness of 3 nm and separated by 5 nm of Si spacer. The Mn content is 6 % in the four layers. The WLs appear with a bright contrast on the HAADF image (Fig. 4.28(a)). Ge, Si and Mn chemical profiles recorded along the two green vertical and horizontal arrows in Fig. 4.28(a) are shown in Fig. 4.28(b) and (c), respectively.

The vertical profile (labeled 1) crosses the WL along the growth direction. Modulations of the Ge and Si profiles clearly demonstrate the presence of the multilayers. Nevertheless Mn is detected all over this profile implying that Mn is present even in Si even if the Mn was only co-evaporated with Ge. The horizontal profile (labeled 2) shows that the Ge content is not higher in the Mn-rich area than in between the WLs. These profiles evidence the presence of a Mn-rich areas, which are attributed to SiMn precipitates. Moreover, no Mn was found outside the SiMn precipitates and in particular no Mn incorporates in the Ge WL, *i.e.* Mn content is less than 1 %, which can be considered as an upper estimation of the detection limit of our experimental set-up here. Moreover, the deformation of the Ge WL visible in the HAADF image and indicated by dashed arrows (Fig. 4.28(a)) evidences a slight perturbation of the front growth. This perturbation can be associated to the formation of the SiMn precipitate during the growth.

To provide a better understanding of this growth process we grew another sample containing a unique GeMn WL of equivalent nominal thickness of 3 ML grown at a substrate temperature of 380 °C. HRTEM cross section and plane view observations of this specimen are shown in Fig. 4.29. HRTEM gives rise to diffraction contrast which allows easy identification of the SiMn precipitates. Moiré fringes observable on the cross-section HRTEM images, inform about the presence of a structure which is not isostructural to Si diamond. The insets in Fig. 4.29(a) shows the power spectra of a precipitate area and Si substrate area. Additional spots are observable for SiMn as compared to Si. The bright-field TEM images give an overview of the distribution of the distances between the precipitates. This distribution is rather broad and ranges from 10 nm to 100 nm. We did not attempt to unambiguously identify these precipitates structure and composition, since they are not of high interest for this study. The important result is that we did not succeed using this growth temperature to incorporate Mn in the Ge WL and instead obtained the formation of some Mn-rich precipitates.

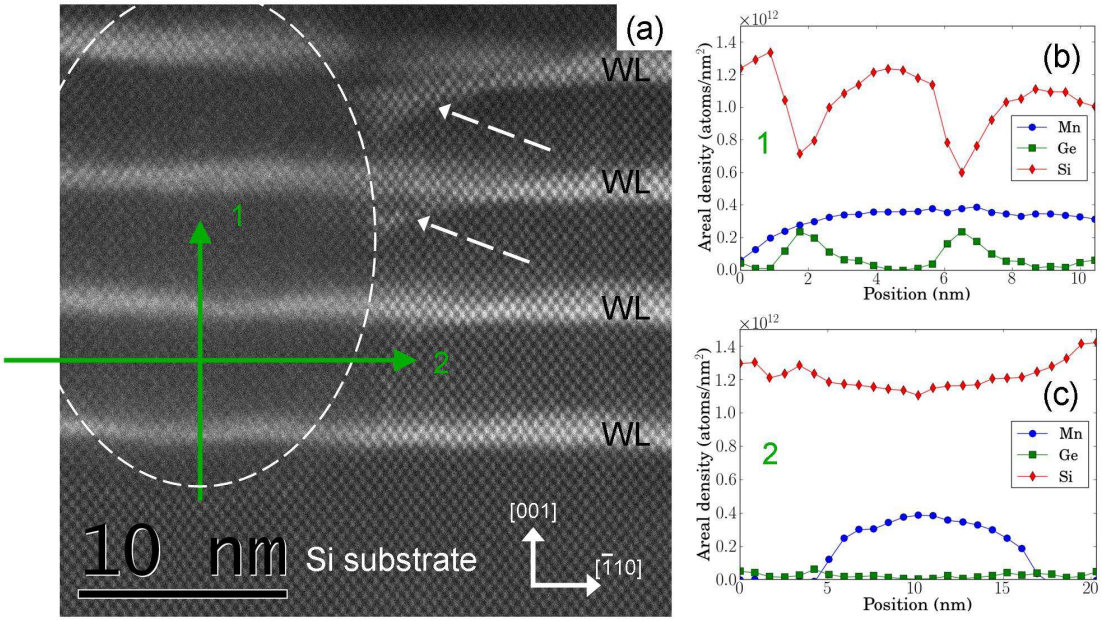

homogenous

Figure 4.28.: STEM-EELS observation of GeMn WL grown at temperature of 380 °C, showing the formation of SiMn precipitate. (a) HAADF image, on which a dash ellipse and the numbered green arrows indicate the position of a SiMn precipitate and of the EELS line scans, respectively. The white dash arrows indicate the deformation of the front growth due to formation of the SiMn precipitate (b) Ge, Mn and Si chemical profiles obtained along the vertical EELS line scan. (c) Ge, Mn and Si chemical profiles obtained along the horizontal EELS line scan. PCA denoising was performed with three components.

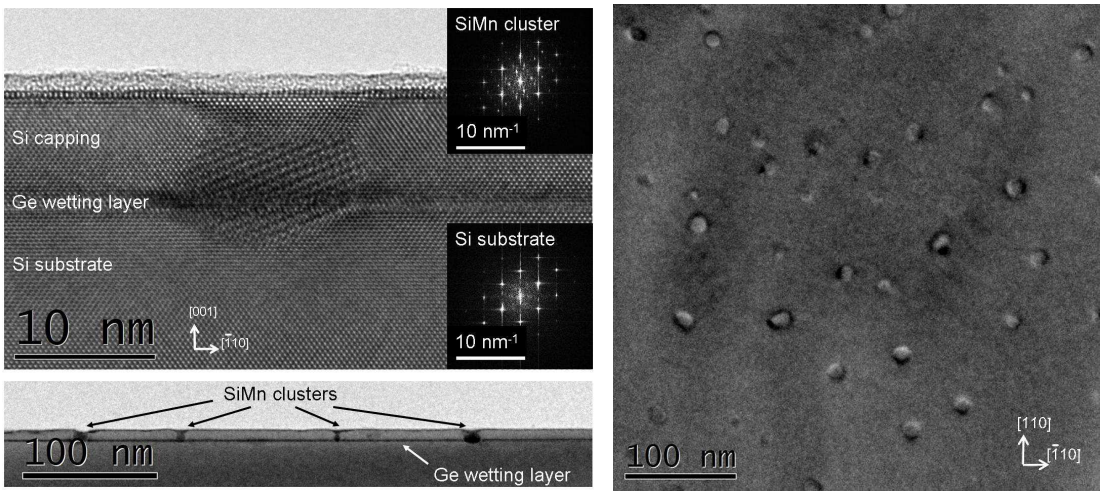

(a) Cross-section view (b) Plan view

Figure 4.29.: HRTEM observations of an unique GeMn WL. (a) Cross-section view images in [110]-zone axis showing SiMn precipitates, which can be recognized with the Moiré pattern on the top HRTEM image. The dark area on the bottom bright-field TEM image correspond to the Moiré pattern. The FFT of SiMn precipitates and the Si substrate are displayed in the insets. (b) Plan-view bright-field TEM image acquired in the [001]-zone axis shows the in-plane distribution of SiMn precipitates.

4.6.2.4. Low-temperature growth of Ge(Mn) wetting layers

The previous observations point out that co-evaporation at 380 °C of GeMn at the early growth of the WL leads to the Mn segregation during the growth and formation of SiMn precipitates instead of GeMn WL. This process is probably thermally activated and the reduction of the growth temperature should limit it. Then to achieve Mn incorporation in the Ge WL, Ge and Mn have been co-deposited at a temperature of 220 °C with the same Mn deposited content of 6 %. Fig. 4.30 shows a cross-sectional STEM-EELS observation of such specimen. The HAADF image in Fig. 4.30(a) shows 3 layers, the bottom one consisting of a 3 ML Ge deposited at the usual temperature (380 °C) and the 2 others consisting of 3 and 4 ML GeMn at lower temperature (220 °C). The first important point is that even at low temperature (220 °C) compared to usual ones for this kind of growth, we succeeded in growing crystalline and epitaxial Ge layers on Si (Fig. 4.30(b)).

The Mn and the Ge maps recorded at the positions indicated by the green square in Fig. 4.30(a) are shown in Fig. 4.30(c) and (d), respectively. In the upper layer grown at lower temperature, Mn is detected along the Ge WL but is not homogeneously distributed. This indicates that Mn still slightly segregate to form heterogeneous GeMn layer, but the segregation is much less than for higher temperatures.

These observations point out that Mn incorporation in Ge WL is possible without the formation of unwanted precipitates, such as the SiMn introduced during the growth of Mn-doped Ge WL at high temperature. To further study the Mn incorporation, we have grown other sample with different Mn contents, *i.e.* different Mn flux. Fig. 4.31 shows STEM-EELS observation of four Mn-doped Ge WLs. The two layers at the bottom were grown at 220 °C with a Mn content of 6 and 10 %, whereas the two top layers were grown at 380 °C with a Mn content of 6 and 10 %. The Ge and the Mn maps are shown in Fig. 4.31(b) and (c).

The formation of large Mn-rich precipitates is observed for the layers 3 and 4 grown at high temperature (380 °C). This is consistent with our previous observation in sec. 4.6.2.3. In the layers 1 and 3 less Mn is measured than in the layers 2 and 4, thus indicating that the Mn content incorporated in the Ge WL increase with increasing the Mn flux, *i.e.* the deposited Mn content. The comparison of layer 1 and 2 grown at low temperature and layer 3 and 4 growth at high temperature demonstrates clearly once again the stronger Mn segregation at higher temperatures. The HAADF image in Fig. 4.31(a) gives some insight on the crystalline quality due to the growth conditions. The first Ge WL has a good crystallinity but the quality of the next layers is degraded due to the perturbation of the front growth during the growth at low temperature for the layer 1 and 2, as mentioned previously. This highlights the difficulty of the growth of SiGe hetero-structures at low temperature.

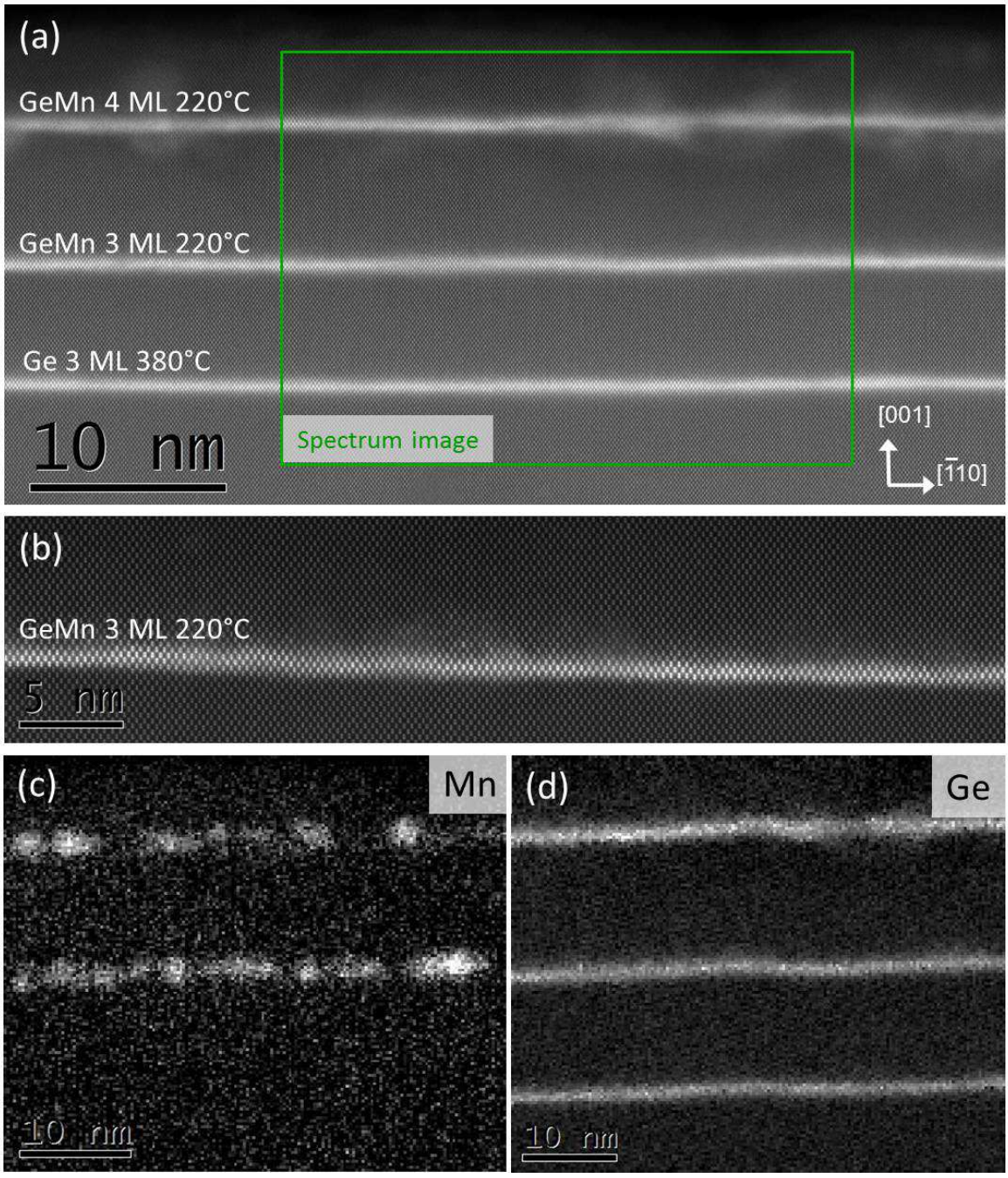

Figure 4.30.: Cross-sectional STEM-EELS observation of Mn-doped Ge WL growth at different temperature. (a) HAADF image of the three layers: the lowest is 3 ML Ge grown at 380 °C, the middle is 3 ML GeMn grown at 220 °C, the top is 4 ML GeMn grown at 220 °C. (b) High resolution HAADF image with high quality crystalline structure of the low temperature grown Mn-doped Ge WL. (c) Mn map and (d) Ge map obtained by EELS in the area indicated by a green square in (a). PCA denoising was performed with five components.

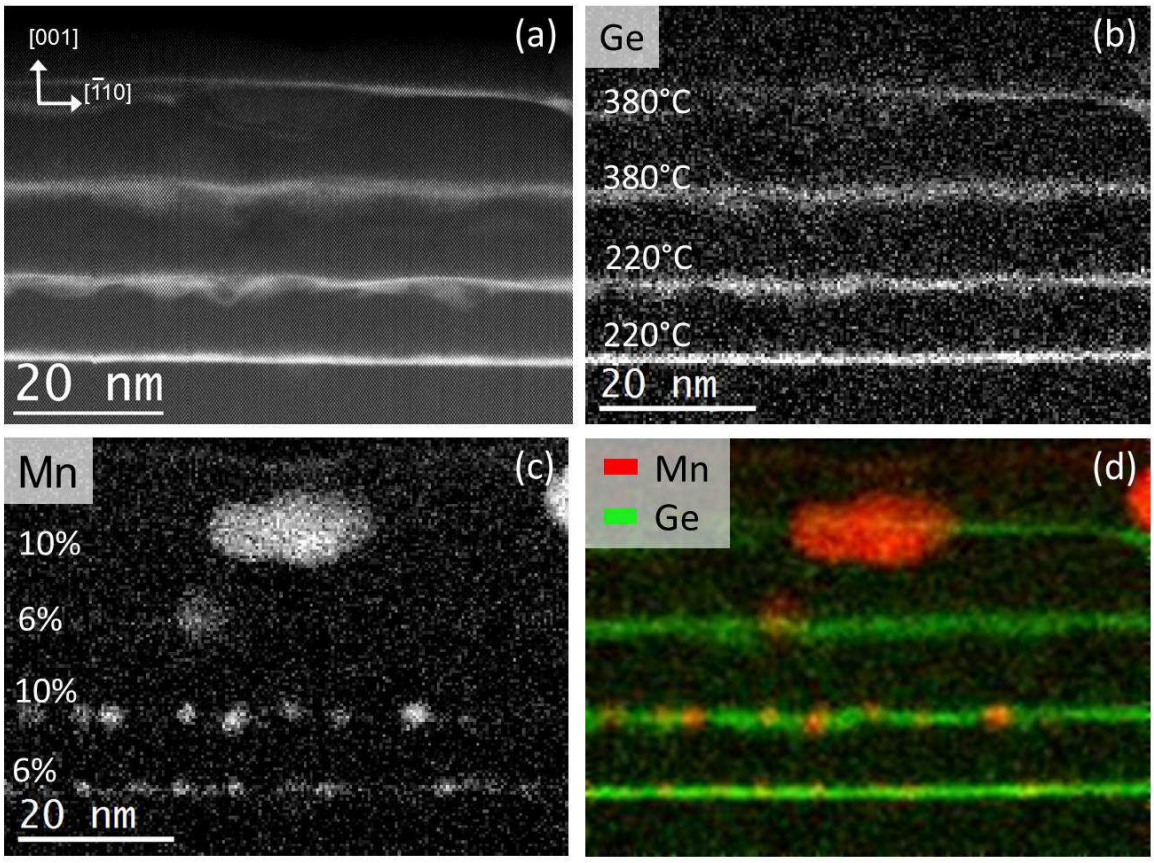

Figure 4.31.: Cross-sectional STEM-EELS observation of Mn-doped Ge WL growth at different temperature and different Mn concentration. (a) HAADF image of the four layers: the two lowest are grown at 220 °C with 6 and 10 % Mn nominal content, and the two at the top are grown at 380 °C with 6 and 10 % Mn nominal content. (b) Ge map and (c) Mn map obtained by EELS in the area indicated by a green square in (a). (d) Mn (green) versus Ge (red) composite map. PCA denoising was performed with five components.

The low growth temperature (220 °C) seems to be a good compromise to succeed in incorporating Mn in Ge QDs if the initial content of Mn is not too high. For 6 % of Mn, a GeMn layer of relatively good crystalline quality has been obtained with still some composition inhomogeneities within the GeMn WL. These inhomogeneities seem to contain more Mn if the nominal Mn content is higher (10 %) but we still obtained a good crystalline quality GeMn WL. As soon as the growth temperature reached (380 °C), the Mn segregation process is too important and Mn is not incorporated in Ge and large SiMn precipitates are formed.

4.6.2.5. Magnetic measurements

Typical magnetic measurements on Ge(Mn) WLs (4 ML) performed using SQUID are shown in Fig. 4.32. The different specimens considered here are: $Ge_{0.94}Mn_{0.06}$ WLs grown at high temperature (Fig. 4.32(a-b)), $Ge_{0.94}Mn_{0.06}$WLs grown at low temperature (Fig. 4.32(c-d)) and a Si substrate (Fig. 4.32(e-f)). The magnetic signals are plotted in emu (1 emu = 10^3 A·m^2). All the magnetization curves (Fig. 4.32(a,c,e)) look very similar for all the specimens, even the Si substrate. This clearly indicates that the measured magnetization can not be attributed to the Mn atoms in the Ge(Mn) layers. Magnetic measurements performed on Ge(Mn) QDs (6 ML) are very similar, and no difference has been observed. Two observations can be made from the temperature dependence of the magnetization. A 1/T parasitic paramagnetic signal coming from the Si substrate is visible below a temperature of 50 K. At higher temperature (> 150 K), the magnetic signal could come from ferromagnetic precipitates in the Si substrate.

Magnetic measurements in this system are very difficult. Indeed, the total amount of magnetic atoms in this system is small (10 % Mn in 6 ML corresponds to $2 \cdot 10^{14}$ Mn/cm^2) and the maximal sample size acceptable for the SQUID magnetometer used in this work is limited to 5 x 5 mm. Assuming an atomic moment of 3 μ_B/Mn and ferromagnetic interactions, the largest possible magnetic signal coming from Mn atoms is around 10^{-6} emu. This value is above the sensitivity of $\sim 1 \cdot 10^{-8}$ emu of the SQUID magnetometer, however it is challenging to detect such signal above the noise coming from the surroundings. The diamagnetic signal from a 5 mm x 5 mm x 500 µm Si substrate as the one used in this work is of $\sim 3 \cdot 10^{-4}$ emu, which is 100 times larger than the upper estimation of Mn magnetic signal given previously. The contribution of the ferromagnetic contaminants present in the Si is not negligible, since the magnetic signal is integrated over the whole Si substrate.

We remove a large part of the Si substrate by back-side polishing of the specimen. We observe a decrease of the magnetic signal at higher temperature (> 150 K), confirming our precedent hypothesis. However, by comparing the same specimen before and after polishing a large part of the substrate, we did not observe significant difference that could be attributed to the Mn magnetic atoms.

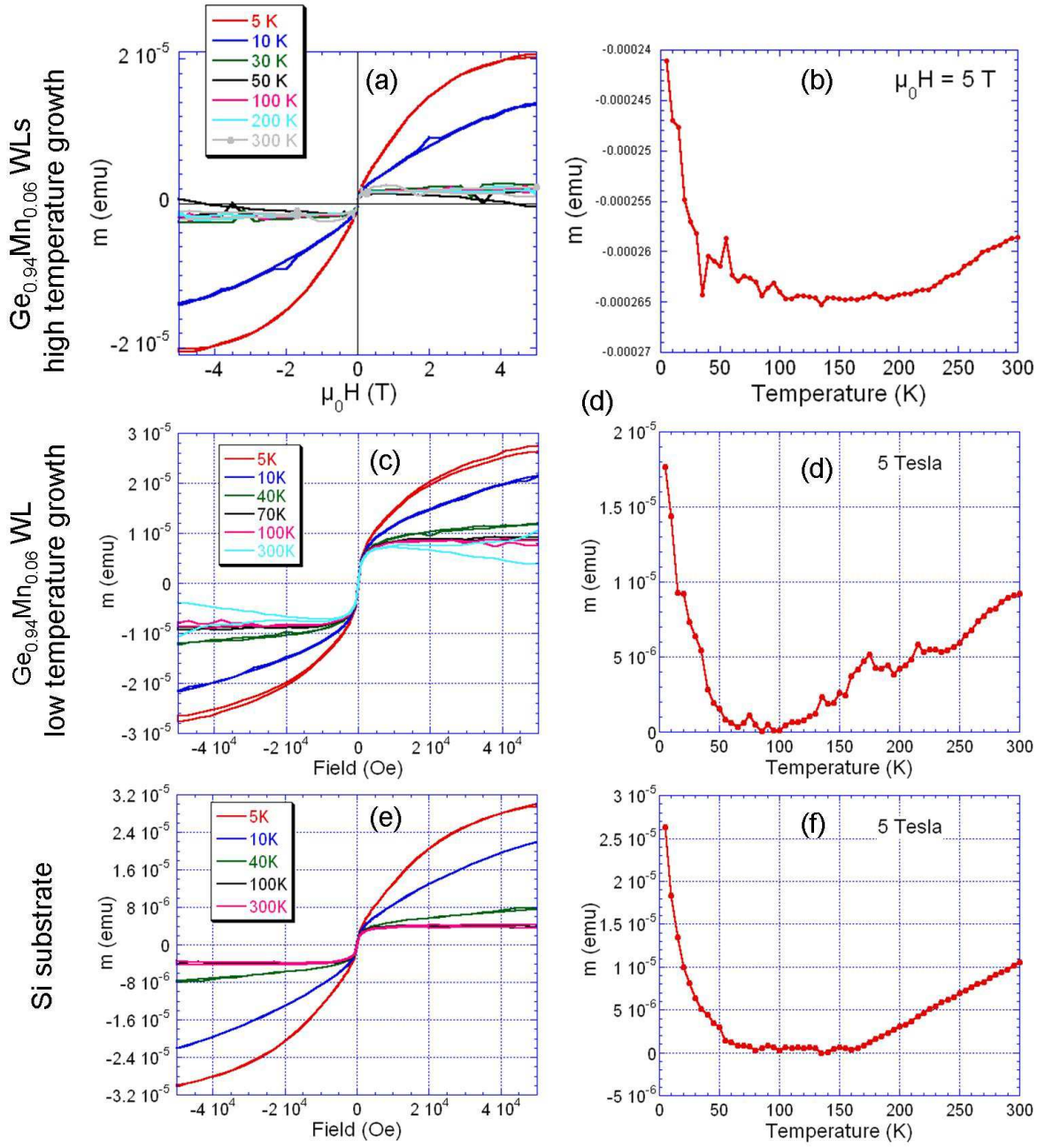

Figure 4.32.: Magnetic investigations using SQUID of different specimen: (a-b) $Ge_{0.94}Mn_{0.06}$ WLs (4 ML) grown at high temperature (380 °C), (c-d) $Ge_{0.94}Mn_{0.06}$ WLs (4 ML) grown at low temperature (220 °C) and (e-f) Si substrate. (a,c,e) Magnetization loop measured at different temperature. (b,d,f) Temperature dependence of the saturation magnetization.

4.6.3. Discussion

We started to investigated the Mn incorporation in Ge nanostructures by considering the case of Ge QDs consisting of 6 ML grown at a temperature of 380 °C in sec. 4.6.2.2. This growth conditions are similar to that of the works reported by Xiu *et al.* [Xiu 10] and Kassim *et al.* [Kass 12a]. The plane view and cross-section investigations clearly evidenced the strong segregation of Mn leading to the formation of SiMn precipitates. This observation is in good agreement with a general trend of the GeMn system: Mn strongly segregates [Jame 06, Li 07, Boug 06].

The experimental results reported here evidence that the co-deposition of Ge with Mn on Si(001) at a growth temperature higher than 380 °C leads to the formation of Mn-rich areas distributed homogeneously with an average distance between them of 70-100 nm. This can be explained by the large diffusion length of Mn atoms on Ge(001), which spans from a few nm at room temperature to several tens of nm at 220 °C [Kass 12a]. EELS measurements reveal that the Ge concentration in the Mn-rich areas is below the detection limits of EELS, *i.e.* less than 0.5 % in the experimental conditions used in this work. The Mn-rich areas can be then attributed to SiMn precipitates. We did not intend to identify the exact chemical composition and crystal structure of the SiMn precipitates since they do not exhibit interesting physical properties. These observations are in very good agreement with the very recent report of Kassim *et al.* [Kass 12a, Kass 12b, Kass 13], since strong lateral segregation of Mn and back diffusion of Mn in Si was observed in most of the cases.

It is known that in the GeMn system, the growth have to be performed at low temperatures, usually smaller than 150 °C, in order to avoid the formation of precipitates. Nevertheless lateral segregation are still observed and leads to the formation of nanocolumns, *i.e.* nanostructures parallel to the growth direction having a few nanometers in section. These GeMn nanocolumns will be considered more in details in the next chapter, but we already mentioned that that the nucleation of GeMn nanocolumns on Ge(001) substrate required a critical thickness of 4 nm to start [Devi 08]. This was explained by a subsurfactant epitaxial growth of the GeMn layers with Mn atoms occupying subsurface interstitial sites [Zeng 08]. It was argued that after the critical thickness the Mn concentration of the front growth is high enough, so that the system undergoes a 2D spinodal decomposition and forms Mn-rich nanocolumns. In this work, we intend to incorporate Mn in small Ge layer ($<$ 1 min) in order to prevent the lateral segregation observed in the case of thicker GeMn layers. However, a temperature growth of 380 °C leads to strong lateral segregation of Mn. This conclusion motivated the growth of Ge(Mn) WLs at lower temperatures (220 °C).

The growth of Ge(Mn) WLs at lower temperatures (220 °C) than the standard one allows to limit the lateral diffusion of Mn in the Ge WL. This is clearly evidenced

by the Ge and Mn maps obtained from EELS SI in Fig. 4.31, where two different Mn concentration (6 % and 10 %) and different growth temperatures were used. To increase the nominal Mn concentration in the Ge WL from 6 % to 10 %, the Mn flux is increased. This experiment clearly indicates that Mn incorporation into Ge and formation of precipitates is very sensitive to the surface diffusion length which increases with temperature and decreases when in-coming flux increases. However, epitaxial growth of SiGe nanostructures with good crystal quality at temperature lower than 200-300 °C is challenging. TEM observations shown in this work point out that the front growth can be disturbed and the surface can become rough. Since the integration of ferromagnetic semiconductors in devices requires a contact on the top of the layer, the growth of heterostructures with good crystal quality is mandatory. Progress is then necessary to improve the crystal structure at low temperature growth or to control the lateral diffusion of Mn.

From the structural and chemical observations reported by Xiu *et al.* and Kassim *et al.*, the Mn spatial distribution was ambiguous. The magnetic properties were attributed to the formation of Ge(Mn) structures, but no clear chemical or structural evidences were provided. The results of this work give more insight in the growth of SiGe(Mn) heterostructure: we found that the Ge(Mn) QDs grown in similar condition than Xiu *et al.* and Kassim *et al.* consist of Ge QDs and SiMn precipitates. Despite the very interesting magnetic properties demonstrated by Xiu *et al.* [Xiu 10], we did not achieve to reproduce their results, since the contribution coming from Mn atoms is very low and therefore very difficult to measure.

Finally, it is to emphasize that the Ge WL and Ge QD consist of SiGe compounds with maximum Ge concentration around 60 %. It implies that the magnetism of such SiGe(Mn) QDs could be then significantly different from that of the expected Ge(Mn) compounds.

4.7. Conclusion

This chapter reports on quantitative analysis of Ge and GeMn quantum dots in Si. The chemical distribution of each species (Si, Ge and Mn) were performed using HAADF and EELS imaging in HRSTEM mode in order to understand growth processes. The first part of this chapter described the methodological development of HAADF quantification we developed to get an accurate quantification of our samples. This method is based on the correlation of HAADF and EELS signals in order to quantify the amplitude of each individual atomic column on the HAADF images. Despite the relatively low atomic number difference between Si and Ge, aberration-corrected HAADF-HRSTEM performed in area thinner than 10 nm allows the observation of diluted

Ge atoms in Si. The HAADF signal of each atomic columns was measured using a combination of template matching method and fitting on the image. The statistical correlation of HAADF and EELS signal acquired simultaneously shows a linear relationship between these two signals in the range of composition between 0 and 50 % of Ge in Si. Using the fitted correlation between HAADF and EELS signals, the HAADF image can then be converted in Ge concentration. Since the visibility of a few Ge atoms as a function of a depth position in the atomic columns can be approximated to a Gaussian distribution, the Ge concentration on the HAADF image has to be measured statistically. It can be performed by averaging profiles or by fitting histogram of concentration (or amplitude) distribution with Gaussian functions. In the latter case, each Gaussian function corresponds to atomic columns containing different number of Ge atoms. Assuming a given specimen thickness, the separation between the different Gaussian function were calibrated using the fitted value of the linear correlation between the HAADF and EELS signal. Finally, the detection of Ge atoms in the Si spacer has been shown and quantified. It is explained as been due to surface segregation of Ge atoms in Si during growth. Note that this observation is only possible thanks to good sample preparation to get thin and flat area analyzed in order to obtain a sufficient visibility of the presence of one Ge atom in a Si atomic column. The Ge distribution in the Si spacer has been modeled with a two-states surface segregation model.

In the second part of this chapter, we investigated the Mn incorporation in the Ge QD. The growth of Ge(Mn) QDs or WLs at 380 °C leads to a strong lateral segregation of Mn. SiMn precipitates are then formed and the Mn concentration in the Ge QDs or WLs is below the detection limits of EELS (<1 % in our experimental conditions). This is in good agreement with the back-diffusion of Mn reported by other groups. We evidenced that this diffusion is due to the presence of SiMn precipitates. However, our observations does not support the formation of diluted magnetic semiconductors of Mn in Ge. Lowering the growth temperature at 220 °C allows to limit the lateral segregation of Mn in Ge WLs. The incorporation of Mn in Ge WLs was then achieved at low temperature growth. However due to the very low Mn content in the specimen (up to 10 % in a few GeMn MLs), it is very difficult to measure a magnetic signal that can be attributed to ferromagnetism induced by Mn atoms.

5. GeMn nanocolumns

Contents

Since the work published in 2001 and 2002 by Park *et al.* [Park 01, Park 02] on Mn-doped germanium films, the GeMn material has been intensively studied. Contrary to the so called diluted magnetic semiconductors (DMS), in which Mn atoms are uniformly distributed in the host matrix - the model system being Mn-doped GaAs [Maha 03]- in GeMn grown on Ge(001), Mn atoms segregate and form Mn-rich nanostructures [Jame 06, Li 07, Boug 06, Boug 09, Devi 07]. The driving force for the study of the physical properties of GeMn is the ferromagnetism observed in such highly disordered systems. In GeMn, structural and magnetic properties strongly depend on the growth conditions. In order to incorporate Mn into Ge, the growth has to be made at very low temperature usually lower than 150°C. This explains why GeMn films are mainly grown by Low Temperature Molecular Beam Epitaxy (LTMBE).

In the first part of this chapter, structural and chemical investigations of GeMn nanocolumns (NCs) are presented. This TEM work is part of larger investigations (atomic simulations, EXAFS, X-Rays diffraction, magnetic measurements, ...) in the laboratory

performed to understand the structure and chemistry of these Mn-rich NCs and make the link to their magnetic properties. Atomic structure inside the nanocolumns but also their morphologies, shape, distribution and interface properties are important features. TEM imaging and STEM have been used but also image simulations of atomic models from numerical simulations were performed to get a better understanding of this remarkable ferromagnetic GeMn phase. The second part of this chapter is focused on the study of GeMn NCs in a GeSn matrix instead of Ge pure matrix. This has been done in order to investigate the effect of strain on the structures and the magnetic properties of the nanocolumns.

5.1. State of the art

Many groups, involved into the research on GeMn were confronted to phase separation during the growth. In most of the cases, the Ge_8M_{11} and Ge_3Mn_5 phase precipitates were found. Between 2005 and 2010 different groups reported on the formation of elongated Mn-rich regions in Ge matrix exhibiting ferromagnetic behavior. The striking characteristic of these report is the absence of intermetallic compounds and the attribution of ferromagnetic properties to an unknown Mn-rich phase.

Generally, the morphology of the columnar features observed by TEM were significantly different: Sugahara *et al.* observed amorphous columnar Mn-rich feature [Suga 05], Bougeard *et al.* reported coherent Mn-rich cubic "string-of-pearls"-like object [Boug 06], the previous work Jamet *et al.* evidenced continuous Mn-rich NC [Jame 06], Li *et al.* reported similar GeMn NC [Li 07]. Depending on the growth conditions, these Mn-rich nanostructures appear in cross section HRTEM images as spherical precipitates, elongated structures looking like cigars, or almost continuous nanocolumns, parallel to the growth direction having few nm in section. The Curie temperature (T_c) of GeMn grown by LTMBE also depends drastically on the growth parameters. In most of the reports, the T_c of GeMn nanostructured films was found to be around 150 K [Boug 06, Devi 07]. These structure are usually intermetallic and metastable [Devi 08]. The formation of NCs is usually explained by a combination of 2D growth mode with a spinodal decomposition [Sato 05]. Their lateral size ranges from 2 to 7 nm and they are oriented along the growth direction. This system is investigated in Grenoble since 2006 [Jame 06] and Fig. 5.1 illustrates the significant changes of the NCs with changing the growth temperature [Devi 07].

At temperature lower than 120 °C, the NC are fully strained by the Ge matrix. Between 120 and 145°C relaxed or partially relaxed ferromagnetic NCs are formed. Increasing the temperature leads to the formation of amorphous NCs and then Ge_3Mn_5 precipitates incoherent with the Ge matrix. The size and the density of the NCs increase

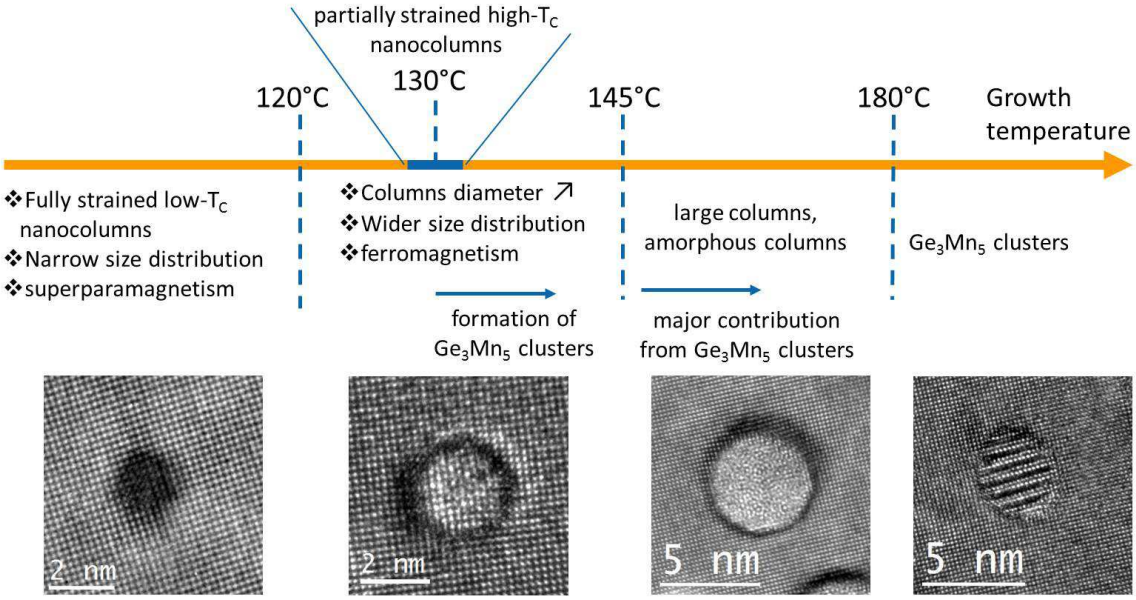

Figure 5.1.: Evolution of the GeMn NCs as a function of the growth temperature. Below a temperature growth of 120°C the NC are fully strained by the matrix. Between 120 and 145°C relaxed ferromagnetic NC are formed. Increasing the temperature leads to amorphous NCs and Ge_3Mn_5 incoherent precipitates. Each kind of NC is illustrated by a corresponding HRTEM image in [001]-zone axis (plane view). Adapted from [Devi 08].

by increasing the growth temperature and the nominal Mn concentration, respectively. More precisely a linear dependence has been found between the volume fraction of the NCs and the nominal Mn concentration for the different growth temperature [Devi 07].

Usually, the magnetic properties were investigated by superconducting quantum interference device (SQUID) and the structural properties by TEM or x-ray scattering techniques. Li et al. observed some degree of disorder with HAADF-STEM in 2 nm NCs [Li 07]. Atom probe tomography (APT) was performed on the "string-of-pearls"-like object [Boug 09]. They observed Mn concentration variation along the growth direction and strong structural disorder. Based on HRTEM observations of NCs with a diameter of 1-2 nm, they concluded that the structure is amorphous.

Rovezzi et al. performed Extended X-ray-absorption fine-structure spectroscopy (EXAFS) on similar specimen than those studied in this work and obtained spectra difficult to interpret [Rove 08]. Finally, they could fit their spectra with a structure similar to one of the building blocks in the Ge_3Mn_5 structures (Ge3-Mn tetrahedron).

The crystalline structure of GeMn NCs was also investigated using grazing incidence x-ray scattering [Tard 11]. The grazing incident geometry was chosen in order to maximize the scattering from the top layer and minimize that of the substrate. No clear sign of a crystalline phase different from Ge diamond could be observed in GeMn layers free from intermetallic precipitates (Ge_3Mn_5).

To summarize, synthesis of homogeneous GeMn films appears to be a very difficult task. There is always some inclusions: either known metallic compounds or unknown phases. They contain high concentration of Mn atoms and account for the ferromagnetic properties. The growth temperature is a key parameter that governs the crystalline structure, magnetic and electronic properties of the GeMn films. During our work, we focused on the study of the relaxed NCs since they have the most interesting ferromagnetic properties. The techniques presented above are mainly broad-beam techniques and the measurements are averaged over large volumes of the materials. For inhomogeneous sample as the GeMn layers, TEM provides local information and is then complementary to get information on individual NC.

5.2. Experimental details

All the samples studied in this work were grown using a Riber MBE 32 chamber with a base pressure of a few 10^{-11} Torr. Standard Knudsen cells were used for Ge, Mn and Sn evaporation. The growth rate of GeMn and GeSnMn layers was 1.3 nm $\cdot$ min^{-1}. Prior to the growth of GeMn or GeSnMn layers, a Ge buffer layer was systematically grown on Ge(001) and annealed at 500 °C during 15 min. Concentrations of Mn and Sn in GeMn and GeMnSn samples were determined by Rutherford backscattering spectroscopy (RBS) in samples specially grown for calibration purposes. High resolution X-ray diffraction (HRXRD) experiments were performed using a Seifert XRD 3003 PTS-HR diffractometer with a beam concentrator prior to the Ge(220) four-bounce monochromator and a Ge(220) double-bounce analyser in front of the detector. Magnetic properties at various temperatures were measured using a superconducting quantum interference device (SQUID).

The TEM investigation were performed using six different microscopes available either in CEA-Grenoble or Karlsruhe Institute of Technology:

- HRTEM observations were performed using a JEOL 4000EX microscope working at 400 1kV (C_s = 1.0 mm), an image-corrected 80-300 kV FEI Titan^3 working at 300 kV, and a double-corrected 80-300 kV FEI Titan^3 Ultimate working at 200 kV. HRTEM images were averaged over several image acquisitions (up to 20) in order to increase the signal-to-noise (SNR) ratio.
- EELS was performed in HRSTEM mode using the probe-corrected mode of the double-corrected 80-300 kV FEI Titan^3 Ultimate working at 200 kV. A probe-corrected 80-300kV FEI Titan working at 300 kV was also used. The acquisitions of EELS data set were performed in a 1D or 2D fashion providing a spectrum line or a spectrum image, respectively. EELS acquisitions were achieved using a

GIF tridiem or a GIF quantum and an energy dispersion of 1 or 2 eV. If available during the acquisition, the dark correction of the CCD camera was improved as explained in sec. 2.6.2. A new gain reference was acquired at the beginning of the session with a average number of counts similar to that of the EELS core-loss range. The gain reference were averaged over 20 acquisitions. The noise of EELS signal was removed using PCA, whose relevant number of component were chosen as explained in sec. 2.6.2. For each edge (Sn $M_{4,5}$ at 485 eV, Mn $L_{2,3}$ at 640 eV and Ge $L_{2,3}$at 1217 eV), the background was removed by subtracting a power law fitted in the region preceding the edge with a width of 40-80 eV (depending on the edge). Element map were obtained by integrating over 60 eV after the edge for Mn and Ge, whereas the Sn signal was integrated between 500 and 530 eV, in order to avoid integrating O signal potentially coming from the O K edge at 532 eV.

- EDXS analysis were performed on a FEI Tecnai Osiris microscope at 200 kV acceleration voltage. This microscope equipped with a X-FEG high brightness gun and four EDX SDD detecteurs (0.9 sr collection solid angle) allows the acquisition of EDX SI with a good SNR. EDX spectra were acquired and analyzed with the Esprit software from the Bruker company.
- Conventionnal selected area electron diffraction (SAED) was performed using a Phillips CM200 FEG/ST (C_s = 1.2 mm) microscope at 200 kV acceleration voltage. Depending on the experiment the SAED were acquired using imaging plate or by averaging several acquisitions performed with a CCD camera.

The plane views and cross-sections of samples were prepared for microscopy observations by mechanical wedge polishing in order to get very thin and clean areas, as explained in sec. 2.7.1. If necessary, between 5 and 10 min ion milling were performed on cross-sectional sample using a Gatan PIPS in single mode at 2,5 keV Ar^+ ion energy.

APT was performed using a CAMECA FlexTAP instrusment. Sharp tips of GeMn specimen were prepared for experiment by lift-out method and standard milling using a dual beam ZEISS Nvision 40 and a FEI Strata 400 [Thom 07].

5.3. GeMn nanocolumns embedded in Ge pure matrix

A typical 200 kV aberration corrected HRTEM images of a $Ge_{0.9}Mn_{0.1}$ thin film grown at 130 °C on a Ge(001) substrate, is shown in Fig. 5.2. The typical thickness of the GeMn layer studied in this work is 80 nm. The Mn-rich NCs can be observed in the plane view, [100]-zone axis (Fig. 5.2(a)) as elongated features and in cross section, [001]-zone axis (Fig. 5.2(b)) as disks due to the projection along the growth direction. The contrast of the cross-section observation in Fig. 5.2(a) shows a superposition of the GeMn NCs with the surrounding Ge matrix, whereas the plane view observation allows the observation of the GeMn NCs without superposition with the Ge matrix, when the thin lamellae is thin enough. The dashed line in (a) indicates the position of the interface between the Ge(001) buffer and the GeMn layer. The NCs range from this interface to the top surface, and as we will see later they exhibit different shapes and are not all perfectly perpendicular to this interface. In these growth conditions, the NCs are homogeneously distributed and separated by ~7 nm, their diameter range from 2 to 3 nm. This section presents quantitative analysis of the composition of these GeMn NCs using EELS acquired on plane view samples with the spectrum imaging (SI) technique.

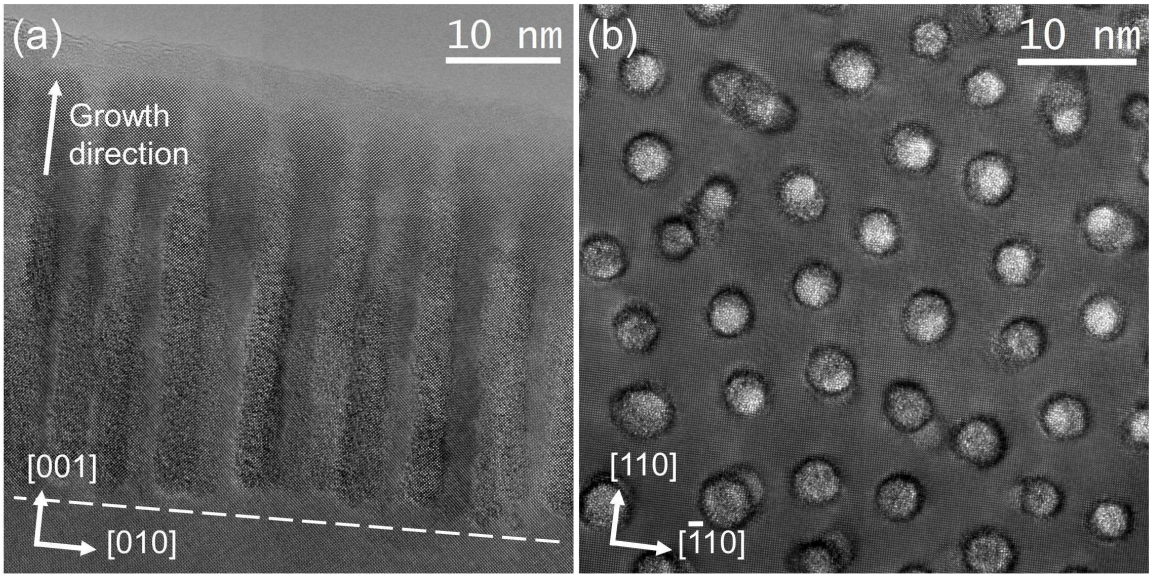

Figure 5.2.: 200 kV aberration corrected HRTEM images of a $Ge_{0.9}Mn_{0.1}$ showing nanocolumns (a) in [100]-zone axis (cross-section view) and (b) in [001]-zone axis (plane view). The dashed in (a) indicate the interface between the Ge(001) buffer and the GeMn layer.

5.3.1. Chemical composition of GeMn nanocolumns

5.3.1.1. Principal component analysis denoising

Before discussing in detail the quantification of the EELS chemical maps, Fig. 5.3 shows the improvement on chemical imaging using a PCA treatment on typical EELS data set. Fig. 5.3(a) is the HAADF image of the area analyzed using SI techniques. The SI data cube has a pixel size of 0.3 nm and a total size of 130 × 121 px acquired in 13 min. Fig. 5.3(b) Fig. 5.3(c) present the two Mn maps obtained from the computing of the raw EELS SI data and after denoising of the data set using 4 components of PCA, respectively. They both show that the dark disks in Fig. 5.3(a) are the Mn-rich NCs.

However, it is clear that the Mn map obtained from the raw EELS data set is much more noisy and that the contrast between the matrix and the NCs is much lower than that of the PCA-denoised EELS data set. This difference is mainly explained by a better power-low extrapolation (required for background subtraction) in the PCA treated data set than in the raw one. Since the elemental signal is integrated over a relatively large window of 60 eV, the noise is averaged and the PCA denoising do not play a significant role in the integration. Fig. 5.3(d-e) compare PCA treated EELS spectra with corresponding raw spectra for two cases:

- signal of one individual pixel,
- signal averaged over a square of 4 pixels.

Both figures show the spectra between 400 and 1400 eV and a zoom on the Mn $L_{2,3}$edge in the inset. In case of a unique pixel, the shape of the Mn can be hardy recognized in the raw spectra, only a cloud of points are visible indicating the presence of some intensity at the Mn $L_{2,3}$ energy, but no more. After PCA treatment, the signal extracted from a unique pixel show clearly the white lines shape of the Mn $L_{2,3}$ edge. After averaging over 4 pixels, the white lines can be recognized but the signal is still noisy and the PCA treatment still improves the SNR. This statistical analysis over a large data set (131 × 121 px) improves drastically the result and is in our case mandatory when acquiring large field of view data set with low acquisition time, necessary to get representative mapping. On Fig. 5.3(c), one can already see that there is some NCs with lower Mn content (appear darker in the Mn map) than the other. We will see in the following that this observation is due to the morphology of the NCs in the Ge matrix.

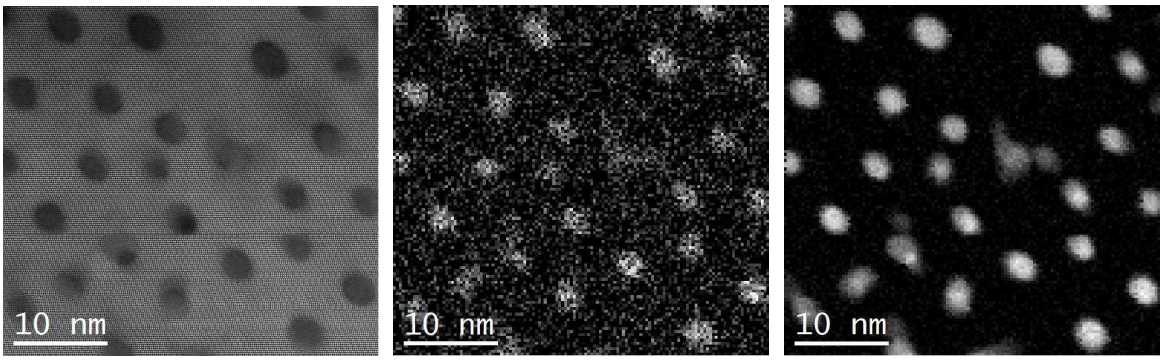

(a) HAADF image (b) Mn map without PCA (c) Mn map with PCA

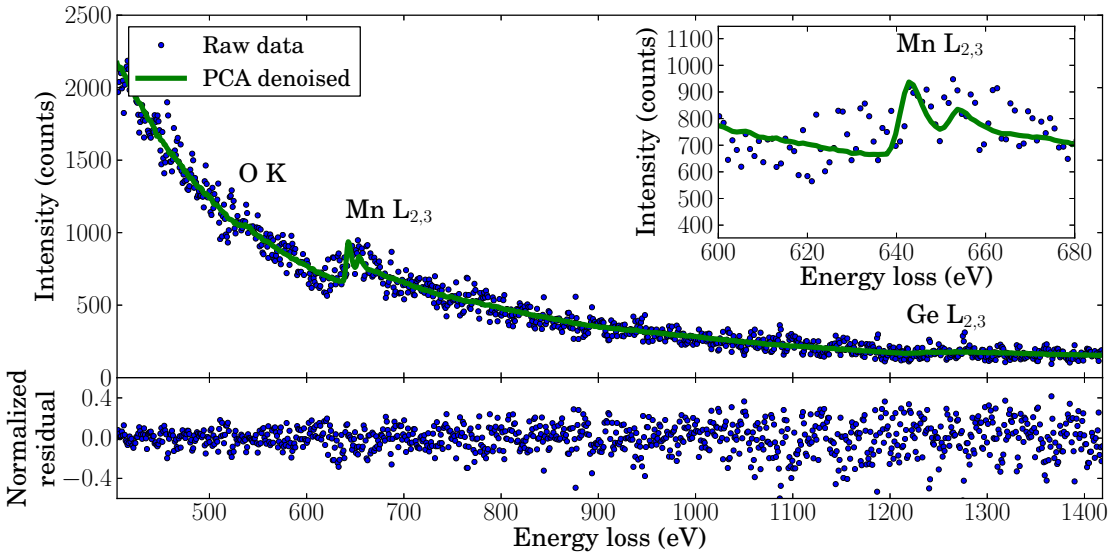

(d) One pixel

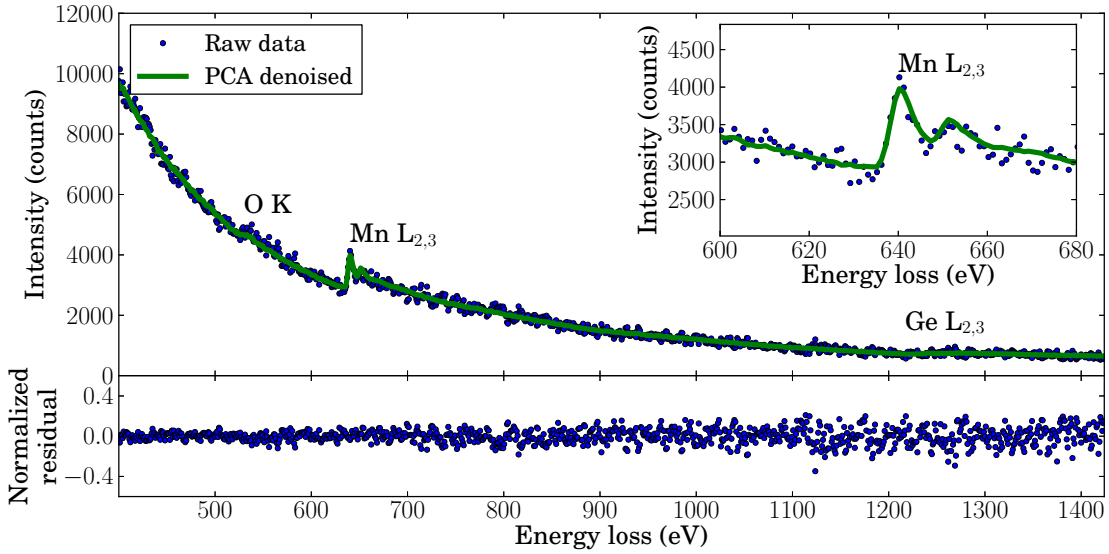

(e) Four pixels

Figure 5.3.: Effect of PCA treatment on the computing of EELS data set. (a) HAADF image acquired simultaneously than the EELS signal. Mn maps obtain from (b) the raw EELS SI and (c) after PCA denoising. Comparison of EELS spectra measured in a GeMn nanocolumns before and after PCA denoising for two cases:(d) signal of one individual pixel and (e) signal summed over 4 pixels. Four components were used for the PCA denoising.

5.3.1.2. Absolute composition measurements

Using EELS SI techniques we analyzed quantitatively the composition of the GeMn NCs. The dual eels acquisition option on the GIF Quantum allows the pseudo-simultaneous acquisition of the zero-loss region of the EELS spectrum and of the edge spectrum for each pixel of the scanned area. This dual acquisition allows to treat afterward quantitatively the data set following Eq. 2.45 having the total number of electrons from the low loss region. This analysis provides a quantitative result of the NCs composition on a absolute scale. Following Eq. 2.45, the areal density n_{den} (atom $\cdot$ nm^{-2}) of each element is measured within the error of the partial cross-section. A good checking of the accuracy of the Hartree-Slater partial cross section used is to integrate the mean Mn concentration of a set of computed maps and check that it corresponds to the expected nominal value of 10 %: we found values ranging from 8.6 to 11.2 % which is a fairly good matching with the nominal Mn concentration of 10 %[1]. Note that in the previous chapter we observed a systematic error on the relative concentration of Ge in Si using the Hartree-Slater partial cross section (see sec. 4.4.3), while here the Mn relative concentration obtained using Hartree-Slater partial cross section gives an accurate measurement within 2 % error in the Ge-Mn system. We are then confident to use the calculated partial cross section for the quantification.

Fig. 5.4 presents the results of the quantification of the Ge and Mn composition. The Mn and Ge areal density maps corresponding to a measured number of Mn or Ge atoms per unit area are shown in Fig. 5.4(a) and (b), respectively. The two main features are:

- the Mn content is fully localized on the GeMn NCs: no Mn is detected in the matrix.
- the mean Ge areal density decrease from 1149 atoms $\cdot$ nm^{-2} in the Ge matrix to 940 atoms $\cdot$ nm^{-2}, corresponding to a diminution of 18 %. The specimen thickness measured by EELS being 24 ± 2 nm, we deduced the average Ge density to be 47 ± 4 atoms $\cdot$ nm^{-3} in the Ge matrix, which is fairly close to the theoretical density of Ge $d_{\text{Ge}} = 44.2$ atoms $\cdot$ nm^{-3} of the diamond structure. This observation also confirms the accuracy of the quantification method.

The sum of the density maps for Mn and Ge provides a map of the total absolute density. The latter shown in Fig. 5.4(c) demonstrated that the total density in the NCs is higher than in the Ge matrix. Moreover, the Mn concentration inside the NCs can reach 70 % as shown by the Mn concentration map in Fig. 5.4(d). These results are important clues to understand the GeMn phase in the NCs, and will be considered more precisely in the following.

[1] The nominal composition was checked using RBS techniques [Devi 08].

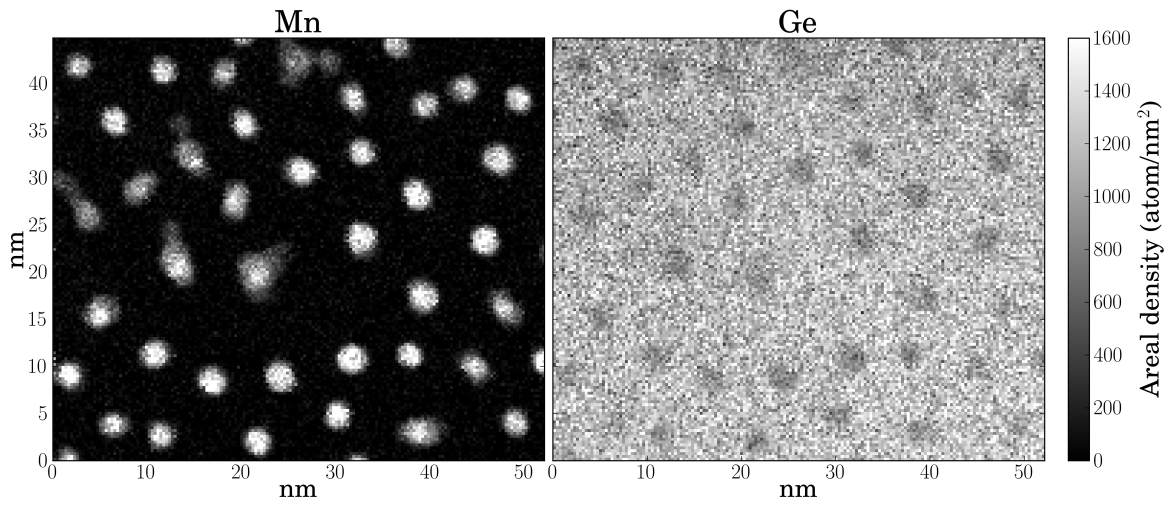

(a) Mn and Ge absolute areal density

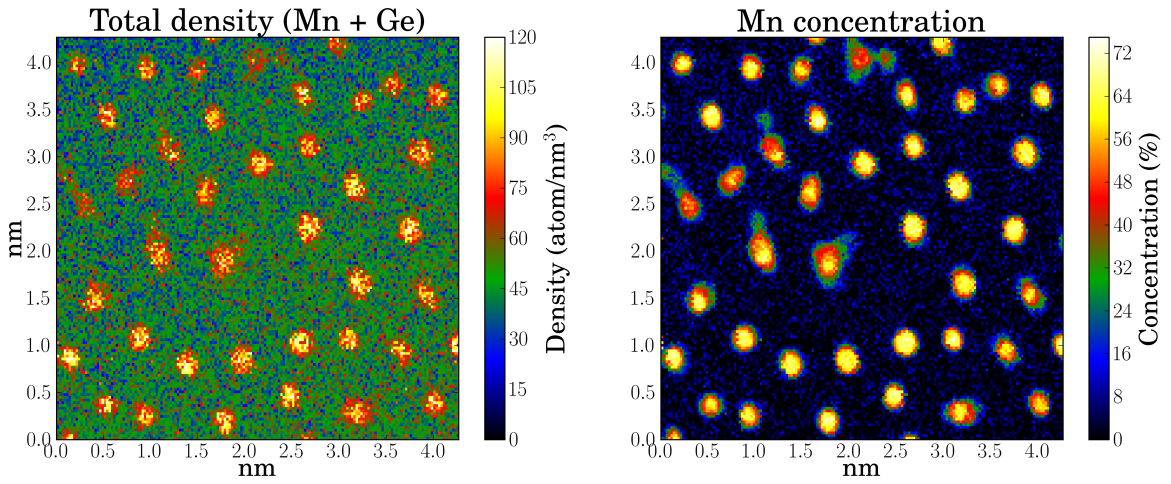

(b) Absolute density and Mn concentration

Figure 5.4.: Composition of GeMn NCs. Absolute areal density in atom · nm^{-2} of (a) Mn and (b) Ge. (c) Total density (Ge + Mn) in atom · nm^{-3} and (d) Mn relative concentration in %.

We now study more precisely the composition variation of individual GeMn NCs. The positions of a series of NCs have been fitted and their radial composition was analyzed. Fig. 5.5 shows the 36 sub-images of NCs cropped from Fig. 5.4(d). There are some NCs which have lower Mn content, *e.g.* the first two ones of the series. This diminution is due to the morphology of the NCs and will be investigated in more detail later. Some NCs are also bent or not aligned along the electron beam direction or even they don't go through the whole layer.

To study the profile concentration in a systematic way, we radially averaged the chemical information of NCs which are almost rotationally invariant (no bending). Radial profiles of Mn relative concentration are plotted on Fig. 5.5(b).

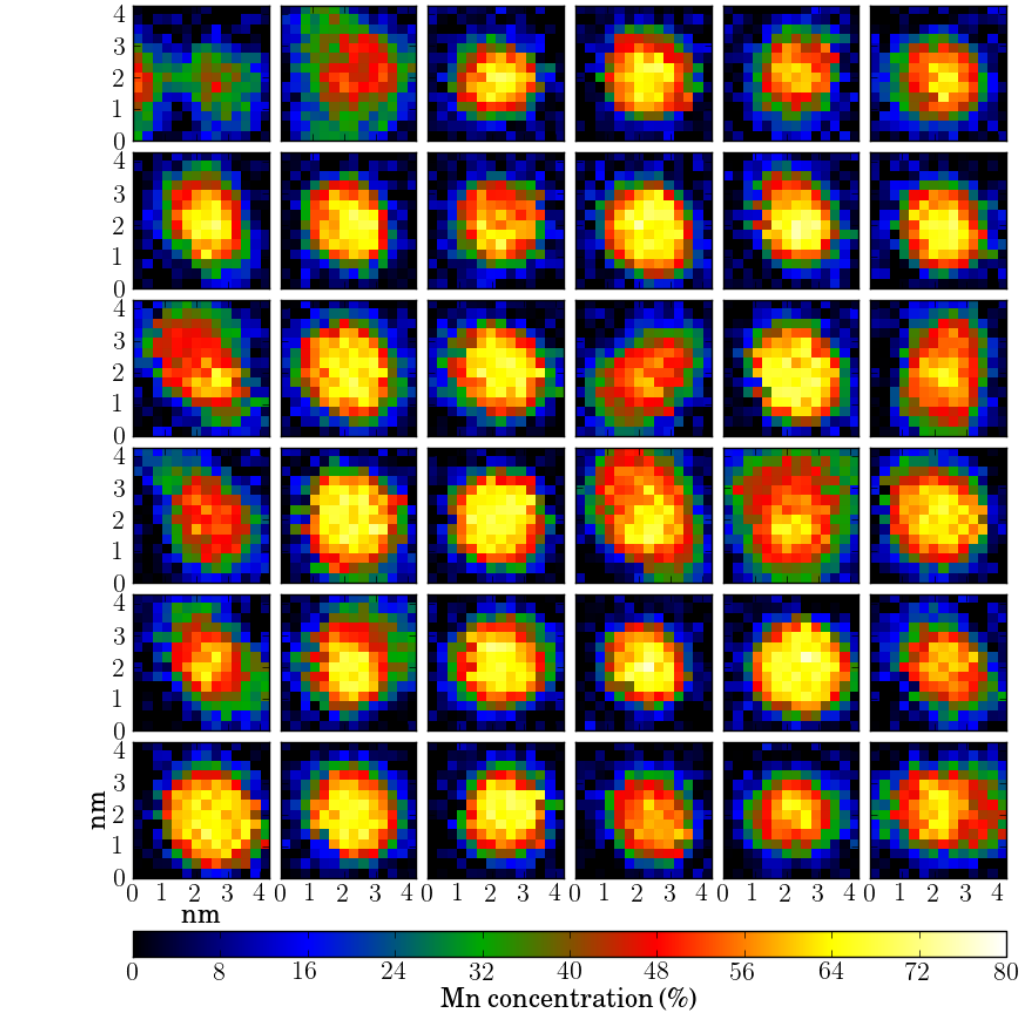

(a)

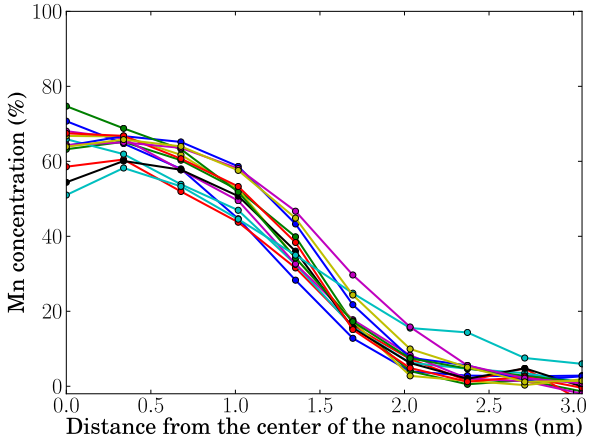

(b) Mn concentration profile

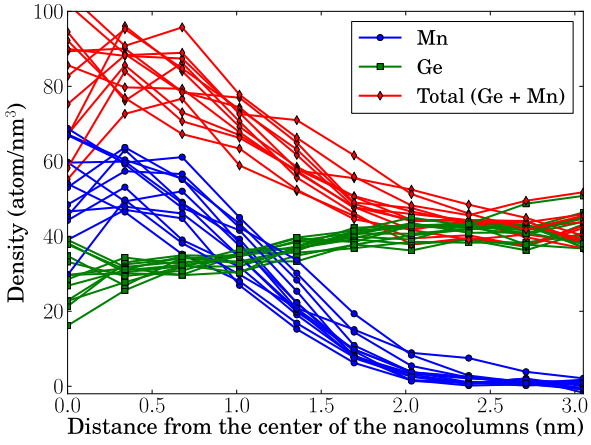

(c) Absolute density profile

Figure 5.5.: (a) Set of NCs used for the statistical analysis of Mn composition in NCs. Radial profile of (b) Mn relative concentration and (c) Mn, Ge and total density. The sub-image in (a) come from the Mn concentration map shown in Fig. 5.4(d) and are displayed on the same color scale. The radial profiles in (b-c) go from the fitted center the NCs to the Ge substrate.

The Mn, Ge and total density are plotted in Fig. 5.5(c). The Mn relative concentration has a core shell like distribution with a high content of 50 to 70 % at the center and slowly decreases over the 1-2 nm shell. This can be either a diffuse interface between the GeMn NC and the Ge matrix, or a consequence of the roughness of the interface. Since we are measuring the Mn concentration in projection we can not discriminate the cause of this diffuse concentration profile. We estimate the average Mn composition over the NC by the average concentration of Mn integrated above a certain concentration threshold. A threshold of 5 % provides a mean Mn concentration of 33 % inside the NCs. Due to the diffused Mn concentration profile a higher threshold value gives an higher Mn average concentration. This value of 33 % is close to the value obtained previously by only considering the volume fraction of the NC and the nominal Mn concentration [Devi 07, Devi 08]. These previous studies were not able to provide the chemical distribution of Mn across the NCs. We note that no correlation between the NCs size and the Mn mean concentration has been observed.

The Mn, Ge and total density plots in Fig. 5.5(c) allow to get more insight on the absolute composition of GeMn NCs. The mean Ge density in the matrix have been normalized to the theoretical value of $d_{\mathrm{Ge}} = 44.2$ atoms $\cdot$ nm^{-3} for a more accurate measurement (the measured value being 47 atoms $\cdot$ nm^{-3}). This normalization does not affect the ratio of the different densities reported here. Contrary to the classical relative concentration calculation where the sum of the two elements is assumed to be 100 %, the Mn and Ge densities are independently measured here following Eq. 2.45. Consequently, we are able to observe a decrease of the Ge density from the Ge matrix (44 atoms $\cdot$ nm^{-3}) to the center of the NCs (30 atoms $\cdot$ nm^{-3}), whereas the Mn density increase from 0 in the Ge matrix to 57 ± 5 atoms $\cdot$ nm^{-3}to the center of the NCs. The sum of the Mn and Ge density in the center of GeMn NCs 82 ± 8 atoms $\cdot$ nm^{-3} is largely above the mean density in the Ge matrix (44 ± 2 atoms $\cdot$ nm^{-3}). This clearly highlights a higher total atomic density in the GeMn NCs in comparison to the pure Ge matrix.

Profiles of areal density and relative concentration measured with the Mn $L_{2,3}$ and Ge $L_{2,3}$ edges and taken across two GeMn NCs are plotted in Fig. 5.6(a-b). Once again the Ge $L_{2,3}$ areal density only slightly decrease in the GeMn, whereas the Mn $L_{2,3}$ areal density strongly increases. The line profile provides more information on the extension of the interface compared to the radial averaging which gave us information on the composition. The line profile shows that there is an abrupt change of the Mn composition at the interface between the NCs and the matrix which takes place over only 3 measured points (0.9 nm) for both the areal density and the relative concentration.

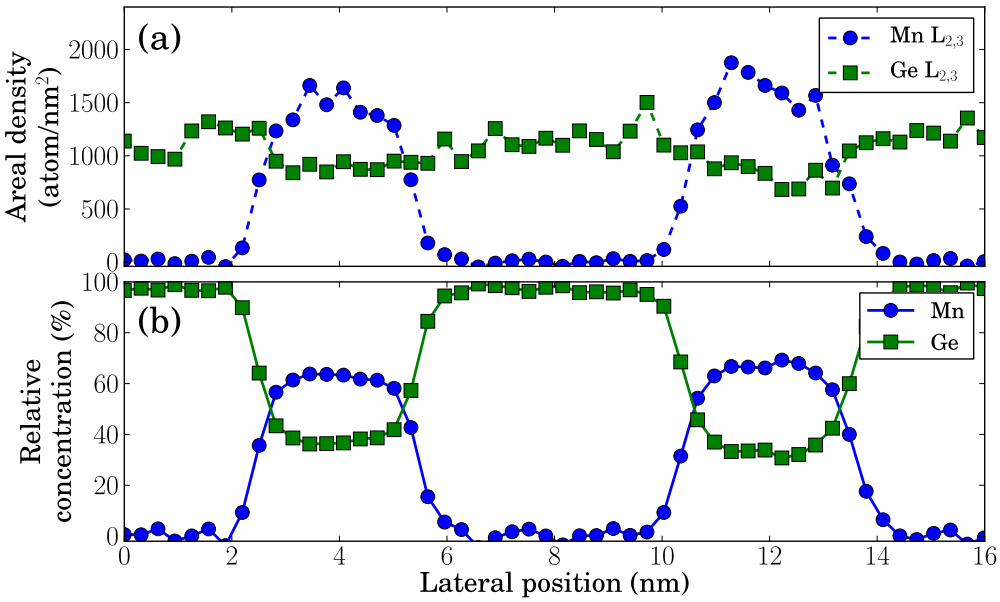

Figure 5.6.: Composition profile across two GeMn NCs: (a) Mn $L_{2,3}$ and Ge $L_{2,3}$ areal density profile, (b) Mn and Ge relative concentration.

5.3.1.3. Atom probe measurements

To get more insight on the composition variation at the interface and on the morphology of the GeMn NCs, some Atom Probe Tomography (APT) has been performed on similar specimen (similar growth temperature and 10 % Mn concentration) on the CEA Cameca Flextap new tool [Gaul 06]. We do not want to give too much details about the technique itself but only some important features observed in the reconstructed volumes. Fig. 5.7 shows reconstructed volume obtained from APT experiment of a tip-shape sample preparated by FIB. The Ge and Mn volumes oriented along the growth direction (similar to TEM plane view) are shown in Fig. 5.7(a) and (b), respectively. The position of the GeMn NCs can be recognized by the Mn-rich area in Fig. 5.7(b). By inspecting corresponding position on the Ge volume, one can observe that the Ge appear higher in the NCs. This is known that the analysis of samples consisting of phases with different evaporation fields may lead to biased composition data [Vurp 00]. Nevertheless, the composition profile measured on the reconstructed volume can be corrected *a posteriori* according to the model of Blavette *et al.* [Blav 01].

Our APT experiment provides an upper limit of 0.1 % for the Mn concentration in the matrix which is in good agreement with our EELS results. The Mn atoms visible in between the NCs in the reconstructed volume shown in Fig. 5.7(b) are due to noise in the mass spectra. The composition of the GeMn NCs was studied more quantitatively within a collaboration with the Groupe de Physique des Matériaux in Rouen. A corrected concentration profile measured across a single Mn-rich NC is shown in Fig. 5.8 at two different heights in the same NC [Mout 12]. This highlights the fluctuation of Mn concentration within a unique NC.

Good agreement is found between composition profiles obtained by APT and EELS, nevertheless APT found slightly less Mn in the NCs (from 35 % to 55 %) as compare to the 60 % of EELS measurements. Even if APT is a technique that counts the number of atoms evaporated from the tip (around 60 % of total number of atoms is count), the quantitative analysis only provides relative concentration and is not able to give absolute quantification as EELS (preceding section).

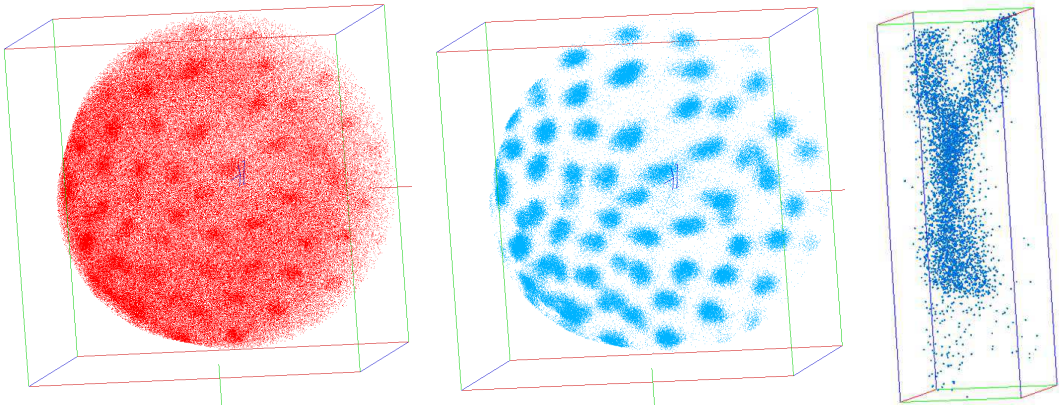

(a) Ge (b) Mn (c) Mn

Figure 5.7.: Reconstructed volume of (a) Ge and (b) Mn obtained from ATP experiment in top view. The volume in (a-b) are oriented along the growth direction. The position of the GeMn NCs can be recognized by the Mn-rich area in (b). (c) Side view of a junction of two GeMn NCs. Experiment performed by Pierre-Henry Jouneau, Bastien Bonef from CEA INAC and Adeline Grenier from CEA LETI.

ATP observations evidence particular NC morphologies: the NCs are not all straight and continuous. Beside bent or interrupted NCs, separation, junction or nucleation of NCs in the GeMn layer were observed. Fig. 5.7(c) is a extraction of the APT volume showing a NC that splits in two emerging branches in the growth direction. The curvature or bending of the NCs can be attributed to surface roughness of the front growth [Devi 08, Yu 10]. These observations explain the different contrast of NCs observed on plane view TEM images. Similar morphologies can be seen on the Mn maps obtained from EELS experiment shown in Fig. 5.3(c), Fig. 5.4(a-b). Fig. 5.9 compare BF and ADF images of a NC with a straight shape and well-oriented along the growth direction (Fig. 5.9(a-b)) and another NC exhibiting a Y shape with two emerging branches as found in APT measurements (Fig. 5.7(c)). The contrast of the ADF images is not straightforward to analyze, due to the strong dechanneling that can be observed in the NC. Moreover, the bright contrast at the interface between the NC and the matrix in the ADF image is mainly due to strain localized at the interface. Lowering the camera length decreases the bright annular feature of the interface. This indicated that strain is still observed, even if these images were recorded in typical HAADF conditions (50-110 mrad collection angle).

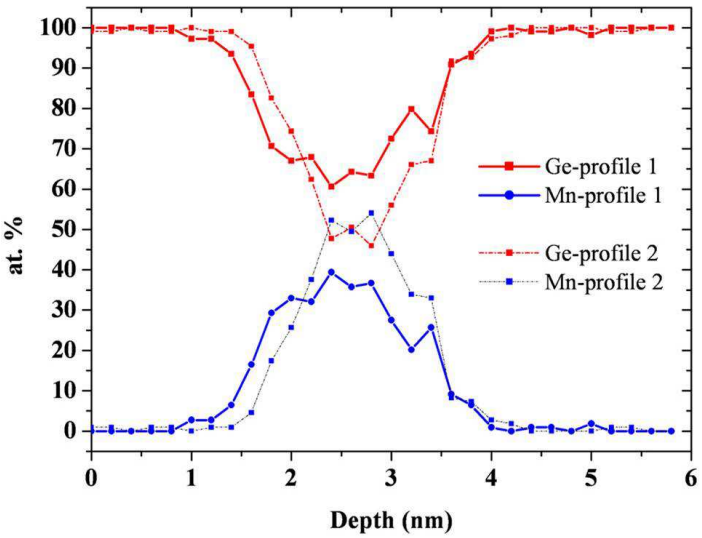

Figure 5.8.: Corrected concentration profile taken across a single NC at two different heights [Mout 12].

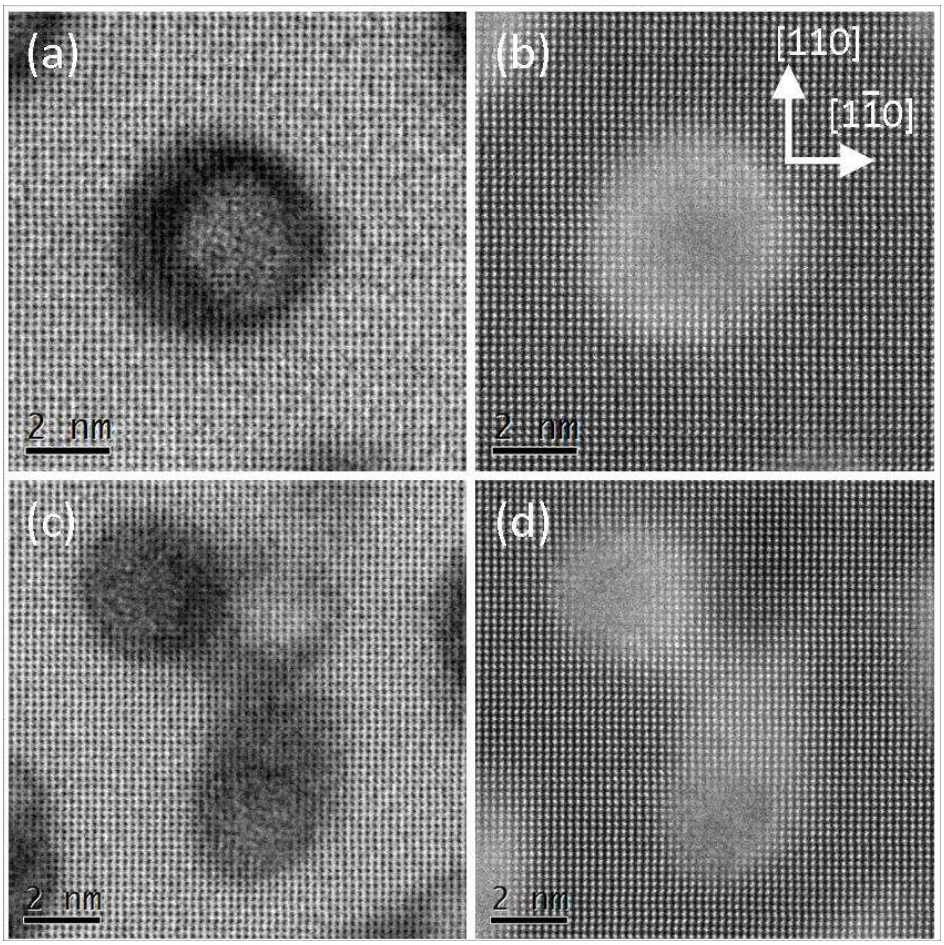

Figure 5.9.: (a) and (b) BF and ADF images respectively of the same emerging NCs with a straight shape. (c) and (d) BF and ADF images respectively of another NC exhibiting a Y shape with two emerging branches as revealed by APT observation shown in Fig. 5.7(c).

5.3.2. Structural analysis

So far classical XRD experiments were not able to provide information on the crystal structure of the NC [Devi 08] because of the very small volume of GeMn NCs investigated. TEM is itself a tool of choice to obtain information on the NC by minimizing the contribution of the surrounding matrix. Therefore, we investigated the structure of NCs using aberration corrected HRTEM mainly in [001]-zone axis where the NC go through the TEM lamella.

Aberration correction allows to acquire HRTEM image close to Gaussian focus preventing unwanted delocalization effect. This is crucial for imaging the GeMn NCs which have a small diameter (2-3 nm). In order to significantly increase the SNR, the HRTEM images have been averaged over numerous acquisitions (up to 20) on the same area and same imaging conditions. No filtering in Fourier space is then used which is of importance for the analysis of the power spectra. Particular attention was taken for the specimen preparation to reduce the damage induced in the specimen during polishing and the thickness of the amorphous layer, since these two parameters are of importance for the HRTEM imaging. Using the wedge polishing method no ion-beam is required and the amorphous layer is measured to be ~1 nm thick (see sec. 2.7).

5.3.2.1. Amorphous nanocolumns

We start by considering HRTEM investigations of $Ge_{0.9}Mn_{0.1}$ layers grown at 150 °C (Fig. 5.10). Their mean diameter is about 6 nm and their structure is amorphous. A general view of the specimen and the corresponding power spectrum are shown in Fig. 5.10(a) and (b), respectively. The reflections indicated by arrows on the power spectrum in Fig. 5.10(b) are due to the presence of a Ge_3Mn_5 precipitate located in the lower left part of the HRTEM image (Fig. 5.10(a)). Since the amorphous are grown at a temperature (150 °C) slightly lower than that of the formation of Ge_3Mn_5 precipitates, it is usual to observe the presence of a few precipitates in the amorphous NCs. A power spectrum of the Ge matrix taken in the area indicated by the dashed square labeled 1 is indexed in Fig. 5.10(c) as a reference. The cubic symmetry of the Ge diamond structure can be recognized with the perpendicular (220) and $(2\bar{2}0)$ Bragg reflections. A zoom on a NC taken in the area indicated by the dashed square labeled 2 is shown in Fig. 5.10(d) and clearly reveals the amorphous structures of the NC. The diffuse ring at 5 nm^{-1} on the corresponding power spectrum shown in Fig. 5.10(e) confirms the amorphous feature. The comparison of the power spectrum taken in the Ge matrix (Fig. 5.10(c)) with that of a GeMn NC (Fig. 5.10(e)) evidences that the diffuse ring visible in the power spectrum of the whole image (Fig. 5.10(c)) is characteristic from the NCs. This indicates that the sample preparation is clean enough to exclude contribution from surface amorphization.

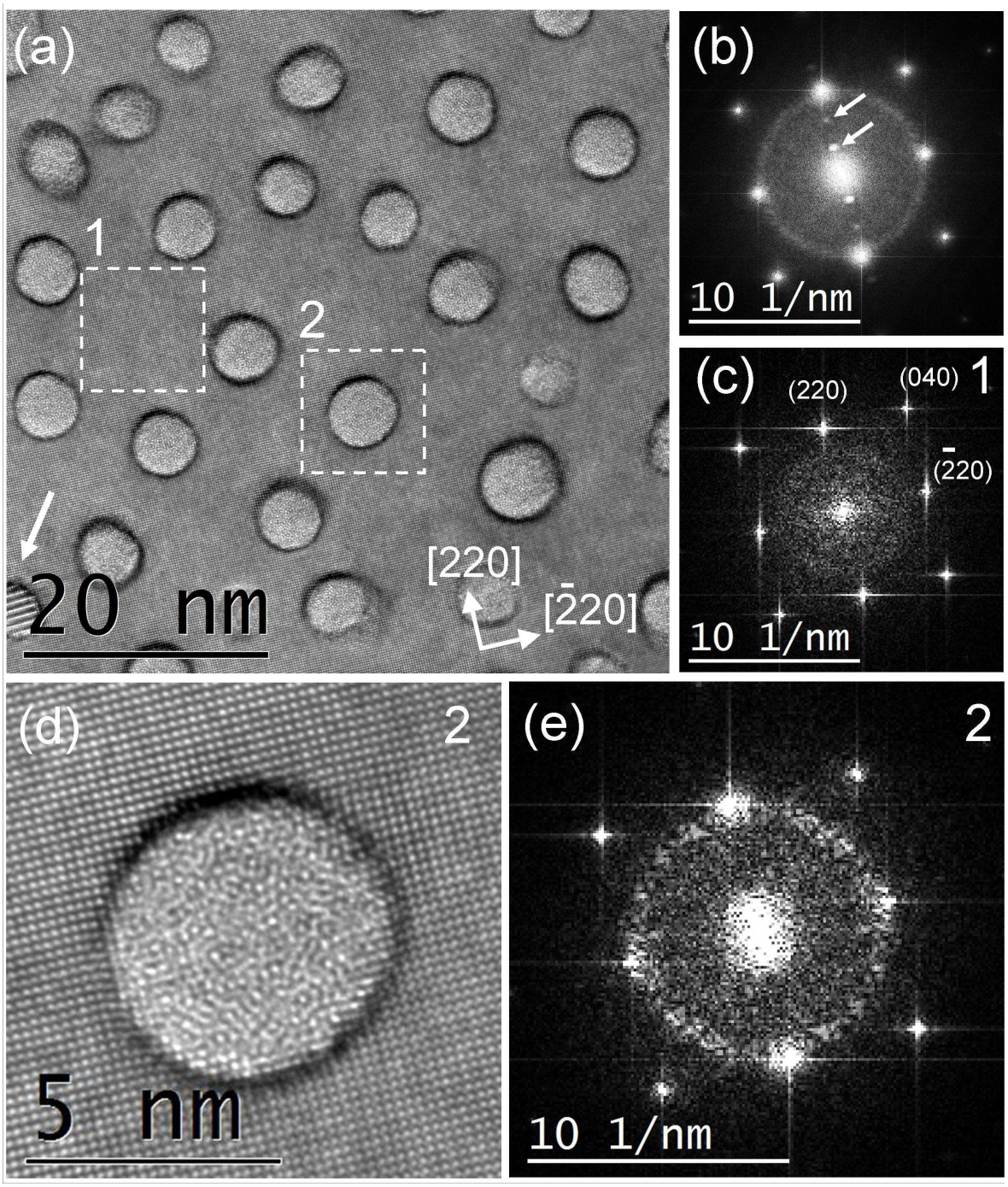

Figure 5.10.: 300kV HRTEM investigations of amorphous NCs in the [001]-zone axis. (a) HRTEM images of NCs. (b) Power spectrum of the whole HRTEM image and (c) of the Ge matrix. (d) Zoom showing the amorphous features in the NC and (e) the corresponding power spectrum. The area of the Ge matrix and the GeMn NC have been taken in the region indicated by dashed square in (a) and numbered 1 and 2, respectively. 3 images have been aligned and integrated providing a mean number of count of 18357. For comparison all the power spectra are displayed on the same scale. The arrows in (b) indicates Bragg reflections due to the presence of a Ge_3Mn_5 precipitate indicated by a white arrow in the lower left part of (a)

5.3.2.2. Crystalline nanocolumns

Let us consider now a specimen containing relaxed crystalline GeMn NCs grown at 130 °C. Fig. 5.11 shows a HRTEM investigation in [001]-zone axis of a $Ge_{0.9}Mn_{0.1}$ layer. The NCs which have a diameter of 2-3 nm can be observed in Fig. 5.11(a). Its power spectrum in Fig. 5.11(b) does not show the diffuse ring observed previously in case of the amorphous NCs (Fig. 5.10). Beside the characteristic {220} and {400} reflections of the Ge matrix, a weak and diffuse reflection close to the forbidden (200) reflection of the Ge diamond structure can be observed. This reflection comes from the NC indicated by the dashed square labeled 1 in Fig. 5.11(a). A zoom of the NC and its corresponding power spectrum are shown in Fig. 5.11(c) and (d), respectively. In the power spectrum, the weak (200) reflection appear clearly and supplementary reflections are present. A set of three weak reflections can be seen close to the forbidden (020) reflection of the Ge diamond structure.

Fig. 5.12 shows a set of different NCs exhibiting crystalline features and their respective power spectra. A pure matrix area is shown as reference. Even if all these NCs appears as crystalline, it is clear that there are not all identical and present disorder structures. It results that many weak reflections located at different position in the reciprocal space coming from the GeMn NCs are observed in the power spectrum of each HRTEM images. The most significant are nevertheless located on a ring corresponding to a distance of about 0.2 nm indicating some similarity between all these NCs. Some reflections can also be observed closer to the direct reflection, but they can be hardy separated from the background of the power spectrum. NCs with a superstructure, as shown in Fig. 5.11(e) was observed only a few time in numerous HRTEM observations. These findings point out that there is no systematic order in the GeMn NCs.

Similar observation were performed directly on Selective Area Electron Diffraction (SAED). Fig. 5.13 shows the SAED patterns acquired in the [001]-zone axis (plane view) of a $Ge_{0.9}Mn_{0.1}$ layers grown at temperature of 130 °C. The selected area was about 100 x 100 nm^2. The same pattern is displayed on different intensity scale in Fig. 5.13(a) and (b) in order to highlights the very weak feature, which are indicated by white arrows in Fig. 5.13(b). These features are located on a ring with a radius of 4.64 ± 0.02 nm^{-1}, corresponding to lattice distance of 0.21 ± 0.02 nm which is in good agreement with the power spectrum results.

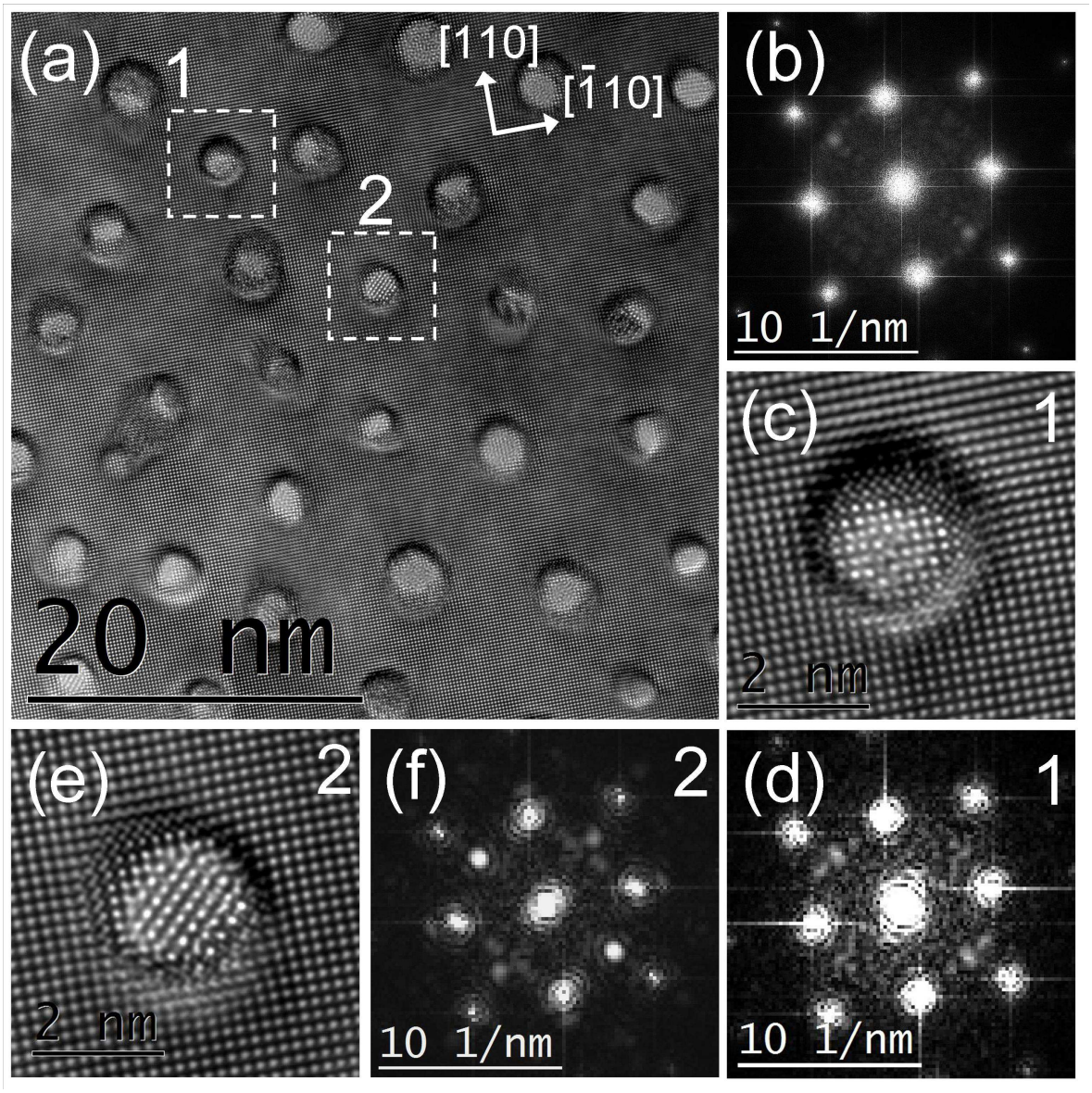

Figure 5.11.: 300kV HRTEM investigations of relaxed crystalline NCs in the [001]-zone axis. (a) HRTEM images of NCs. (b) Power spectrum of the whole HRTEM image and of the Ge matrix. (c, d) Zoom on NCs and their corresponding power spectrum are shown in (d, f), respectively. The zoomed area have been taken in the region indicated by dashed square in (a) and numbered 1 and 2. 7 images have been aligned and integrated providing a mean number of count of 18939. For comparison all the power spectra are displayed on the same scale.

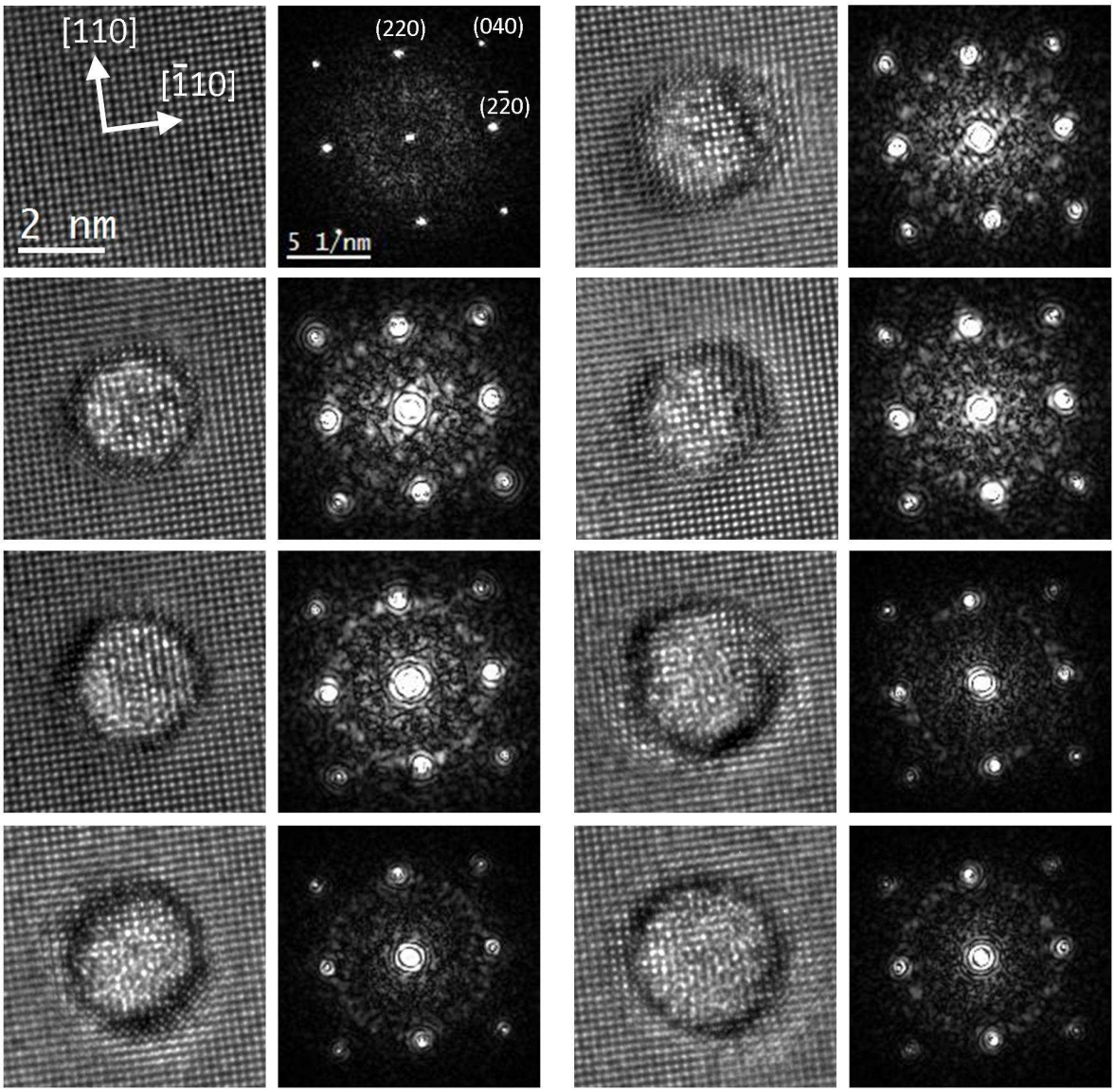

Figure 5.12.: HRTEM images of relaxed crystalline NCs in the [001]-zone axis and their respective power spectra. All the power spectra are displayed on the same intensity scale.

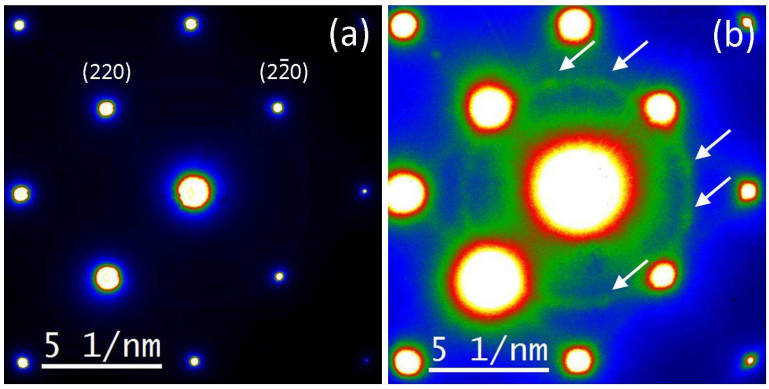

Figure 5.13.: SAED pattern of $Ge_{0.9}Mn_{0.1}$ layers grown at temperature of 130 °C. The same pattern is displayed on different intensity scale: (a) the whole intensity range (0 to 65535), whereas in (b) the intensity is saturated at 6110.

5.3.2.3. HRTEM image simulation

HRTEM image simulations of different structures have been performed and compared with experimental HRTEM observations. Within a collaboration with the atomistic simulation group of our institute (Emmanuel Arras, Frédéric Lançon and Pascale Pochet at L_Sim), we studied different atomic models to describe the structure of the GeMn NCs in a Ge matrix. Using first-principles calculation, they discovered a family of low-energy intermetallic structures based on a Ge_2Mn, which is isostructural to α-$FeSi_2$ [Arra 10]. This structure called α-phase can have different Mn concentration, as illustrated by Fig. 5.14. The phase is based on the simple cubic Ge lattice with Mn atoms placed in interstitial positions. The stoichiometry can be tuned by different filling of the interstitial sites. The lattice parameter of this phase is very close to the one of the Ge diamond structure. The α-phase has a striking structural proximity with the diamond Ge. The a and c lattice parameters of the α-phase are only of 2.5 % and 1.0 % higher than diamond Ge parameter, respectively.

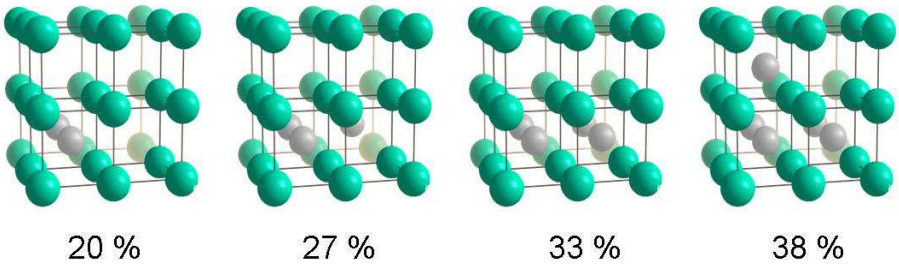

Figure 5.14.: α-phase for different Mn concentration. Ge and Mn atoms are in green and grey color respectively

The HRTEM image simulations were performed using the JEMS software [Stad 87], and the exit waves were calculated within the multislice algorithm. The partial temporal coherence of the incident electron wave was described by a defocus spread of ΔC = 4 nm (see sec. 2.4.2), corresponding to that of the FEI Titan^3 80-300 in Karlsruhe, which was used for the acquisition of aberration corrected HRTEM images shown in the preceding section. The spherical aberration was set to 1 µm in simulations which corresponds to the typical experimental value obtained with the aberration corrector. The thickness considered in the different atomic models was 17 nm and the defocus was set to 10 nm.

Fig. 5.15 shows HRTEM image simulations based on two different atomic models of a 2 nm (Ge,Mn) NC in Ge: a solid solution model based on diamond Ge and a α-phase compound.

A solid-solution may be acceptable in principle because of the strong similarity between the Ge matrix and the NC [Boug 06, Li 07]. A supercell was then build with Mn

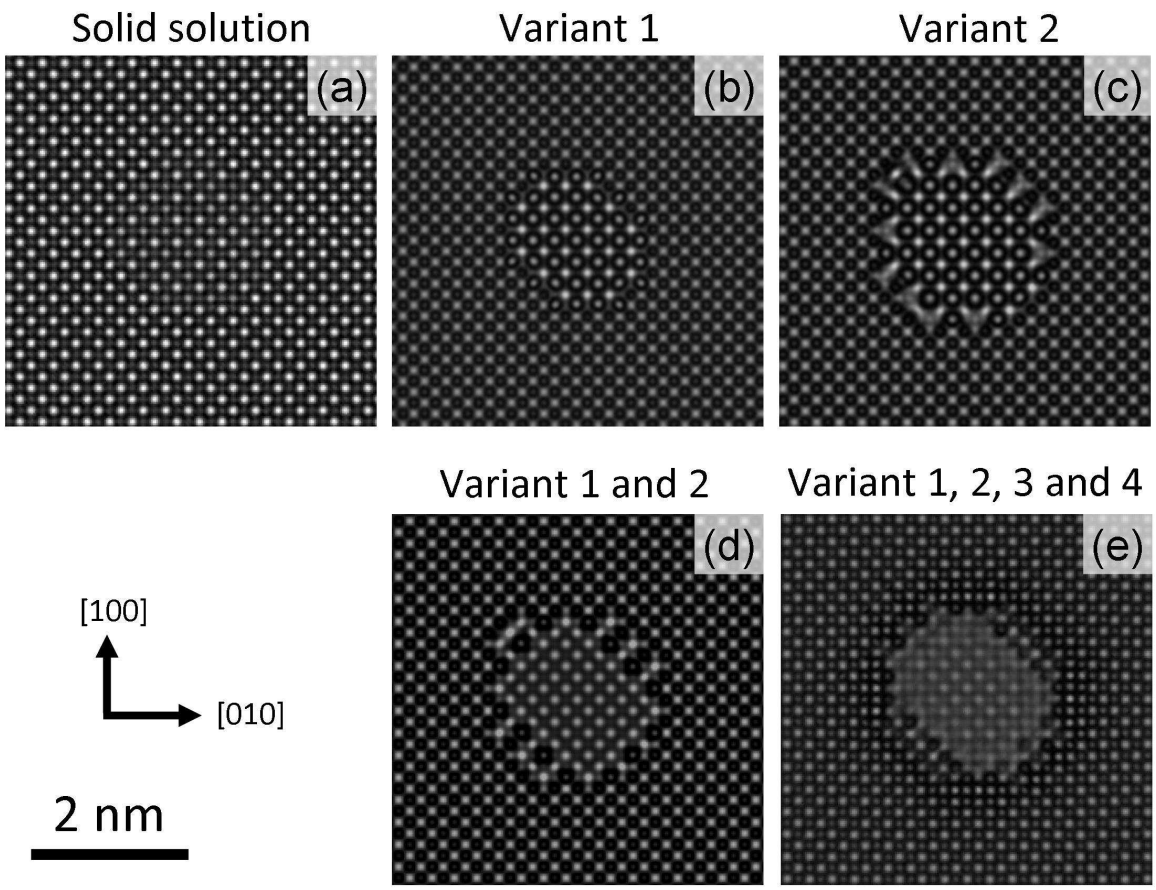

Figure 5.15.: HRTEM image simulation of GeMn NC with different structure model. (a) Solid solution. (b) α-phase with the variant n°1. (c) α-phase with the variant n°2. (d) α-phase with the variants n°1 and n°2. (e) α-phase with the variant n°1, 2, 3 and 4.

atoms placed randomly only in substitutional position. Fig. 5.15(a) shows the result of the image simulation. Since the Mn atoms are in substitutional position, the contrast between the matrix and the NC is very low. Fig. 5.15(b) shows the simulated HRTEM image of a NC with the α-phase described previously. The localization of the NC is easier due to the cubic (as opposed to diamond) character of the α-phase. The presence of two nonequivalent sublattices in the cell for Ge and Mn leads to a superstructure which can be seen in the simulation Fig. 5.15(b). The brighter atomic columns corresponds to the germanium pure atomic columns, whereas the atomic column in between are Mn pure (the unit cell shown in Fig. 5.14 is viewed from the top). The two sublattices can generate two variants depending on the position of the cell origin with respect to the diamond-Ge cell. Fig. 5.15(c) shows simulated HRTEM image of the second possible sublattice. Beside the superstructure, the interface between the NC and the matrix appears more clearly due to the discontinuity of the lattice between the α-phase and the diamond Ge, *i.e.* incoherent interface. The interface energy between two variants being very low (10 meV $\cdot$ Å^{-2} [Arra 12]) the two variants of the α-phase are supposed

to coexist inside each column. As can be observed on the HRTEM image simulation in Fig. 5.15(d) the introduction of two variants cancel the superstructure contrast of the α-phase. Another interesting point is the presence of a dark ring around the NCs, that is due to the lattice discontinuity between the α-phase and the diamond-Ge structure of the matrix. Variants can be generated by changing the origin of the α-structure lattice with respect to the diamond structure. An offset of half a lattice parameter of the diamond structure can be added to the origin of the α-structure lattice parallel or perpendicular to the growth direction. Up to 6 different variants can be introduced in the NC [Arra 12]. Fig. 5.15(e) shows the evolution of the contrast when the number of variants of the α-phase is increased up to 4.

Fig. 5.16 shows a qualitative comparison of simulated and experimental HRTEM images in [110]- and [001]-zone axis. Experimental images on Fig. 5.16(a) and (d) are compared to the simulated images (Fig. 5.16(b) and (e)) using a model of NC filled with a α-phase consisting of 4 variants. The different variants can be observed in the atomic model shown in Fig. 5.16(c) and (f).

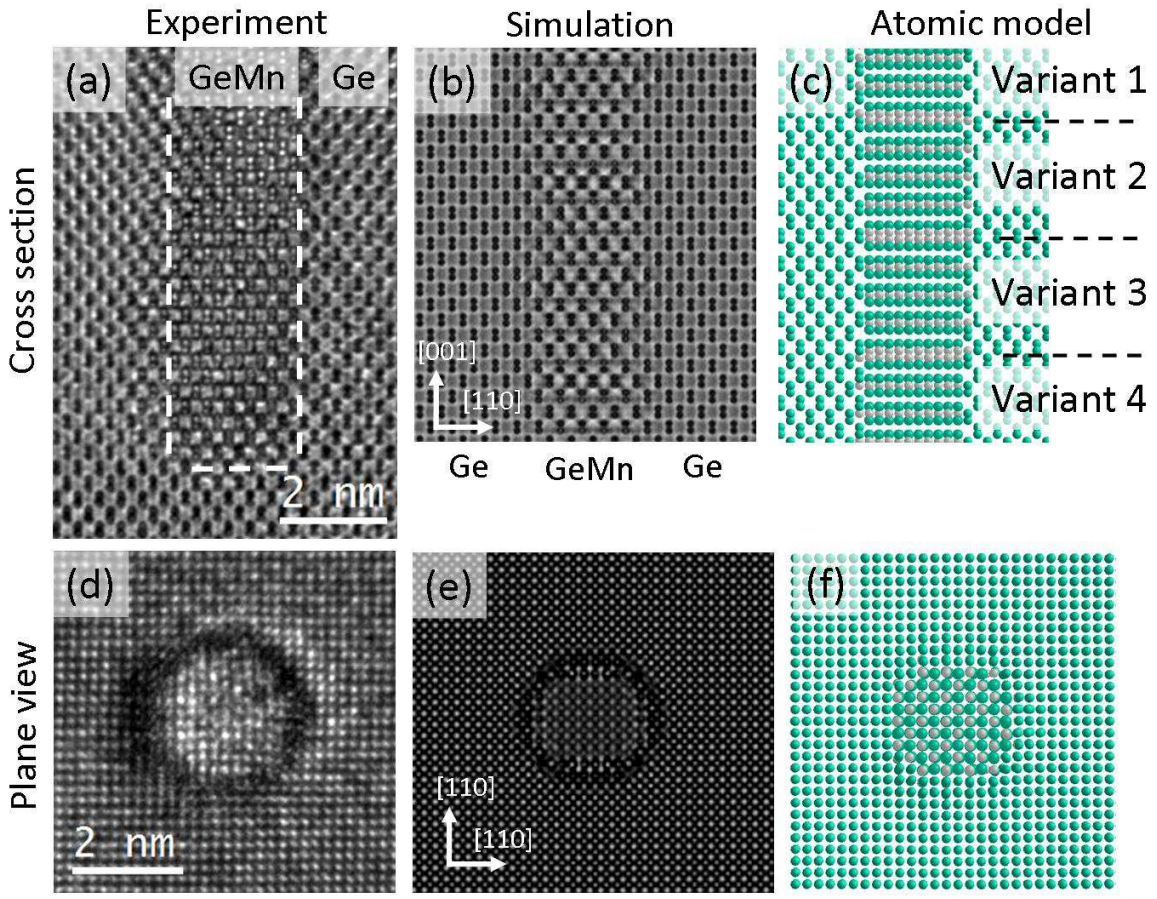

Figure 5.16.: Comparison of experimental and simulated HRTEM image of a GeMn NC. (a) Cross-section and (c) plane view experimental HRTEM image. (b, d) Corresponding HRTEM image simulation with a α-phase in the NC.

These results show that the α-phase proposed by the atomistic models is compatible with the HRTEM observations if more than one variant is introduced. It is interesting to note that the α-phase also fits with the ferromagnetic properties of this system. The HRTEM simulations are indeed in good agreement with the experimental images: equivalent contrast in the NC and presence of the dark ring at the interface with the matrix.

5.3.3. Strain in the Ge matrix

Facing a two-phase system, strain distribution is also an important aspect for investigating the structure and the relaxation state. The strain distribution in the Ge matrix around NCs has been investigated using the so-called Geometrical Phase Analysis (GPA) [Take 96, Hytc 98]. The GPA method consists of numerical treatment of HRTEM images to get strain mapping. Displacements of the crystalline planes in strained areas with respect to an unstrained area, are measured from the Fourier transform of the HRTEM image. This is possible because the phase of the Fourier components is directly related to the component of the displacement field [Take 96, Hytc 98] . However, a quantitative analysis requires a "good" reference area. In our case of plane view geometry, the reference lattice parameter is measured over the whole image. Since the GeMn layer is grown epitaxially on the Ge substrate, the average in-plane lattice parameter in the GeMn layer is identical to that of the Ge substrate and can then be used as reference.

Using two non-collinear reflections in the Fourier transform of the HRTEM image (here the (220) and $(2\bar{2}0)$ reflections), the 2D strain tensor was calculated. The strain along the [110] direction was calculated as $\varepsilon_{xx} = \partial u_x/\partial x$ and the one along the $[1\bar{1}0]$ direction as $\varepsilon_{yy} = \partial u_y/\partial y$, where u_x and u_y are the components of the displacements field along the [110] and $[1\bar{1}0]$ directions, respectively. The shearing ε_{xy} is calculated as $\varepsilon_{xy} = (\partial u_y/\partial x + \partial u_x/\partial y)/2$ [Rouv 05].

5.3.3.1. Amorphous nanocolumns

Fig. 5.17 shows GPA analysis on experimental and simulated images of an amorphous NC. The experimental HRTEM image acquired at 400 kV on the JEOL 4000EX microscope, is shown in Fig. 5.17(a). A Wiener filter implemented as a plug-in[2] in Digital Micrograph was applied to the experimental HRTEM image to remove noise [Mark 96, Kila 98]. The upper row (Fig. 5.17 (b, c, d)) show the experimental $\varepsilon_{x.x}$, ε_{yy} and ε_{xy} strain map obtained after processing this experimental HRTEM image.

[2]See Dave Mitchell's Digital Micrograph scripting website to download the HRTEM filter: www.dmscripting.com/hrtem_filter.html

The lower row (Fig. 5.17 (e, f, g)) show ε_{xx}, ε_{yy} and ε_{xy} strain map calculated using a simulated HRTEM image of a relaxed amorphous NC. The atomic model used in the simulation was provided by Fréderic Lançon from INAC and was obtained with atomistic simulations conducted using Stillinger-Weber potentials [Stil 85]. The disorder was introduced in the NCs by placing Ge atoms at random positions inside them with the same density as in the diamond structure. This results in compressing strain exerted to the Ge matrix [Tard 10].

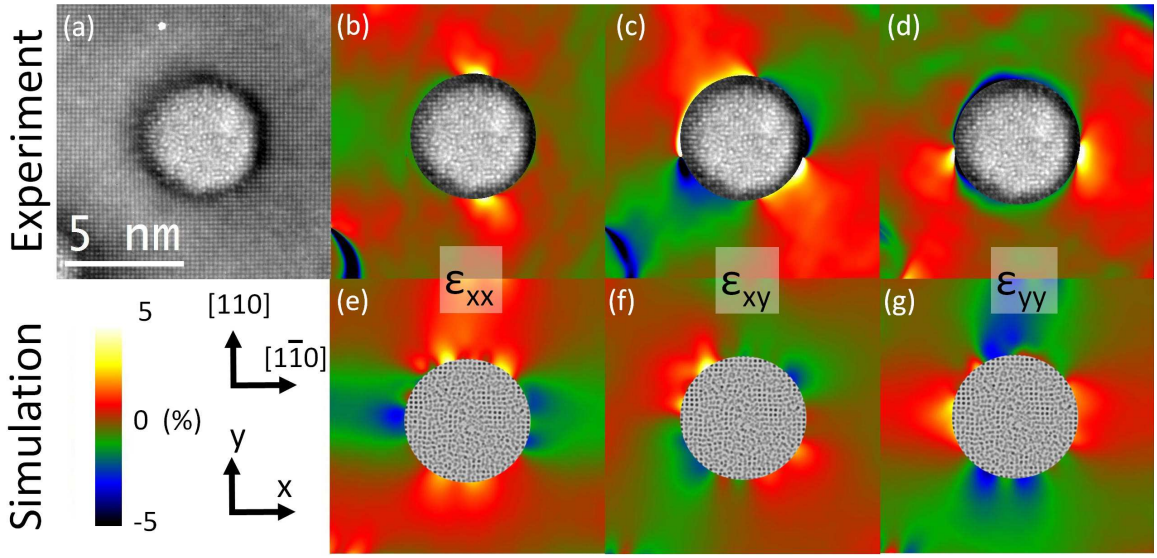

Figure 5.17.: GPA around an amorphous NC. (a) HRTEM image of an amorphous NC. (b, c, d) experimental ε_{xx}, ε_{yy} and ε_{xy} strain map obtained from the HRTEM image shown in (a). (e, f, g) Simulated ε_{xx}, ε_{yy} and ε_{xy} strain map.

The experimental and simulated ε_{xx} strain map are shown in Fig. 5.17(b) and (e), respectively. The x-direction is defined as parallel to the $[1\bar{1}0]$ direction. Since the NC compressed the Ge matrix, the distance between the $(2\bar{2}0)$ planes is smaller than the reference value at the left and the right of the NC, leading to $\varepsilon_{xx} < 0$ (green-blue colors) at these positions. Consequently, at the top and the bottom of the NC, the (220) planes are larger than the reference value because of the elastic volume conservation leading to $\varepsilon_{xx} > 0$ (red-yellow colors) at the top and the bottom of the NC. Due to the symmetry of the compression exerted by the amorphous NC on the matrix, the same trend is observed in the ε_{yy} strain map (Fig. 5.17(d) and (g)) with respect to the (220) planes, the y-direction being defined as parallel to the [110] direction. Good agreement is found between experimental and simulated maps confirming the compressive state of the matrix.

Fig. 5.18 shows the GPA of several amorphous NCs. The same trend is observed as in case of a unique amorphous NC Fig. 5.17, confirming that the amorphous NCs exert compressive strain to the Ge matrix.

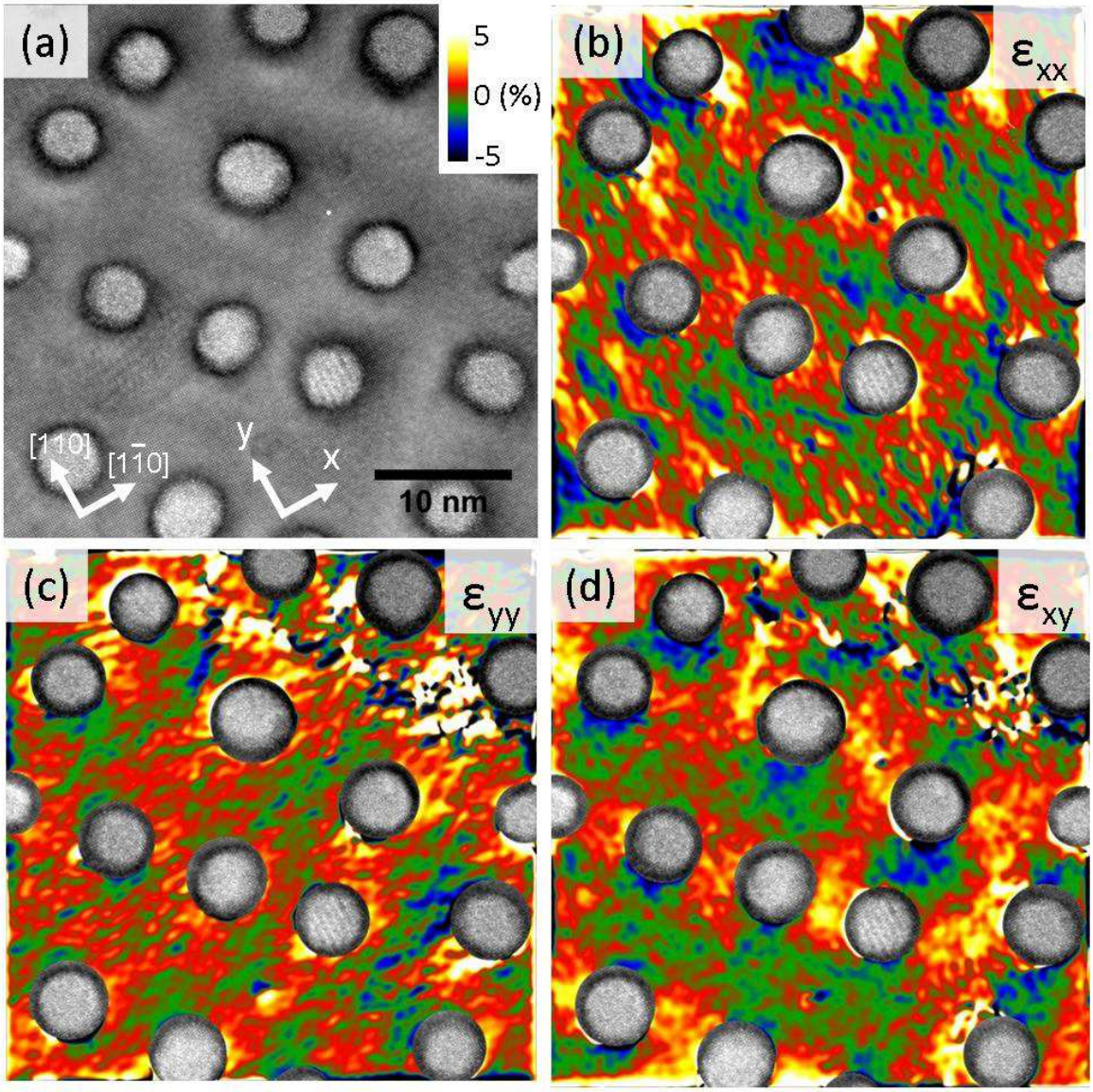

Figure 5.18.: GPA of the Ge matrix of a GeMn sample containing amorphous NCs. (a) Plane view 400 kV HRTEM images. (b, c, d) ε_{xx}, ε_{yy} and ε_{xy} strain map. Piece of image have crop in the HRTEM and paste on the strain map as guide to the eye.

5.3.3.2. Crystalline nanocolumns

Fig. 5.19 shows the GPA of crystalline NCs performed on a ADF-HRSTEM image which was acquired at 200 kV with a collection angle of 50-160 mrad. Note that new highly stable microscope allows now to perform such GPA of ADF-STEM images which was not possible before [Chun 10, Rouv 11]. In this collection condition, strain effect can still be observed with a bright contrast at the interface matrix/NC. Lowering the camera length reduces the contrast due to strain, but also reduce the SNR. Since we are not interesting in the analysis of HAADF contrast, the ADF-HRSTEM image have been acquired at camera length which provides high SNR. This allows to decrease the pixel acquisition time down to 4 µs without sacrificing the SNR. The acquisition of large images (up to 6144 × 6144 px) is then possible in an reasonable time (about 2 min).

The field of view of the image shown in Fig. 5.19 is 2.5 times larger than that of the HRTEM image shown in Fig. 5.18. The crystalline NCs have a diameter of 2-3 nm to be compared to 5-7 nm for the amorphous ones. For the same nominal Mn concentration, the NC density is then higher as can be seen in Fig. 5.19, with a distance between the NC of about 5 nm.

Because of the structural disorder in the NCs we discussed before, the contribution of the high resolution patterns in ADF-HRSTEM images is very low inside the NCs. It follows that the amplitude of the Fourier component at these positions is very low and can be used to segment the position of the NCs. Using this method, the strain value was set to zero at the position of the NCs, in order to recognized the position of the NCs. We note here that the ADF-HRSTEM imaging mode compared to HRTEM offers easier measurement of the strain due to the following reason: the ADF signal being incoherent, it is not so sensitive to phase discontinuities (due to thickness, focal variation or lattice plane bending) as compared to the coherent imaging. This effect can be observed in the upper right part or the ε_{yy} and ε_{xy} strain map shown in Fig. 5.18(c) and (d), respectively. In this particular case, there is phase discontinuities in the phase image of the $(2\bar{2}0)$ reflections that create strong strain variations in the upper right part of the ε_{yy} and ε_{xy} strain maps. In good stability conditions of the system, GPA are more robust on HAADF than on HRTEM images and provide larger field of view (up to 400 x 400 nm^2 [**?**]).

The acquisition of the image is performed lines by lines and scanning instabilities can be observed as small shifts between lines. They can be corrected on the phase image [Chun 10, Rouv 11]. For example, in the case of the ε_{xx} strain map (x is defined as parallel to the $[1\bar{1}0]$ direction), the scanning instabilities have been corrected by measuring the scanning distortion in the [110] direction, the latter being perpendicular to the $[1\bar{1}0]$ direction. For the ε_{yy} strain map, another image with a rotation of 90° have

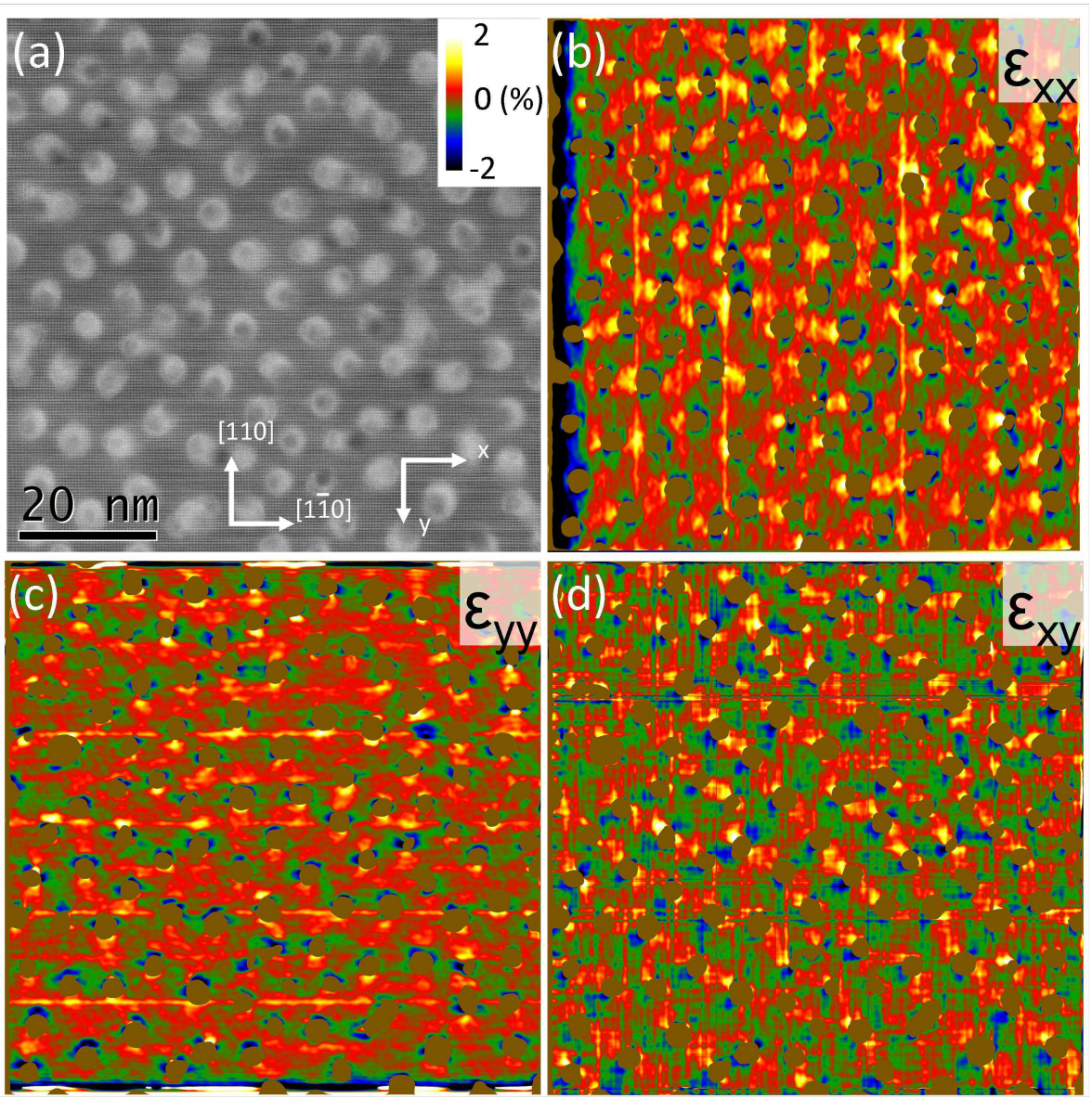

Figure 5.19.: GPA of the Ge matrix of a GeMn sample containing crystalline NCs. (a) Plane view 200kV ADF-HRSTEM images. (b, c, d) ε_{xx}, ε_{yy} and ε_{xy} strain maps. The position of the NC are reported in the strain map by using a threshold on the amplitude map of the Fourier component (not shown here).

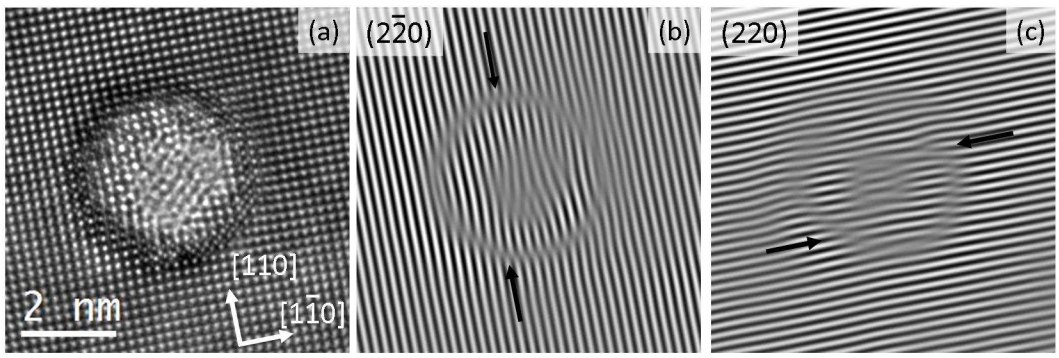

Figure 5.20.: (a) HRTEM images of a NC in the [001]-zone axis. (b) ($\bar{2}$20)- and (c) (220)-Bragg filtered images. The dislocations are indicated by arrows in (b) and (c).

been acquired and the scanning distortions have been corrected. Nevertheless, vertical and horizontal lines can be observed in the ε_{xx} and ε_{yy} strain maps, respectively. They are due to systematic shift with the lines caused by the scanning unit (Gatan Digiscan 2).

Finally, we found out that the measured strain distribution in the case of crystalline NCs is in the opposite side of that of amorphous NCs. At the left and the right of NCs the ε_{xx} value is positive, meaning that the distance between the $(2\bar{2}0)$ plane is larger than the averaged value. At the top and the bottom the ε_{xx} value is negative. Corresponding observation can be made with the ε_{yy} strain map. This may have two explanations:

1. an in-plane lattice parameter of the crystalline GeMn NC smaller than the Ge diamond,
2. an in-plane lattice parameter of the crystalline GeMn NC larger than the Ge diamond with an incoherent interface.

Fig. 5.20 shows an HRTEM images of a NC and the corresponding $(\bar{2}20)$- and (220)-Bragg filtered images. The Bragg filtered images clearly evidence the incoherent interface between the NC and the matrix. Dislocations can be observed as indicated by the black arrows in Fig. 5.20(b,c). This indicates that from the two cases mentioned above, the second one is the most relevant.

5.3.4. Discussion

All the results presented above provide detailed insights on the composition and the structure of the GeMn NCs embedded in Ge matrix. Note that up to now, only few quantitative and accurate results have been reported, in that way our studies provides new experimental results.

First of all, we showed that the sample preparation is as explained in the previous chapter a key parameter to control in order to obtain an artifact-free and clean sample. We have used the wedge-polishing method which has provided very good TEM specimens for both EELS and HRTEM analysis.

Absolute chemical measurements using STEM-EELS in SI mode evidenced:

- a significant increase of the total atomic density inside the NCs (up to 82 ± 8 atoms $\cdot$ nm^{-3}) as compared to the Ge matrix atomic density (44 ± 1 atoms $\cdot$ nm^{-3}). This is in good agreement with the general trend in the GeMn system which consists in an increase of the density with increasing the Mn concentration.
- No Mn was detected in the Ge matrix in the limit of the experimental measurement method (< 1 %)

- We measured the chemical profiles of Mn and Ge and evidence i) a Mn concentration significantly high in the GeMn NCs [Arra 11] up to 60 % in the center with an average value integrated over the whole NC of 33 %, ii) a reduction of the Ge atomic density inside the NCs compare to the Ge matrix

Complementary APT experiments showed that the Mn concentration in the matrix is lower than 0.1 % which is in good agreement with EELS measurements. Significant Mn concentration fluctuations or even discontinuity along the NCs is observed on the reconstructed volume. The paramagnetic contribution at very low temperature in the magnetization curve was so far attributed to diluted Mn atoms in the matrix [Devi 08]. The APT observation allows us to revise this hypothesis and propose that the paramagnetic signal is rather explained by the presence of fragments of NCs in which the Mn concentration is reduced down to the limit where Mn atoms are paramagnetic.

Correlation of APT experiments and TEM investigations highlights interesting features on the morphology of the NCs. Indeed it was evidenced that the NC can be bent or not go through the whole GeMn layer thickness which may have a significant effect on the determination of the Mn concentration on measurement made on TEM projected sample. Moreover, splitting of some of the NCs has been clearly observed both in APT reconstruction and plane view TEM imaging.

The theoretical work of Arras *et al.* [Arra 12] highlighted the existence of a metastable phase: the α-phase. It was argued that the α-phase family gives rise to a second minimum of energy formation versus stoichiometry, compatible with a spinodal decomposition mechanism. This simple cubic phase exhibits the same Ge density than the diamond Ge phase, but have supplementary interstitial Mn atoms in the unit-cell. Our experimental chemical measurements show that the Ge density slightly decrease from 44 ± 1 atoms $\cdot$ nm^{-3} in the Ge matrix to 35 ± 1 atoms $\cdot$ nm^{-3} in the GeMn NCs, whereas the Mn density increases from 0 in the matrix to 55 ± 5 atoms $\cdot$ nm^{-3} in the NCs. It follows that the overall atomic density increases in the NCs as compare to the matrix. From this observation, it is clear that the GeMn NCs does not form a solid solution. However, even if the α-phase can have different stoichiometry (see Fig. 5.14), the Mn concentration is not supposed to exceed 50 % with the Ge and Mn density of 43.6 atoms $\cdot$ nm^{-3}[3]. Theoretically, the maximal atomic density in the α-phase can be as high as 87.2 atoms $\cdot$ nm^{-3}. We can then assume that the decrease of Ge density is compensated by substitution by Mn atoms. The phase in the GeMn NCs could then consist on a phase based on the geometry of the α-phase, but with substitutional Mn atoms on Ge sites. In that way we can explain both the high concentration of Mn and the decrease of the Ge atomic density inside the NCs and then confirm the presence of a α-phase based structure. These new results should now be confirmed by simulations.

[3]The calculated lattice parameter of the α-phase are taken in [Arra 12].

To complete the chemical results, the structure of GeMn NCs has been studied using HRTEM imaging:

- The investigations of GeMn layers grown at 150 °C allows to clearly attribute the diffuse ring observed in ED or on power spectrum to the amorphous structure of the NCs. Surface amorphization due to sample preparation can be then ruled out.
- The amorphous ring is absent on HRTEM observations of GeMn layers grown at 130 °C indicating that these NCs are not amorphous. Indeed, highly distorted crystal patterns and corresponding Bragg reflections can be observed in HRTEM images and their power spectrum, respectively. Most the GeMn NCs being continuous and the specimen thinner than the nominal GeMn layer thickness, the superposition of NCs with Ge substrate can be ruled out. The observation of relaxed structure and discontinuity of the lattice at the interface NC/matrix confirms this hypothesis. Crystalline ordering located on NCs in HRTEM images of plane view specimen can be then attributed to the crystal structure the NC. The absence of systematic order between the NC and the matrix is in good agreement with the experimental observation concerning the absence of additional Bragg reflections in x-ray scattering or ED investigations [Devi 08, Tard 11].

The HRTEM observations on crystalline NCs were compared to the model of the α-phase suggested by Arras and co-workers. The symmetry of the α-phase being different from that of the diamond Ge, a super-structure should appear on observations in the [001]-zone axis which is not the case on most of the NCs. The α-phase can generate two variants by changing the origin of the lattice with respect to the diamond Ge matrix, and the combination of these two different variants cancels the super-structures. The interface energy between these two variants being low, the total energy formation is found to be still lower than the other possible crystal structures [Arra 12]. The combination of different variants of the α-phase is then expected. Nevertheless experimentally, the presence of a superstructure was observed only a few time as shown in Fig. 5.11(e). Its occurrence could be explained in truncated NC, *i.e.* NC that does no go through the whole lamella as revealed by the APT experiment. In this case, it could possible that a NC have only one variant, thus exhibiting the super-structure.

HRTEM investigations were also performed in cross-section view along the [100]- and [110]-zone axis, with the aim to find additional reflections that could allow the determination of the crystal structure. Due to the superposition of the disordered interfacen the matrix and the NC, it is too hard task to detect any supplementary Bragg reflections on the FFT of the HRTEM images.

Finally, the strain in the Ge matrix due to the presence of the NCs was studied using GPA performed on HRTEM or ADF-HRSTEM images. A strong difference was observed between the amorphous and the crystalline NCs:

- in the amorphous case, the NCs exert compressive strain to the Ge matrix,
- whereas in the crystalline case, the Ge matrix is submitted to tensile strain.

The second case can be explained by a larger in-plane lattice parameter in the NC and a incoherent interface between the NC and the matrix. This is in good agreement with the observation of additional Bragg reflections on the power spectrum of HRTEM images or SAED patterns (see sec. 5.3.2.2), if we assume that they could be attributed to a cubic structure with a slightly larger lattice parameter. Finally, this could corresponds to the calculated lattice parameter of the α-phase, that is 2.5 % higher in the a direction.

5.4. GeMn nanocolumns embedded in GeSn matrix

In the previous section, it was shown that Ge(Mn) gown by MBE on Ge stabilizes during growth in Ge(Mn) nanocolumns embedded in a Ge matrix. These nanocolumns present remarkable ferromagnetic properties. The possible incorporation of Mn into strained Ge nanostructures leading to the formation of a GeMn diluted magnetic phases, free of Mn-rich precipitates, is an extremely interesting phenomenon, which clearly requires further investigations [Xiu 10]. In order to give some more insight into the incorporation of Mn in strained materials, we report here on the structural and magnetic properties of Ge_{1-x-y} Sn_xMn_y alloys epitaxially grown on Ge (001). This system has been investigated as the lattice parameter of $Ge_{1-x}Sn_x$ is larger than the one of Ge and increases with Sn concentration. The lattice parameter difference between Ge and Sn is of about 15 %.

5.4.1. Pseudomorphic growth of GeSn and GeSnMn films

GeSn alloy with up to few percent of Sn, can be grown coherently on Ge(001), being strained by the Ge (001) substrate [Mene 04, Baue 02, Vinc 11]. In Fig. 5.21, we show a HRXRD reciprocal space map (obtained by Edith Bellet-Almaric at INAC) around the $(\bar{1}\bar{1}5)$ Bragg peak of a 250 nm thick $Ge_{0.94}Sn_{0.06}$ layer grown on Ge(001). Two peaks have been observed: the more intense corresponding to the Ge Bragg peak and the second one corresponding to the GeSn Bragg peak. Both peaks have the same Q_x, *i.e.* in-plane parameter showing clearly that the 250 nm thick GeSn layer containing 6 % of Sn is still fully strained to Ge substrate. However the GeSn Bragg peak shows a small asymmetry towards lower Q_z values (*i.e.* lower 2θ values) which may indicate the beginning of lattice relaxation.

For this work, two GeMn samples, one GeSn sample and three GeSnMn samples named S1 to S6 have been grown on Ge(001). The grown layers are 80 nm thick except in the case of S4, which has been 240 nm thick. Their respective concentrations of Sn and Mn are indicated in Tab. Tab. 5.1.

Sample name	Sn concentration (at. %)	Mn concentration (at. %)
S1	0	10
S2	1.4	6
S3	3.6	10
S4	3.6	0
S5	0	6
S6	3.6	6

Table 5.1.: Sn and Mn concentrations in samples S1 to S6.

In Fig. 5.22(a) we show the $\theta - 2\theta$ HRXRD spectra around the (004) Ge reflection (around 66 deg) for samples S1, S2 and S3. For both samples S2 and S3 a clear peak corresponding to the epitaxial layer is observed. The position of the different peaks is identical to their counterpart without Mn (not shown here). This shows that the codeposition of Mn with Ge and Sn, does not influence the out-of-plane parameter of the epitaxial layer. In all three spectra one can also notice thickness interferences, which are signature of a homogeneous layer thickness and very low interface roughness. Fig. 5.22(b) shows the reciprocal space map around the $(\bar{1}\bar{1}5)$ Bragg peak of sample S3, with the highest content of Sn and Mn investigated in this work. The peak corresponding to the GeSnMn layer has the same in-plane lattice parameter as the Ge substrate, meaning that all the three GeMnSn layers are fully strained to the Ge(001).

In Fig. 5.23 we show HRTEM observations of sample S3: in cross-section (Fig. 5.23(a)) and in plane view (Fig. 5.23(b)). Cross-section observations reveal the existence of nanometer sized, vertical columns, almost continuous along the growth direction confirmed by the plane view observations. Moreover, the interface Ge/GeSnMn is perfectly coherent, confirming the HRXRD observations. The growth condition (Mn concentration and temperature) of sample S3 were the same than that of the GeMn sample shown in Fig. 5.11. The same distribution than in case of the GeMn sample is observed, with a NC size distribution and average slightly broader and larger than expected. This could be due to the presence of Sn atoms or by a higher substrate temperature during the growth coming from the radiation of the Sn effusion cell. As mentioned previously, increasing the growth temperature increase the NC size.

An HRTEM images in the [001]-zone axis of sample S2 and its corresponding power spectrum are shown in Fig. 5.24(a) and (b), respectively.

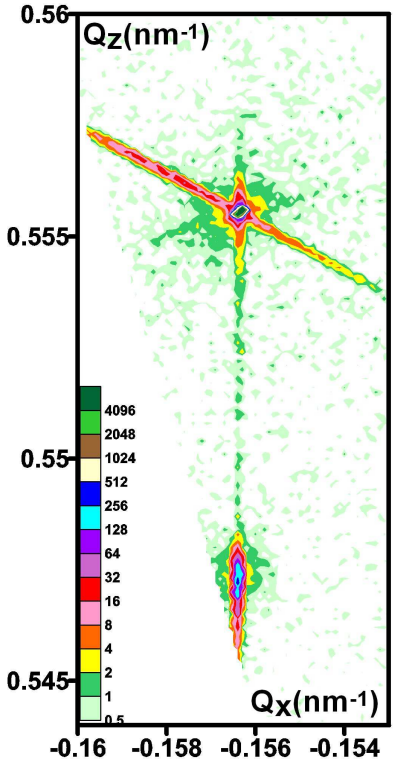

Figure 5.21.: X-ray map around the $[\bar{1}\bar{1}5]$ Bragg peak of a 250 nm thick $Ge_{0,94}Sn_{0,06}$ layer grown on Ge(001).

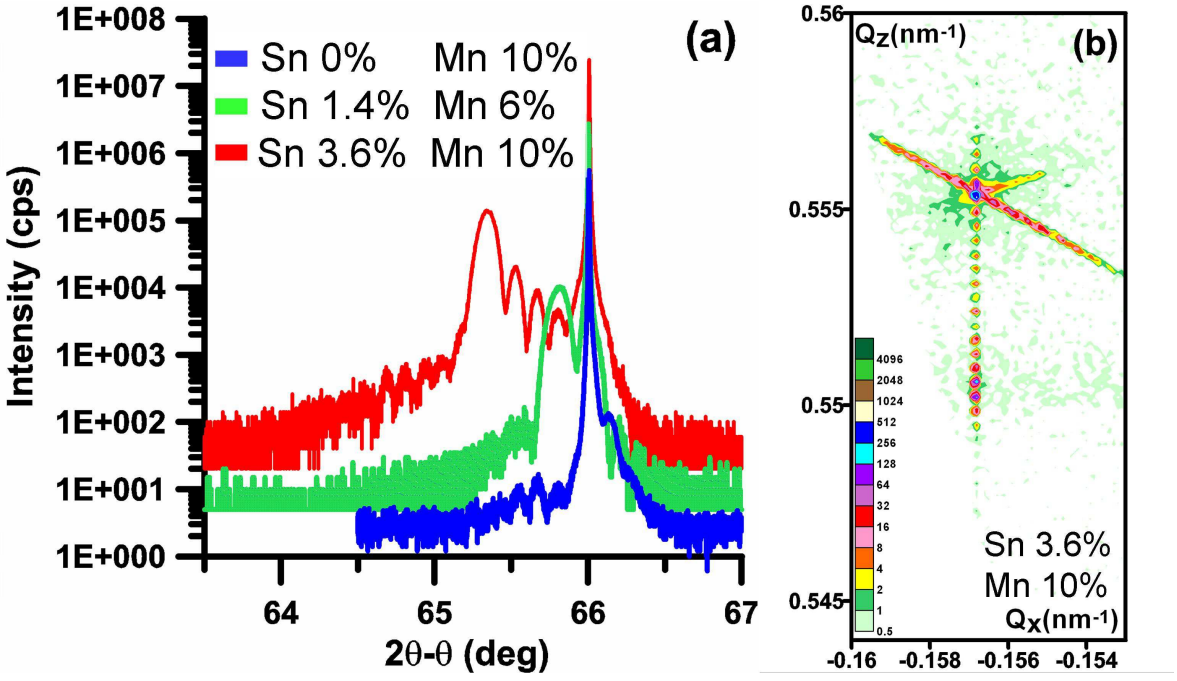

Figure 5.22.: (a) $\theta-2\theta$ X-ray diffraction spectra for samples S1, S2 and S3. (b) X-ray map around the Bragg peak of the S3 sample.

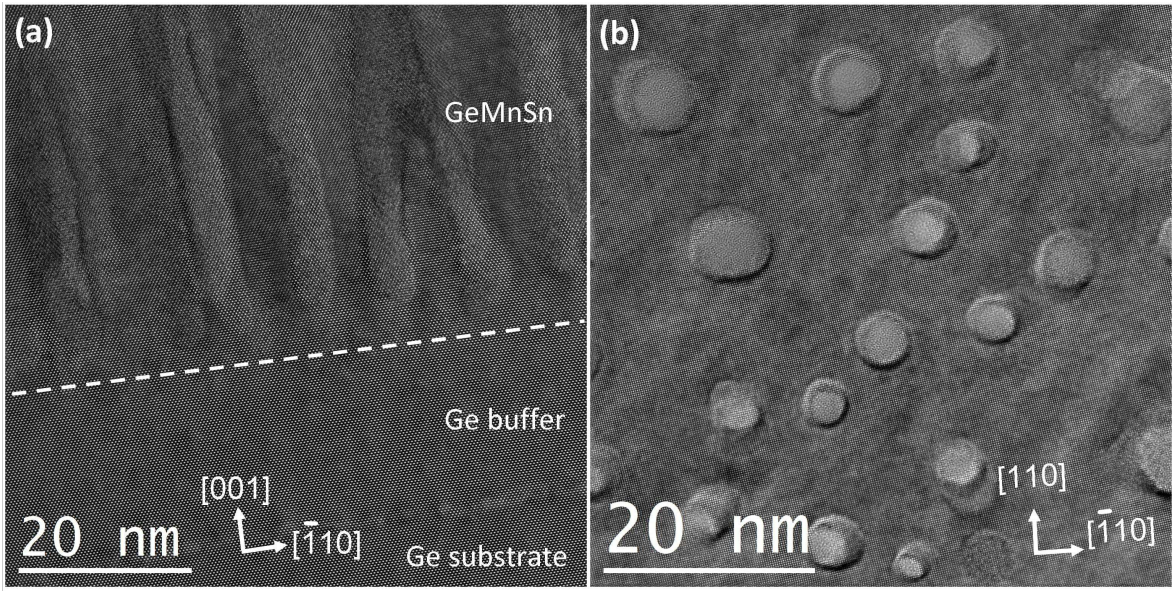

Figure 5.23.: HRTEM observations of the S3 sample: in cross section (a) and in plane view (b).

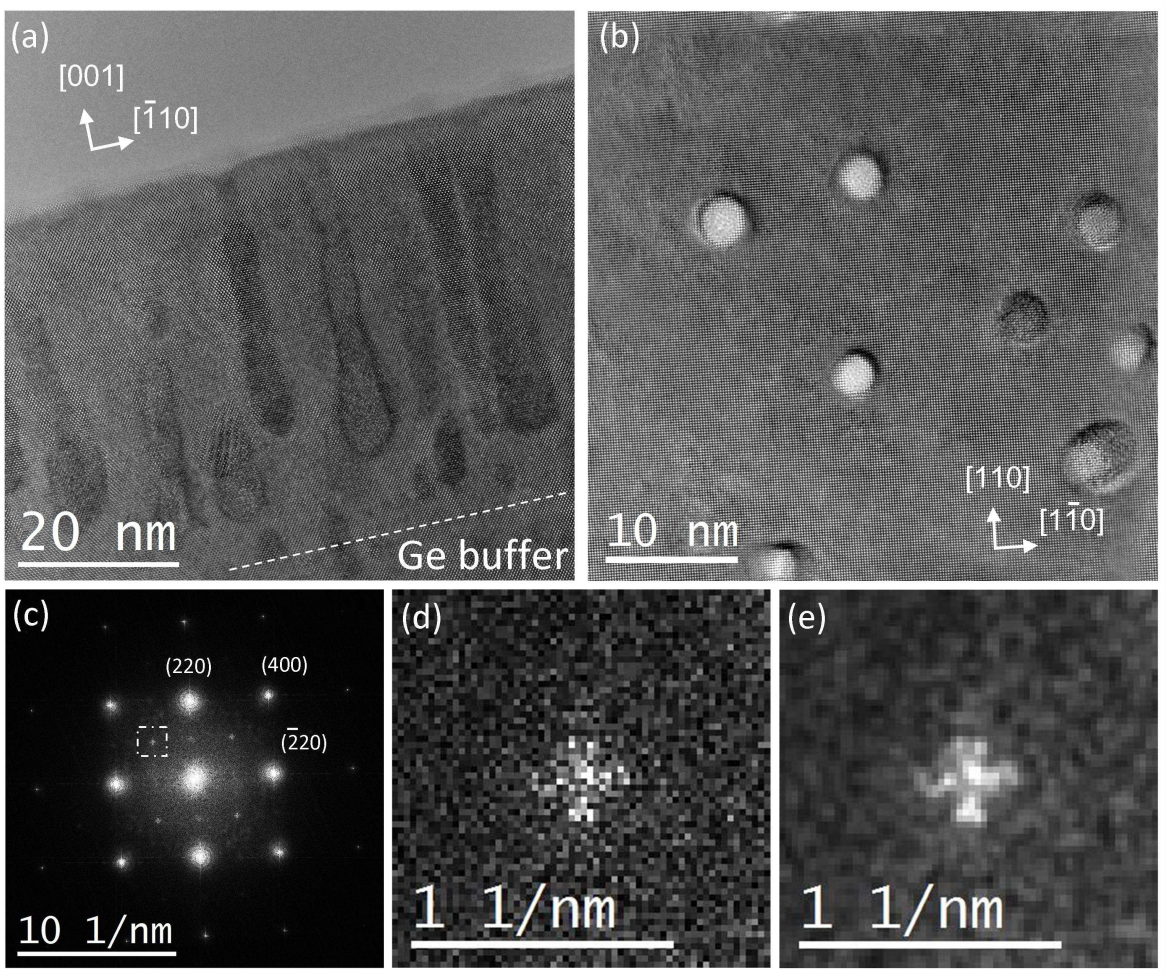

Figure 5.24.: (a-b) HRTEM images of the S2 sample in the [110]- and the [001]-zone axis. (c) Power spectrum of the whole image in (b). (a) Zoom on the {020} reflections as indicated by the dashed square in (c). (e) Smoothed image of (d).

As it can be seen on the typical HRTEM images the density of the NC is lower as it was already noticed for GeMn layer: lower concentration (6 % for sample S2) provides lower NC density. A zoom in the area indicated by a dashed square in Fig. 5.24(c) is shown in Fig. 5.24(d). It points out the presence of a weak reflection located at the {200} reflections of Ge crystal structure, indicating that the symmetry of the Ge diamond structure is broken. A smoothed image of this reflection shown in Fig. 5.24(e) highlights more clearly the particular symmetry of this reflection. SAED patterns have been also acquired (Fig. 5.25) and showed that the {200} reflections have the symmetry of a cross with the two branches oriented along the [110] and [1$\bar{1}$0] directions (Fig. 5.25(c)). The presence of these reflections is characteristic of the GeSnMn layers since it has been observed neither in GeSn layers nor in GeMn layers. Fig. 5.26(a) shows a HAADF-HRSTEM images of S2 sample.

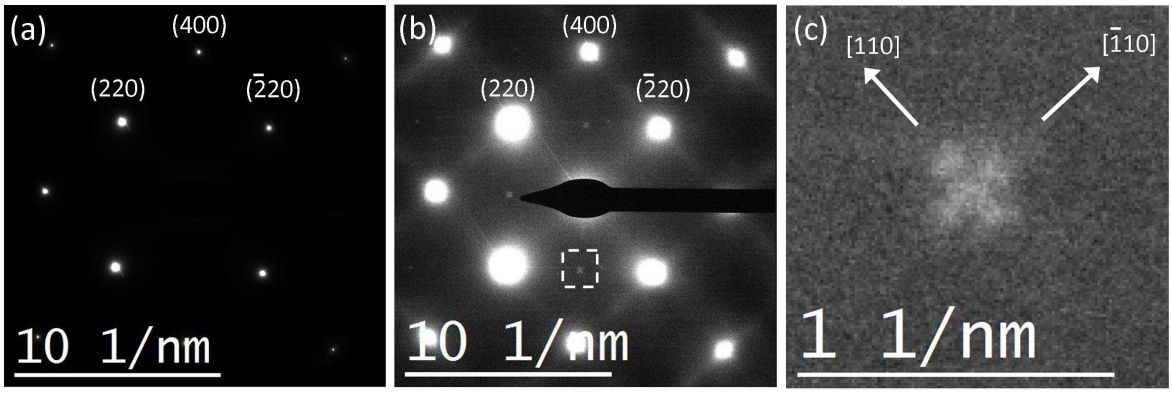

Figure 5.25.: SAED observation of S2 sample. (a) and (b) display the same pattern on two different intensity scale: the full range intensity for (a) and saturated intensity for (b). (c) zoom on the (0$\bar{2}$0) reflections.

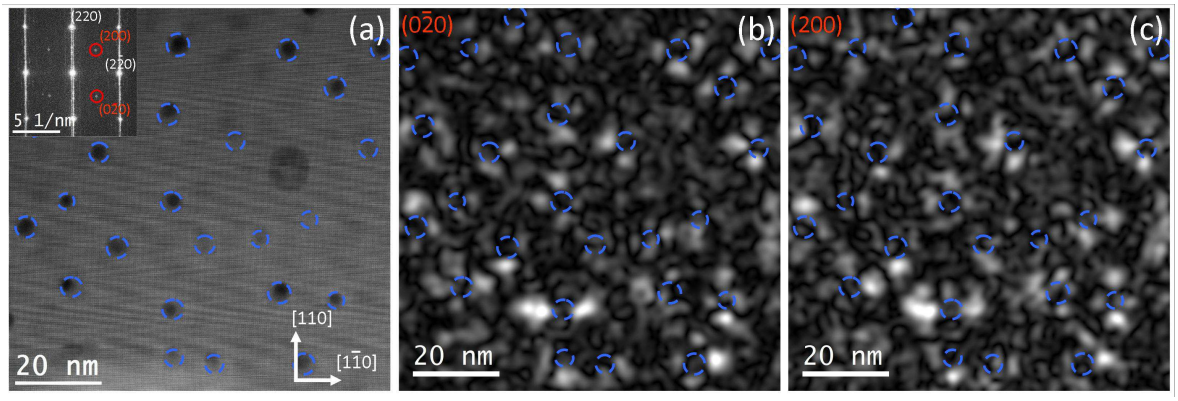

Figure 5.26.: (a) HAADF-HRSTEM image of S2 samples. In the inset of (a) shows the power spectrum of the HAADF images in (a). (b, c) Amplitude of the Fourier component corresponding to the (0$\bar{2}$0) and (200) forbidden Bragg reflections, which are marked by red fill circles in the inset of (a). The blue dashed circle indicated the position of the NCs.

The {200} forbidden Bragg reflections can be observed once again in the power spectrum shown in the inset of Fig. 5.26(a) and marked by red fill circles. In order to locate these reflections in the direct space, we investigated the amplitude of the Fourier components corresponding to these reflections. Fig. 5.26(b) and (c) shows the amplitude maps of the {200} reflections. The blue dashed circles indicate the positions of the NCs as determined from the HAADF-HRSTEM images shown in Fig. 5.26(a). These amplitude maps evidence that the reflections comes from region located close to the NCs and the amplitude distribution has a particular cross shape which is higher in the [110]- and the [1$\bar{1}$0]-directions than in the [100]- and the [010]-directions, similarly to the symmetry of the {200} forbidden Bragg reflections in Fig. 5.25(c). This result will be considered in more details in the following and correlate with EELS measurements. We can notice here that this analysis performed using HAADF-HRSTEM images provides less noisy results than using HRTEM images: SNR of such weak reflections in the fast Fourier transform is much higher in HAADF images than in BF/HRTEM images.

5.4.2. Chemical analysis by EELS

Fig. 5.27 shows the Ge, Mn and Sn maps obtained by chemical analysis using HRSTEM-EELS on plane-view measurements (along the [001] zone axis) of S2 sample. We observe:

- in the Ge map (Fig. 5.27(a)), the dark disks corresponding to the NCs, which have lower Ge contents with respect to the matrix,
- in the Mn map (Fig. 5.27(b)), it appears clearly that the Mn content is high inside the nanocolumns and no Mn is detected in the surrounding matrix. This means that the Mn content is much less than 1 % in the matrix,
- the Sn map (Fig. 5.27(c)) shows that the Sn content is homogeneous in the GeSn matrix forming a GeSn solid solution and that no Sn is detected inside the nanocolumns.

The interesting new feature is located at the interface between the nanocolumns and the GeSn matrix and around nanocolumns: an increase of the Sn content is observed, much higher than in the matrix. A typical area is indicated by a dashed circle in Fig. 5.27(c). The Mn (red) versus Sn (green) composite image in Fig. 5.27(d) highlights this feature showing also the Sn and Mn content profiles across a GeMn nanocolumn and the GeSn matrix in the inset.

The inhomogeneous Sn distribution can also be seen in the Sn and Mn map of S2 sample obtained by EELS on a cross section sample in Fig. 5.28. The comparison of the Mn and Sn maps confirms that the Mn rich NCs are Sn poor and that the NC are not completely continuous in the lower part of the GeSnMn layer. This indicates a small perturbation of the NCs nucleation due to the codeposition with Sn.

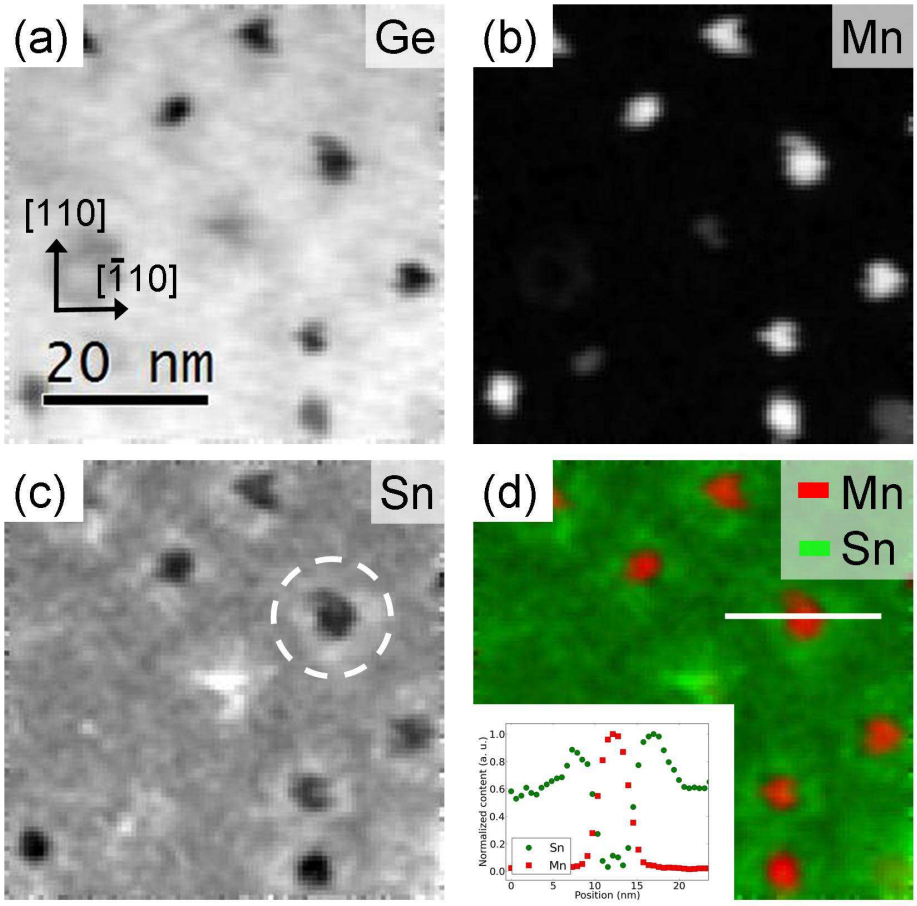

Figure 5.27.: Plane-view composition analysis obtained by STEM-EELS measurements of S2 sample: EELS maps of (a) Ge $L_{2,3}$, (b) Mn $L_{2,3}$,(c) Sn $M_{4,5}$. (d) Mn (red) versus Sn (green) composite image. An elemental profile of Mn and Sn across a GeMn nanocolunm and the GeSn matrix at the position marked by a while line in (d) is shown in the inset of (d).

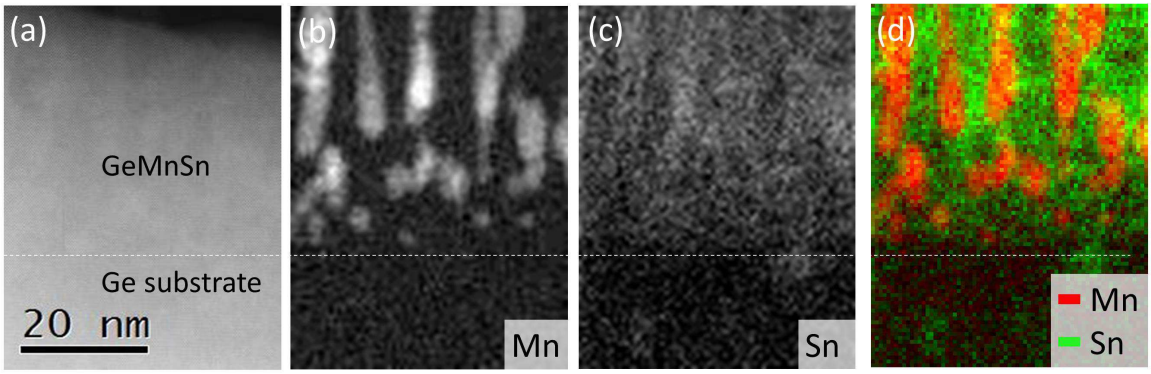

Figure 5.28.: Cross-section composition analysis obtained by STEM-EELS measurements of S2 sample: (a) HAADF images recorded simultaneously. (b) Mn $L_{2,3}$ and (c) Sn $M_{4,5}$ map. (d) Mn (red) versus Sn (green) composite image.

5.4.3. Local strain analysis

To complete, we also investigated strain distribution in the GeSnMn films using GPA. The strain mapping of sample S3, corresponding to the HRTEM image shown in Fig. 5.22(a) is displayed in Fig. 5.29. The non-collinear $(\bar{1}11)$ and $(1\bar{1}1)$ reflections have been used to obtain the in-plane (ε_{xx}) and out-of-plane (ε_{zz}) strain map represented on a color scale in Fig. 5.29(a) and (b) respectively.

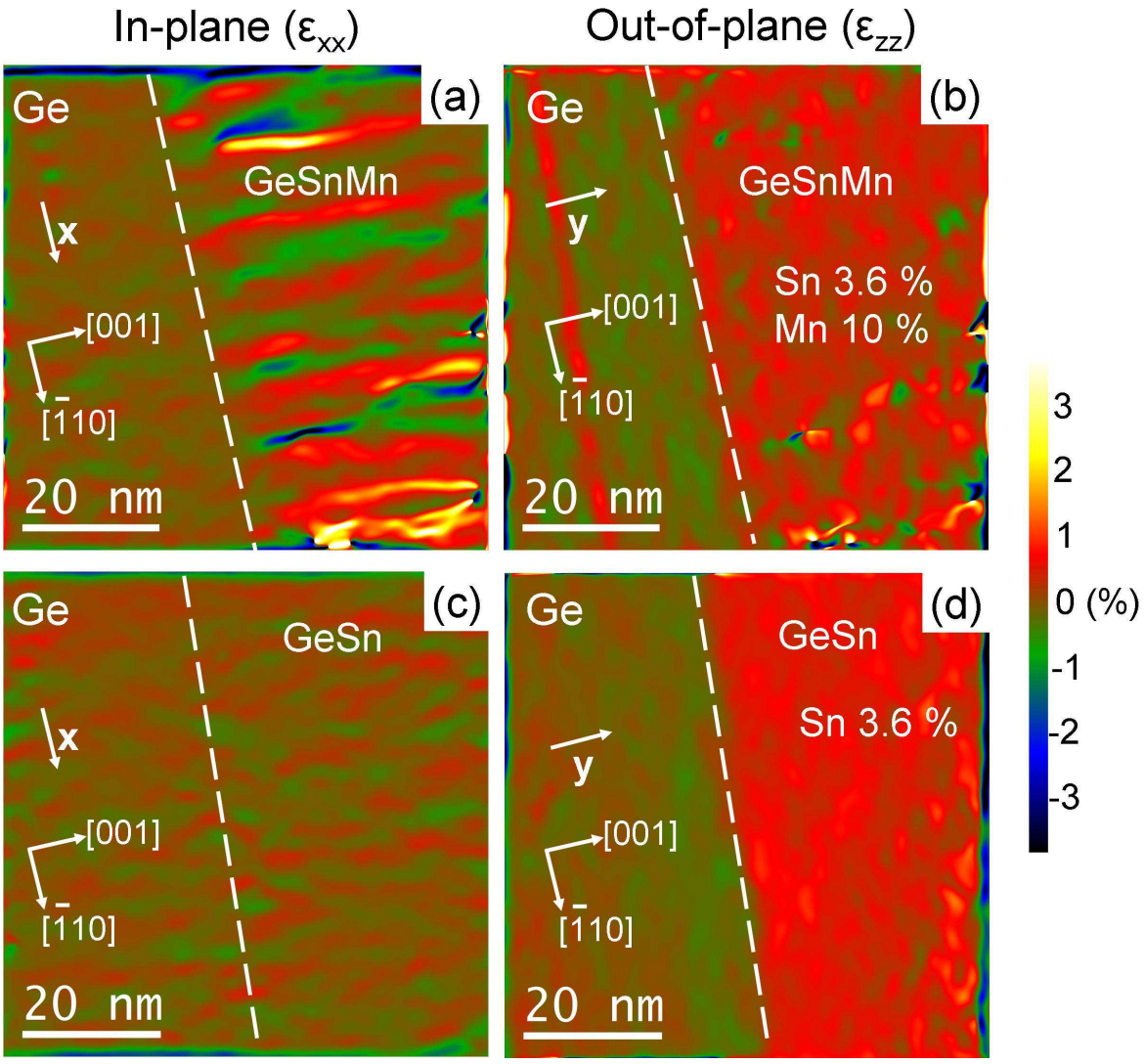

Figure 5.29.: GPA performed on HRTEM images of a $Ge_{0,84}Sn_{0,06}Mn_{0,10}$ film in [110]-zone axis (a-b) and a $Ge_{0,94}Sn_{0,06}$ film (c-d), both with 6 % Sn. (a,c) In-plane (ε_{xx}) and (b,d) out-of-plane (ε_{zz}) strain maps.

We also compare strain analysis of sample S3 with sample S4 (without Mn) to investigate the effect of the presence of the NCs on the GeSn matrix. The in-plane strain (ε_{xx}) and the out-of-plane strain (ε_{zz}) of sample S4 are shown in Fig. 5.29(c) and Fig. 5.29(d) respectively. The ε_{xx} maps of S3 and S4 films show that the average in-plane lattice

parameter is identical to the Ge one in both cases, in agreement with a perfectly coherent interface with the Ge substrate. Nevertheless, the presence of GeMn nanocolumns (Fig. 5.29(a)) leads to small fluctuation of the in-plane lattice parameter in the GeSn matrix around nanocolumns [Tard 10]. Moreover, the out-of-plane (ε_{zz}) deformation is homogeneous in the GeSnMn and GeSn films and is in both case positive, indicating tensile strain (compressive in-plane strain) with average value $\varepsilon_{zz} = (0.9 \pm 0.3)$ % (the same value was measured by HRXRD).

In-plane ε_{xx}, ε_{yy} and ε_{xy} strain maps obtained by GPA analysis on HAADF-HRSTEM image of a plane view sample, are displayed in Fig. 5.30. Qualitatively, same results are obtained as in case of GeMn layers consisting of crystalline NCs (see sec. 5.3.3.2): at the left and the right of NCs the ε_{xx} value is positive, meaning that the distance between the $(2\bar{2}0)$ plane is larger than its averaged value. At the top and the bottom the ε_{xx} value is negative. Corresponding observation can be made with the ε_{yy} strain map. The GPA (local analysis) and HRXRD (global analysis) shows that the presence of Mn-rich nanocolumns induces in-plane strain in the GeSn matrix around the nanocolumns, which however does not affect the out-of-plane deformation.

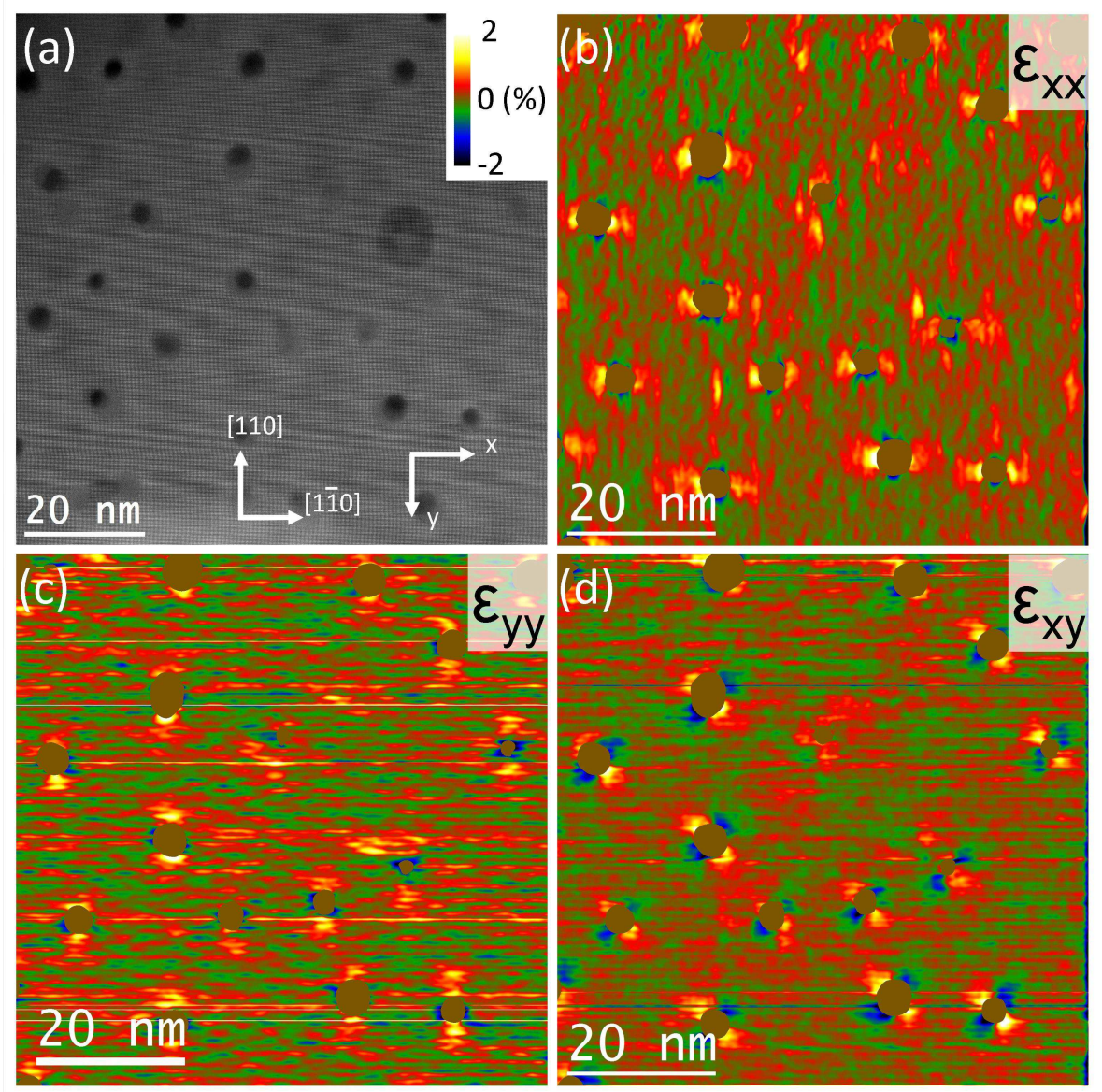

Figure 5.30.: GPA performed on HAADF-HRSTEM images of a $Ge_{0,926}Sn_{0,014}Mn_{0,06}$ film in [001]-zone axis. (a) HAADF-HRSTEM images and corresponding (b,c) in-plane ε_{xx}, ε_{yy} and ε_{xy} strain maps.

5.4.4. Magnetic properties

SQUID measurements are shown in Fig. 5.31 for two sets of samples containing 6 % and 10 % of Mn (measurement performed by Matthieu Jamet at INAC). For the fixed 6 % Mn content, we have studied three different samples with different Sn concentrations: sample S5, S2 and S6. Samples S1 and S3 with 10 % Mn have also been studied . The magnetic signals have been normalized to the sample mass and given in emu $\cdot$ g^{-1} in order to compare qualitatively the saturation magnetization of GeMn nanocolumns. As a whole, the magnetization curves look very similar with and without Sn.

However, in the following, we will not discuss about the Curie temperature of nanocolumns since their superparamagnetic behavior makes its accurate determination very difficult. Moreover, at low temperature, see Fig. 5.31(a,d), a $1/T$ parasitic paramagnetic signal from the Ge substrate, which varies from sample to sample, prevents from a direct comparison of saturation magnetization curves below 100 K. In the inset of Fig. 5.31(b,e), we show the magnetization curves recorded at 5 K for the highest content of Sn (3.6 %). At this temperature GeMn nanocolumns are ferromagnetic and their coercive field is of the order of 0.1 T irrespective of the Mn and Sn contents. In Fig. 5.31(a,b,d,e), it can be seen that, above 100K the incorporation of Sn in GeMn samples increases the magnetic signal and hence the magnetic moment per Mn atom. The same increase is observed in Zero Field Cooled-Field Cooled (ZFC-FC) curves as shown in Fig. 5.31(c,f). In addition, the ZFC peak is systematically shifted to higher temperatures which means that the columns blocking temperature is also increased by the incorporation of Sn. The blocking temperature is proportional to the columns volume and the magnetic anisotropy constant. In previous work [Jain 10], we have shown that the magnetic anisotropy of nanocolumns is dominated by shape anisotropy and thus proportional to M_S^2 where M_S is the saturation magnetization. Since M_S increases with the incorporation of Sn, we expect the blocking temperature to be higher, that is in agreement with the experimental findings. In parallel, the columns diameter in GeSnMn ($\sim$4 nm) is larger than in GeMn ($\sim$3 nm) grown in the same conditions. This difference can be due to the presence of Sn atoms or to a slightly higher substrate temperature during the growth (for instance from the radiation of the Sn effusion cell) which tends to increase the columns diameter. Increasing the columns diameter also leads to higher blocking temperatures as observed experimentally.

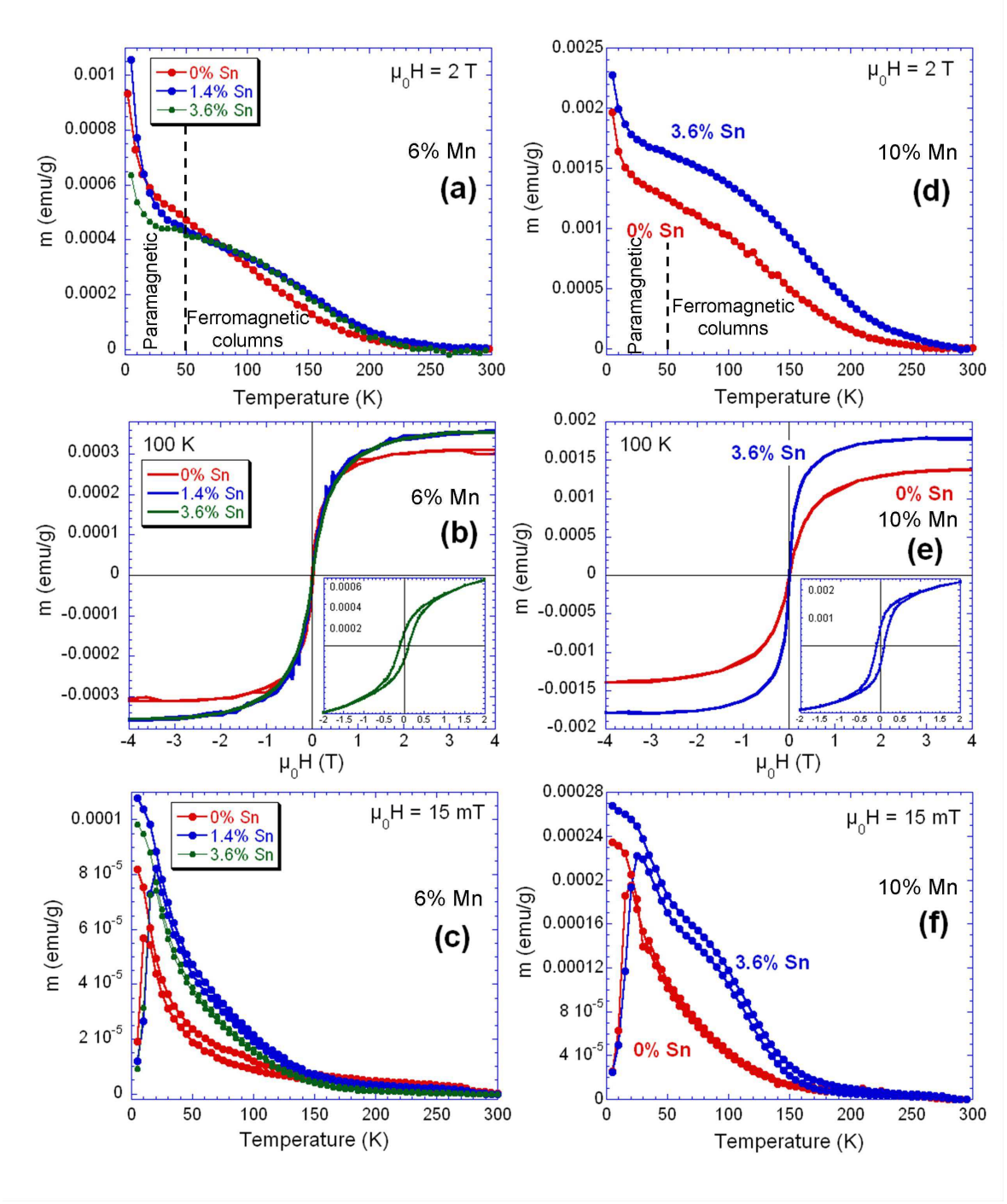

Figure 5.31.: SQUID results of GeSnMn film with 6 % Mn (a-c) and 10 % Mn (d-f). (a,d) Temperature dependence of the saturation magnetization. (b,e) Magnetization loops at 100 K, after subtracting the diamagnetic contribution from the substrate. (c,f) Zero field cooled-field cooled measurements carried out at 15 mT.

5.4.5. Discussion on GeMnSn films

HRXRD and HRTEM investigations of GeSnMn layers evidenced a pseudomorphic growth on Ge substrate. More precisely, HRTEM observations reveal the formation of NCs having similar features to those of GeMn layers. STEM-EELS mapping demonstrated that the GeSnMn layers consists of GeMn NCs embedded in a GeSn solid solution matrix. Sn segregation was observed at the interface between the GeSn matrix and the GeMn NC. The nucleation of the GeMn NCs appears slightly perturbed by the Sn codeposition. Nevertheless, the out-of-plane strain caused by the pseudomorphogic growth of GeSn matrix (up to 1 %) does not affect significantly the morphology and the structure of the GeMn NCs.

Local strain analysis obtained by GPA in plane view evidenced in-plane tensile strain around the NCs. This observation is similar to that of GeMn NCs in Ge pure matrix, confirming that the NC are formed of the same phase than in the GeMn layers.

The Sn segregation observed around the NCs could be strain-induced in order to released the in-plane tensile strain in the Ge matrix around the NCs. It is also interesting to note that the Sn segregation presents a particular shape: Sn segregates preferentially along the [110] and [1$\bar{1}$0] directions, exhibiting a cross shape. This can be explained by stress released in the anisotropic Ge materials. Due to its intrinsic anisotropy the Young's modulus is larger in the [110] direction than in the [100] directions [Wort 65]. The stress will be then preferentially released along the [110] directions, leading to a strain-driven Sn segregation not only at the interface GeMn/GeSn, but preferentially along the [110] directions.

The presence of the {200} forbidden Bragg reflections was observed in GeSnMn specimen oriented along the [001]-zone axis. It should be underlined that these reflections were only measured in case of plane view observations of GeMn and GeSn specimens, indicating that the occurrence of these {200} reflections is characteristic of the GeSnMn specimen. These reflections have the particularity to exhibit a cross shape oriented along the the [110]- and [1$\bar{1}$0]-directions and the amplitude of the Fourier component of the {200} reflections demonstrated that they originate from areas close to the nanocolumns. Correlation is found between the chemical Sn segregation and the amplitude distribution of the Fourier component of the {200} Bragg reflections. This indicates that the {200} Bragg reflections are due to the Sn segregation at the interface GeSn/GeMn. To obtain more details on the origin of these forbidden reflections and its particular symmetry, it could be interesting to simulate the diffraction of NC, in order to get more insight in the consequence on the Sn segregation at the interface GeMn/GeSn. This should allows to obtain information in the morphology of the Sn segregation. Atomistic simulation would be also of interest to understand this particular segregation phenomena.

The magnetization was observed to increase with the Sn incorporation, that might be due to either strain or to interface effects. GeMn nanocolumns experience an uniaxial out-of-plane tensile strain imposed by the GeSn matrix which increases with the Sn content. Moreover, due to the presence of the Sn-rich ring around the nanocolumns, Mn atoms at the interface between the column and the GeSn matrix have different chemical environments in GeMn and GeSnMn samples. The magnetic measurements (Fig. 5.31(b)) show that the incorporation of Sn increases the overall magnetic signal, but remains constant irrespective of the Sn content. This enhancement of magnetic moment may not be attributed to strain but rather to an interface effect, *i.e.* due to modification of the electronic structure of Mn atoms in contact with the Sn-rich ring around the NCs. This phenomenon clearly requires future investigations.

5.5. Conclusion

In the first part of this chapter, chemical composition, structure and strain distribution of GeMn layers have been extensively studied by TEM and completed by APT volume reconstruction. Results show that i) the atomic density inside the NCs is almost two times higher than in the Ge matrix, ii) a decrease of the Ge density has been observed inside the NCs, iii) the Mn concentration in the Ge matrix is lower than the detection limit of the APT instrument, *i.e.* lower than 0.1 % iv) Mn concentration inside the NCs can reach 60 %, v) reconstructed volume and plane view TEM imaging evidence that the NCs can be bent or interrupted or exhibit branching.

The strain measurements in the Ge matrix evidence a strong difference between the amorphous and the crystalline NCs: in the amorphous case, the NC exert compressive strain to the Ge matrix, whereas in the crystalline case, the Ge matrix is submitted to tensile strain close to the NC. The second case was explained by a larger in-plane lattice parameter in the NC and an incoherent interface between the NC and the matrix.

The structure of NCs has been investigated using HRTEM imaging. Even if the crystalline NCs exhibit a high degree of disorder, a clear difference was observed between amorphous and crystalline NC. Supplementary Bragg reflection were observed in the power spectrum localized on the NCs, but we could not evidence a particular crystal structure for the NCs. The α-phase model supported by atomic simulation was then considered. HRTEM imaging coupled with image simulations showed that NCs could consist of this phase only if different variants are introduced to cancel reflection due to order. The α-phase is also coherent with chemical results if part of the Ge are substituted by Mn atoms. We then end up with a GeMn α-phase-based structure with a high content of Mn.

In the second part of this chapter, X-ray diffraction and high resolution electron microscopy were used to investigate GeSnMn films containing up to 3.6 % of Sn and up to 10 % of Mn grown pseudomorphically on Ge(001) substrates. Results show : i)despite the strain induced by Sn, GeMn rich nanocolumns are formed similar to those of the GeMn layers, ii) inside the nanocolumns, the Sn concentration is lower than the EELS detection limit (< 1 %) iii) the matrix has a homogeneous GeSn composition iv) a strain-induced segregation of Sn atoms is observed around NCs leading to a cross shape chemical distribution with branches aligned along the [110] and [1$\bar{1}$0] directions.

The strain in GeSnMn layers was investigated using the geometrical phase analysis. The presence of GeMn nanocolumns leads to variations of the in-plane lattice parameter in GeSnMn films, but its average value is the same than the Ge substrate. GPA and HRXRD demonstrated that the presence of GeMn nanocolumns does not change the out-of-plane lattice parameter for a given Sn concentration.

Finally, the comparison between these two systems show that the magnetic moment per Mn atom is higher in samples containing Sn compared to GeMn samples. In light of our investigations we attributed this phenomenon to an interface effect related to the modification of the electronic structure of Mn atoms inside nanocolumns surrounded by Sn.

6. General conclusion and outlook

The first chapter introduces the motivation of this work. Different systems have been studied using TEM methods: coarsening of Pt NPs on amorphous carbon, the Ge QDs, the Mn incorporation in Ge QDs and the GeMn NCs embedded in Ge or GeSn matrix.

The second chapter reviews rapidly the basics of transmission electron microscopy for HRTEM, HRSTEM and EELS imaging. It presents the techniques and quantification procedures we have used for this work. The opportunities that offers modern electron microscopy have been explored and the optimal experimental conditions have been highlighted for the different TEM techniques. The sample preparation and data processing were emphasized to achieve accurate and precise measurements with TEM methods.

Coarsening of Pt nanoparticles

The third chapter deals with the coarsening of Pt NPs. The coarsening of the NP ensemble was studied by TEM after annealing at temperatures between 200 °C and 300 °C for up to 160 h. The possible influence of 200 keV electrons on the coarsening was systematically studied by illuminating the same sample region for 20 min in HRTEM. Neither enhanced SR nor a significant change of the NP sizes was observed under the chosen illumination conditions. However, HRSTEM imaging can change significantly the smallest NPs since a single cross scan can already induce an atomic-scale reorganization of the material.

High-resolution TEM was applied to analyze the NP shape. Experimental and simulated images along the [100]- and [110]-zone axes were compared to distinguish between cuboctahedral and truncated octahedral fcc NP structures. [100]-zone axis HRTEM images are suitable to discriminate between these two NP types which yield a truncated octahedral shape as being relevant in our study. Measured NP-size distributions yield average radii which increase with annealing time and temperature. Coarsening proceeds fast during the first 2 hours of annealing and slows down for longer annealing times. An in-situ TEM annealing experiment demonstrates that coarsening is dominated by a very active coalescence of small mobile NPs via SR during the first

coarsening stage ($t < 2$ h). SR can be neglected during the second ripening stage for annealing times of more than 2 hours. The coarsening kinetics during the second stage is best described by surface OR with a diffusion-limited kinetics. The Arrhenius-type dependence of the surface mass transport diffusion coefficient is exploited to derive the activation energy for surface diffusion of Pt atoms $E_d = 0.84 \pm 0.08$ eV·atom^{-1} on an a-C substrate. The limitation of the OR process by surface diffusion as opposed to reaction limitation can be understood by the reduction of the detachment activation energy of Pt atoms in small NPs and the high bonding energies between Pt atoms and the carbon support.

The coarsening on different substrates would be of interest for comparison with the observations of Pt NP coarsening on a-C reported in this work. Amorphous substrate, such as Al_2O_3 or SiO_2 could be used, since there are model system for catalysis. Concerning crystalline substrate, graphene could also be of interest, since clean graphene allows to study the interaction of adatoms or NPs with a well defined crystalline structure. In this favorable case, direct comparison with first-principle calculations should be possible. The effect of the number of layer on the binding energy of Pt adatom or NPs with the substrate could be then investigated. However, systematic study of NP coarsening process on graphene rises the problem of the control of the fabrication of clean and large graphene area. The preparation of large and clean graphene for TEM is still a very difficult task: the number of layer, the presence of defects or wrinkles and the contamination are crucial parameters that have to be well controlled.

Ge and Ge(Mn) quantum dots

The fourth chapter reports on quantitative analysis of Ge and GeMn quantum dots in Si. The chemical distribution of each species (Si, Ge and Mn) were performed using HAADF and EELS imaging in HRSTEM mode in order to understand growth processes. The first part of this chapter described the methodological development of HAADF quantification we developed to get accurate quantification of our samples. This method is based on the correlation of HAADF and EELS signals in order to quantify the contrast of each individual atomic column on the HAADF images. Despite the relatively low atomic number different between Si and Ge, aberration-corrected HAADF-HRSTEM performed in area thinner than 10 nm allows the observation of diluted Ge atoms in Si. The HAADF signal of each atomic columns was measured using a combination of template matching and fitting methods on the image. The statistical correlation of HAADF and EELS signal acquired simultaneously shows a linear relationship between these two signals in the range of composition between 0 and 50 % of Ge in Si. Using the fitted correlation between HAADF and EELS signals,

the HAADF image can be then converted in Ge concentration. Since the visibility of a few Ge atoms as a function of a depth position in the atomic columns can be approximated to a Gaussian distribution, the Ge concentration on the HAADF image has to be measured statistically. It can be performed by averaging profiles or by fitting histogram of concentration (or amplitude) distribution with Gaussian functions. In the latter case, each Gaussian function corresponds to atomic columns containing different number of Ge atoms. Assuming a specimen thickness, the separation between the different Gaussian function were calibrated using the fitted value of the linear correlation between the HAADF and EELS signal. Finally, the detection of Ge atoms in the Si spacer has been shown and quantify and is explained as been due to surface segregation of Ge atoms in Si during growth. Note that this observation is only possible thanks to good sample preparation to get thin and flat area in order to obtain a sufficient visibility of the presence of one Ge atom in a Si atomic column. The Ge distribution in the Si spacer has been modeled with a two-states surface segregation model.

In the second part of the fourth chapter, we investigated the Mn incorporation in the Ge QD. The growth of Ge(Mn) QDs or WLs at 380 °C leads to the strong lateral segregation of Mn. SiMn precipitates are then formed and the Mn concentration in the Ge QDs or WLs is below the detection limits of EELS (<1 % in our experimental conditions). This is in good agreement with the back-diffusion of Mn reported by other groups. We evidenced that this diffusion is due to the presence of SiMn precipitates. However, our observations does not support the formation of diluted magnetic semiconductors of Mn in Ge. Lowering the growth temperature at 220 °C allows to limit the lateral segregation of Mn in Ge WLs. The incorporation of Mn in Ge WLs was then achieved at low temperature growth. However due to the very low Mn content in the specimen (up to 10 % in a few GeMn MLs), it is very difficult to measure a magnetic signal that can be attributed to ferromagnetism induced by Mn atoms.

GeMn nanocolumns

In the first part of the fifth chapter, chemical composition, structure and strain distribution of GeMn layers have been extensively studied by TEM and completed by APT volume reconstruction. Results show that i) the atomic density inside the NCs is much higher than in the Ge matrix, ii) a decrease of the Ge density has been observed inside the NCs, iii) the Mn concentration in the Ge matrix is lower than the detection limit of the APT instrument, *i.e.* lower than 0.1 % iv) Mn concentration inside the NCs can reach 60 %, v) reconstructed volume and plane view TEM imaging evidence that the NCs can be bent or interrupted or exhibit branching.

The strain measurements in the Ge matrix evidence a strong difference between the amorphous and the crystalline NCs: in the amorphous case, the NC exerts compressive strain to the Ge matrix, whereas in the crystalline case, the Ge matrix is submitted to tensile strain close to the NC. The second case was explained by a larger in-plane lattice parameter in the NC and an incoherent interface between the NC and the matrix.

The structure of NCs has been investigated using HRTEM imaging. Even if the crystalline NCs exhibit a high degree of disorder, a clear difference was observed between amorphous and crystalline NC. Supplementary Bragg reflection were observed in the power spectrum localized on the NCs, but we could not evidence a particular crystal structure for the NCs. The α-phase model supported by atomic simulation was then considered. HRTEM imaging coupled with image simulations showed that NCs could consist of this phase only if different variants are introduced to cancel supplementary Bragg reflection due to the introduced order. The α-phase is also coherent with chemical results if part of the Ge are substituted by Mn atoms. We then end up with a GeMn α-phase-based structure with a high content of Mn. The new experimental insights in the phase of the GeMn NCs obtained from chemical measurement (higher density and presence of substitutional Mn) could be explored by first-principles calculations.

In the second part of the fifth chapter, X-ray diffraction and TEM were used to investigate GeSnMn films containing up to 3.6 % of Sn and up to 10 % of Mn grown pseudomorphically on Ge(001) substrates. Results show: i) despite the strain induced by Sn, GeMn rich nanocolumns are formed similar to those of the GeMn layers, ii) inside the nanocolumns, the Sn concentration is lower than the EELS detection limit ($<$ 1 %) iii) the matrix has a homogeneous GeSn composition iv) a strain-induced segregation of Sn atoms is observed around NCs leading to a cross shape chemical distribution with branches aligned along the [110] and [1$\bar{1}$0] directions. It could be interesting to better understand the particular shape of Sn segregation observed around the NCs. Experimental observations indicate that the Sn segregation at the interface GeMn NC and GeSn matrix leads to the presence of the {220} forbidden Bragg reflections. Atomic simulations and simulations of ED patterns could be performed to precisely determine the origin of the Sn segregation and get more insight in the structure of the interface.

The strain in GeSnMn layers was investigated using the GPA. The presence of GeMn nanocolumns leads to variation of the in-plane lattice parameter in GeSnMn films, but its average value is the same than the Ge substrate. GPA and HRXRD demonstrated that the presence of GeMn nanocolumns does not change the out-of-plane lattice parameter for a given Sn concentration.

Finally, the comparison between these two systems shows that the magnetic moment per Mn atom is higher in samples containing Sn as compared to GeMn samples. In light of our investigations we attributed this phenomenon due to an interface effect

related to the modification of the electronic structure of Mn atoms inside nanocolumns surrounded by Sn. The increase of magnetization by an interface effect is a very interesting phenomenon, that clearly requires further investigations. Exploration of these experimental findings by first-principles calculations could provide more insights in this phenomenon.

A. EELS quantification using k factors

This appendix describes some of the basics for the composition quantification using reference specimens.

Fundamentals

Following the Castaing's approach [Cast 52] for quantitative analysis of EDX spectra, we assume that the concentration c_i of a given element i generates an intensity of characteristic signal I_i. Using a known composition specimen (called standard) with a concentration $c_{(i)}$ of the element i, we can derive the concentration c_i of the unknown specimen by measuring the ratio [Cast 52, Will 09]:

$$\frac{c_i}{c_{(i)}} = K\frac{I_i}{I_{(i)}} \tag{A.1}$$

where I_i and $I_{(i)}$ are the measured intensity of the unknown and known composition specimen, respectively. K is a sensitivity factor dependent on the detector. This approach implies that the experimental conditions are exactly the same to obtained accurate quantification.

Cliff and Lorimer extended the Castaing's approach and rewrite Eq. A.1 as a ratio of two element A and B [Clif 75]. The ratio of the concentration of each element c_A and c_B is then related to the ratio of the measured intensity of each element I_A and I_B by:

$$\frac{c_\mathrm{A}}{c_\mathrm{B}} = k_\mathrm{AB}\frac{I_\mathrm{A}}{I_\mathrm{B}} \tag{A.2}$$

where k_AB is the Cliff-Lorimer factor. k_AB can be seen as the ratio of the partial cross-section $\sigma_k(\beta, \Delta)$ of each element. The concentration of each element can be derived by assuming:

$$\sum_\mathrm{N} c_\mathrm{N} = 1 \tag{A.3}$$

in case of a specimen consisting of N elements.

Determination of the EELS $k_{\mathrm{Ge\ L_{2,3}}}$ factor

To experimentally determine the EELS $k_{\mathrm{Ge\ L_{2,3}}}$ factor, we have used a standard consisting of four SiGe layers of different concentrations. An HAADF-STEM images of such a specimen is shown in Fig. 4.13. The Ge concentrations of the four SiGe layers obtained by secondary ion mass spectrometry are 20%, 31%, 38% and 45% from the bottom to the top layer, as reported in [Bech 09, Coop 09]. We are confident with the quality of the standard specimen, *i.e.* composition of each layer, because the SIMS results are in good agreement with strain measurement obtained by different methods [Bech 09, Coop 09].

We start by removing the background of the Ge $L_{2,3}$ and Si K edges in the EELS spectra. Then, we measure the ratio $I_{\mathrm{Ge\ L_{2,3}}}/I_{\mathrm{Si\ K}}$ of intensity integrated over 60 eV after the Ge $L_{2,3}$ and Si K edges (at 1217 eV and 1838 eV, respectively).

Finally, for each layer of known Ge concentration c_{Ge}, the $k_{\mathrm{Ge\ L_{2,3}}}$ factor is determined according to Eq. A.2:

$$k_{\mathrm{Ge\ L_{2,3}}} = \frac{c_{\mathrm{Ge}}}{1 - c_{\mathrm{Ge}}} \frac{I_{\mathrm{Si\ K}}}{I_{\mathrm{Ge\ L_{2,3}}}}$$

Concentration determination using $k_{\mathrm{Ge\ L_{2,3}}}$ factor

The Ge concentration c_{Ge} can be determined by combining Eq. A.2 and Eq. A.3:

$$\frac{c_{\mathrm{Ge}}}{c_{\mathrm{Si}}} = k_{\mathrm{Ge\ L_{2,3}}} \frac{I_{\mathrm{Ge\ L_{2,3}}}}{I_{\mathrm{Si\ K}}} \quad \text{and} \quad c_{\mathrm{Ge}} + c_{\mathrm{Si}} = 1$$

It follows:

$$\begin{aligned} \frac{c_{\mathrm{Ge}}}{1 - c_{\mathrm{Ge}}} &= k_{\mathrm{Ge\ L_{2,3}}} \frac{I_{\mathrm{Ge\ L_{2,3}}}}{I_{\mathrm{Si\ K}}} \\ c_{\mathrm{Ge}} &= k_{\mathrm{Ge\ L_{2,3}}} \frac{I_{\mathrm{Ge\ L_{2,3}}}}{I_{\mathrm{Si\ K}}} (1 - c_{\mathrm{Ge}}) \\ c_{\mathrm{Ge}} \left(1 + k_{\mathrm{Ge\ L_{2,3}}} \frac{I_{\mathrm{Ge\ L_{2,3}}}}{I_{\mathrm{Si\ K}}}\right) &= k_{\mathrm{Ge\ L_{2,3}}} \frac{I_{\mathrm{Ge\ L_{2,3}}}}{I_{\mathrm{Si\ K}}} \end{aligned}$$

Finally, the Ge concentration is given by:

$$c_{\mathrm{Ge}} = \frac{k_{\mathrm{Ge\ L_{2,3}}} \frac{I_{\mathrm{Ge\ L_{2,3}}}}{I_{\mathrm{Si\ K}}}}{1 + k_{\mathrm{Ge\ L_{2,3}}} \frac{I_{\mathrm{Ge\ L_{2,3}}}}{I_{\mathrm{Si\ K}}}} \tag{A.4}$$

B. Cut-off of the microscope in STEM

This appendix gives complementary information on the cut-off of the microscope mentioned in the sec. 2.5.5.2, which is of importance for the calibration of the collection of HAADF detector in STEM mode. In the following, we consider the Fishione detector as HAADF detector.

We present here the measurement performed on the FEI Titan^3 Ultimate microscope working at 200 kV. The images have been acquired in a thick area of the sample in order to have a lot of electrons scattering at high angle. Fig. B.1 display distribution of scattered electrons observed in the diffraction plane. The images were acquired for three different camera length using the FEI FluCam camera.

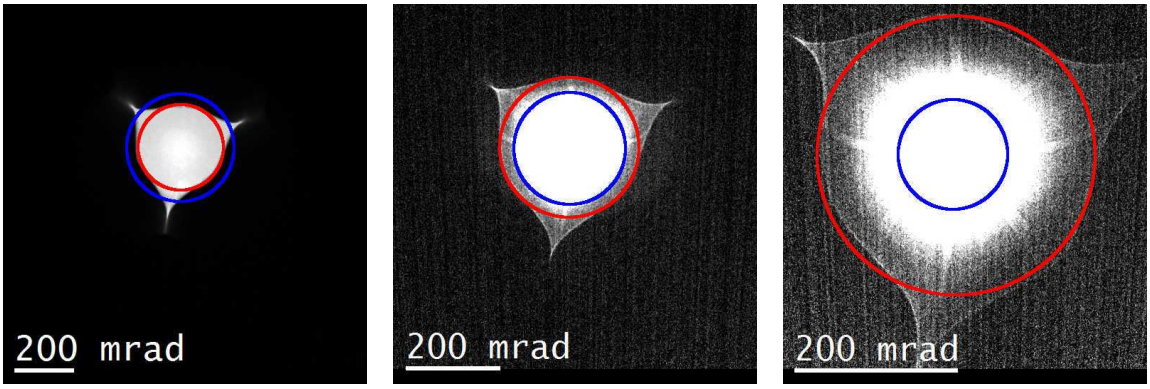

(a) $L = 29.5$ mm (b) $L = 46$ mm (c) $L = 91$ mm

Figure B.1.: Images of the distribution of scattered electrons in the diffraction plane illustrating the dependence of the cut-off of the microscope in STEM mode on the camera length. The images have been acquired using the FEI FluCam camera in diffraction mode for three different camera length: (a) $L = 29.5$ mm, (b) $L = 46$ mm and (c) $L = 91$ mm. The blue and red circles correspond to the inner collection angle of the HAADF detector and the cut-off of the microscope, respectively.

In Fig. B.1 shows that the distribution of scattered electron is contained within a 3-fold symmetrical feature, whose limit is indicated by the red circle and corresponds to the cut-off of the microscope in STEM mode - electrons scattered at higher angle are not transmitted to the detector. We note here, that the 3-fold symmetry can be

attributed to the double hexapoles of the post-specimen aberration corrector[1]. From these acquisitions, it is possible to determinate the cut-off of the microscope in STEM mode. The red circle illustrated how the cut-off have been measured. The outer collection angle θ_{outer} being determined by the maximal angle at which the electrons reach the detector: it is given by either by the value of the the cut-off $\theta_{\text{cut-off}}$ or the maximum angle allowed by the geometry of the detector $(6.3 \pm 0.2) \times \theta_{\text{inner}}$. It follows that:

$$\theta_{\text{outer}} = \min \{\theta_{\text{cut-off}}, (6.3 \pm 0.2) \times \theta_{\text{inner}}\} \tag{B.1}$$

The data plotted in Fig. 2.17(a) were determined using this method. The blue circles drawn on the images correspond to the inner collection angle. By comparing the position of the blue and red circles, we can observe that at low camera length (L = 29.5 mm) the inner collection angle of the HAADF detector is higher than the cut-off of the microscope, meaning that no electron can reach the HAADF detector at this camera length, *i.e.* no image can be obtained using the Fishione HAADF detector considered here.

Fig. B.2 shows that the cut-off can be also observed directly on the HAADF detector. Similarly to the Fig. 2.16 in chapter 2, an image of the HAADF detector images have been acquired by scanning the detector with the electron probe while the projector system of the microscope was set in image mode. After leaving the probe for a few minutes on a thick area of the sample, one can observe persistence on the detector due to previous electron illumination.

The two images in Fig. B.2 were obtained from the same raw image. Fig. B.2(a) correspond to a detector image with a linear display, while the gamma value of the image in Fig. B.2(b) have been changed to highlight the feature corresponding to the cut-off of the microscope. Using this method, we obtained a value of 160 ± 5 mrad for the cut-off. This value is in fair agreement with the previous measurement illustrated in Fig. B.1 using the FEI FluCam (166 ± 6 mrad) confirming the validity of the previous method.

[1]Similar experiment performed on a probe-corrected FEI Titan (without post-specimen aberration corrector) exhibit perfect circular feature for the cut-off.

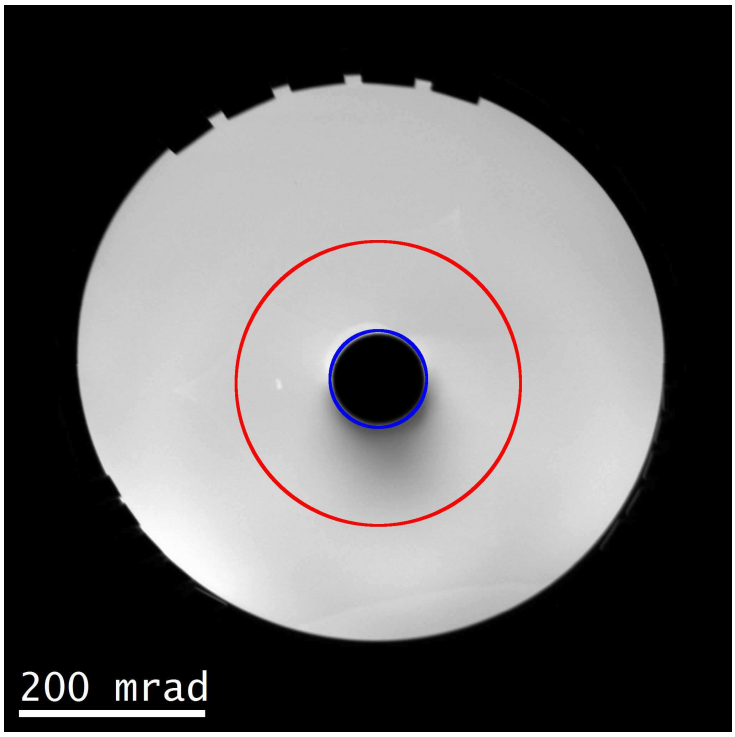

(a)

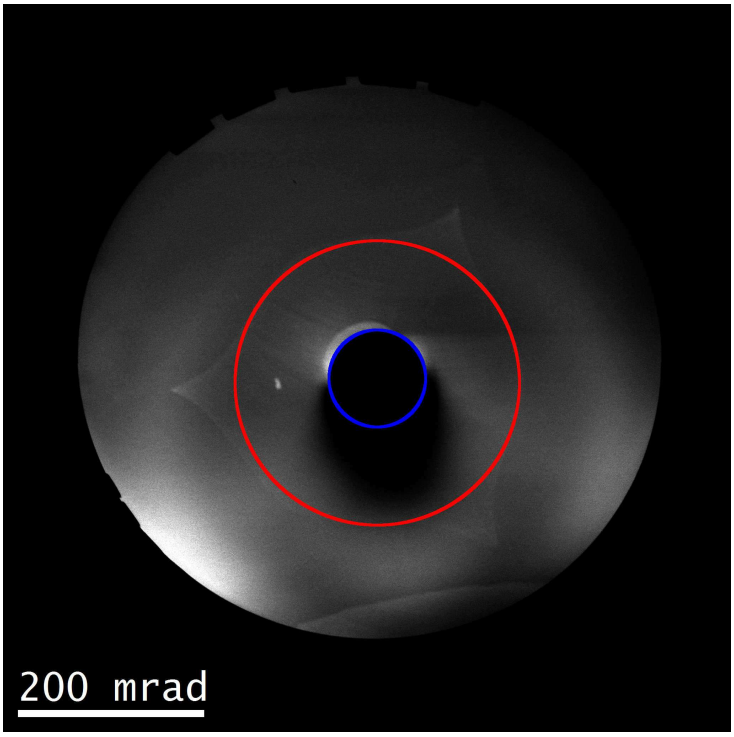

(b)

Figure B.2.: Direct observation of the cut-off of the microscope in the STEM mode on the Fishione detector. Both images were obtained from the same raw image, but there are displayed using two different settings: (a) with linear display and (b) and with appropriate gamma value. For the acquisition, the microscope was set in STEM mode with a camera length of 115 mm and the projector was in image mode. The blue and red circles correspond to the inner collection angle of the HAADF detector and the cut-off of the microscope, respectively.

Bibliography

[Allo 07] D. Alloyeau, C. Langlois, C. Ricolleau, Y. Le Bouar, and A. Loiseau. "A TEM in situ experiment as a guideline for the synthesis of as-grown ordered CoPt nanoparticles". *Nanotechnology*, Vol. 18, p. 375301, Sep. 2007. URL: http://iopscience.iop.org/0957-4484/18/37/375301. 65

[Allo 09] D. Alloyeau, C. Ricolleau, C. Mottet, T. Oikawa, C. Langlois, Y. Le Bouar, N. Braidy, and A. Loiseau. "Size and shape effects on the order-disorder phase transition in CoPt nanoparticles". *Nat Mater*, Vol. 8, No. 12, pp. 940–946, 2009. URL: http://dx.doi.org/10.1038/nmat2574. 3

[Allo 12] D. Alloyeau, T. Oikawa, J. Nelayah, G. Wang, and C. Ricolleau. "Following Ostwald ripening in nanoalloys by high-resolution imaging with single-atom chemical sensitivity". *Appl. Phys. Lett.*, Vol. 101, No. 12, pp. 121920–121920–4, Sep. 2012. URL: http://apl.aip.org/resource/1/applab/v101/i12/p121920_s1. 81

[Andr 02] P. Andreazza, C. Andreazza-Vignolle, J. Rozenbaum, A.-L. Thomann, and P. Brault. "Nucleation and initial growth of platinum islands by plasma sputter deposition". *Surf. Coat. Tech.*, Vol. 151-152, pp. 122–127, March 2002. URL: http://www.sciencedirect.com/science/article/pii/S0257897201016048. 3

[Arra 10] E. Arras. *Étude théorique de la structure et de la stabilité des alliages GeMn dans le cadre de la spintronique. Un prototype de semiconducteur magnétique confronté aux résultats expérimentaux.* PhD thesis, 2010. URL: http://hal.archives-ouvertes.fr/index.php?halsid=93n5ajsteq99nujl9b0ccscvk4&view_this_doc=tel-00489879&version=2. 165

[Arra 11] E. Arras, D. Caliste, T. Deutsch, F. Lançon, and P. Pochet. "Phase diagram, structure, and magnetic properties of the Ge-Mn system: A first-principles study". *Phys. Rev. B*, Vol. 83, No. 17, p. 174103, 2011. URL: http://link.aps.org/doi/10.1103/PhysRevB.83.174103. 174

[Arra 12] E. Arras, F. Lançon, I. Slipukhina, É. Prestat, M. Rovezzi, S. Tardif, A. Titov, P. Bayle-Guillemaud, F. d'Acapito, A. Barski, V. Favre-Nicolin,

M. Jamet, J. Cibert, and P. Pochet. "Interface-driven phase separation in multifunctional materials: The case of the ferromagnetic semiconductor GeMn". *Physical Review B*, Vol. 85, No. 11, p. 115204, March 2012. URL: http://link.aps.org/doi/10.1103/PhysRevB.85.115204. 166, 167, 174, 175

[Ayac 10] J. Ayache, L. Beaunier, J. Boumendial, G. Ehret, and D. Laub. *Sample Preparation Handbook for Transmission Electron Microscopy*. Springer, 2010. URL: http://www.springer.com/materials/characterization+&+evaluation/book/978-1-4419-5974-4. 53, 55

[Baib 88] M. N. Baibich, J. M. Broto, A. Fert, F. N. Van Dau, F. Petroff, P. Etienne, G. Creuzet, A. Friederich, and J. Chazelas. "Giant Magnetoresistance of (001)Fe/(001)Cr Magnetic Superlattices". *Phys. Rev. Lett.*, Vol. 61, No. 21, pp. 2472–2475, Nov. 1988. URL: http://link.aps.org/doi/10.1103/PhysRevLett.61.2472. 4

[Banh 08] F. Banhart, Ed. *In-Situ Electron Microscopy At High Resolution*. World Scientific, July 2008. URL: http://www.worldscientific.com/doi/abs/10.1142/9789812797346_fmatter. 78

[Bari 06] J.-M. Baribeau, X. Wu, and D. J. Lockwood. "Probing the composition of Ge dots and $Si/Si_{1-x}Ge_x$ island superlattices". pp. 663–667, AVS, 2006. URL: http://link.aip.org/link/?JVA/24/663/1. 96

[Bart 10] J. Barthel and A. Thust. "Aberration measurement in HRTEM: Implementation and diagnostic use of numerical procedures for the highly precise recognition of diffractogram patterns". *Ultramicroscopy*, Vol. 111, No. 1, pp. 27–46, 2010. URL: http://www.sciencedirect.com/science/article/B6TW1-513F91T-1/2/d250f330dc48e71ec96b62b815199d55. 22

[Bass 70] D. W. Bassett and M. J. Parsley. "Field ion microscope studies of transition metal adatom diffusion on (110), (211) and (321) tungsten surfaces". *J. Phys. D: Appl. Phys.*, Vol. 3, pp. 707–716, May 1970. URL: http://iopscience.iop.org/0022-3727/3/5/309. 3

[Bass 78] D. Bassett and P. Webber. "Diffusion of single adatoms of platinum, iridium and gold on platinum surfaces". *Surf. Sci.*, Vol. 70, No. 1, pp. 520–531, Jan. 1978. URL: http://www.sciencedirect.com/science/article/pii/0039602878904296. 86

[Baue 02] M. Bauer, J. Taraci, J. Tolle, A. V. G. Chizmeshya, S. Zollner, D. J. Smith, J. Menendez, C. Hu, and J. Kouvetakis. "Ge–Sn semiconductors for band-gap and lattice engineering". *Applied Physics Letters*, Vol. 81,

No. 16, pp. 2992–2994, Oct. 2002. URL: http://apl.aip.org/resource/1/applab/v81/i16/p2992_s1. 176

[Bech 09] A. Béché. *Mesure de déformation à l'échelle nanométrique par microscopie électronique en transmission*. PhD thesis, Institut National Polytechnique de Grenoble - INPG, Oct. 2009. URL: http://tel.archives-ouvertes.fr/tel-00489867. 110, 198

[Bene 03] A. Benedetti, D. J. Norris, C. J. D. Hetherington, A. G. Cullis, D. J. Robbins, and D. J. Wallis. "Strain and Ge concentration determinations in SiGe/Si multiple quantum wells by transmission electron microscopy methods". *J. Appl. Phys.*, Vol. 93, No. 7, pp. 3893–3899, Apr. 2003. URL: http://jap.aip.org/resource/1/japiau/v93/i7/p3893_s1. 96

[Benn 03] R. A. Bennett, D. M. Tarr, and P. A. Mulheran. "Ripening processes in supported and pinned nanoclusters—experiment, simulation and theory". *J. Phys.: Condens. Matter*, Vol. 15, pp. S3139–S3152, Oct. 2003. URL: http://iopscience.iop.org/0953-8984/15/42/011. 64, 65

[Bent 06] K. van Benthem, A. R. Lupini, M. P. Oxley, S. D. Findlay, L. J. Allen, and S. J. Pennycook. "Three-dimensional ADF imaging of individual atoms by through-focal series scanning transmission electron microscopy". *Ultramicroscopy*, Vol. 106, No. 11-12, pp. 1062–1068, Oct. 2006. URL: http://www.sciencedirect.com/science/article/B6TW1-4KBDVCY-D/2/38b6e6ffb2406c04226b02b24ebaf9c4. 39

[Bern 98] S. Bernal, F. J. Botana, J. J. Calvino, C. López-Cartes, J. A. Pérez-Omil, and J. M. Rodríguez-Izquierdo. "The interpretation of HREM images of supported metal catalysts using image simulation: profile view images". *Ultramicroscopy*, Vol. 72, No. 3-4, pp. 135–164, 1998. URL: http://www.sciencedirect.com/science/article/B6TW1-3VF6SK3-4/2/fcf1924f3b69ace541ea774122cbfc63. 76

[Beso 04] L. Besombes, Y. Léger, L. Maingault, D. Ferrand, H. Mariette, and J. Cibert. "Probing the Spin State of a Single Magnetic Ion in an Individual Quantum Dot". *Phys. Rev. Lett.*, Vol. 93, No. 20, p. 207403, Nov. 2004. URL: http://link.aps.org/doi/10.1103/PhysRevLett.93.207403. 5

[Beth 28] H. Bethe. "Theorie der Beugung von Elektronen an Kristallen". *Ann. Phys.-Berlin*, Vol. 392, No. 17, p. 55–129, 1928. URL: http://onlinelibrary.wiley.com/doi/10.1002/andp.19283921704/abstract. 14

[Bina 89] G. Binasch, P. Grünberg, F. Saurenbach, and W. Zinn. "Enhanced magnetoresistance in layered magnetic structures with antiferromagnetic inter-

layer exchange". *Phys. Rev. B*, Vol. 39, No. 7, pp. 4828–4830, March 1989. URL: http://link.aps.org/doi/10.1103/PhysRevB.39.4828. 4

[Bisk 12] J. Biskupek, P. Hartel, M. Haider, and U. Kaiser. "Effects of residual aberrations explored on single-walled carbon nanotubes". *Ultramicroscopy*, Vol. 116, No. 0, pp. 1–7, May 2012. URL: http://www.sciencedirect.com/science/article/pii/S0304399112000502. 22

[Blac 94] J. A. Blackman, B. L. Evans, and A. I. Maaroof. "Analysis of island-size distributions in ultrathin metallic films". *Phys. Rev. B*, Vol. 49, No. 19, pp. 13863–13871, 1994. URL: http://link.aps.org/doi/10.1103/PhysRevB.49.13863. 3

[Blav 01] D. Blavette, F. Vurpillot, P. Pareige, and A. Menand. "A model accounting for spatial overlaps in 3D atom-probe microscopy". *Ultramicroscopy*, Vol. 89, No. 1–3, pp. 145–153, Oct. 2001. URL: http://www.sciencedirect.com/science/article/pii/S0304399101001206. 157

[Bonn 99] N. Bonnet, N. Brun, and C. Colliex. "Extracting information from sequences of spatially resolved EELS spectra using multivariate statistical analysis". *Ultramicroscopy*, Vol. 77, No. 3–4, pp. 97–112, 1999. URL: http://www.sciencedirect.com/science/article/pii/S030439919900042X. 49

[Bosm 08] M. Bosman and V. J. Keast. "Optimizing EELS acquisition". *Ultramicroscopy*, Vol. 108, No. 9, pp. 837–846, Aug. 2008. URL: http://www.sciencedirect.com/science/article/pii/S0304399108000260. 49

[Bott 10] G. A. Botton, S. Lazar, and C. Dwyer. "Elemental mapping at the atomic scale using low accelerating voltages". *Ultramicroscopy*, Vol. 110, No. 8, pp. 926–934, 2010. URL: http://www.sciencedirect.com/science/article/B6TW1-4YP8TTG-2/2/a38af16a1297327dc9ebea60a05ba145. 48

[Boug 06] D. Bougeard, S. Ahlers, A. Trampert, N. Sircar, and G. Abstreiter. "Clustering in a Precipitate-Free GeMn Magnetic Semiconductor". *Phys. Rev. Lett.*, Vol. 97, No. 23, p. 237202, 2006. URL: http://link.aps.org/doi/10.1103/PhysRevLett.97.237202. 5, 141, 145, 146, 165

[Boug 09] D. Bougeard, N. Sircar, S. Ahlers, V. Lang, G. Abstreiter, A. Trampert, J. M. LeBeau, S. Stemmer, D. W. Saxey, and A. Cerezo. "Ge_{1-x} Mn_x Clusters: Central Structural and Magnetic Building Blocks of Nanoscale Wire-Like Self-Assembly in a Magnetic Semiconductor". *Nano Lett.*, Vol. 9, No. 11, pp. 3743–3748, Nov. 2009. URL: http://dx.doi.org/10.1021/nl901928f. 5, 145, 147

[Breh 08] M. Brehm, M. Grydlik, H. Lichtenberger, T. Fromherz, N. Hrauda, W. Jantsch, F. Schäffler, and G. Bauer. "Quantitative determination of Ge profiles across SiGe wetting layers on Si(001)". *Appl. Phys. Lett.*, Vol. 93, No. 12, pp. 121901–121901–3, Sep. 2008. URL: http://apl.aip.org/resource/1/applab/v93/i12/p121901_s1. 96

[Buba 10] J. P. Buban, Q. Ramasse, B. Gipson, N. D. Browning, and H. Stahlberg. "High-resolution low-dose scanning transmission electron microscopy". *J Electron Microsc (Tokyo)*, Vol. 59, No. 2, pp. 103–112, Apr. 2010. URL: http://jmicro.oxfordjournals.org/content/59/2/103. 83

[Butz 92] R. Butz and S. Kampers. "(2×n) surface structure of SiGe layers deposited on Si(100)". *Appl. Phys. Lett.*, Vol. 61, No. 11, pp. 1307–1309, Sep. 1992. URL: http://apl.aip.org/resource/1/applab/v61/i11/p1307_s1. 95

[Buze 07] C. Buzea, I. I. Pacheco, and K. Robbie. "Nanomaterials and nanoparticles: Sources and toxicity". *Biointerphases*, Vol. 2, No. 4, pp. MR17–MR71, Dec. 2007. URL: http://link.springer.com/article/10.1116/1.2815690. 3

[Cast 52] R. Castaing. *Application des sondes électroniques à une méthode d'analyse ponctuelle chimique et cristallographique*. PhD thesis, 1952. URL: http://publications.onera.fr/exl-doc/DOC77514_s1.pdf. 197

[Chak 67] B. K. Chakraverty. "Grain size distribution in thin films—1. Conservative systems". *J. Phys. Chem Solids*, Vol. 28, No. 12, pp. 2401–2412, 1967. URL: http://www.sciencedirect.com/science/article/pii/0022369767900261. 64, 65, 70, 85

[Chan 06] L. Chang, A. Kirkland, and J. Titchmarsh. "On the importance of fifth-order spherical aberration for a fully corrected electron microscope". *Ultramicroscopy*, Vol. 106, No. 4–5, pp. 301–306, March 2006. URL: http://www.sciencedirect.com/science/article/pii/S0304399105002160. 20

[Chen 07] J. Chen, K. L. Wang, and K. Galatsis. "Electrical field control magnetic phase transition in nanostructured MnxGe1-x". *Appl. Phys. Lett.*, Vol. 90, No. 1, pp. 012501–012501–3, Jan. 2007. URL: http://apl.aip.org/resource/1/applab/v90/i1/p012501_s1. 127

[Chun 10] J. Chung, G. Lian, and L. Rabenberg. "Practical and Reproducible Mapping of Strains in Si Devices Using Geometric Phase Analysis of Annular Dark-Field Images From Scanning Transmission Electron Microscopy". *IEEE Electr device L*, Vol. 31, No. 8, pp. 854–856, 2010. URL: http://dx.doi.org/10.1109/LED.2010.2049562. 171

[Clif 75] G. Cliff and G. W. Lorimer. "The quantitative analysis of thin specimens". *J. Microsc.*, Vol. 103, No. 2, p. 203–207, 1975. URL: http://onlinelibrary.wiley.com/doi/10.1111/j.1365-2818.1975.tb03895.x/abstract. 197

[Coop 09] D. Cooper, J.-P. Barnes, J.-M. Hartmann, A. Béché, and J.-L. Rouviere. "Dark field electron holography for quantitative strain measurements with nanometer-scale spatial resolution". *Appl. Phys. Lett.*, Vol. 95, No. 5, pp. 053501–053501–3, Aug. 2009. URL: http://apl.aip.org/resource/1/applab/v95/i5/p053501_s1. 111, 198

[Cope 89] M. Copel, M. C. Reuter, E. Kaxiras, and R. M. Tromp. "Surfactants in epitaxial growth". *Phys. Rev. Lett.*, Vol. 63, No. 6, pp. 632–635, 1989. URL: http://link.aps.org/doi/10.1103/PhysRevLett.63.632. 95, 96

[Cowl 57] J. M. Cowley and A. F. Moodie. "The scattering of electrons by atoms and crystals. I. A new theoretical approach". *Acta Cryst.*, Vol. 10, No. 10, pp. 609–619, Oct. 1957. URL: http://scripts.iucr.org/cgi-bin/paper_yard?a02113. 14

[Daty 06] A. K. Datye, Q. Xu, K. C. Kharas, and J. M. McCarty. "Particle size distributions in heterogeneous catalysts: What do they tell us about the sintering mechanism?". *Catal. Today*, Vol. 111, No. 1-2, pp. 59–67, Jan. 2006. URL: http://www.sciencedirect.com/science/article/pii/S092058610500711X. 65

[De P 12] P. De Padova, B. Olivieri, J.-M. Mariot, L. Favre, I. Berbezier, C. Quaresima, B. Paci, A. Generosi, V. Rossi Albertini, A. Cricenti, C. Ottaviani, M. Luce, A. M. Testa, D. Peddis, D. Fiorani, M. Scarselli, M. De Crescenzi, O. Heckmann, M. C. Richter, K. Hricovini, and F. d'Acapito. "Ferromagnetic Mn-doped $Si_{0.3}Ge_{0.7}$ nanodots self-assembled on Si(100)". *J. Phys.: Condens. Matter*, Vol. 24, No. 14, p. 142203, Apr. 2012. URL: http://iopscience.iop.org/0953-8984/24/14/142203. 127, 128, 131

[Devi 07] T. Devillers, M. Jamet, A. Barski, V. Poydenot, P. Bayle-Guillemaud, E. Bellet-Amalric, S. Cherifi, and J. Cibert. "Structure and magnetism of self-organized $Ge_{1-x}Mn_x$ nanocolumns on Ge(001)". *Phys. Rev. B*, Vol. 76, No. 20, p. 205306, Nov. 2007. URL: http://link.aps.org/doi/10.1103/PhysRevB.76.205306. 5, 145, 146, 147, 156

[Devi 08] T. Devillers. *Etude des propriétés physiques des phases de $Ge_{1-x}Mn_x$ ferromagnétiques pour l'électronique de spin.* PhD thesis, Nov. 2008. URL: http://hal.archives-ouvertes.fr/

index.php?halsid=mdi9bipui7kbuhas015ofv57p3&view_this_doc=tel-00367396&version=2. 141, 146, 147, 153, 156, 158, 160, 174, 175

[Diet 02] T. Dietl. "Ferromagnetic semiconductors". *Semicond. Sci. Technol.*, Vol. 17, No. 4, p. 377, Apr. 2002. URL: http://iopscience.iop.org/0268-1242/17/4/310. 4

[Duja 06] R. Dujardin. *Epitaxie par jets moléculaires de nanostructures isolées de germanium sur silicium.* PhD thesis, Université Joseph Fourier de Grenoble, Grenoble, 2006. URL: http://tel.archives-ouvertes.fr/tel-00133594/en/. 94

[Dwye 12] C. Dwyer, C. Maunders, C. L. Zheng, M. Weyland, P. C. Tiemeijer, and J. Etheridge. "Sub-0.1 nm-resolution quantitative scanning transmission electron microscopy without adjustable parameters". *Appl. Phys. Lett.*, Vol. 100, No. 19, pp. 191915–191915–4, May 2012. URL: http://apl.aip.org/resource/1/applab/v100/i19/p191915_s1. 43, 107

[Dyck 80] D. V. Dyck. "Fast computational procedures for the simulation of structure images in complex or disordered crystals: a new approach". *J. Microsc.*, Vol. 119, No. 1, p. 141–152, 1980. URL: http://onlinelibrary.wiley.com/doi/10.1111/j.1365-2818.1980.tb04084.x/abstract. 13, 14

[Eger 11] R. F. Egerton. *Electron Energy-Loss Spectroscopy in the Electron Microscope.* 2011. URL: http://www.springer.com/materials/characterization+&+evaluation/book/978-1-4419-9582-7. 11, 12, 45, 46, 47, 50

[Eger 13] R. Egerton. "Beam-Induced Motion of Adatoms in the Transmission Electron Microscope". *Microsc. Microanal.*, Vol. 19, No. 02, pp. 479–486, 2013. URL: http://journals.cambridge.org/action/displayAbstract?fromPage=online&aid=8864199. 83, 84

[Eger 93] R. Egerton. "Oscillator-strength parameterization of inner-shell cross sections". *Ultramicroscopy*, Vol. 50, No. 1, pp. 13–28, 1993. URL: http://www.sciencedirect.com/science/article/pii/030439919390087E. 53

[Erni 09] R. Erni, M. D. Rossell, C. Kisielowski, and U. Dahmen. "Atomic-Resolution Imaging with a Sub-50-pm Electron Probe". *Phys. Rev. Lett.*, Vol. 102, No. 9, p. 096101, March 2009. URL: http://link.aps.org/doi/10.1103/PhysRevLett.102.096101. 8, 36

[Erni 10] R. Erni. *Aberration-Corrected Imaging in Transmission Electron Microscopy.* Imperial College Press, Aug. 2010. URL: http://www.worldscientific.com/doi/abs/10.1142/9781848165373_fmatter. 21, 22, 24, 25, 30, 34, 35

[Evan 94] B. L. Evans, A. I. Maaroof, and S. Xu. “Nucleation and growth of platinum and nickel films on amorphous carbon substrates”. *J. Appl. Phys.*, Vol. 76, p. 900, 1994. URL: http://link.aip.org/link/JAPIAU/v76/i2/p900/s1&Agg=doi. 3

[Feyn 60] R. P. Feynman. “There’s Plenty of Room at the Bottom”. *Eng. Sci*, Vol. 23, No. 5, pp. 22–36, Feb. 1960. URL: http://resolver.caltech.edu/CaltechES:23.5.1960Bottom. 8

[Find 13] S. Findlay and J. LeBeau. “Detector non-uniformity in scanning transmission electron microscopy”. *Ultramicroscopy*, Vol. 124, No. 0, pp. 52–60, Jan. 2013. URL: http://www.sciencedirect.com/science/article/pii/S0304399112002288. 40

[Flue 88] M. Flüeli, P. Buffat, and J.-P. Borel. “Real time observation by high resolution electron microscopy (HREM) of the coalescence of small gold particles in the electron beam”. *Surface Science*, Vol. 202, No. 1–2, pp. 343–353, Aug. 1988. URL: http://www.sciencedirect.com/science/article/pii/0039602888900799. 78

[Fran 76] J. Franck and R. Wade. “Determinatino of source size and energy spread from electron-micrographs using method of youngs fringes.”. *Optik*, Vol. 44, No. 4, pp. 379–391, 1976. 26

[Fuji 91] K. Fujita, S. Fukatsu, H. Yaguchi, Y. Shiraki, and R. Ito. “Involvement of the topmost Ge layer in the Ge surface segregation during Si/Ge heterostructure formation”. *Appl. Phys. Lett.*, Vol. 59, No. 18, pp. 2240–2241, Oct. 1991. URL: http://apl.aip.org/resource/1/applab/v59/i18/p2240_s1. 96

[Fuka 91] S. Fukatsu, K. Fujita, H. Yaguchi, Y. Shiraki, and R. Ito. “Self-limitation in the surface segregation of Ge atoms during Si molecular beam epitaxial growth”. *Appl. Phys. Lett.*, Vol. 59, No. 17, pp. 2103–2105, Oct. 1991. URL: http://apl.aip.org/resource/1/applab/v59/i17/p2103_s1. 92, 95, 96

[Gamm 12] B. Gamm, H. Blank, R. Popescu, R. Schneider, A. Beyer, A. Gölzhäuser, and D. Gerthsen. “Quantitative High-Resolution Transmission Electron Microscopy of Single Atoms”. *Microsc. Microanal.*, Vol. 18, No. 01, pp. 212–217, 2012. URL: http://journals.cambridge.org/action/displayAbstract?fromPage=online&aid=8476789. 81

[Gan 08] Y. Gan, L. Sun, and F. Banhart. “One- and Two-Dimensional Diffusion of Metal Atoms in Graphene”. *Small*, Vol. 4, No. 5, pp. 587–591, 2008. URL: http://dx.doi.org/10.1002/smll.200700929. 86

[Gaul 06] B. Gault, F. Vurpillot, A. Vella, M. Gilbert, A. Menand, D. Blavette, and B. Deconihout. "Design of a femtosecond laser assisted tomographic atom probe". Vol. 77, No. 4, pp. 043705–043705–8, Apr. 2006. URL: http://rsi.aip.org/resource/1/rsinak/v77/i4/p043705_s1?isAuthorized=no. 157

[Gehr 11] H. Gehrke, J. Pelka, C. G. Hartinger, H. Blank, F. Bleimund, R. Schneider, D. Gerthsen, S. Bräse, M. Crone, M. Türk, and D. Marko. "Platinum nanoparticles and their cellular uptake and DNA platination at non-cytotoxic concentrations". *Arch Toxicol*, Vol. 85, No. 7, pp. 799–812, July 2011. URL: http://link.springer.com/article/10.1007/s00204-010-0636-3. 3

[Godb 92] D. J. Godbey and M. G. Ancona. "Ge profile from the growth of SiGe buried layers by molecular beam epitaxy". *Appl. Phys. Lett.*, Vol. 61, No. 18, pp. 2217–2219, Nov. 1992. URL: http://apl.aip.org/resource/1/applab/v61/i18/p2217_s1. 95

[Grah 11] J. F. Graham, C. D. Kell, J. A. Floro, and R. Hull. "Coupled effects of ion beam chemistry and morphology on directed self-assembly of epitaxial semiconductor nanostructures". *Nanotechnology*, Vol. 22, No. 7, p. 075301, Feb. 2011. URL: http://iopscience.iop.org/0957-4484/22/7/075301. 57

[Gril 08] V. Grillo, E. Carlino, and F. Glas. "Influence of the static atomic displacement on atomic resolution Z-contrast imaging". *Phys. Rev. B*, Vol. 77, No. 5, p. 054103, 2008. URL: http://link.aps.org/doi/10.1103/PhysRevB.77.054103. 107

[Grut 93] D. A. Grützmacher, T. O. Sedgwick, A. Powell, M. Tejwani, S. S. Iyer, J. Cotte, and F. Cardone. "Ge segregation in SiGe/Si heterostructures and its dependence on deposition technique and growth atmosphere". *Appl. Phys. Lett.*, Vol. 63, No. 18, pp. 2531–2533, Nov. 1993. URL: http://apl.aip.org/resource/1/applab/v63/i18/p2531_s1. 95

[Haid 98] M. Haider, H. Rose, S. Uhlemann, E. Schwan, B. Kabius, and K. Urban. "A spherical-aberration-corrected 200 kV transmission electron microscope". *Ultramicroscopy*, Vol. 75, No. 1, pp. 53–60, Oct. 1998. URL: http://www.sciencedirect.com/science/article/pii/S0304399198000485. 19

[Hain 04] J. F. Hainfeld, D. N. Slatkin, and H. M. Smilowitz. "The use of gold nanoparticles to enhance radiotherapy in mice". *Phys. Med. Biol.*, Vol. 49, No. 18, pp. N309–N315, Sep. 2004. URL: http://iopscience.iop.org/0031-9155/49/18/N03. 3

[Hart 02] J. Hartmann, V. Loup, G. Rolland, P. Holliger, F. Laugier, C. Vannuffel, and M. Séméria. "SiGe growth kinetics and doping in reduced pressure-chemical vapor deposition". *Journal of Crystal Growth*, Vol. 236, No. 1–3, pp. 10–20, March 2002. URL: http://www.sciencedirect.com/science/article/pii/S0022024801020851. 110

[Hert 12] M. I. den Hertog, F. González-Posada, R. Songmuang, J. L. Rouviere, T. Fournier, B. Fernandez, and E. Monroy. "Correlation of Polarity and Crystal Structure with Optoelectronic and Transport Properties of GaN/AlN/GaN Nanowire Sensors". *Nano Lett.*, Oct. 2012. URL: http://pubs.acs.org/doi/abs/10.1021/nl302890f. 57

[Hoeg 94] M. Horn-von Hoegen, M. Copel, J. C. Tsang, M. C. Reuter, and R. M. Tromp. "Surfactant-mediated growth of Ge on Si(111)". *Phys. Rev. B*, Vol. 50, No. 15, pp. 10811–10822, Oct. 1994. URL: http://link.aps.org/doi/10.1103/PhysRevB.50.10811. 95

[Hou 09] V.-D. Hou. "Reduce Correlated Noise in EELS Spectrum with High Quality Dark Reference". *Microsc. Microanal.*, Vol. 15, No. Supplement S2, pp. 226–227, 2009. URL: http://journals.cambridge.org/action/displayAbstract?fromPage=online&aid=5909576. 48, 49

[Hytc 98] M. J. Hÿtch, E. Snoeck, and R. Kilaas. "Quantitative measurement of displacement and strain fields from HREM micrographs". *Ultramicroscopy*, Vol. 74, No. 3, pp. 131–146, Aug. 1998. URL: http://www.sciencedirect.com/science/article/B6TW1-3VF6TB2-2C/2/6efd607cf6c3e1c16b0bc23209ae1f54. 168

[Imre 00] Á. Imre, D. L. Beke, E. Gontier-Moya, I. A. Szabó, and E. Gillet. "Surface Ostwald ripening of Pd nanoparticles on the MgO (100) surface". *Appl Phys A*, Vol. 71, No. 1, pp. 19–22, July 2000. URL: http://link.springer.com/article/10.1007/PL00021085. 84, 85

[Imre 99] Á. Imre, E. Gontier-Moya, D. Beke, I. Szabó, and G. Erdélyi. "Ostwald ripening of Pd particles on the (101?2?) surface of sapphire". *Surf. Sci.*, Vol. 441, No. 1, pp. 133–139, Oct. 1999. URL: http://www.sciencedirect.com/science/article/pii/S0039602899008456. 84, 85

[Inta 08] V. Intaraprasonk, H. L. Xin, and D. A. Muller. "Analytic derivation of optimal imaging conditions for incoherent imaging in aberration-corrected electron microscopes". *Ultramicroscopy*, Vol. 108, No. 11, pp. 1454–1466, Oct. 2008. URL: http://www.sciencedirect.com/science/article/pii/S0304399108001812. 36

[Jain 10] A. Jain, M. Jamet, A. Barski, T. Devillers, C. Porret, P. Bayle-Guillemaud,

S. Gambarelli, V. Maurel, and G. Desfonds. "Investigation of magnetic anisotropy of (Ge,Mn) nanocolumns". *Applied Physics Letters*, Vol. 97, No. 20, pp. 202502–202502–3, Nov. 2010. URL: http://link.aip.org/link/doi/10.1063/1.3505501. 186

[Jain 11] A. Jain, L. Louahadj, J. Peiro, J. C. Le Breton, C. Vergnaud, A. Barski, C. Beigné, L. Notin, A. Marty, V. Baltz, S. Auffret, E. Augendre, H. Jaffrès, J. M. George, and M. Jamet. "Electrical spin injection and detection at Al2O3/n-type germanium interface using three terminal geometry". *Appl. Phys. Lett.*, Vol. 99, p. 162102, 2011. URL: http://link.aip.org/link/APPLAB/v99/i16/p162102/s1&Agg=doi. 4

[Jame 06] M. Jamet, A. Barski, T. Devillers, V. Poydenot, R. Dujardin, P. Bayle-Guillemaud, J. Rothman, E. Bellet-Amalric, A. Marty, J. Cibert, R. Mattana, and S. Tatarenko. "High-Curie-temperature ferromagnetism in self-organized $Ge_{1-x}Mn_x$ nanocolumns". *Nat Mater*, Vol. 5, No. 8, pp. 653–659, 2006. URL: http://dx.doi.org/10.1038/nmat1686. 5, 141, 145, 146

[Jeon 10] K.-R. Jeon, B.-C. Min, H.-S. Lee, I.-J. Shin, C.-Y. Park, and S.-C. Shin. "Single crystalline CoFe/MgO tunnel contact on nondegenerate Ge with a proper resistance-area product for efficient spin injection and detection". *Appl. Phys. Lett.*, Vol. 97, p. 022105, 2010. URL: http://link.aip.org/link/APPLAB/v97/i2/p022105/s1&Agg=doi. 4

[Jian 12] N. Jiang and J. C. Spence. "On the dose-rate threshold of beam damage in TEM". *Ultramicroscopy*, Vol. 113, No. 0, pp. 77–82, Feb. 2012. URL: http://www.sciencedirect.com/science/article/pii/S0304399111003354. 83

[Jins 11] J. R. Jinschek, E. Yucelen, H. A. Calderon, and B. Freitag. "Quantitative atomic 3-D imaging of single/double sheet graphene structure". *Carbon*, Vol. 49, No. 2, pp. 556–562, 2011. URL: http://www.sciencedirect.com/science/article/pii/S0008622310007074. 22

[Jose 01] M. José-Yacamán, J. A. Ascencio, H. B. Liu, and J. Gardea-Torresdey. "Structure shape and stability of nanometric sized particles". *J. Vac. Sci. Technol. B*, Vol. 19, No. 4, pp. 1091–1103, 2001. URL: http://link.aip.org/link/?JVB/19/1091/1. 75

[Jose 05] M. José-Yacamán, C. Gutierrez-Wing, M. Miki, D.-Q. Yang, K. N. Piyakis, and E. Sacher. "Surface Diffusion and Coalescence of Mobile Metal Nanoparticles". *J. Phys. Chem. B*, Vol. 109, No. 19, pp. 9703–9711, 2005. URL: http://dx.doi.org/10.1021/jp0509459. 63, 65

[Kabi 09] B. Kabius, P. Hartel, M. Haider, H. Muller, S. Uhlemann, U. Loebau,

J. Zach, and H. Rose. “First application of Cc-corrected imaging for high-resolution and energy-filtered TEM”. *J. Electron Microsc.*, Vol. 58, No. 3, pp. 147–155, June 2009. URL: http://jmicro.oxfordjournals.org/cgi/content/abstract/58/3/147. 20

[Karl 08] H. L. Karlsson, P. Cronholm, J. Gustafsson, and L. Möller. “Copper Oxide Nanoparticles Are Highly Toxic: A Comparison between Metal Oxide Nanoparticles and Carbon Nanotubes”. *Chem. Res. Toxicol.*, Vol. 21, No. 9, pp. 1726–1732, Sep. 2008. URL: http://dx.doi.org/10.1021/tx800064j. 3

[Kass 12a] C. A. N. J. K. Kassim, J. A. Floro, and P. Reinke. “Surface Driven Mn-Doping of Ge Quantum Dots - Mn-Interaction with the Ge QD{105} Facet and the Wetting Layer”. *arXiv*, Oct. 2012. URL: http://arxiv.org/abs/1210.7851. 141

[Kass 12b] J. Kassim, C. Nolph, M. Jamet, P. Reinke, and J. Floro. “Mn solid solutions in self-assembled Ge/Si(001) quantum dot heterostructures”. *J. Appl. Phys.*, Vol. 101, No. 24, pp. 242407–242407–5, Dec. 2012. URL: http://apl.aip.org/resource/1/applab/v101/i24/p242407_s1. 127, 128, 131, 141

[Kass 13] J. Kassim, C. Nolph, M. Jamet, P. Reinke, and J. Floro. “$Ge_{1-x}Mn-x$ heteroepitaxial quantum dots: Growth, morphology, and magnetism”. *J. Appl. Phys.*, Vol. 113, No. 7, pp. 073910–073910–7, Feb. 2013. URL: http://jap.aip.org/resource/1/japiau/v113/i7/p073910_s1. 141

[Kell 90] G. L. Kellogg and P. J. Feibelman. “Surface self-diffusion on Pt(001) by an atomic exchange mechanism”. *Phys. Rev. Lett.*, Vol. 64, No. 26, pp. 3143–3146, 1990. URL: http://link.aps.org/doi/10.1103/PhysRevLett.64.3143. 3, 86

[Kell 92] G. L. Kellogg. “Surface diffusion of Pt adatoms on Ni surfaces”. *Surf. Sci.*, Vol. 266, No. 1-3, pp. 18–23, 1992. URL: http://www.sciencedirect.com/science/article/pii/003960289290991E. 3

[Kell 93a] G. L. Kellogg. “Diffusion behavior of Pt adatoms and clusters on the Rh(100) surface”. *Appl. Surf. Sci.*, Vol. 67, No. 1-4, pp. 134–141, 1993. URL: http://www.sciencedirect.com/science/article/pii/016943329390305U. 3

[Kell 93b] G. L. Kellogg. “Diffusion of individual Pt atoms on single-crystal surfaces of rhodium”. *Phys. Rev. B*, Vol. 48, No. 15, pp. 11305–11312, Oct. 1993. URL: http://link.aps.org/doi/10.1103/PhysRevB.48.11305. 3

[Kell 94] G. Kellogg. “Field ion microscope studies of single-atom surface diffusion and cluster nucleation on metal surfaces”. *Surf. Sci. Rep.*, Vol. 21, No. 1-2, pp. 1–88, 1994. URL: http://www.sciencedirect.com/science/article/pii/0167572994900078. 3

[Kila 98] R. Kilaas. “Optimal and near-optimal filters in high-resolution electron microscopy”. *J Microsc*, Vol. 190, No. 1-2, pp. 45–51, Apr. 1998. URL: http://onlinelibrary.wiley.com/doi/10.1046/j.1365-2818.1998.3070861.x/abstract;jsessionid=15A0991706621641226O6AD4363001E1.d01t01. 168

[Kim 11] S. Kim, Y. Oshima, H. Sawada, T. Kaneyama, Y. Kondo, M. Takeguchi, Y. Nakayama, Y. Tanishiro, and K. Takayanagi. “Quantitative annular dark-field STEM images of a silicon crystal using a large-angle convergent electron probe with a 300-kV cold field-emission gun”. *J. Electron Microsc.*, Vol. 60, No. 2, pp. 109 –116, Apr. 2011. URL: http://jmicro.oxfordjournals.org/content/60/2/109.abstract. 43

[Kim 12] S. Kim, Y. Oshima, Y. Tanishiro, and K. Takayanagi. “Study on probe current dependence of the intensity distribution in annular dark field images”. *Ultramicroscopy*, Vol. 121, No. 0, pp. 38–41, Oct. 2012. URL: http://www.sciencedirect.com/science/article/pii/S0304399112001635. 43

[Kim 13] H. Kim, Y. Meng, J.-L. Rouviére, D. Isheim, D. N. Seidman, and J.-M. Zuo. “Atomic resolution mapping of interfacial intermixing and segregation in InAs/GaSb superlattices: A correlative study”. *J. Appl. Phys.*, Vol. 113, No. 10, pp. 103511–103511–6, March 2013. URL: http://jap.aip.org/resource/1/japiau/v113/i10/p103511_s1. 104, 106

[Kim 97] H. Kim, N. Taylor, J. R. Abelson, and J. E. Greene. “Effects of H coverage on Ge segregation during $Si_{1-x}Ge_x$ gas-source molecular beam epitaxy”. *J. Appl. Phys.*, Vol. 82, No. 12, pp. 6062–6066, Dec. 1997. URL: http://jap.aip.org/resource/1/japiau/v82/i12/p6062_s1. 95

[Kirc 71] H. O. K. Kirchner. “Coarsening of grain-boundary precipitates”. *Met. Trans.*, Vol. 2, No. 10, pp. 2861–2864, Oct. 1971. URL: http://link.springer.com/article/10.1007/BF02813264. 65

[Kirk 10] E. Kirkland. *Advanced Computing in Electron Microscopy. Chemistry and Materials Science*, 2nd Ed., 2010. URL: http://www.springer.com/physics/optics+&+lasers/book/978-1-4419-6532-5. 13, 15, 16, 19, 33, 36, 103

[Kirk 13] E. Kirkland. “Computation of Transmission Electron Micrographs”. 2013. URL: http://people.ccmr.cornell.edu/~kirkland/. 31

[Kisi 08] C. Kisielowski, B. Freitag, M. Bischoff, H. van Lin, S. Lazar, G. Knippels, P. Tiemeijer, M. van der Stam, S. von Harrach, M. Stekelenburg, M. Haider, S. Uhlemann, H. M?ller, P. Hartel, B. Kabius, D. Miller, I. Petrov, E. Olson, T. Donchev, E. Kenik, A. Lupini, J. Bentley, S. Pennycook, I. Anderson, A. Minor, A. Schmid, T. Duden, V. Radmilovic, Q. Ramasse, M. Watanabe, R. Erni, E. Stach, P. Denes, and U. Dahmen. "Detection of Single Atoms and Buried Defects in Three Dimensions by Aberration-Corrected Electron Microscope with 0.5-Å Information Limit". *Microsc. Microanal.*, Vol. 14, No. 05, pp. 469–477, 2008. URL: http://journals.cambridge.org/action/displayAbstract?fromPage=online&aid=2203340. 20

[Klep 87] S. J. Klepeis, J. P. Benedict, and R. M. Anderson. "A Grinding/Polishing Tool for TEM Sample Preparation". In: *MRS Online Proceedings Library*, 1987. 55

[Knob 00] R. Knobel, N. Samarth, S. Crooker, and D. Awschalom. "Spin-polarized quantum transport and magnetic field-dependent carrier density in magnetic two-dimensional electron gases". *Physica E: Low-dimensional Systems and Nanostructures*, Vol. 6, No. 1–4, pp. 786–789, 2000. URL: http://www.sciencedirect.com/science/article/pii/S1386947799002386. 89

[Ko 08] V. Ko, K. L. Teo, T. Liew, T. C. Chong, T. Liu, A. T. S. Wee, A. Y. Du, M. Stoffel, and O. G. Schmidt. "Correlation of structural and magnetic properties of ferromagnetic Mn-implanted $Si_{1-x}Ge_x$ films". *J. Appl. Phys.*, Vol. 103, No. 5, p. 053912, 2008. URL: http://link.aip.org/link/JAPIAU/v103/i5/p053912/s1&Agg=doi. 127

[Kong 06] K.-J. Kong, Y. Choi, B.-H. Ryu, J.-O. Lee, and H. Chang. "Investigation of metal/carbon-related materials for fuel cell applications by electronic structure calculations". *Mater. Sci. Eng. C*, Vol. 26, No. 5-7, pp. 1207–1210, July 2006. URL: http://www.sciencedirect.com/science/article/B6TXG-4HDG9C1-2/2/182eef6354f652740080fc628efd7104. 86

[Kriv 03] O. Krivanek, P. Nellist, N. Dellby, M. Murfitt, and Z. Szilagyi. "Towards sub-0.5 Å electron beams". *Ultramicroscopy*, Vol. 96, No. 3–4, pp. 229–237, Sep. 2003. URL: http://www.sciencedirect.com/science/article/pii/S0304399103000901. 37

[Kriv 08] O. Krivanek, G. Corbin, N. Dellby, B. Elston, R. Keyse, M. Murfitt, C. Own, Z. Szilagyi, and J. Woodruff. "An electron microscope for the aberration-corrected era". *Ultramicroscopy*, Vol. 108, No. 3, pp. 179–195,

Feb. 2008. URL: http://www.sciencedirect.com/science/article/B6TW1-4PYGW49-6/2/627fbeada8b1dc980f40418e11d9890b. 36

[Kriv 10] O. L. Krivanek, M. F. Chisholm, V. Nicolosi, T. J. Pennycook, G. J. Corbin, N. Dellby, M. F. Murfitt, C. S. Own, Z. S. Szilagyi, M. P. Oxley, S. T. Pantelides, and S. J. Pennycook. "Atom-by-atom structural and chemical analysis by annular dark-field electron microscopy". *Nature*, Vol. 464, No. 7288, pp. 571–574, March 2010. URL: http://dx.doi.org/10.1038/nature08879. 97

[Kuma 08] V. Kumar and Y. Kawazoe. "Evolution of atomic and electronic structure of Pt clusters: Planar, layered, pyramidal, cage, cubic, and octahedral growth". *Phys. Rev. B*, Vol. 77, No. 20, p. 205418, May 2008. URL: http://link.aps.org/doi/10.1103/PhysRevB.77.205418. 75, 76, 86

[Lars 12] E. M. Larsson, J. Millet, S. Gustafsson, M. Skoglundh, V. P. Zhdanov, and C. Langhammer. "Real Time Indirect Nanoplasmonic in Situ Spectroscopy of Catalyst Nanoparticle Sintering". *ACS Catal.*, Vol. 2, No. 2, pp. 238–245, 2012. URL: http://dx.doi.org/10.1021/cs200583u. 86

[Lebe 08a] J. Lebeau and S. Stemmer. "Experimental quantification of annular dark-field images in scanning transmission electron microscopy". *Ultramicroscopy*, Vol. 108, No. 12, pp. 1653–1658, Nov. 2008. URL: http://www.sciencedirect.com/science/article/pii/S0304399108001903. 39, 40

[LeBe 08b] J. M. LeBeau, S. D. Findlay, L. J. Allen, and S. Stemmer. "Quantitative Atomic Resolution Scanning Transmission Electron Microscopy". *Phys. Rev. Lett.*, Vol. 100, No. 20, p. 206101, 2008. URL: http://link.aps.org/doi/10.1103/PhysRevLett.100.206101. 43

[LeBe 10] J. M. LeBeau, S. D. Findlay, L. J. Allen, and S. Stemmer. "Position averaged convergent beam electron diffraction: Theory and applications". *Ultramicroscopy*, Vol. 110, No. 2, pp. 118–125, Jan. 2010. URL: http://www.sciencedirect.com/science/article/B6TW1-4XFFJTC-1/2/d7837d689bfa913feee45ab1d2a7058a. 42

[Lee 98] I. Lee, K.-Y. Chan, and D. L. Phillips. "Growth of electrodeposited platinum nanocrystals studied by atomic force microscopy". *Appl. Surf. Sci.*, Vol. 136, No. 4, pp. 321–330, 1998. URL: http://www.sciencedirect.com/science/article/pii/S0169433298003559. 3

[Li 07] A. P. Li, C. Zeng, K. van Benthem, M. F. Chisholm, J. Shen, S. V. S. Nageswara Rao, S. K. Dixit, L. C. Feldman, A. G. Petukhov, M. Foygel, and H. H. Weitering. "Dopant segregation and giant magnetoresistance in manganese-doped germanium". *Phys. Rev. B*, Vol. 75, No. 20, p. 201201,

2007. URL: http://link.aps.org/doi/10.1103/PhysRevB.75.201201. 5, 141, 145, 146, 147, 165

[Li 95] Y. Li, G. G. Hembree, and J. A. Venables. "Quantitative Auger electron spectroscopic analysis of Ge surface segregation in Si/Ge/Si(100) heterostructures". *Appl. Phys. Lett.*, Vol. 67, No. 2, pp. 276–278, July 1995. URL: http://apl.aip.org/resource/1/applab/v67/i2/p276_s1. 95

[Lifs 61] I. Lifshitz and V. Slyozov. "The kinetics of precipitation from supersaturated solid solutions". *J. Phys. Chem Solids*, Vol. 19, No. 1-2, pp. 35–50, 1961. URL: http://www.sciencedirect.com/science/article/pii/0022369761900543. 64

[Lind 99] T. R. Linderoth, S. Horch, L. Petersen, S. Helveg, E. Lægsgaard, I. Stensgaard, and F. Besenbacher. "Novel Mechanism for Diffusion of One-Dimensional Clusters: Pt/Pt(110)-(1×2)". *Phys. Rev. Lett.*, Vol. 82, No. 7, pp. 1494–1497, 1999. URL: http://link.aps.org/doi/10.1103/PhysRevLett.82.1494. 3

[Loof 93] P. Loof, B. Stenbom, H. Norden, and B. Kasemo. "Rapid Sintering in NO of Nanometer-Sized Pt Particles on γ-Al2O3 Observed by CO Temperature-Programmed Desorption and Transmission Electron Microscopy". *J. Catal.*, Vol. 144, No. 1, pp. 60–76, Nov. 1993. URL: http://www.sciencedirect.com/science/article/pii/S002195178371314X. 86, 87

[Maha 03] P. Mahadevan and A. Zunger. "Ferromagnetism in Mn-doped GaAs due to substitutional-interstitial complexes". *Physical Review B*, Vol. 68, No. 7, p. 075202, Aug. 2003. URL: http://link.aps.org/doi/10.1103/PhysRevB.68.075202. 145

[Mali 88] T. Malis, S. C. Cheng, and R. F. Egerton. "EELS log-ratio technique for specimen-thickness measurement in the TEM". *J. Electron Microsc.*, Vol. 8, No. 2, pp. 193–200, 1988. URL: http://dx.doi.org/10.1002/jemt.1060080206. 52, 58

[Mark 96] L. D. Marks. "Wiener-filter enhancement of noisy HREM images". *Ultramicroscopy*, Vol. 62, No. 1-2, pp. 43–52, Jan. 1996. URL: http://www.sciencedirect.com/science/article/B6TW1-3VSPXHM-5/2/0daa1550a94f4e5880198a7b2cca8849. 168

[McLe 66] M. McLean and H. Mykura. "The temperature dependence of the surface energy anisotropy of platinum". *Surf. Sci.*, Vol. 5, No. 4, pp. 466–481, Dec. 1966. URL: http://www.sciencedirect.com/science/article/pii/0039602866900422. 85

[Mene 04] J. Menéndez and J. Kouvetakis. "Type-I Ge/Ge1-x-ySixSny strained-layer heterostructures with a direct Ge bandgap". *Applied Physics Letters*, Vol. 85, No. 7, pp. 1175–1177, Aug. 2004. URL: http://apl.aip.org/resource/1/applab/v85/i7/p1175_s1. 176

[Meye 08] J. C. Meyer, C. Kisielowski, R. Erni, M. D. Rossell, M. F. Crommie, and A. Zettl. "Direct Imaging of Lattice Atoms and Topological Defects in Graphene Membranes". *Nano Lett.*, Vol. 8, No. 11, pp. 3582–3586, Nov. 2008. URL: http://dx.doi.org/10.1021/nl801386m. 20

[Miga 04] D. B. Migas, P. Raiteri, L. Miglio, A. Rastelli, and H. von Känel. "Evolution of the Ge/Si(001) wetting layer during Si overgrowth and crossover between thermodynamic and kinetic behavior". *Phys. Rev. B*, Vol. 69, No. 23, p. 235318, 2004. URL: http://link.aps.org/doi/10.1103/PhysRevB.69.235318. 92

[Mkho 08] K. Mkhoyan, S. Maccagnano-Zacher, E. Kirkland, and J. Silcox. "Effects of amorphous layers on ADF-STEM imaging". *Ultramicroscopy*, Vol. 108, No. 8, pp. 791–803, 2008. URL: http://www.sciencedirect.com/science/article/pii/S0304399108000211. 54

[Mout 12] I. Mouton, R. Lardé, E. Talbot, E. Cadel, C. Genevois, D. Blavette, V. Baltz, E. Prestat, P. Bayle-Guillemaud, A. Barski, and M. Jamet. "Composition and morphology of self-organized Mn-rich nanocolumns embedded in Ge: Correlation with the magnetic properties". *Journal of Applied Physics*, Vol. 112, No. 11, pp. 113918–113918–7, Dec. 2012. URL: http://jap.aip.org/resource/1/japiau/v112/i11/p113918_s1. 157, 159

[Mull 96] P. Müller and R. Kern. "The physical origin of the two-dimensional towards three-dimensional coherent epitaxial Stranski-Krastanov transition". *Applied Surface Science*, Vol. 102, pp. 6–11, Aug. 1996. URL: http://www.sciencedirect.com/science/article/pii/0169433296000098. 91

[Mura 92] K. Muraki, S. Fukatsu, Y. Shiraki, and R. Ito. "Surface segregation of In atoms during molecular beam epitaxy and its influence on the energy levels in InGaAs/GaAs quantum wells". *Appl. Phys. Lett.*, Vol. 61, No. 5, pp. 557–559, Aug. 1992. URL: http://apl.aip.org/resource/1/applab/v61/i5/p557_s1. 125

[Nie 07] A. Nie, J. Wu, C. Zhou, S. Yao, C. Luo, R. C. Forrey, and H. Cheng. "Structural evolution of subnano platinum clusters". *Int. J. Quantum. Chem.*, Vol. 107, No. 1, p. 219–224, 2007. URL: http://onlinelibrary.wiley.com/doi/10.1002/qua.21011/abstract. 75, 86

[Niko 08] D. E. Nikonov and G. I. Bourianoff. "Operation and Modeling of Semiconductor Spintronics Computing Devices". *J Supercond Nov Magn*, Vol. 21, No. 8, pp. 479–493, Dec. 2008. URL: http://link.springer.com/article/10.1007/s10948-008-0343-y. 90

[Okaz 10] K. Okazaki-Maeda, Y. Morikawa, S. Tanaka, and M. Kohyama. "Structures of Pt clusters on graphene by first-principles calculations". *Surf. Sci.*, Vol. 604, No. 2, pp. 144–154, Jan. 2010. URL: http://www.sciencedirect.com/science/article/B6TVX-4XNF883-1/2/be6426b4b32c72179696a899e3f77586. 86

[Okun 10] H. Okuno, J.-L. Rouvière, P.-H. Jouneau, P. Bayle-Guillemaud, and B. Daudin. "Visualization of Tm dopant atoms diffused out of GaN quantum dots". *Appl. Phys. Lett.*, Vol. 96, No. 25, p. 251908, 2010. URL: http://link.aip.org/link/APPLAB/v96/i25/p251908/s1&Agg=doi. 39, 104

[Ostw 00] W. Ostwald. "Über die vermeintliche Isomerie des roten und gelben Quecksilberox- yds und die Oberflächenspannung fester Körper". *Z. Phys. Chem.*, Vol. 34, p. 495, 1900. 64

[Ourm 89] A. Ourmazd, D. W. Taylor, J. Cunningham, and C. W. Tu. "Chemical Mapping of Semiconductor Interfaces at Near-Atomic Resolution". *Phys. Rev. Lett.*, Vol. 62, No. 8, pp. 933–936, 1989. URL: http://link.aps.org/doi/10.1103/PhysRevLett.62.933. 104

[Park 01] Y. D. Park, A. Wilson, A. T. Hanbicki, J. E. Mattson, T. Ambrose, G. Spanos, and B. T. Jonker. "Magnetoresistance of Mn:Ge ferromagnetic nanoclusters in a diluted magnetic semiconductor matrix". *Appl. Phys. Lett.*, Vol. 78, No. 18, pp. 2739–2741, Apr. 2001. URL: http://apl.aip.org/resource/1/applab/v78/i18/p2739_s1. 5, 145

[Park 02] Y. D. Park, A. T. Hanbicki, S. C. Erwin, C. S. Hellberg, J. M. Sullivan, J. E. Mattson, T. F. Ambrose, A. Wilson, G. Spanos, and B. T. Jonker. "A Group-IV Ferromagnetic Semiconductor: Mn_xGe_{1-x}". *Science*, Vol. 295, No. 5555, pp. 651–654, Jan. 2002. URL: http://www.sciencemag.org/cgi/content/abstract/295/5555/651. 5, 145

[Pena 11] F. de la Peña, M.-H. Berger, J.-F. Hochepied, F. Dynys, O. Stephan, and M. Walls. "Mapping titanium and tin oxide phases using EELS: An application of independent component analysis". *Ultramicroscopy*, Vol. 111, No. 2, pp. 169–176, Jan. 2011. URL: http://www.sciencedirect.com/science/article/pii/S030439911000255X. 50

[Penn 88] S. J. Pennycook and L. A. Boatner. "Chemically sensitive structure-imaging with a scanning transmission electron microscope". *Nature*,

Vol. 336, No. 6199, pp. 565–567, Dec. 1988. URL: http://www.nature.com/nature/journal/v336/n6199/abs/336565a0.html. 97

[Poga 68] A. P. Pogany and P. S. Turner. "Reciprocity in electron diffraction and microscopy". *Acta Crystallogr. A*, Vol. 24, No. 1, pp. 103–109, Jan. 1968. URL: http://scripts.iucr.org/cgi-bin/paper?S0567739468000136. 32

[Pope 09] R. Popescu, R. Schneider, D. Gerthsen, A. Böttcher, D. Löffler, P. Weis, and M. Kappes. "Coarsening of mass-selected Au clusters on amorphous carbon at room temperature". *Surf. Sci.*, Vol. 603, No. 20, pp. 3119–3125, 2009. URL: http://www.sciencedirect.com/science/article/B6TVX-4X49YB1-1/2/55e7e983004876160271a2af1593069d. 65

[Porc 10] E. Porcel, S. Liehn, H. Remita, N. Usami, K. Kobayashi, Y. Furusawa, C. L. Sech, and S. Lacombe. "Platinum nanoparticles: a promising material for future cancer therapy?". *Nanotechnology*, Vol. 21, p. 085103, Feb. 2010. URL: http://iopscience.iop.org/0957-4484/21/8/085103. 3

[Radt 13] G. Radtke, L. Favre, M. Couillard, G. Amiard, I. Berbezier, and G. A. Botton. "Atomic-scale Ge diffusion in strained Si revealed by quantitative scanning transmission electron microscopy". *Phys. Rev. B*, Vol. 87, No. 20, p. 205309, May 2013. URL: http://link.aps.org/doi/10.1103/PhysRevB.87.205309. 104, 117, 119

[Rast 02] A. Rastelli, E. Müller, and H. von Känel. "Shape preservation of Ge/Si(001) islands during Si capping". *Appl. Phys. Lett.*, Vol. 80, No. 8, pp. 1438–1440, Feb. 2002. URL: http://apl.aip.org/resource/1/applab/v80/i8/p1438_s1. 95

[Reim 08] L. Reimer and H. Kohl. *Transmission Electron Microscopy. Springer Series in Optical Sciences*, Springer, 5 Ed., 2008. URL: http://www.springer.com/materials/book/978-0-387-40093-8. 17

[Rose 09] A. Rosenauer, K. Gries, K. Müller, A. Pretorius, M. Schowalter, A. Avramescu, K. Engl, and S. Lutgen. "Measurement of specimen thickness and composition in AlxGa1-xN/GaN using high-angle annular dark field images". *Ultramicroscopy*, Vol. 109, No. 9, pp. 1171–1182, 2009. URL: http://www.sciencedirect.com/science/article/B6TW1-4W91PY1-2/2/377d9008104d5889aa5e83786389aaaa. 39, 40, 43, 107

[Rose 11] A. Rosenauer, T. Mehrtens, K. Müller, K. Gries, M. Schowalter, P. Venkata Satyam, S. Bley, C. Tessarek, D. Hommel, K. Sebald,

M. Seyfried, J. Gutowski, A. Avramescu, K. Engl, and S. Lutgen. "Composition mapping in InGaN by scanning transmission electron microscopy". *Ultramicroscopy*, Vol. 111, No. 8, pp. 1316–1327, 2011. URL: http://www.sciencedirect.com/science/article/pii/S0304399111001598. 107

[Rose 99] G. Rosenfeld, K. Morgenstern, M. Esser, and G. Comsa. "Dynamics and stability of nanostructures on metal surfaces". *Appl. Phys. A-Mater.*, Vol. 69, pp. 489–496, Nov. 1999. URL: http://www.springerlink.com/content/dm9xntuyrur8u2p6/. 62

[Rouv 05] J. Rouvière and E. Sarigiannidou. "Theoretical discussions on the geometrical phase analysis". *Ultramicroscopy*, Vol. 106, No. 1, pp. 1–17, 2005. URL: http://www.sciencedirect.com/science/article/B6TW1-4GKW5VX-1/2/0dd8d37c77ee1f93ce1f11086b58e424. 168

[Rouv 11] J. L. Rouvière, A. Mouti, and P. Stadelmann. "Measuring strain on HR-STEM images: application to threading dislocations in $Al_{0.8}In_{0.2}N$". *J. Phys.: Conf. Ser.*, Vol. 326, No. 1, p. 012022, Nov. 2011. URL: http://iopscience.iop.org/1742-6596/326/1/012022. 171

[Rove 08] M. Rovezzi, T. Devillers, E. Arras, F. d'Acapito, A. Barski, M. Jamet, and P. Pochet. "Atomic structure of Mn-rich nanocolumns probed by x-ray absorption spectroscopy". *Appl. Phys. Lett.*, Vol. 92, No. 24, p. 242510, 2008. URL: http://link.aip.org/link/APPLAB/v92/i24/p242510/s1&Agg=doi. 147

[Sato 05] K. Sato, H. Katayama-Yoshida, and P. H. Dederichs. "High Curie Temperature and Nano-Scale Spinodal Decomposition Phase in Dilute Magnetic Semiconductors". *Jpn. J. Appl. Phys.*, Vol. 44, No. 30, pp. L948–L951, 2005. URL: http://jjap.jsap.jp/link?JJAP/44/L948/. 5, 146

[Sawa 08] H. Sawada, T. Sannomiya, F. Hosokawa, T. Nakamichi, T. Kaneyama, T. Tomita, Y. Kondo, T. Tanaka, Y. Oshima, Y. Tanishiro, and K. Takayanagi. "Measurement method of aberration from Ronchigram by autocorrelation function". *Ultramicroscopy*, Vol. 108, No. 11, pp. 1467–1475, Oct. 2008. URL: http://www.sciencedirect.com/science/article/pii/S0304399108001824. 20

[Scha 09] B. Schaffer, U. Hohenester, A. Trügler, and F. Hofer. "High-resolution surface plasmon imaging of gold nanoparticles by energy-filtered transmission electron microscopy". *Phys. Rev. B*, Vol. 79, No. 4, p. 041401, Jan. 2009. URL: http://link.aps.org/doi/10.1103/PhysRevB.79.041401. 20

[Sche 36] O. Scherzer. "Über einige Fehler von Elektronenlinsen". *Z. Phys.*, Vol. 101, No. 9-10, pp. 593–603, 1936. 18

[Sche 47] O. Scherzer. “Sphärische Und Chromatische Korrektur Von Elektronen-Linsen”. *Optik*, Vol. 2, No. 2, pp. 114–132, 1947. 19

[Sche 49] O. Scherzer. “The Theoretical Resolution Limit of the Electron Microscope”. *J. Appl. Phys.*, Vol. 20, No. 1, pp. 20–29, Jan. 1949. URL: http://jap.aip.org/resource/1/japiau/v20/i1/p20_s1. 18, 35

[Schm 00] G. Schmidt, D. Ferrand, L. W. Molenkamp, A. T. Filip, and B. J. van Wees. “Fundamental obstacle for electrical spin injection from a ferromagnetic metal into a diffusive semiconductor”. *Phys. Rev. B*, Vol. 62, No. 8, pp. R4790–R4793, 2000. URL: http://link.aps.org/doi/10.1103/PhysRevB.62.R4790. 4

[Shao 07] Y. Shao-Horn, W. C. Sheng, S. Chen, P. J. Ferreira, E. F. Holby, and D. Morgan. “Instability of Supported Platinum Nanoparticles in Low-Temperature Fuel Cells”. *Top. Catal.*, Vol. 46, No. 3-4, pp. 285–305, Nov. 2007. URL: http://link.springer.com/article/10.1007/s11244-007-9000-0?null. 3

[Simo 10] S. B. Simonsen, I. Chorkendorff, S. Dahl, M. Skoglundh, J. Sehested, and S. Helveg. “Direct Observations of Oxygen-induced Platinum Nanoparticle Ripening Studied by In Situ TEM”. *J. Am. Chem. Soc.*, Vol. 132, No. 23, pp. 7968–7975, 2010. URL: http://dx.doi.org/10.1021/ja910094r. 3

[Simo 11] S. B. Simonsen, I. Chorkendorff, S. Dahl, M. Skoglundh, J. Sehested, and S. Helveg. “Ostwald ripening in a Pt/SiO_2 model catalyst studied by in situ TEM”. *J. Catal.*, Vol. 281, No. 1, pp. 147–155, 2011. URL: http://www.sciencedirect.com/science/article/pii/S0021951711001333. 3

[Smol 16] M. V. Smoluchowski. “Drei Vortrage uber Diffusion, Brownsche Bewegung und Koagulation von Kolloidteilchen”. *Zeitschrift fur Physik*, Vol. 17, pp. 557–585, 1916. URL: http://adsabs.harvard.edu/abs/1916ZPhy...17..557S. 63

[Stad 87] P. Stadelmann. “EMS - a software package for electron diffraction analysis and HREM image simulation in materials science”. *Ultramicroscopy*, Vol. 21, No. 2, pp. 131–145, 1987. URL: http://www.sciencedirect.com/science/article/B6TW1-46JGKP6-3/2/c0d4152d2136ea0e6997b14e7dd98384. 76, 165

[Ster 83] S. R. Sternberg. “Biomedical Image Processing”. Vol. 16, No. 1, pp. 22–34, 1983. 117

[Stil 85] F. H. Stillinger and T. A. Weber. “Computer simulation of local order in condensed phases of silicon”. *Phys. Rev. B*, Vol. 31, No. 8, pp. 5262–

5271, Apr. 1985. URL: http://link.aps.org/doi/10.1103/PhysRevB.31.5262. 169

[Suga 05] S. Sugahara, K. L. Lee, S. Yada, and M. Tanaka. "Precipitation of Amorphous Ferromagnetic Semiconductor Phase in Epitaxially Grown Mn-Doped Ge Thin Films". *Jpn. J. Appl. Phys.*, Vol. 44, No. 48, pp. L1426–L1429, 2005. URL: http://jjap.jsap.jp/link?JJAP/44/L1426/. 146

[Sutt 98] P. Sutter and M. G. Lagally. "Embedding of Nanoscale 3D SiGe Islands in a Si Matrix". *Phys. Rev. Lett.*, Vol. 81, No. 16, pp. 3471–3474, Oct. 1998. URL: http://link.aps.org/doi/10.1103/PhysRevLett.81.3471. 95

[Taka 11] K. Takayanagi, S. Kim, S. Lee, Y. Oshima, T. Tanaka, Y. Tanishiro, H. Sawada, F. Hosokawa, T. Tomita, T. Kaneyama, and Y. Kondo. "Electron microscopy at a sub-50 pm resolution". *Journal of Electron Microscopy*, Vol. 60, No. supplement 1, pp. S239–S244, Aug. 2011. URL: http://jmicro.oxfordjournals.org/content/60/suppl_1/S239.abstract?etoc. 8

[Take 96] M. Takeda and J. Suzuki. "Crystallographic heterodyne phase detection for highly sensitive lattice-distortion measurements". *J. Opt. Soc. Am. A*, Vol. 13, No. 7, pp. 1495–1500, 1996. URL: http://josaa.osa.org/abstract.cfm?URI=josaa-13-7-1495. 168

[Tang 11] Y. Tang, Z. Yang, and X. Dai. "Trapping of metal atoms in the defects on graphene". *J. Chem. Phys.*, Vol. 135, No. 22, pp. 224704–224704–7, Dec. 2011. URL: http://jcp.aip.org/resource/1/jcpsa6/v135/i22/p224704_s1. 86

[Tard 10] S. Tardif, V. Favre-Nicolin, F. Lançon, E. Arras, M. Jamet, A. Barski, C. Porret, P. Bayle-Guillemaud, P. Pochet, T. Devillers, and M. Rovezzi. "Strain and correlation of self-organized $Ge_{1-x}Mn_x$ nanocolumns embedded in Ge (001)". *Physical Review B*, Vol. 82, No. 10, p. 104101, 2010. URL: http://link.aps.org/doi/10.1103/PhysRevB.82.104101. 169, 184

[Tard 11] S. Tardif. *Nanocolonnes de GeMn : propriétés magnétiques et structurales à la lumière du synchrotron*. PhD thesis, Université de Grenoble, Jan. 2011. URL: http://tel.archives-ouvertes.fr/tel-00585130. 147, 175

[Ters 94] J. Tersoff and F. K. LeGoues. "Competing relaxation mechanisms in strained layers". *Phys. Rev. Lett.*, Vol. 72, No. 22, pp. 3570–3573, 1994. URL: http://link.aps.org/doi/10.1103/PhysRevLett.72.3570. 93

[Thom 07] K. Thompson, D. Lawrence, D. Larson, J. Olson, T. Kelly, and B. Gorman. "In situ site-specific specimen preparation for atom probe tomography". *Ultramicroscopy*, Vol. 107, No. 2–3, pp. 131–139, Feb.

2007. URL: http://www.sciencedirect.com/science/article/pii/S0304399106001203. 149

[Thus 96] A. Thust, M. Overwijk, W. Coene, and M. Lentzen. "Numerical correction of lens aberrations in phase-retrieval HRTEM". *Ultramicroscopy*, Vol. 64, No. 1-4, pp. 249–264, Aug. 1996. URL: http://www.sciencedirect.com/science/article/pii/0304399196000228. 18

[Treb 90] P. Trebbia and N. Bonnet. "EELS elemental mapping with unconventional methods I. Theoretical basis: Image analysis with multivariate statistics and entropy concepts". *Ultramicroscopy*, Vol. 34, No. 3, pp. 165–178, Dec. 1990. URL: http://www.sciencedirect.com/science/article/pii/0304399190900703. 49

[Tson 75] T. T. Tsong and G. Kellogg. "Direct observation of the directional walk of single adatoms and the adatom polarizability". *Phys. Rev. B*, Vol. 12, No. 4, pp. 1343–1353, 1975. URL: http://link.aps.org/doi/10.1103/PhysRevB.12.1343. 3

[Urba 13] K. W. Urban, J. Mayer, J. R. Jinschek, M. J. Neish, N. R. Lugg, and L. J. Allen. "Achromatic Elemental Mapping Beyond the Nanoscale in the Transmission Electron Microscope". *Phys. Rev. Lett.*, Vol. 110, No. 18, p. 185507, 2013. URL: http://link.aps.org/doi/10.1103/PhysRevLett.110.185507. 20

[Utla 80] M. Utlaut. "Direct observation of the behavior of heavy single atoms on amorphous carbon substrates". *Phys. Rev. B*, Vol. 22, No. 10, pp. 4650–4660, Nov. 1980. URL: http://link.aps.org/doi/10.1103/PhysRevB.22.4650. 86

[Vinc 09] B. Vincent, W. Vandervorst, M. Caymax, and R. Loo. "Influence of Si precursor on Ge segregation during ultrathin Si reduced pressure chemical vapor deposition on Ge". *Appl. Phys. Lett.*, Vol. 95, No. 26, pp. 262112–262112–3, Dec. 2009. URL: http://apl.aip.org/resource/1/applab/v95/i26/p262112_s1. 95

[Vinc 11] B. Vincent, F. Gencarelli, H. Bender, C. Merckling, B. Douhard, D. H. Petersen, O. Hansen, H. H. Henrichsen, J. Meersschaut, W. Vandervorst, M. Heyns, R. Loo, and M. Caymax. "Undoped and in-situ B doped GeSn epitaxial growth on Ge by atmospheric pressure-chemical vapor deposition". *Applied Physics Letters*, Vol. 99, No. 15, pp. 152103–152103–3, Oct. 2011. URL: http://apl.aip.org/resource/1/applab/v99/i15/p152103_s1. 176

[Voig 01] B. Voigtländer. “Fundamental processes in Si/Si and Ge/Si epitaxy studied by scanning tunneling microscopy during growth”. *Surface Science Reports*, Vol. 43, No. 5–8, pp. 127–254, Sep. 2001. URL: http://www.sciencedirect.com/science/article/pii/S0167572901000127. 91, 93

[Voyl 02] P. M. Voyles, D. A. Muller, J. L. Grazul, P. H. Citrin, and H.-J. L. Gossmann. “Atomic-scale imaging of individual dopant atoms and clusters in highly n-type bulk Si”. *Nature*, Vol. 416, No. 6883, pp. 826–829, Apr. 2002. URL: http://dx.doi.org/10.1038/416826a. 39, 107, 119

[Voyl 03] P. M. Voyles, J. L. Grazul, and D. A. Muller. “Imaging individual atoms inside crystals with ADF-STEM”. *Ultramicroscopy*, Vol. 96, No. 3-4, pp. 251–273, Sep. 2003. URL: http://www.sciencedirect.com/science/article/B6TW1-48MYFVN-1/2/ba3a91157a6325bc62955414295b929d. 55, 56, 119

[Vurp 00] F. Vurpillot, A. Bostel, and D. Blavette. “Trajectory overlaps and local magnification in three-dimensional atom probe”. *Appl. Phys. Lett.*, Vol. 76, No. 21, pp. 3127–3129, May 2000. URL: http://apl.aip.org/resource/1/applab/v76/i21/p3127_s1. 157

[Wagn 61] C. Wagner. “Theorie der Alterung von Niederschlägen durch Umlösen (Ostwald-Reifung)”. *Z. Elektrochem.*, Vol. 65, No. 7-8, pp. 581–591, Sep. 1961. URL: http://onlinelibrary.wiley.com/doi/10.1002/bbpc.19610650704/abstract. 64

[Walt 99] T. Walther and C. Humphreys. “A quantitative study of compositional profiles of chemical vapour-deposited strained silicon–germanium/silicon layers by transmission electron microscopy”. *Journal of Crystal Growth*, Vol. 197, No. 1–2, pp. 113–128, 1999. URL: http://www.sciencedirect.com/science/article/pii/S0022024898009300. 96

[Wang 00] Z. L. Wang. “Transmission Electron Microscopy of Shape-Controlled Nanocrystals and Their Assemblies”. *J. Phys. Chem. B*, Vol. 104, No. 6, pp. 1153–1175, 2000. URL: http://dx.doi.org/10.1021/jp993593c. 75

[Wang 10] D. Wang, C. V. Subban, H. Wang, E. Rus, F. J. DiSalvo, and H. D. Abruña. “Highly Stable and CO-Tolerant $Pt/Ti_{0.7}W_{0.3O2}$ Electrocatalyst for Proton-Exchange Membrane Fuel Cells”. *J. Am. Chem. Soc.*, Vol. 132, No. 30, pp. 10218–10220, 2010. URL: http://dx.doi.org/10.1021/ja102931d. 3

[Wata 13] M. Watanabe. “Microscopy Hacks: development of various techniques to assist quantitative nanoanalysis and advanced electron microscopy”.

Microscopy (Tokyo), Vol. 62, No. 2, pp. 217–241, Apr. 2013. URL: http://jmicro.oxfordjournals.org/content/62/2/217. 49

[Weic 91] A. Weickenmeier and H. Kohl. "Computation of absorptive form factors for high-energy electron diffraction". *Acta Crystallogr. A*, Vol. 47, No. 5, pp. 590–597, Sep. 1991. URL: http://scripts.iucr.org/cgi-bin/paper?S0108767391004804. 76

[Weic 95] A. L. Weickenmeier, W. Nüchter, and J. Mayer. "Quantitative characterization of point spread function and detection quantum efficiency for a YAG scintillator slow scan CCD camera". *Optik*, Vol. 99, No. 4, pp. 147–154, June 1995. 27, 76

[Will 09] D. B. Williams and C. B. Carter. *Transmission Electron Microscopy*. springer Ed., 2009. URL: http://www.springer.com/materials/characterization+&+evaluation/book/978-0-387-76500-6. 10, 11, 53, 197

[Wort 65] J. J. Wortman and R. A. Evans. "Young's Modulus, Shear Modulus, and Poisson's Ratio in Silicon and Germanium". Vol. 36, No. 1, pp. 153–156, Jan. 1965. URL: http://jap.aip.org/resource/1/japiau/v36/i1/p153_s1. 188

[Wynb 75] P. Wynblatt and N. Gjostein. "Supported metal crystallites". *Progress in Solid State Chemistry*, Vol. 9, pp. 21–58, 1975. URL: http://www.sciencedirect.com/science/article/pii/0079678675900138. 65, 70, 85

[Xin 08] H. L. Xin, V. Intaraprasonk, and D. A. Muller. "Depth sectioning of individual dopant atoms with aberration-corrected scanning transmission electron microscopy". *Appl. Phys. Lett.*, Vol. 92, No. 1, pp. 013125–013125–3, Jan. 2008. URL: http://apl.aip.org/resource/1/applab/v92/i1/p013125_s1. 39

[Xin 11] H. L. Xin, C. Dwyer, and D. A. Muller. "Quantitative chemical mapping at the atomic scale". *arXiv*, Oct. 2011. URL: http://arxiv.org/abs/1110.5018. 101

[Xiu 10] F. Xiu, Y. Wang, J. Kim, A. Hong, J. Tang, A. P. Jacob, J. Zou, and K. L. Wang. "Electric-field-controlled ferromagnetism in high-Curie-temperature $Mn_{0.05}Ge_{0.95}$ quantum dots". *Nat Mater*, Vol. 9, No. 4, pp. 337–344, Apr. 2010. URL: http://dx.doi.org/10.1038/nmat2716. 5, 90, 127, 128, 131, 141, 142, 176

[Yoon 10] I. Yoon. "Ferromagnetism of M_5Ge_3 Precipitates in Mn-implanted Self-organized Ge/Si Quantum Dots". *J. Supercond. Nov. Magn.*, Vol. 23,

No. 3, pp. 319–323, 2010. URL: http://dx.doi.org/10.1007/s10948-009-0532-3. 127

[Yu 10] I.-S. Yu, M. Jamet, T. Devillers, A. Barski, P. Bayle-Guillemaud, C. Beigné, J. Rothman, V. Baltz, and J. Cibert. "Spinodal decomposition to control magnetotransport in (Ge,Mn) films". *Phys. Rev. B*, Vol. 82, No. 3, p. 035308, July 2010. URL: http://link.aps.org/doi/10.1103/PhysRevB.82.035308. 158

[Zalm 89] P. C. Zalm, G. F. A. van de Walle, D. J. Gravesteijn, and A. A. van Gorkum. "Ge segregation at $Si/Si_{1-x}Ge_x$ interfaces grown by molecular beam epitaxy". *Appl. Phys. Lett.*, Vol. 55, No. 24, pp. 2520–2522, Dec. 1989. URL: http://apl.aip.org/resource/1/applab/v55/i24/p2520_s1. 95, 96

[Zanc 01] D. Zanchet, B. D. Hall, and D. Ugarte. "X-ray Characterization of Nanoparticles". In: e. Z. L. Wang, Ed., *Characterization of Nanophase Materials*, p. 13–36, Wiley-VCH Verlag GmbH, 2001. URL: http://onlinelibrary.wiley.com/doi/10.1002/3527600094.ch2/summary. 72

[Zeng 08] C. Zeng, Z. Zhang, K. van Benthem, M. F. Chisholm, and H. H. Weitering. "Optimal Doping Control of Magnetic Semiconductors via Subsurfactant Epitaxy". *Phys. Rev. Lett.*, Vol. 100, No. 6, p. 066101, Feb. 2008. URL: http://link.aps.org/doi/10.1103/PhysRevLett.100.066101. 141

[Zhan 09] Z. Zhang and D. Su. "Behaviour of TEM metal grids during in-situ heating experiments". *Ultramicroscopy*, Vol. 109, No. 6, pp. 766–774, 2009. URL: http://www.sciencedirect.com/science/article/pii/S0304399109000229. 65

[Zink 92] M. Zinke-Allmang, L. C. Feldman, and M. H. Grabow. "Clustering on surfaces". *Surf. Sci. Rep.*, Vol. 16, No. 8, pp. 377–463, 1992. URL: http://www.sciencedirect.com/science/article/pii/016757299290006W. 62, 64

Nomenclature

Acronyms

a-C	Amorphous carbon
ADF	Annular dark field
AES	Auger electron spectroscopy
APT	Atom Probe Tomography
BF	Bright field
CBED	convergent beam electron diffraction
CCD	Charge coupled device
CL	Core-loss
CO	cuboctahedral
CTEM	Conventional transmission electron microsopy
ED	Electron diffraction
EDX	Energy-dispersive X-ray
EELS	Electron energy loss spectroscopy
EXAFS	Extended X-ray-absorption fine-structure spectroscopy
fcc	Face-centered cubic
FEG	Field emission gun
FFT	Fast Fourier transform
FIB	Focused Ion Beam
FMS	Ferromagnetic Semiconductors

FWHM	Full width at half maximum
GIF	Gatan Imaging Filter
HAADF	High angle annular dark field
HOLZ	High Order Laue Zone
HRSTEM	High resolution scanning transmission electron microscopy
HRTEM	High resolution transmission electron microscopy
HRXRD	High resolution X-ray diffraction
LL	Loss-low
LTMBE	Low temperature molecular beam epitaxy
MEIS	Medium-energy ion scattering
ML	Monolayer
MTF	Modulation transfer function
NC	Nanocolumn
NP	Nanoparticle
OR	Ostwald ripening
PACBED	Position average convergent beam electron diffraction
PCA	Principal component analysis
PCTF	Phase contrast transfer function
PSF	Point spread function
RBS	Rutherford backscattering spectroscopy
RHEED	Reflection high-energy electron diffraction
RMS	Root-mean square
RPCVD	Reduced pressure-chemical vapor deposition
SAED	Selected area electron diffraction
SBR	Signal-to-background ratio

SI	Spectrum imaging
SIMS	Secondary ion mass spectrometry
SK	Stranski-Krastanov
SNR	Signal-to-noise ratio
SQUID	Superconducting QUantum Interference Device
SR	Smoluchowski ripening
STEM	Scanning transmission electron microsopy
STM	Scanning Tunneling Microscopy
TDS	Thermal diffuse scattering
TEM	Transmission electron microscopy
TF	Transfer function
TO	truncated-octahedral
WL	Wetting layer
WPOA	Weak phase object approximation
XPS	X-ray photo-electron spectroscopy
ZL	Zero-loss

Symbols

α	Convergence angle
$\bar{r}(t)$	Average radius of nanoparticles
β	Collection angle
ΔC	Defocus spread
ΔE	FWHM of the energy distribution of the incident electron beam
Δf	Defocus
λ	Electron wavelenght
$\mathcal{F}$	Fast Fourier transform

$\mathscr{F}$	Fourier transform
$\sigma(\theta)$	differential elastic cross section
$\sigma_k(\beta, \Delta)$	Partial cross section of ionization of an electron
θ	Semi angle between the electron ray and the optical axis
θ_E	Characteristic scattering angle
$\theta_{\text{cut-off}}$	Cut-off angle of the microscope in STEM mode
$\theta_{\text{cut-off}}$	Outer collection angle of ADF detector
θ_{inner}	Inner collection angle of ADF detector
θ_{outer}	Outer collection angle of ADF detector
$\vec{k}$	Wave vector in the spatial frequency space
a_0	Bohr radius of an atom
C	Coefficient in the power law describing the coarsening
c	Velocity of light
C_c	Chromatic aberration coefficient
C_3	Spherical aberration coefficient
C_5	Fifth order spherical aberration coefficient
c_{A}	Concentration of element A
d_{rate}	Dose rate
d_{total}	Electron dose
D'_s	surface mass-transport diffusion coefficient
E	Incident electron beam energy
E_{d}	Activation energy for surface diffusion of Pt adatoms
$f(\theta)$	Atomic-scattering factor
I_{beam}	Incident beam current
k_{B}	Boltzmann's constant

L	Camera length
m_0	Rest mass of the electron
N	Number of the monolayer
n	Exponent in the power law describing the coarsening
n_{den}	Areal density (atom/nm^2)
R	Segregation efficiency
T	Temperature
t	Annealing time
t_{exp}	Indicated exposure time
t_{pixel}	Pixel acquisition time
w	Residual
Z	Atomic number

Units

µm	Micrometer
eV	Electronvolt
f.i.b.	Fraction of incident beam
keV	Kiloelectronvolt
kV	Kilovolt
min	Minute
mrad	Milliradian
ms	Millisecond
nm	Nanometer
pA	Picoampere
px	Pixel
s	Second
Å	Ångström

List of Figures

List of Tables

Own scientific communications

7 peer-review publications, 1 submitted, 3 oral presentations, 5 poster presentations

Referred Journal Publications

E. Prestat, A. Barski, E. Bellet-Amalric, J.-F. Jacquot, R. Morel, D. Tainoff, A. Jain, C. Porret, P. Bayle-Guillemaud, M. Jamet, Structure and magnetism in strained $Ge_{1-x-y}Sn_xMn_y$ films grown on Ge(001) by low temperature molecular beam epitaxy, *Appl. Phys. Lett.*, **103** (2013), 012403. URL: http://link.aip.org/link/doi/10.1063/1.4813117

D. Tainoff, A. Barski, E. Prestat, D. Bourgault, E. Hadji, Y. Liu, P. Bayle-Guillemaud, O. Bourgeois, Thermoelectric properties of high quality nanostructured Ge:Mn thin films, *Submitted*. URL: http://arxiv.org/abs/1301.1319

E. Prestat, R. Popescu, H. Blank, R. Schneider, and D. Gerthsen, Coarsening of Pt nanoparticles on amorphous carbon film, *Surface Science*, **609** (2013), 195–202. URL: http://dx.doi.org/10.1016/j.susc.2012.12.014

I. Mouton, R. Lardé, E. Talbot, E. Cadel, C. Genevois, D. Blavette, V. Baltz, E. Prestat, P. Bayle-Guillemaud, A. Barski, M. Jamet. Composition and morphology of self-organized Mn-rich nanocolumns embedded in Ge: Correlation with the magnetic properties, *J. of Appl. Phys.*, **112** (2012), 113918. URL: http://link.aip.org/link/doi/10.1063/1.4768723

A. Jain, J.-C. Rojas-Sanchez, M. Cubukcu, J. Peiro, J. C. Le Breton, E. Prestat, C. Vergnaud, L. Louahadj, C. Portemont, C. Ducruet, V. Baltz, A. Barski, P. Bayle-Guillemaud, L. Vila, J.-P. Attané, E. Augendre, G. Desfonds, S. Gambarelli, H. Jaffrès, J.-M. George, M. Jamet. Crossover from spin accumulation into interface states to spin injection in the germanium conduction band, *Phys. Rev. Lett.*, **109** (2012) 106603. URL: http://link.aps.org/doi/10.1103/PhysRevLett.109.106603

A. Jain, C. Vergnaud, J. Peiro, J. C. Le Breton, E. Prestat, L. Louahadj, C. Portemont, C. Ducruet, V. Baltz, A. Marty, A. Barski, P. Bayle-Guillemaud, L. Vila, J.-P. Attané,

E. Augendre, H. Jaffrès, J.-M. George, and M. Jamet, Electrical and thermal spin accumulation in germanium, *Appl. Phys. Lett.*, **101** (2012), 022402. URL: http://link.aip.org/link/doi/10.1063/1.4733620

E. Arras, F. Lançon, I. Slipukhina, E. Prestat, M. Rovezzi, S. Tardif, A. Titov, P. Bayle-Guillemaud, F. d'Acapito, A. Barski, V. Favre-Nicolin, M. Jamet, J. Cibert, P. Pochet, Interface-driven phase separation in multifunctional materials: The case of the ferromagnetic semiconductor GeMn, *Phys. Rev. B*, **85** (2012), 115204. URL: http://link.aps.org/doi/10.1103/PhysRevB.85.115204

S. Laureti, S. Y. Suck, H. Haas, E. Prestat, O. Bourgeois, and D. Givord. Size dependence of exchange bias in Co/CoO nanostructures, *Phys. Rev. Lett.*, **108** (2012) 077205. URL: http://link.aps.org/doi/10.1103/PhysRevLett.108.077205

Presentations in national/international conferences

E. Prestat, J. M. Zuo, P. Bayle-Guillemaud, A. Barski, and M. Jamet, "Atomic scale quantification of Ge surface segregation in Si by correlative analysis of STEM and EELS imaging," *Oral presentation* at the EDGE 2013, St-Maxime, 2013.

E. Prestat, J. M. Zuo, P. Bayle-Guillemaud, A. Barski, and M. Jamet, "Atomic scale quantification of Ge diffusion in Si by correlative analysis of STEM and EELS imaging," *Oral presentation* at the JEELS 2012, Aix-les-Bains, 2012.

E. Prestat, P. Bayle Guillemaud, J. M. Zuo, A. Barski, and M. Jamet, "Atomic scale quantification of Ge diffusion in Si by correlative analysis of HAADF and EELS imaging," *Oral presentation* at the EMC 2012, Manchester, 2012. URL: http://www.emc2012.org/documents/Abstracts/Abstracts/EMC2012_0983.pdf

E. Prestat, F. Lançon, P. Bayle-Guillemaud, P. H. Jouneau, C. Bougerol, A. Barski, A. Jain, and M. Jamet, "HRTEM investigation of GeMn nanocolumns embedded in Ge for spintronics applications," *Poster presentation* at the EMC 2012, Manchester, 2012.

E. Prestat, F. Lançon, P. Bayle-Guillemaud, T. Devillers, A. Barski, A. Jain, and M. Jamet, "HRTEM investigation of GeMn nanocolumns embedded in Ge for spintronics applications," *Poster presentation* at the MC 2011, Kiel, 2011.

E. Prestat, F. Lançon, P. Bayle-Guillemaud, T. Devillers, A. Barski, A. Jain, and M. Jamet, "Etude de semiconduteurs ferromagnétique GeMn par microscopie électronique en transmission," *Poster presentation* at the Sfmu 2011, Strasbourg, 2011.

E. Prestat, F. Lançon, P. Bayle-Guillemaud, T. Devillers, A. Barski, A. Jain, and M. Jamet, "Etude de semiconduteurs ferromagnétique GeMn par microscopie électronique en transmission," *Poster presentation* at the JMC 2011, Troyes, 2010.

E. Prestat, R. Popescu, R. Schneider, H. Blank, and D. Gerthsen, "Coarsening of Pt clusters on amorphous carbon substrate," *Poster presentation* at the MC 2009, Graz, 2009.

Abstract

In this work, different systems have been studied using transmission electron microscopy (TEM) methods: Pt nanoparticles (NPs) on amorphous carbon, Ge quantum dots (QDs), Mn incorporation in Ge QDs and GeMn nanocolumns (NCs) embedded in Ge or GeSn matrix.

The coarsening of Pt NPs on amorphous carbon film was studied by TEM after annealing at temperatures between 200 °C and 300 °C for periods of up to 160 h. A significant increase of the average particle size is observed with increasing annealing time for all investigated temperatures. An in-situ annealing experiment reveals two coarsening stages. The first coarsening stage is dominated by Smoluchowski ripening whereas the second coarsening stage is dominated by surface Ostwald ripening. The Arrhenius-type dependence of the derived surface mass-transport coefficients yields an activation energy $E_\mathrm{d} = 0.84 \pm 0.08$ eV·atom^{-1} for the surface diffusion of Pt atoms on an amorphous carbon substrate.

Advanced TEM techniques have be used to obtain direct determination of composition profile with atomic resolution and large field of view by correlation of high angle annular dark field (HAADF) and electron energy loss spectroscopy (EELS) signals. Correlation of template amplitude with the simultaneously acquired EELS signal, allows an accurate quantification of Ge concentration at the atomic level for the SiGe system. The Ge concentration profile along the growth direction was explained by Ge surface segregation during the growth with a two-state exchange model. The Ge(Mn) QDs have been grown by molecular beam epitaxy (MBE). At growth temperature of 380 °C, SiMn precipitates are formed. Lowering the growth temperature at 220 °C allows limiting the lateral segregation of Mn in Ge.

Absolute composition obtained by STEM-EELS evidenced that the total atomic density in Ge(Mn) NCs is much higher than in the Ge matrix. Structural analysis by high resolution TEM (HRTEM) shows that the crystalline NCs exhibit a high degree of disorder. Experimental observations can be model with a modified α-phase structure if variants are introduced to cancel supplementary Bragg reflections and Ge atoms are substituted by Mn atoms. The structural and magnetic properties of Sn-doped GeMn layers have been studied. The matrix exhibits a GeSn solid solution while there is a Sn-rich GeSn shell around GeMn NCs. The magnetization in GeSnMn layers is higher than in GeMn films. This magnetic moment enhancement in GeSnMn is probably related to the modification of the electronic structure of Mn atoms in the NCs by the Sn-rich shell, which is formed around the NCs.

Résumé

Dans ce travail, différent systèmes ont été étudiés par des méthodes de microscopie électronique en transmission (TEM) : des nanoparticules (NPs) de Pt sur du carbone amorphe, des boîtes quantiques (QDs) de Ge, l'incorporation du Mn dans les QDs de Ge and des nanocolonnes (NCs) GeMn dans une matrice de Ge pure ou de GeSn.

Le mûrissement de NPs de Pt sur un film de carbone amorphe a été étudié par TEM haute résolution (HRTEM) après des recuits à des températures comprises entre 200 °C et 300 °C pour des durées allant jusqu'à 160 h. Une augmentation significative de la taille moyenne des particules est observée en augmentant la durée du recuit pour toutes les températures étudiées. Une expérience de recuit in-situ a révélé deux étapes de mûrissement : la première est dominée par le mûrissement de Smoluchowski tandis que la seconde est dominée par le mûrissement d'Oswald de surface. La dépendance de type Arrhenius du coefficient de transport de masse de surface donne une énergie d'activation de $E_\mathrm{d} = 0.84 \pm 0.08$ eV·atome^{-1} pour la diffusion des atomes de Pt sur un substrat de carbone amorphe.

Des techniques de TEM avancée ont été utilisées pour déterminer de manière direct des profiles de concentration à l'échelle atomique et avec un grand champ de vue par corrélation de signaux de champ sombre annulaire à grand angle (HAADF) et de spectroscopie de perte d'énergie d'électron (EELS). Cette méthode a été appliquée à l'étude de la concentration de Ge à l'échelle atomique dans le system SiGe. Le profile de concentration le long de la direction de croissance est expliqué par la ségrégation de surface des atomes de Ge pendant la croissance avec un modèle d'échange à deux états. L'incorporation de Mn dans les boîtes de Ge a été effectuée par croissance par jets moléculaire (MBE) de GeMn. Des précipités de SiMn sont formés pour des températures de croissance de 380 °C. La diminution de la température de croissance à 220 °C permet de limiter la ségrégation latérale de Mn et d'incorporer le Mn dans les QDs de Ge.

Les compositions absolues obtenues par STEM-EELS montrent que la densité atomique totale dans les NCs de GeMn est plus élevée que dans la matrice de Ge. Des études structurales par HRTEM indiquent que les NCs cristallines sont très désordonnées. Les observations expérimentales ont pu être modélisées par une structure de phase α modifiée, si des variants sont introduits afin d'annuler des réflections de Bragg supplémentaires et des atomes de Ge sont substituées par des atomes de Mn. Les propriétés structurales et magnétiques de films GeMn dopés Sn ont été étudiées. La matrice présente une solution solide tandis qu'une coquille riche en Sn est formée autour des NCs de GeMn. La magnétisation dans les couches de GeSnMn est plus élevée que dans celles de GeMn. L'augmentation du moment magnétique dans les couches de GeSnMn est probablement due à la modification de la structure électronique des atomes de Mn dans les NCs par la coquille de Sn.